Doctoral theses at NTNU, 2024:67

George-Claudiu Savulescu

The influence of asphaltenes and pour point depressants on the paraffin wax crystallization investigated by nuclear magnetic resonance and atomic force microscopy

Doctoral thesis

NTNU
Norwegian University of Science and Technology
Thesis for the Degree of
Philosophiae Doctor
Faculty of Natural Sciences
Department of Chemical Engineering

NTNU
Norwegian University of
Science and Technology

George-Claudiu Savulescu

The influence of asphaltenes and pour point depressants on the paraffin wax crystallization investigated by nuclear magnetic resonance and atomic force microscopy

Thesis for the Degree of Philosophiae Doctor

Trondheim, February 2024

Norwegian University of Science and Technology
Faculty of Natural Sciences
Department of Chemical Engineering

NTNU
Norwegian University of
Science and Technology

NTNU
Norwegian University of Science and Technology

Thesis for the Degree of Philosophiae Doctor

Faculty of Natural Sciences
Department of Chemical Engineering

ISBN 978-82-326-7734-4 (printed ver.)
ISBN 978-82-326-7733-7 (electronic ver.)
ISSN 1503-8181 (printed ver.)
ISSN 2703-8084 (online ver.)

Doctoral theses at NTNU, 2024:67

Printed by NTNU Grafisk senter

Preface

This thesis is submitted in partial fulfillment of the doctoral degree in the Faculty of Natural Sciences (NV) at the Norwegian University of Science and Technology (NTNU). It consist of four publications, focused on work produced at Ugelstad Laboratory in the Department of Chemical Engineering, under the supervision of Prof. Gisle Øye and the co-supervision of Dr. Sebastien Simon and Prof. Geir Sørland.

I obtained my Master's in Chemical Engineering at Imperial College London in United Kingdom in June 2020. Afterwards, I started pursuing my PhD degree in August 2020. The PhD work was carried out as part of SUBPRO (Subsea Production and Processing Center) from 2020 to 2024. This project was funded by the Norwegian Research Council, alongside with key partners from the energy industry in Norway, such as ABB, Aker Solutions, Aker BP, DNV GL, Neptune Energy, Lundin Energy and Equinor.

Acknowledgements

The last three and a half years in which I worked for my PhD degree have been inspiring for me. The prevailing reason for that was the number of great people which I met and helped me achieve my goals. In this page, I would like to express my gratitude for all the support and guidance.

Firstly, I would like to express my sincere gratitude to my main supervisor, Prof. Gisle Øye for all the guidance, scientific discussions, corrections, encouragement, and his help in defining research objectives.

Furthermore, my greatest gratitude goes to my co-supervisor, Dr. Sébastien Simon, for his dedication to supervise and mentor, for the scientific feedback, the corrections, the collaboration in the laboratory and most importantly, for his patience and empathy, which stimulated me to do better research.

I would also like to thank my second co-supervisor, Prof. Geir Sørland, for his help and dedication to design NMR experiments and all the scientific discussion, interpretation, and guidance, which followed.

I would like to also thank Prof. Maja Rücker, for hosting me for a research stay at Eindhoven University of Technology in the Netherlands, to develop stronger knowledge about atomic force microscopy. I would also like to acknowledge her contribution for scientific discussions and interpretation. It was a pleasure to work with her and her group.

I consider myself very lucky for the opportunity to have such a great team of supervisors. Without their continuous guidance, advice and encouragement, this thesis would not have been possible.

Furthermore, I would like to thank all the people involved in SUBPRO for offering me opportunities to expand my knowledge about subsea production and processing and to exchange great ideas with other researchers or partners from the energy industry all over the world.

I would also like to acknowledge the staff of Ugelstad Laboratory and in particular Jens Normann, for keeping the lab organized, for the training for lab equipment and for scientific feedback.

Lastly, I would like to thank all the other PhDs, postdocs, researchers and professors in Ugelstad lab who have been there throughout my three and a half years and have offered me great discussions and a nice social circle.

Abstract

Wax crystallization in pipelines in cold environments is a key challenge for flow assurance during crude oil production. Pour point depressants have been used to delay wax crystallization and gelling, by modifying rheological properties of the bulk fluid during wax crystallization. Asphaltenes, the most polar crude oil components have also been estimated to interact with wax during crystallization. Despite significant advances, the mechanism of interactions between wax and PPD or asphaltenes at molecular scale during crystallization is not yet fully understood and is often based on assumptions, which are not experimentally verified. This thesis aims to (a) introduce novel quantitative methods for the characterization of wax-inhibitor interactions during crystallization (b) use the developed method to achieve a better understanding of the wax-inhibitor interaction mechanism during crystallization.

Novel low field nuclear magnetic resonance (NMR) techniques were developed to relatively quantify the mobility of wax, inhibitor and solvent molecules in model systems. NMR results showed that an amount of dissolved wax lost mobility during cooling in a wax-only system. The formation of a wax crystal network with large pores led to a decrease in the mobility of dissolved species, which became trapped in the resulting matrix. This amount increased once asphaltenes were added and their concentration reached a critical value. NMR studies found that the critical threshold corresponded to a shift in the asphaltene aggregation state towards larger nanoaggregates and nanoclusters. The precipitation of PPD did not lead to the trapping of dissolved wax, which highlighted an altered crystallization mechanism, based on wax-PPD modified complexes. The toluene molecules had a higher level of freedom through the wax crystal network when a higher asphaltene concentration was used and an even higher level of freedom when the PPD was added. This demonstrated that asphaltene addition generated better solvent flowability, despite the higher amount of trapped wax.

Co-crystallization of wax with asphaltene and PPD was quantitatively demonstrated by high resolution NMR methods. Atomic force microscopy (AFM) was then introduced as a technique to characterize the resulting solid crystal networks, altered by the co-crystallization mechanism. The topography and elasticity of crystal network surfaces were investigated. The former led to the quantification of changes in crystal size, shape and in the interlocking patterns of the crystal network. The latter demonstrated that an amorphous, softer layer of wax (50-100 nm), formed on the top of wax and wax-asphaltene crystal networks, because of steric hindrance during crystallization or co-crystallization, which prevented a part of the wax to reach fully crystalline phases. The presence of asphaltene nanoaggregates and nanoclusters during crystallization

generated a loss in stiffness and a swelling of this layer. This suggested that higher amounts of trapped dissolved wax observed by NMR could be correlated with a lower degree of crystallinity for the resulting crystal network.

Wax crystallization rates were determined at the surface of the crystals by multiple low field NMR techniques, which were applied to both model systems and complex crude oils, containing asphaltenes and resins. The accuracy of NMR for wax content determination was compared against differential scanning calorimetry (DSC). NMR FID (free induction decay) allowed for a lower cooling rate, closer to thermodynamic crystallization conditions. It also used less thermodynamic assumptions and generated a good level of reproduction for samples with high wax content (>15%).

The techniques developed in this thesis could be used on a wider range of systems, to establish a relationship between interactions during crystallization at molecular scale and rheological phenomena observed at industrial scale. This would facilitate the prediction of flow assurance problems that might arise in oils with known chemical composition (wax, asphaltene, added PPD).

List of Publications

Paper I

George Claudiu Savulescu, Sébastien Simon, Geir Sørland, Gisle Øye

New NMR approaches on the evolution of wax mobility during wax crystallization

Energy&Fuels **2022**, *36(1),* p. 350-360, doi: 10.1021/acs.energyfuels.1c03613

Paper II

George Claudiu Savulescu, Sébastien Simon, Geir Sørland, Gisle Øye

Understanding the effect of asphaltenes and wax inhibitors on wax crystallization by improved NMR techniques

Ind. Eng. Chem. Res. **2023***, 62(44),* p. 18251-18262, doi: 10.1021/acs.iecr.3c02218

Paper III

George Claudiu Savulescu, Maja Rücker, Sébastien Simon, Gisle Øye

Alterations in paraffin wax crystal networks induced by asphaltenes and pour point depressants, investigated by atomic force microscopy

To be submitted in Colloids and Interfaces A: Physicochemical and Engineering Aspects

Paper IV

George Claudiu Savulescu, Sébastien Simon, Geir Sørland, Gisle Øye

Novel NMR techniques to assess the wax precipitation evolution in crude oil systems

Energy & Fuels **2023**, *37* (1), 291–300. doi : 10.1021/acs.energyfuels.2c03309.

Conferences

Oral presentation at the 21st International Conference on Petroleum Phase Behavior and Fouling

Authors: George Claudiu Savulescu, Sébastien Simon, Geir Sørland, Gisle Øye

Title: New NMR approaches on the quantification of wax-inhibitor interactions in crude oils

Location and date: Remote (online); June 2021

Oral presentation at the 22nd International Conference on Petroleum Phase Behavior and Fouling

Authors: George Claudiu Savulescu, Sébastien Simon, Geir Sørland, Gisle Øye

Title: Novel NMR techniques to assess the wax precipitation evolution in crude oil systems

Location and date: Bucaramanga, Colombia; June 2022

Oral presentation at BN-SOC (Brazil-Norway Subsea Operations Consortium) INTPART Workshop

Authors: George Claudiu Savulescu, Sébastien Simon, Geir Sørland, Gisle Øye

Title: Flow Improvers for Waxy Crudes

Location and date: Rio de Janeiro, Brazil; November 2022

Poster presentation at the 37th European Colloid and Interface Science (ECIS)

Authors: George Claudiu Savulescu, Maja Rücker, Sébastien Simon, Gisle Øye

Title: Atomic force microscopy for the investigation of wax crystal network alterations induced by crystal modifiers

Location and date: Naples, Italy; September 2023

Table of Contents

1.Introduction

In 2021, crude oil represented the most used primary energy source (Figure 1), generating around 190 EJ (10^{18} J) or 52.000 TWh of energy, which accounts for 30.9% of the world primary energy demand [1]. This corresponds to a global oil supply of about 101 million barrels per day. Recent forecasts by the International Energy Agency (IEA) estimate that despite the ongoing energy transition, a global oil supply of 54.8 million barrels per day will still be needed in 2050 [2]. The crude oil extraction on the Norwegian continental shelf of the North Sea currently covers about 2% of the global crude oil production [3].

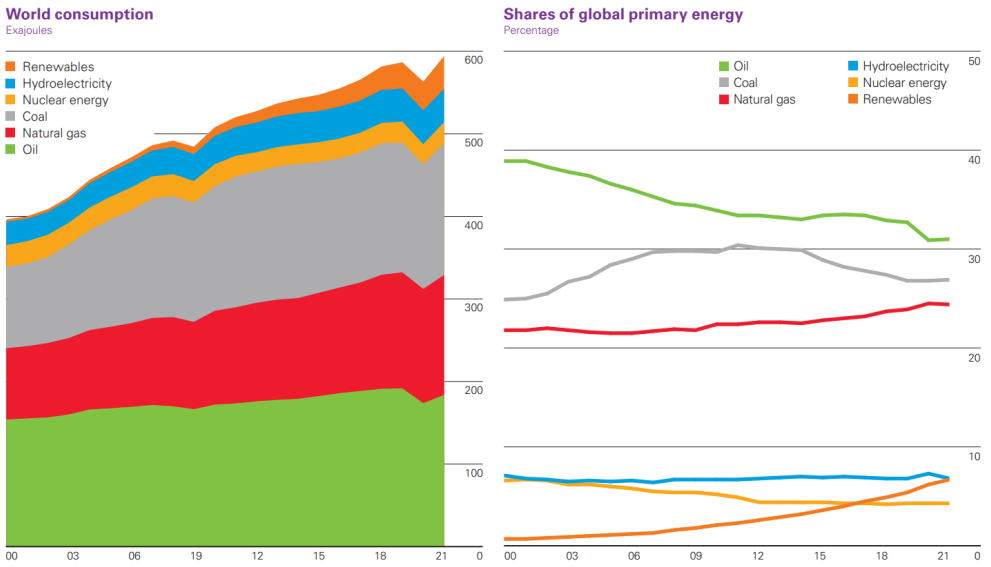

Figure 1: Global primary energy consumption by energy type: absolute values of consumptions by type – left side, share of global primary energy by energy type – right side [1].

The oil industry aims to extend its traditional operations by transporting oil through deep marine environments, using subsea production systems [4 5]. This type of transport is performed in pipelines at very low temperatures occurring on the seabed (i.e. 4 °C), aggravating issues related to flow assurance. The gelation and crystallization of paraffin wax represent some of the main difficulties encountered during subsea extractions [5 6]. As the waxy oil is transported from the well to the production platform, the low temperature conditions often induce the deposition of wax on pipeline walls during flow or wax gelation during shutdown. The latter

usually results in a transformation of the entire crude oil fluid into a gel matrix with high viscosity [5] [6]. Consequences could range from a reduction in the production efficiency to difficulties of restarting the systems or a complete shutdown of the operation field [5] [6]. The latter often leads to a very high economic impact. Therefore, wax management has become a major topic for the crude oil industry [7].

One of the main techniques used for wax management is chemical prevention, which is based on the use of designated wax inhibitors, such as polymeric pour point depressants [8]. These substances are designed to interfere with wax gelation and crystallization, reducing the undesired effects. The economic benefit of the elimination of flow assurance problems often exceeds the chemical costs by a significant margin [5] [6]. Asphaltenes, which are surface-active crude oil components, could also interact with wax, generating comparable effects to the ones of PPDs [5] [9] [10] . The effects of PPDs and asphaltenes were researched significantly, by performing tests at large scale on the rheological properties of crude oils [11] [12]. However, the exact mechanism of interaction at molecular level between wax and asphaltene or PPDs were only briefly proposed in literature. Contradicting results about interactions during the phases of crystallization have often been reported in multiple studies [9] [10] [13]. The exact composition of the crude oil also varies, according to each extraction field. This uncertainty thereby decreases the efficiency of wax management and often induces inconclusive results about the choice of the most suitable wax management methods [5] [6]. Therefore, there is a need for a more thorough understanding of interactions between wax and inhibitors at molecular level, which could predict the properties of crude oils as a function of oil composition, asphaltene content and added PPD.

2. Crude oil properties

2.1. Crude oil – origin and formation

Crude oil is a mixture of hydrocarbons and other organic components found in geological formations, often in sedimentary rocks. Crude oil represents a fossil fuel, alongside with natural gas and coal. It is derived from fossilized organic materials, coming from once living organisms, such as algae and zooplankton [13] [14]. These organisms settled on the bottom of seas and lakes, under layers of water with little to no oxygen or under sedimentary formations. Over time, this promoted a build-up of heat and pressure which facilitated anaerobic decay. The result of the anaerobic decay was the formation of kerogen, a complex waxy mixture of hydrocarbon compounds, incorporating some remaining nitrogen and sulfur [15] [16] . Kerogen transformed to fossil fuels over a period of million of years, mostly by radical rearrangements. This process is also known as crude oil maturation and has a very complex nature, usually leading to the formation of very complex crude oil deposits, with different composition from one location to another.

2.2. Elemental composition

The high hydrocarbon content in crude oil generates an elemental composition dominated by carbon and hydrogen (Table 1). Nonetheless, other elements such as nitrogen, oxygen or sulfur are present in some crude oils, depending on the type of maturation process. Metals, such as vanadium, nickel, copper or iron could also be present in crude oils in small quantities.

Table 1: Elemental composition of typical crude oils [15].

Element	Percentage
Carbon	83-87%
Hydrogen	10-14%
Nitrogen	0.1-2%
Oxygen	0.05-1.5%
Sulfur	0.05-6%
Metals (V, Ni, Cu, Fe)	<1000 ppm

2.3. Crude oil fractionation

A standardized procedure, also known as SARA analysis, was developed to characterize four fractions of crude oils: saturates (S), aromatic (A). resins (R) and asphaltenes (A) [17] [18]. The different fractions could be separated due to differences in polarity and solubility.

The least polar group, the saturates, is mainly composed of saturated hydrocarbons with a linear, branched or cyclic chain. Paraffin waxes and naphthenes, containing one or more ring structures, are often part of this fraction. Aromatics are more polar than saturates, mainly due to the presence of aromatic rings and heteroatoms, such as sulfur, oxygen and nitrogen, in their chemical structure. They often include benzene derivates, such as naphthalene, tetralin or anthracene. Resins and asphaltenes are the most polar fractions of the crude oils. Alike aromatics, they often contain aromatic rings and heteroatoms. However, asphaltenes and resins typically include more aromatic rings, stronger polar moieties and more complex chemical structures. The complex and often unknown structures of resins and asphaltenes make it difficult to distinguish between the fraction of aromatics and individual resins or individual asphaltenes. On the other hand, asphaltenes and resins could be separated by their solubility in light alkanes, such as n-pentane, n-hexane or n-heptane. Asphaltenes precipitate in such solvents, while resins solubilize [17] [18].

Asphaltene precipitation in low molecular weight alkane is often used as the first step of SARA analysis. This is followed by asphaltene recovery by filtrating the precipitate. The de-asphalted oil, also known as maltenes is further separated into saturates, aromatics and resins by high performance liquid chromatography (HPLC) [17] or other methods that were tailored for this purpose [19]. SARA fractionation could also take place during crude oil refining, where the difference in boiling points is used to separate the four fractions. Final products, such as gasoline, diesel or kerosene, often tailored to the demands of the market, could be obtained by adjusting the separation process during refining [16] [20].

Although SARA is effective for an approximate determination of the fractions in crude oils, its use for flow assurance is rather limited, because it cannot provide information about the exact chemical structure of asphaltenes or about the exact content of paraffin wax with a specific chemical composition.

2.4. Paraffin wax

Paraffin waxes are n-, iso- or cyclo- alkanes, with a number of carbons between 16 and 50, or sometimes higher [21]. Waxes are part of the higher molecular weight part of the crude oils. Crude oils contain waxes in variable concentrations, usually dependent on the extraction field.

Wax comprising mostly of n-alkanes is defined as macrocrystalline wax, while wax with branched (iso-) and cycloalkanes is defined as microcrystalline wax (Figure 2) [22] [23]. Macrocrystalline wax typically comprises of shorter chain alkanes, with 16 to 40 carbon atoms. Although microcrystalline wax also starts from alkanes with 16 carbon atoms, it is usually present in crude oils as alkanes with higher molecular weight than for macrocrystalline wax. Macrocrystalline wax has a tendency to form large rod or needle-like crystals, while microcrystalline wax forms smaller, rounder and more amorphous crystals [24]. Consequently, macrocrystalline wax is more difficult to deal with during oil extraction, as it forms larger, more crystalline structures, which generate higher viscosity and higher gel yield strength in the remaining fluid [25]. The presence of microcrystalline wax has been shown to modify the mechanism of precipitation for macrocrystalline wax [26]. The addition of as little as 1% microcrystalline wax in a solution with 5% macrocrystalline wax shifted the behavior of macrocrystalline wax completely. In the resulting system, the macrocrystalline wax had the same crystallization pattern as microcrystalline wax [26].

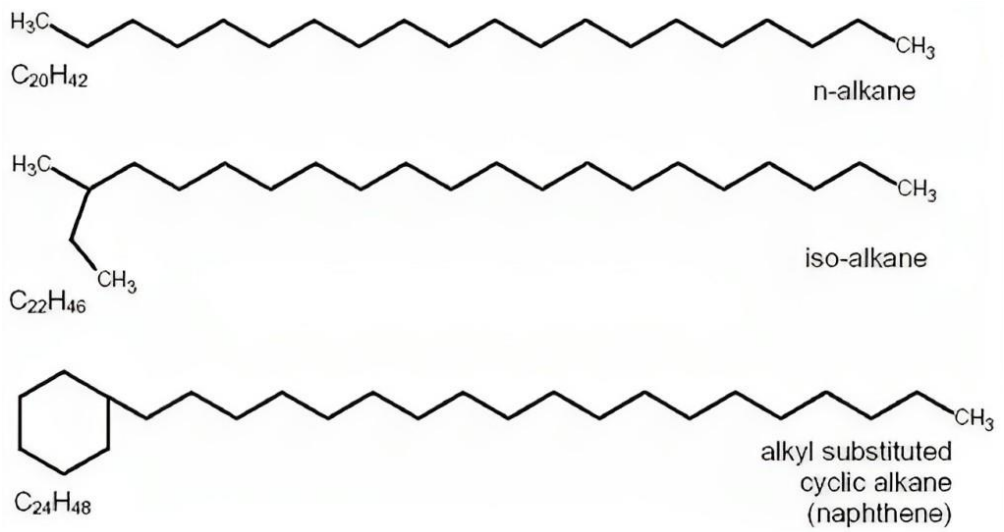

Figure 2: Chemical structure of linear paraffin wax (n-alkane), branched paraffin wax (iso-alkane) or paraffin wax containing cycloalkanes (alkyl substituted cyclic alkane).

The thermodynamic properties of paraffin wax have also been investigated for its applications as a phase change building material [27] [28] [29]. The exothermic crystallization of wax facilitates heat storage for renewable heating systems.

2.5. Asphaltenes

Asphaltenes represent the part of crude oil with a higher level of polarity [5] [30] . Their definition and method of preparation rely on the principle that asphaltenes are constituents of crude oil that are insoluble in strongly non-polar n-alkanes with low molecular weight, such as n-hexane or n-heptane, but that are soluble in less non-polar aromatic solvents, such as toluene [5] [31].

The chemical structure of asphaltenes consists of polycyclic aromatic hydrocarbons with aliphatic chains. Both contain heteroatoms such as oxygen, sulfur and nitrogen. Traces of heavy metals such as vanadium, nickel and iron could also be present. The exact chemical composition of asphaltenes is dependent on the oil field they were extracted from. The molecular masses can vary between 400 g/mol and 1500 g/mol. Two models were proposed for the chemical structure of asphaltenes: the archipelago and the continental models (Figure 3) [32] [33]. In the archipelago model, the structure is based on multiple, smaller polyaromatic centers bonded together by aliphatic or naphthenic moieties. In the continental model, the polyaromatic components are focused in one center, comprising of more fused rings than in the archipelago model [34] [35] [36].

Asphaltenes self-aggregate when they are in specific concentration intervals in solution or in crude oil systems. The Yen-Mullins model was proposed to explain the aggregation mechanism and the properties of resulting colloidal suspensions (Figure 4) [34] . The concentration of asphaltenes was a decisive factor for the aggregation state. A 2-step transition was observed when the concentration was increased. Firstly, asphaltene monomers (1.5 nm in diameter) self-associate to form nanoaggregates (2 nm in diameter) when the critical asphaltene nanoaggregate concentration (CNAC) was reached. Secondly, at higher concentrations, asphaltenes arrange into nanoclusters (5nm and higher in diameter), which replace the nanoaggregates. The calculation of CNAC and the demonstration of the Yen-Mullins model have been researched with various techniques such as SAXS (small-angle X-ray scattering), SANS (small-angle neutron scattering) [37] [38] and AFM (atomic force microscopy) [39] [40]. However, there are still uncertainties about the ring size of asphaltenes and about the effect of chemical composition on the Yen-Mullins model [34].

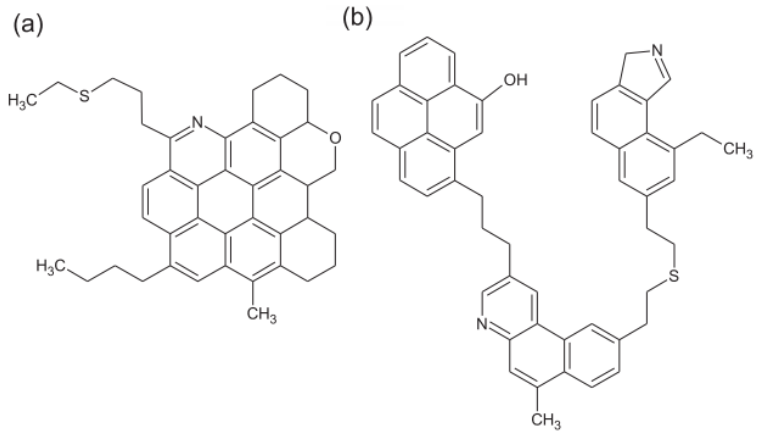

Figure 3: Proposed asphaltene chemical structures: (a) “island” asphaltene model, (b) “archipelago” asphaltene model [35 41].

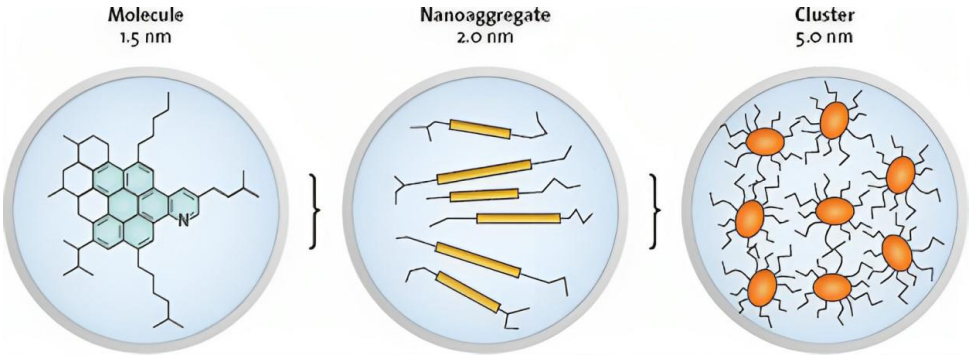

Figure 4: Yen-Mullins asphaltene model: once the critical nanoaggregate asphaltene concentration (CNAC) is reached, asphaltene molecules (left) rearrange into nanoaggregates (center). At higher concentrations, nanoaggregates (center) rearrange into larger clusters (right) [Copyright from [34]].

3. Flow Assurance

Flow assurance is an engineering topic in the oil and gas industry, whose main focus is to ensure an efficient flow of hydrocarbons, increasing economic feasibility and profitability of the process [5] [6]. Flow assurance aims to alleviate issues which arise due to the chemical and physical behavior of the fluid and the corresponding intermediate states which form during transport.

3.1. Problems related to wax appearance.

The gelation and deposition of wax could occur during continuous flow in pipelines due to low temperatures. The most frequent arising issues are restarting problems caused by the gelling of the oil, a reduction of the flow or plugging of the pipeline, increased pumping pressure generated by increased viscosity, reduced operating efficiency with interruptions and shutdowns in production, high costs of wax removal (especially in pipelines located in subsea environments) and interference with operation of valves and instruments which could lead to safety hazards [5] [6].

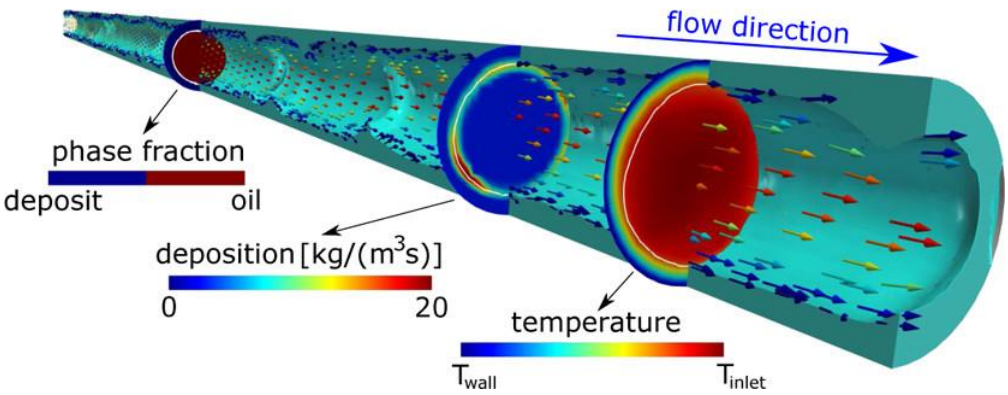

Figure 5: Schematics of wax deposition induced by a radial temperature gradient. Wax deposition is ongoing on pipeline walls, due to a high radial temperature gradient. [Copyright from [42]].

When the pipeline wall reaches or drops below the wax appearance temperature (WAT), wax starts depositing on the pipeline wall (Figure 5). A radial temperature gradient within the bulk oil is common in such systems (Figure 5), where the pipeline wall is affected more strongly than the inner bulk fluid by the low temperature in the surrounding environment. If the temperatures are low enough, crystallization continues, generating thicker layers on the walls

of the pipelines. Paraffin wax with higher molecular weights tend to precipitate first on the walls, leading to a decreased molecular weight for the remaining bulk fluid [5 6 42].

When production is shut down and the flow is stopped, the crystallization of wax is more likely to affect the bulk fluid. Paraffin waxes separate as needle or plate crystals, which interact with each other, generating a crystal network in which lighter oil components lose mobility and become trapped. This process results in a crude oil gel matrix, which increases the fluid viscosity to critical levels, inducing a significantly lowered oil flowability and a consequent pressure loss in the pipelines. A percentage of wax as low as 2% was found to cause gelling [43]. Other crude oil components such as asphaltenes and naphthenic acids have been demonstrated to interact with wax during gelation and to influence the resulting properties of the crude oil gel matrix [10 44]. However, more research needs to be done to understand the exact mechanism of interaction. The gelling of the crude oil leads to severe problems during production restart. The determination of the pour point, the point at which the oil stops flowing, is therefore more relevant for assessing the impact of gelation than the WAT, which is more relevant for the characterization of the deposition onset.

3.2. Wax management techniques

Several strategies have been proposed to combat wax-related problems in crude oils. A first focus for the wax-related flow assurance strategy has been to decrease the effect of the cold environment on the pipeline. Insulation and heating of the fluid downhole or along the flowline are common techniques to increase the temperature inside the pipeline. For example, vacuum insulation has been applied to multiple subsea extraction fields [45]. Pipeline heating is a more expensive option, but it can have an increased feasibility if it alleviates other flow assurance problems, such as gas hydrates, at the same time [46]. Electricity or hot water are often used for the heating procedures. The systems are based on pipeline bundles or on pipe-in-pipe systems. A method which is more suitable for subsea environments, also known as the shock chilling method, is currently being researched. It is based on the application of a cold flow, which eliminates the radial temperature gradient, promoting the precipitation of the wax in the bulk fluid, rather than on the walls. The crude oil will subsequently be extracted as a dispersion of wax particles [47].

Mechanical wax management strategies are also used in industry. Pigging of pipelines is carried out frequently on installations with high risk for wax formation [48]. This process eliminates the deposited wax and prevents the build-up of a thick wax layer which affects

flowability. Some disadvantages of pigging include the incapacity to remove the entire layer of deposited wax and the extensive timeframe for operation shutdown required to execute the process. Therefore, pigging is often accompanied by other wax management techniques, such as chemical treatment of the oil [5]. Less popular wax management strategies are the use of wireline cutters or of acoustic/sonic treatment, the latter of which was only investigated on an experimental scale [49].

Lastly, chemical wax management strategies have been created. Wax inhibitors, such as polymeric pour point depressants (PPDs) or dispersants and surfactants are often used for this purpose. The PPDs alter the wax crystallization mechanism, acting as a crystal modifier (Figure 6), by various mechanisms of interaction with wax (i.e. co-crystallization). The result is a distortion of the properties of both the resulting wax crystal networks (Figure 7) and the crude oil gel matrix which could form during shutdown [13] [50]. This process often improves the flowability of the oil and alleviates the wax-related problems. One concern with the use of PPDs is the economic costs for high quantities of PPD. Therefore, there is a high focus on designing PPDs with strong impact in low quantities. Wax dispersants and surfactants interfere with the ability of wax to attach to the pipeline wall, by reducing wax-wall interactions [51] [52]. Moreover, they stimulate the dispersion of the wax particles in the bulk fluid.

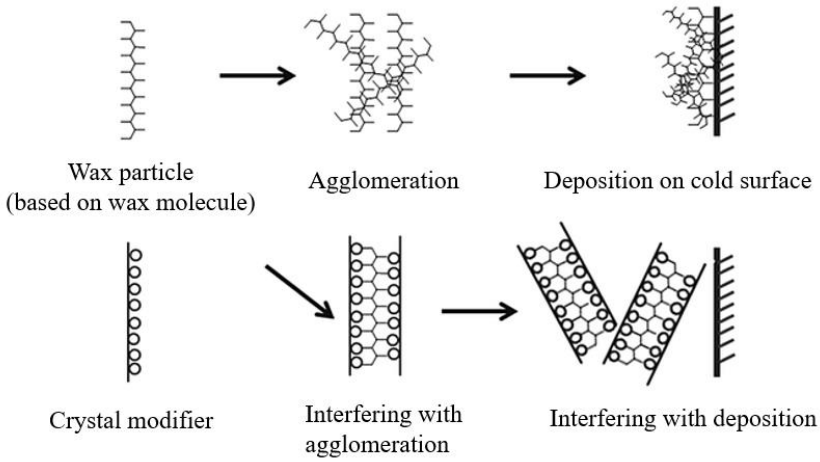

Figure 6: Effect of crystal modifier on wax deposition on the wall. The addition of crystal modifier prevents deposition and promotes dispersion towards the bulk fluid, due to steric hindrance between wax-modifier complexes [Adapted from [8] - copyright].

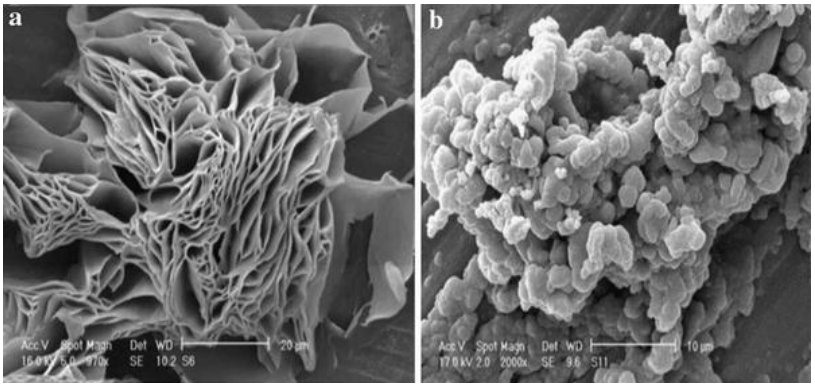

Figure 7: Scanning electron microscopy (SEM) scans of wax crystal network (a) and wax-PPD crystal network (b). The PPD alters the shape and the size of the crystals, modifying the topography of the resulting crystal network [Copyright from [50]].

3.3. Asphaltene deposition and management

Asphaltenes could also deposit during extraction, generating flow assurance problems. Asphaltene deposition represents a major issue both in the upstream and the downstream parts of the process. It can cause blockages in reservoir pores in the near-well area, as well as in the production tubing and downstream pipelines and further facilities [5] [53]. Asphaltene deposition is facilitated by minor increases in the polarity of the crude oil. The onset could be triggered by factors such as acid stimulation, pressure drops leading to breakout of gases, scale inhibitor treatments or crude oil mixing [5].

Asphaltene deposition could be prevented mainly by chemical treatment with asphaltene inhibitors, dispersants and dissolvers [5] [54]. In crude oils, polar resins are believed to stabilize asphaltene by adsorbing on the surface of asphaltene nanoaggregates. The asphaltene inhibitors have the same behavior of resins and can strengthen the stability of asphaltenes in crude oils with insufficient asphaltene stability. Asphaltene dispersants stimulate the formation of a stable dispersion of the asphaltene particles in the bulk fluid, by reducing the size of the flocs. Asphaltene dissolvers, typically based on aromatic solvents, could be used to eliminate asphaltene deposits. Xylene is the most used dissolver, but toluene or pyridine also work with lower efficiency [5].

3.4. Other flow assurance issues

Wax and asphaltene deposition could also be accompanied by other flow assurance issues. Some of these include the formation of gas hydrates and scale.

Gas hydrates are ice-like clathrate solids, with a cage-like structure in which the gas molecules are trapped by the network formed by hydrogen-bonded water molecules. Their formation is promoted by subsea conditions, which induce a very low temperature and high pressure in the pipelines[5] [55].The prevention of gas hydrates could be achieved by imposing temperature and pressure conditions outside the range for hydrate formation. Other strategies for gas hydrate management include water separation (dehydration), modification of the gas phase by introducing another gas or chemical treatment [5].

Scale is formed by ionic compounds from aqueous solution. The most common salts causing scales are calcium carbonate ($CaCO_3$), sulfates of Group II metals, such as calcium sulfate ($CaSO_4$), strontium sulfate ($SrSO_4$), barium sulfate ($BaSO_4$), sulfides of heavy metals, such as iron sulfide (FeS), lead sulfide (PbS) or zinc sulfide (ZnS) or sodium chloride (NaCl) [5]. To inhibit these scales, industry often uses polymers based on polyphosphates, phosphate esters, nonpolymeric phosphonates, polyphosphonates or polycarboxylates [5] [56].

4. Wax crystallization mechanism

Paraffin nucleation is a stochastic process, which requires supercooling for initiation [57]. This implied that the start of crystal formation does not coincide with the highest thermodynamic solid-liquid equilibrium temperature. Instead, it is required that the fluid reaches a certain temperature below saturation, known as a metastable state, which initiates the crystal nucleation process. The difference between the saturation temperature and the crystallization temperature is known as the degree of supercooling [57].

Wax crystallization typically includes 3 steps: nucleation, crystal growth, and agglomeration of crystal particles. When the wax appearance temperature is reached, supersaturated waxes in the oil start forming crystal nuclei. Wax nuclei grow and sometimes aggregate, forming wax crystal particles. The wax crystal particles self-associate, generating a three-dimensional crystal network [13 58] .

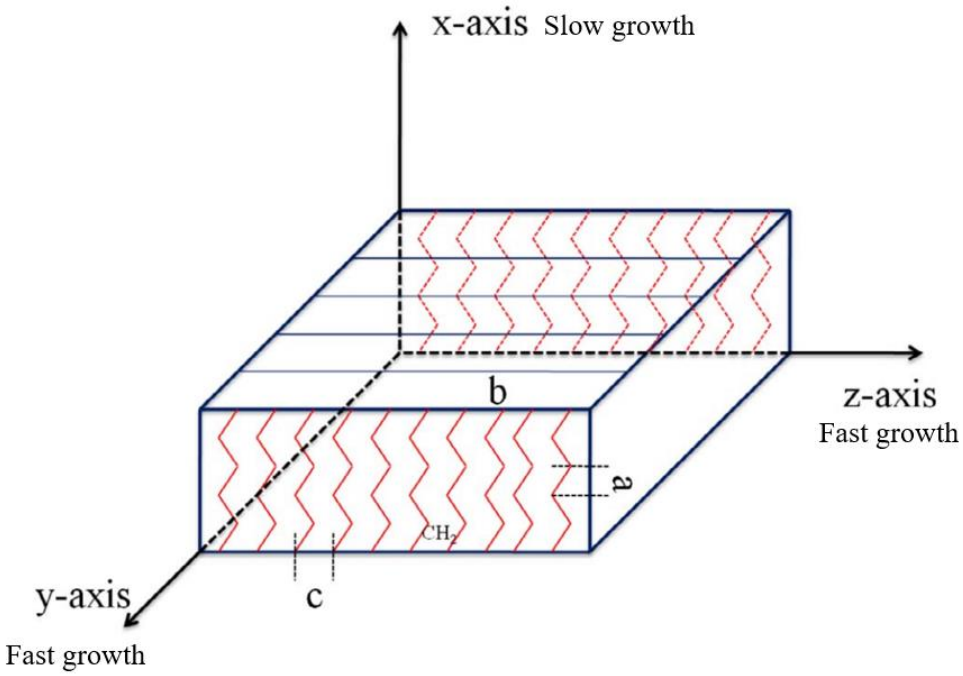

Figure 8: Mechanism of crystal growth for n-alkanes. The shape of the long chain alkanes promotes a fast growth in 2 directions (y, z) and a slow growth in the third direction (y). The result is the formation of crystals with the shape of a needle/plate [Copyright from [59]].

Wax molecules have a spin structure, which is organized to achieve the minimum potential energy possible. This structure determines the molecular arrangement and the level of

restriction between individual wax molecules [13]. When the temperature decreases below the WAT, the attraction between wax molecules is greater than that between wax and solvent molecules in the crude oil, which leads to the start of wax precipitation through nucleation. The first wax crystals act as a nucleation site for the remaining dissolved wax, which accelerates the crystallization process [13 60].

During the phase of crystal growth, wax crystals are expected to grow in 2 dimensions, forming plate-like crystals (Figure 8). This is due to co-crystallization of n-alkanes with long carbon chains, which prefer a parallel alignment, promoting a needle, rod or plate crystal shape [43 61]. However, if the chemical structure of wax is more branched, a deviation from needle shape was noticed [22 26 62]. The branched chemical structure sterically hinders the parallel alignment of alkanes and promotes stronger growth in the third direction (x in Figure 8). Therefore, in such cases, the crystal shape could be rounder and more dendritic.

During agglomeration, wax crystals interlock, generating three-dimensional networks. It is very common for crude oil liquid and solvents to become trapped in the newly formed crystal network in the initial phases of agglomeration [63 64] . This phenomenon leads to a reduction in the molecular mobility of the components in the liquid, often causing the formation of a gel matrix, which dominates the entire bulk fluid. The properties of the resulting gel matrix often depend on the type of chemical composition of the wax. N-alkanes form a wax crystal network with larger pores (Figure 9, (A)), due to the plate shape of the crystals [62]. On the other hand, branched alkanes with rounder crystal shapes form crystal networks with smaller pores (Figure 9, (B)). Therefore, a higher quantity of fluid could lose mobility and become trapped when n-alkanes are present. This implies that the presence of branched alkanes reduces the ability of the crystal network to trap dissolved species and delays the gelation of the bulk fluid. The result is a weakened gel, with lower gel yield strength [25]. Moreover, the presence of branched alkanes does not increase the viscosity of crude oils to the same extent as the n-alkanes, mainly due to the rounder, more dendritic shape of the crystals.

Branched alkanes were reported to influence the behavior of n-alkanes even in small quantities. A previous study investigated the effect of the addition of a percentage of branched alkanes (microcrystalline wax) as low as 1% to a system with 5% n-alkane (macrocrystalline wax). This completely changed the behavior of the gel, which behave as a fully microcrystalline wax system [26].

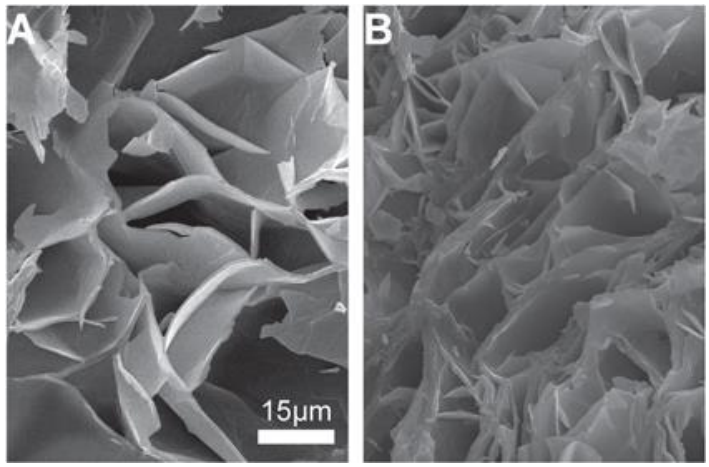

Figure 9: Cryo-scanning electron microscopy (cryo-SEM) scans of wax crystal networks from: (A) macrocrystalline wax, (B) microcrystalline wax [Copyright from [62]].

The gelling of wax could also be affected by thermal history. A high cooling rate and a consequent fast crystallization could prevent the crystals from achieving full growth. This results in a crystal network with smaller pores, which could trap a lower amount of dissolved species. A weaker gel will therefore be formed [65].

5. Wax inhibition by chemical methods

Wax inhibitors are widely used to reduce problems generated by wax deposition and gelation. The chemical structure and the mechanism of inhibition vary among the most common inhibitors. Economical concerns are also considered about the amounts of inhibitors needed for inhibition and about inhibitor removal processes [5].

5.1. Relevant terminology

The comparison of the efficiency of different wax inhibition methods is often carried out by comparing a range of parameters, created for this purpose. This sub-chapter presents an overview of the most used such parameters.

5.1.1. Wax Appearance Temperature (WAT)

The wax appearance temperature (WAT) is the highest temperature when wax crystallization is present, during cooling [5 6]. For thermodynamic analysis, the opposite of the WAT, also known as the wax dissolution temperature (WDT), has also been proposed [66]. The WDT corresponds to the highest temperature at which wax crystals are present, during heating. Thermal history may create a hysteresis between the WAT and WDT, which was investigated in multiple studies [66] . The WAT itself is usually lower than the thermodynamic solubility limit, partially due to thermal history (i.e. high cooling rates) and partially due to detection limits of the analytical methods available for this purpose. Methods used for WAT determination include differential scanning calorimetry (DSC), cross polarized microscopy (CPM), nuclear magnetic resonance (NMR), Fourier transform infrared spectroscopy (FTIR), density variation testing, sonic testing [5 6 61 67 68 69]. It is inconclusive which WAT determination method is the most accurate, because most of them rely on thermodynamic and chemical assumptions or produce an error due to the detection limit.

WAT defines the point of the wax deposition start. Therefore, it is a standard parameter used to characterize wax deposition, as highlighted earlier in Section 3.1. To define gelation processes, the pour point (Section 5.1.3) is more relevant.

5.1.2. Wax Precipitation Curve

The wax precipitation curve measures the cumulative percentage of precipitated wax at each temperature. Therefore, some of the techniques used for WAT determination, such as CPM, or

density variation testing, are not suitable for WPC determination. The most common technique to measure the WPC is DSC, which can quantify the total heat released by wax from the start of crystallization to the measurement point. A relationship between the released heat and the amount of precipitated wax has been proposed in multiple studies [67] [70] [71], but there is no consensus on the most suitable approach. Low field NMR has been proposed as a method to calculate the WPC, by quantifying the amount of protons from liquid state wax with temperature [61] [68] [72]. However, a protocol remained to be developed to improve the detection limit for complex crude oil systems [61].

5.1.3. Pour Point

The pour point is the temperature at which the liquid cannot flow freely, during cooling. The pour point usually occurs after the complete gelation of the wax system. While the WAT determines the point of the start of deposition on pipeline walls, the pour point is used to measure the point at which the liquid in the pipeline stops flowing, due to cooling during pipeline shutdown. The pour point is usually measured by standardized methods [73] [74] [75] [76]. These methods rely on detection of the movement of the crude oil sample visually [73] [76] or with a camera [74]. More advanced methods use a non-rotating piston, which is partially submerged in the crude oil sample[75]. When the pour point occurs, viscosity increases above a threshold which causes the deflection of the piston, which is pushed outside the system.

5.1.4. Gel Yield Strength

For waxy gels, gel yield strength is conventionally defined as the maximum shear stress recorded during gel breakage [25]. When a shear force is applied, the waxy gels initially follow Hookean behavior (i.e. the measured stress is proportional with the applied strain)[77]. When the shear stress reaches a threshold, the system undergoes gel breakage. The gel yield strength is conventionally referred to as the maximum shear stress during this phase. After gel breakage, gel degradation processes occur, reducing the shear stress.

The measurement of gel yield strength is performed with rheological methods and show good accuracy when the shear rate is sufficiently low (below 0.1 s^{-1}) [78].

5.2. Wax inhibitors

As mentioned in Section 3.2., wax inhibitors could be classified into pour point depressants, crystal modifiers, surfactant and dispersants [5]. Some inhibitors have a pronounced effect on the

WAT and are also known as thermodynamic inhibitors. Others have a pronounced effect on the pour point and they are known as pour point depressants (PPDs). However, PPDs could also affect the WAT [61]. Moreover, PPDs could also act as crystal modifiers, by interfering with the wax crystallization mechanism and by distorting the resulting crystal networks[13]. Dispersants and surfactants often change the wettability of the pipeline wall surface to water-like wettability. Some dispersants and surfactants induce the formation of a weak layer to which wax crystals cannot attach as effectively as on the wall. Therefore, the turbulent flow often shear off the crystals, preventing the accumulation on the walls [5 51 52] .

5.2.1. Pour point depressants

PPDs are typically based on a polymer configuration. Three main classes of PPDs have been identified in previous studies: ethylene polymers or ethylene-based copolymers, comb polymers and branched polymers with long alkyl groups (Figure 10) [5]. Polyethylene has been investigated in previous studies for its behavior as PPD. However, the results were not satisfactory [79], since better PPDs were obtained with ethylene copolymers, such as ethylene-propylene, ethylene vinyl-acetate (EVA) or ethylene-acrylonitrile copolymers [5 13 61]. Comb polymers are generally considered the most effective for wax inhibition. They are often based on acrylate esters, methacrylate esters or maleic anhydride. Other PPDs could include alkylphenol-formaldehyde resins, polyethyleneimines or lactone/alkylene oxides [5].

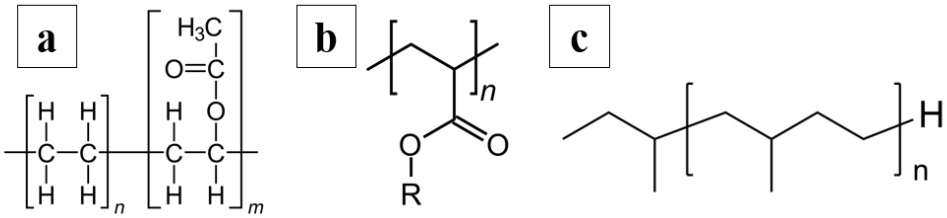

Figure 10: Chemical structures of (a) poly-ethyl-vinyl acetate (poly-EVA), (b) polyacrylate, (c) polypropylene ethylene.

5.2.2. Petroleum components which affect wax crystallization

Asphaltenes have been demonstrated to interact with wax crystallization, by similar mechanisms as the PPDs. They have also been referred to as PPD active substances in several studies [44 80 81 82]. However, the complex chemical composition of asphaltenes often caused

inconclusive results about the effect of asphaltenes on wax. For example, some studies concluded that the presence of asphaltenes generates an increase in the wax precipitation rate, while other studies concluded the opposite [9] [10] [83]. More research needs to be performed to understand the effect of asphaltenes on the deposition rate during flow operation and on the resulting crude oil gel matrix during shutdown. The exact mechanism of molecular interactions between wax and asphaltenes during each of the crystallization phase is also not fully understood [10].

Resins and naphthenic acids have also been demonstrated to interact with wax during crystallization [5]. However, the effect of asphaltenes is often dominating and has thereby been the focus of the most recent literature [5].

6. Interactions between wax and inhibitors

This Chapter provides a review of the current understanding of wax-asphaltene and wax-inhibitor interactions during the crystallization stages. The main suggested interaction mechanisms and the corresponding literature gaps are addressed. This provides a context for the main purpose of this thesis, which is to advance the knowledge about these interactions, by introducing novel, more robust quantitative techniques.

6.1. Wax-asphaltene interactions

Interactions between wax and asphaltenes during wax crystallization were reported in previous literature studies [9] [10] [84] [85] [86] [87] [88] [89]. In model systems, asphaltenes are present as dissolved monomers in toluene or other aromatic solvents. However, as mentioned in section 2.5., when asphaltene concentration increases, nanoaggregates (2 nm in diameter) and nanoclusters (5nm or higher in diameter) form, at a concentration point often referred to as critical nanoaggregate concentration (C.N.A.C) [9] [34]. In crude oils, asphaltenes could dissolve into other components or could be present as larger aggregates or even flocs/solids [90]. The exact composition of the crude oil influences this behavior.

Asphaltene nanoaggregates and nanoclusters interfere with wax during the main stages of crystallization [9] [10]. As presented earlier in this thesis, when the temperature decreases below the WAT in wax-only systems, the attraction between wax molecules exceeds the one between wax and solvent molecules in the crude oil. The first wax crystals act as a nucleation site for the remaining dissolved wax, which accelerates the crystallization process. When asphaltenes nanoaggregates and nanoclusters are present, they replace wax to act as nucleation sites, due to their large size. This provides additional surface for heterogenous nucleation [9]. Previous studies linked this phenomenon with an increased rate of wax crystallization.

However, the interaction between asphaltene and wax can manifest differently during later crystallization stages. During crystal growth, the non-polar groups of asphaltene molecules behave as binders between the wax molecules [10] [88] [89]. This restricts the parallel alignment of long chain alkanes and consequently reduces the growth of wax in 2 dimensions. On the other hand, it promotes a stronger growth in the third dimension, leading to rounder, more dendritic crystals [80]. Other effects are the delay of full crystal formation, the decrease in gel strength and the weakening of the wax crystal network [10] [88] [84]. Moreover, asphaltenes can flocculate and grow independently of wax, generating large crystals which could sterically and spatially hinder wax crystal growth. The competition between asphaltene solid particle formation and

wax crystallization could therefore lead to altered wax-asphaltene crystal networks with modified crystal and pore properties, such as size and shape.

Steric hindrance from larger particles could also induce trapping of dissolved and amorphous wax phases inside model crystal networks [61 64 91]. This could decrease the crystallinity of resulting phases and could result in crystals with stronger defects [80]. The steric hindrance between large wax-asphaltene configurations, could also cause the formation of amorphous phases, due to lack of space for complete crystal growth. The effects will be highly noticeable during agglomeration and gelation, when a crude oil gel matrix is generated, in which the wax, wax-asphaltene and asphaltene particles are dispersed and the remaining dissolved components are the continuous phase. Lower crystallinity of the wax crystals present in the matrix could influence rheological properties of the remaining fluid, such as viscosity and gel yield strength and delay the pour point [80]. The change of gelation properties was also associated with the presence of adsorbed polar asphaltene groups on the wax crystal surface, caused by the interaction of asphaltene with wax during previous crystallization stages [92].

The chemical composition of asphaltenes was linked to changes in wax precipitation patterns. Asphaltenes with a high level of aromaticity were found to sterically hinder crystal growth to a higher extent, generating weak and unstable wax structures during gelation phase [86]. Resulting wax-asphaltene co-crystals were reported to have a smaller size, with larger aspect ratio.

Although the properties of modified wax-asphaltene co-crystals, such as lower gel strength, and lower crystal size, would allow for lower viscosity and better crude oil flow, they were reported to have opposing effects on the WAT and the wax precipitation rate [88 81 44 93 94]. As expected from the concurrent and sometimes opposing effects, results of multiple studies generate contradicting conclusions about the role of asphaltenes during wax precipitation[10].

Some studies showed that asphaltenes inhibit wax precipitation in certain concentration regions, but promote wax precipitation in other concentration regions, specific to each type of crude oil or wax-asphaltene model system [9 83]. For example, Kriz et al [9] showed that the concentration and the level of dispersion of asphaltenes have the dominating effect on wax crystallization. They reported that at very low concentration, the asphaltenes are either dispersed or dissolved in the crude oil matrix. When the crude oil reached precipitation conditions, the wax crystals incorporated asphaltenes in an ordered configuration, up to a

threshold concentration where the crystallinity was the strongest and WAT was the highest. Above this concentration, the asphaltene molecules tended to aggregate with each other and then flocculate, attaching weakly to the wax crystal networks. The crystal matrix was broken, and the gel was weak and unstable, generating lower WAT.

The pattern of the concentration ranges for crystallization inhibition or promotion is in most cases irregular, probably because of the polydisperse character of asphaltenes and variable chemical composition of asphaltenes in each individual crude oil [10 95]. Therefore, the exact mechanism behind the impact of asphaltenes on wax precipitation remains to be studied through further quantitative methods which could be adapted to a variety of asphaltenes from crude oils with different origins and compositions.

6.2. Wax-PPD interactions

The effect of PPDs on wax crystallization was investigated more extensively than the effect of asphaltenes [13 61 96]. The addition of PPD alters the motion of wax molecules and the interacting force between wax molecules. The adjacent atoms in the wax molecules rotate around the C-C single bond in the absence of PPD [13]. The addition of PPD modifies this motion, by steric hindrance. The PPD interferes with wax during all stages of crystallization: nucleation, crystal growth, gelation.

The PPD molecules often tend to precipitate ahead of wax due to their high molecular weight [97 98]. Therefore, similarly to asphaltenes, the PPD molecules will replace the wax molecules as nucleation sites during the nucleation phase of crystallization. At the same time, PPDs can self-associate, forming micelle-like aggregates. These structures result in larger nucleation sites which inhibit wax crystal growth, promoting the formation of smaller wax crystals [61 98 99]. During nucleation stage, a percentage of wax molecules will adsorb on the surfaces of polymeric PPD, forming wax-PPD complexes. At this stage, wax molecules are likely coated with solvent molecules from the crude oil, causing precipitation with a short-range order (regular and predictable arrangement i.e. crystal lattice) [13].

For the phase of crystal growth, one of the current theories is that wax molecules grow in a two-dimensional way in the absence of PPD, resulting in crystals with needle shape [13 100]. The wax crystal network is an agglomeration of the individual needle crystals, which interlocked with large pores between individual crystals. The addition of more polar PPD molecules, with a larger size, sterically hinders the parallel alignment of alkanes and the growth of the wax crystal in 2 dimensions, promoting the growth in the third direction (Figure 11). Therefore, a

higher concentration of PPD is likely to generate dendritic wax crystals, which deviate from the original needle-like shape. The resulting crystal network will also follow a dendritic pattern, with reduced pore sizes [13] [100].

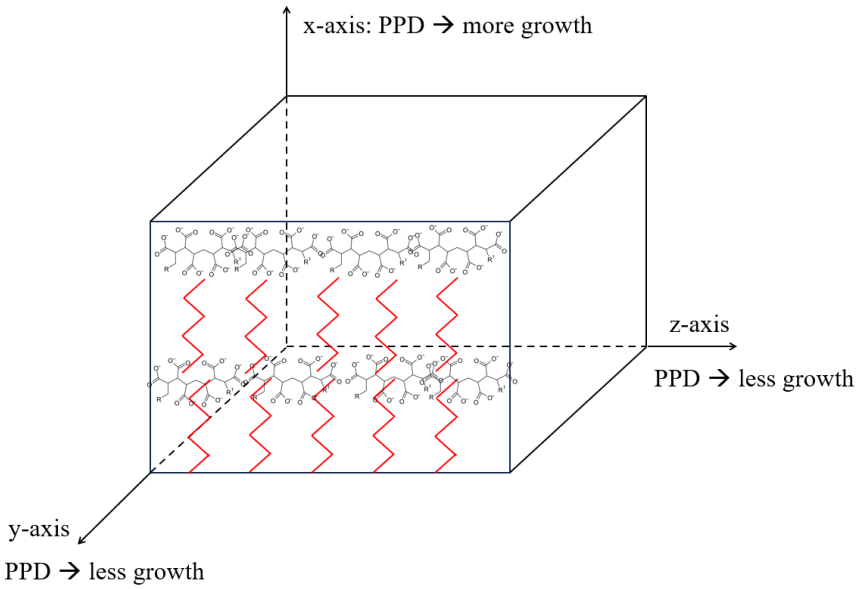

Figure 11: Mechanism of crystallization of n-alkanes, interacting with the PPD. The large, dendritic PPD molecule sterically hinders the otherwise dominant growth of wax in the y and z directions (in the absence of PPD) and promotes a three-dimensional growth. This results in rounder, more dendritic crystals [Inspired from [59]]. This figure should be compared to Figure 8, in absence of PPD.

During gelation phase, in the absence of PPD, there is a large solid-liquid interface between the wax particle surface and the dissolved components inside the crude oil gel matrix [101] [102]. This results in an unstable high energy system. The formation of round or dendritic structures, facilitated by the PPD reduces the energy of the system, making it more thermodynamically stable (i.e. it requires more energy to change phase) [101] [102]. The high degree of dispersion that the PPD surfaces could provide by interaction with wax improves the flowability and the viscosity of the remaining dissolved phases, delaying the pour point [13] [103].

At the end of the gelation phase, the polar groups of the PPD remain on the surface of the co-crystal structure formed by polymeric additive molecules and wax crystal. This induces the formation of a solvation layer, which decreases the surface energy in the system and prevents

the connection between the wax crystals, inhibiting the formation of a wax crystal network [13] [22] [104] [105]. This solvation layer is one of the features that distinguish asphaltenes from PPDs. It is unclear whether asphaltenes prevents the connection between wax crystals or if it facilitates dissolution to the same extent that the PPD does. Moreover, highly effective PPDs are more likely to generate a more ordered crystal network with wax, while asphaltenes with complex chemical composition will often produce crystal defects and crystal network irregularities.

The composition of the PPD (i.e. EVA copolymer, comb-type copolymer, and nano-hybrid PPD) also influences the wax inhibition mechanism [5] [6]. Most effective PPDs have been demonstrated to delay the pour point and reduce the wax precipitation rate, generating better viscosity and flowability in the remaining dissolved phases.

6.3. Quantification of wax-inhibitor interactions and corresponding wax precipitation curves

The effect of asphaltenes and PPDs on wax crystallization was previously investigated quantitatively, using multiple analytical methods such as differential scanning calorimetry (DSC), cross-polarized microscopy (CPM), isothermal titration calorimetry (ITC), scanning electron microscopy (SEM) or rheological measurements [10] [61] [62] [84] [101] [106].

DSC was used to calculate the heat of crystallization and the wax precipitation rate in model systems [61] [67]. Delays in nucleation and crystallization were observed for PPD and asphaltenes, although for asphaltenes the effect was minor. DSC is an established method for calculations of the wax content in crude oils, but significant thermodynamic assumptions, are made (i.e. latent enthalpy of wax/wax-inhibitor systems, thermal delay from cooling rate) [61] [67]. This can alter the results, leaving a gap between the measured and the real thermodynamic behavior.

CPM and SEM were used to assess crystal size and shape in presence and in absence of wax inhibitors and to calculate fractal dimension [12] [61]. Although results showed a trend for smaller and rounder crystals in two-dimensional images when PPDs and asphaltenes were added, a gap remains about the three-dimensional features and the exact quantification of size and shape.

The analysis of wax precipitation by low field NMR was introduced by Pedersen et al, who calculated wax content in crude oil, from relaxation time data [72]. They correlated the NMR signal intensity with the amount of wax generated by an established precipitation method for 17 crude oils. The procedure has been significantly extended through the analysis of the NMR

Free Induction Decay (FID) signal [107] [108], but the sensitivity to the crude oil composition remained to be improved.

Recently, wax crystallization has been characterized by an adapted Carr-Purcell-Meiboom-Gill (CPMG) sequence [109] [110], which focuses on the effect of asphaltene and PPD in model wax-based systems. The effect of PPD on the variation of wax precipitation rate with temperature was assessed by Zhao et al with NMR CPMG [68]. Ruwoldt et al used PPDs with more varied chemical composition and considered the influence of asphaltenes for the first time [61]. NMR CPMG used less thermodynamic assumptions than DSC. It also quantifies the mobility of molecules, enabling the distinction between high mobility and low mobility phases in the liquid and gel matrixes before and during crystallization, showing higher potential for studies of wax-inhibitor interaction.

7. Experimental techniques

This thesis aims to develop new methods to characterize wax-inhibitor interactions. The main purpose is to solve limitations and uncertainties encountered with established experimental methods (DSC, rheology, ITC, GC/MS). A majority of previous studies focused on the effect of inhibitors in wax through the measurement of wax-related properties (i.e. precipitation rate, WAT) in crude oils or model systems resembling crude oils. This thesis shifts the focus to interactions between wax and inhibitors at a molecular scale, which could explain macro-scale observations from previous studies. For this purpose, novel techniques were utilized. Low field and high field NMR, as well as AFM were used to characterize wax-inhibitor interactions. DSC, a more established method, was compared to NMR in terms of limitations and result accuracy.

7.1. Nuclear Magnetic Resonance

Charged atomic nuclei have an intrinsic angular momentum and that produces a magnetic dipole defined as nuclear spin [111] [112] [113]. In NMR, such a nuclear spin interacts with an external static magnetic field B_0, leading to a nuclear energy level diagram having distinct eigenvalues, correlated with eigenstates in which an atom can exist (Figure 12). In the case of lower energy states, the z-component of the nuclear magnetic moment is positive (m=+1/2), while in the higher state, it is negative (m=-1/2). Also, in the case of lower energy state, the net magnetization of the spinning nucleus tends to align with the external magnetic field, while in the higher state the magnetic moment of the spinning nucleus is opposed with the external magnetic field [114]. The difference between the energy of the 2 states is given by Equation (1), where h is Planck's constant, γ is the gyromagnetic ratio and B_0 the strength of the magnetic field:

$$\Delta E = \frac{h\gamma B_0}{2\pi} \quad \text{(Eq. 1)}$$

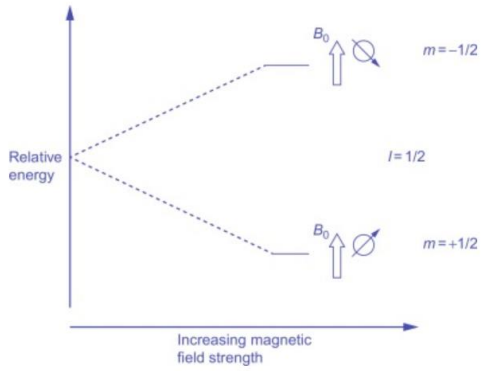

Figure 12: Division of nuclear spin energy in an external magnetic field [Copyright from [114]].

The interaction between the nuclear spin and the external magnetic field also causes the spin to undergo a precession around the static field at a frequency ω_0, also known as Larmor frequency. In addition, the spin experiences interactions with the local electric and magnetic fields and that generates changes in the precession by a frequency ω with respect to ω_0 [115]

Hydrogen atoms have been particularly studied with NMR spectroscopy due to their high sensitivity to the technique. In this thesis, applications are divided into low field and high field NMR. The main difference between the two categories is the intensity of the frequency generated by the magnet. High resolution NMR uses high field superconducting magnets.

7.1.1. Low field NMR

When protons are placed in an external magnetic field, the nuclear magnetic moment of the protons will align against this field, as described before. Low field NMR is based on the application of an oscillating magnetic field at the resonance frequency, which represents the frequency at which enough energy is reached to generate the transition between the nuclear energy levels. This phenomenon shifts the nuclear spins into an excited state, outside of the normal thermal equilibrium. When the oscillating magnetic field is stopped, the nuclear magnetic moment will re-establish the thermal equilibrium at a rate specific to each component in the system. Relaxation times quantify the time required to re-establish the thermal equilibrium. A change in the magnetic flux will also be generated, inducing an electrical current through a coil in the NMR system (Figure 13). The current is proportional to the amount of hydrogen atoms, while the variation in intensity is proportional to the relaxation times [109 112]

[113] [114] [115]. By measuring the current and its intensity, the relaxation times and the proton content at each relaxation time could be quantified.

T_1 and T_2 relaxation times are dependent on variations in the NMR signal intensity. The relaxation times depend on the field (ω_0) and on the motions of the molecules. The global molecular translations and rotations driven by Brownian motions are considered slow, while internal motions such as bond vibrations are much faster and studied with high field. The optimal observation frequency is around 20 MHz for typical global motions. Therefore, T_1 and T_2 measurements with low field NMR (20 MHz) have become common approaches to study the relative mobility of molecules in liquid systems with phase fluctuations[110] (Figure 14).

In this thesis, three low field NMR experiments have been used: the Carr-Purcell-Meiboom-Gill (CPMG) sequence, the Free Induction Decay (FID) experiment and a pulsed field gradient (PFG) diffusion experiment.

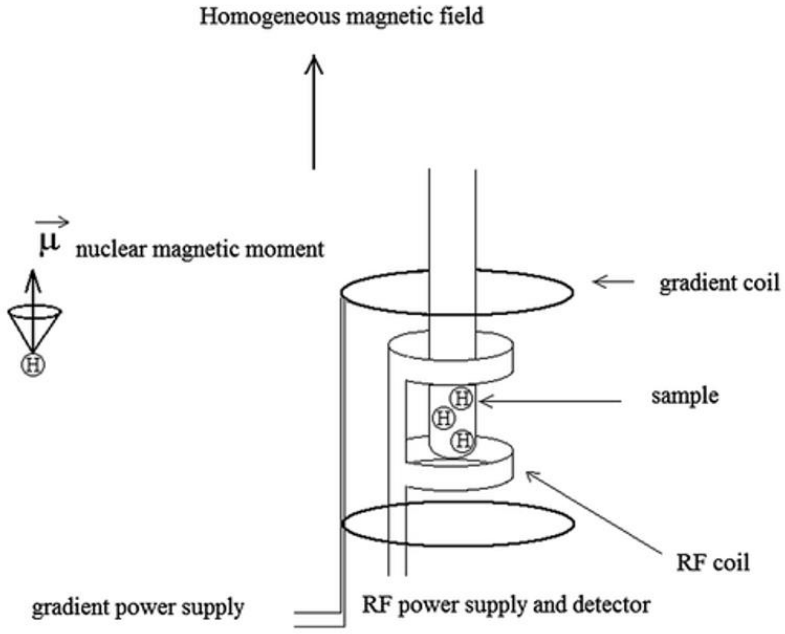

Figure 13: Schematics of low field NMR setup. A radio frequency (RF) flips the nuclear magnetic moment at an angle of 90° from the direction of the external field. Gradient coil is sometimes used to produce deliberate variations in the main field. (see Section 7.1.1.1) [Adapted from [112]].

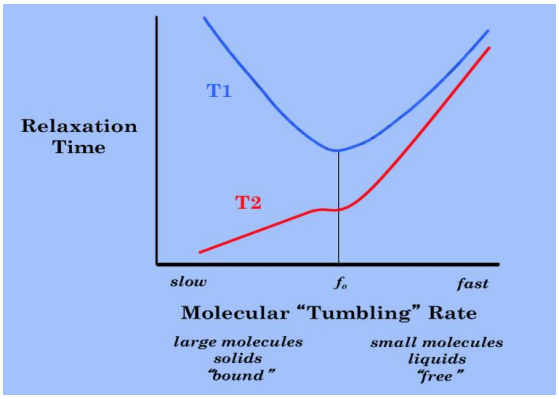

Figure 14: Relaxation time as a function of molecular diffusion, from solid state to liquid state [116].

7.1.1.1 Carr–Purcell–Meiboom–Gill (CPMG) sequence

The first low field NMR technique used in this thesis is based on the Carr–Purcell–Meiboom–Gill (CPMG) sequence [109 110]. This experiment consists of an initial oscillating magnetic field pulse with a radio frequency, known as RF, which flips the nuclear magnetic moment at an angle of 90° from the direction of the external field into the transverse plane relative to the external magnetic field. The next step in the CPMG sequence is the application of 180° RF pulses, with intervals of 2τ between them, by using the gradient coil. (Figure 15). The sequence will induce a current which is measured by the NMR instrument. The sampled NMR signal (echo maxima in Figure 15), I, will decay as a function of the transverse relaxation time T_2 and with the corresponding fraction as follows:

$$I = \sum_i I_i e^{-\frac{2n\tau}{T_2^i}} \quad \text{(Eq. 2)}$$

where I is the component number, T_2^i the relaxation time of the component, I_i the corresponding intensity, τ half of the interecho spacing, and n the echo number [109 110]. The experimental data often has a multi-exponential decay and is fitted with an inverse Laplace transform [117] to generate a distribution of absolute values for T_2 and the corresponding proton content at each T_2.

In this thesis, the CPMG sequence had 2 echo intervals with 2 different τ values (τ_1 and τ_2 in Figure 15), which allowed to place a greater focus on the species with low relaxation times. The exact procedures are described in the corresponding research papers.

For CPMG, the focus is on T_2 distributions. The CPMG sequence is adapted to resolve inhomogeneities in the magnetic field and therefore could provide an accurate quantification of T_2. This was used to characterize the rate of wax crystallization and the mobility of dissolved wax and asphaltene molecules with temperature in model systems. Liquids display higher T_2 ranges, conventionally set at above 3×10^{-3} s, while solids are characterized by low T_2 values, below the measured values for CPMG with the available NMR facilities.

Initial studies were performed before on model systems based on wax, using the CPMG sequences [61 68]. The method showed high potential for the characterization of wax phases with intermediate mobility, which could influence the crystallization mechanism [61].

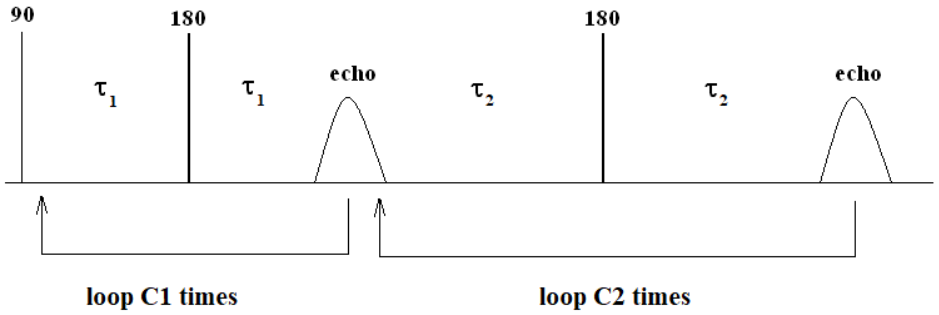

Figure 15: CPMG sequence used for the NMR procedure.

7.1.1.2. Pulsed field gradient-stimulated echo (PFGSTE) sequence

The CPMG sequence was used to measure the mobility of wax or asphaltenes, which underwent significant phase changes during the corresponding experiments. This was facilitated by the use of deuterated solvent, which enabled the NMR to only focus on protons from wax and asphaltenes. However, this technique did not allow the measurement of the mobility of solvent molecules, because deuterated wax, asphaltenes or PPDs were not available. Therefore, a second NMR technique was introduced to measure the mobility of the solvent molecules through the developing wax crystal network.

A pulsed field gradient-stimulated echo sequence with bipolar gradients[118] was used to acquire the diffusion coefficient at increasing observation times (Δ). Also, a pulsed field gradient spin echo sequence with bipolar gradients [119] was used to measure the diffusion coefficient at the shortest observation time possible. This method allowed the direct quantification of restricted and unrestricted diffusion coefficient for the solvent molecules. The unrestricted diffusion coefficient was approximated to the coefficient measured at the shortest observation time possible (Figure 16). The dead time of the instrument was 2.7 ms, which caused a minor underestimation of the unrestricted diffusion coefficient. However, the dead time was similar to all measured system and a relative quantification was still valid. The restricted diffusion coefficient was acquired at the time-values at which the measured diffusion stopped depending on time and became constant (Figure 16). At these values, the displacement of the diffusing solvent molecules through the constricting space was much larger than the length scale of the constricting space [120 121]. However, its absolute value was dependent on the type of constricting space, which in this case was the resulting wax or wax–inhibitor crystal networks and the corresponding intermediate gels. The results could therefore quantify the extent to which wax or wax-inhibitor crystal networks restricted the mobility of solvent molecules.

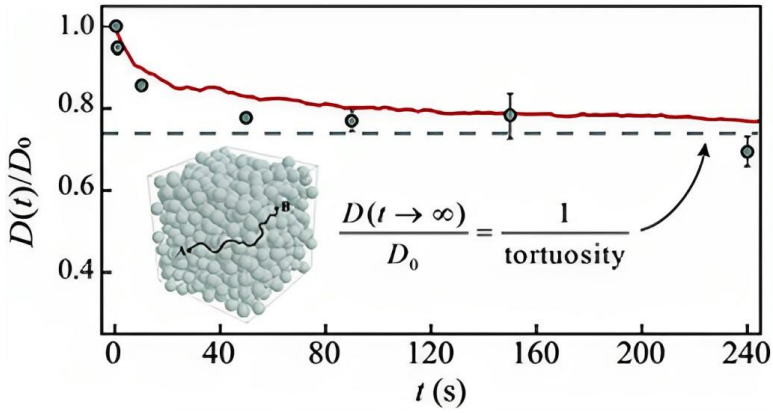

Figure 16: Diffusion as a function of acquired time, by pulsed field gradient stimulated echo (PFGSTE) NMR. The point at t=0 corresponds to unrestricted diffusion, the molecular diffusion of the solvent in the absence of constraining crystal networks/porous media. The asymptotic diffusion value at high time corresponds to the restricted diffusion, the molecular diffusion of the solvent after restriction from crystal networks/porous media is imposed [Copyright from [120]].

The PFGSTE technique has been extensively used before, mainly for the analysis of tortuosity in porous media [122] [123]. For wax crystallization, this technique represents a novelty which this thesis aims to introduce as an alternative to established methods.

7.1.1.3. Free Induction Decay (FID) technique

The FID was used in this thesis as an alternative to the CPMG method to calculate solid content during crystallization in systems based on crude oils with very complex chemical composition and a higher range of intermediate solid-liquid phases. Liquid state NMR was used for this purpose.

Unlike the CPMG and the PFGSTE, which are based on a pulse sequence, the FID experiment provides an NMR signal induced by a single pulse, corresponding to the non-equilibrium precessing of the nuclear spin magnetization about the external magnetic field. This can be achieved by the application of a magnetic pulse at a radio frequency with values at or near the Larmor frequency [113]. The FID signal is limited by the relaxation time T_2 [113] [124] [125]. However, its exact quantification cannot be achieved. The FID is faster than the CPMG, allowing to identify solid phases at very short relaxation times. This occurs because with FID, the wait for an echo is removed. On the other hand, the FID does not solve the undesired effects of heterogeneity in the system. Therefore, instead of the T_2, a modified relaxation time, T_2^*, which is limited and related to the T_2, could be quantified. The modified relaxation time becomes predominant above a certain delay of acquisition, due to inhomogeneity of the sample and the magnetic field. Like CPMG, the FID signal provides a relative quantification of the mobility of molecules. The main advantage of FID is that the acquisition starts earlier, allowing for the quantification of the proton content at very low relaxation times specific to crystalline, solid state. The FID has a multi-exponential decay, composing of a sum of separate exponentials at each separate relaxation time. Each exponential corresponds to the intensity of the proton content at the corresponding relaxation time. The raw data acquired for this thesis only allowed for the separation of 2 exponentials from this FID data (Figure 17), because the instrument could acquire a new data point after an interval of minimum 1 μs from the previous one. The following Equation was used to summarize the intensity of the FID signal:

$$I \approx \mathrm{L}e^{\frac{-t^2}{T_l^2}-} + \mathrm{S}e^{\frac{-t^2}{T_s^2}} \quad \text{(Eq. 3)}$$

where **L** represents a parameter proportional to the amount of protons in the non-crystalline phase, T_l represents the approximate average modified FID relaxation time for the non-

crystalline phase, **S** represents a parameter proportional to the amount of protons in the crystalline phase, T_s represents the approximate average modified FID relaxation time for the crystalline phase, and t is the acquisition time. The ratio between crystalline and non-crystalline phase becomes similar to the ratio between S and L.

In literature, FID was used to calculate the solid content in crude oils before, but with a lower degree of accuracy than in this thesis. Pedersen et al. introduced FID for the wax content calculation in oils [72]. They established a relationship between NMR signal intensity and wax amount, by comparing the NMR signal intensity with the amount of wax generated by a modified acetone precipitation method performed at −20 °C for 17 crude oils. The procedure has been improved more recently [107] [108], but robust algorithms for calculation of the solid content from the NMR signal are still lacking. The NMR FID technique has been used to a higher extent for the characterization of fat crystallization in food science applications [124] [126] [127] [128] . However, crude oils often have significantly lower crystalline percentages than fats analyzed in food science. This thesis aims to overcome this limitation and adapt the NMR FID technique to crude oil systems and wax-based model systems.

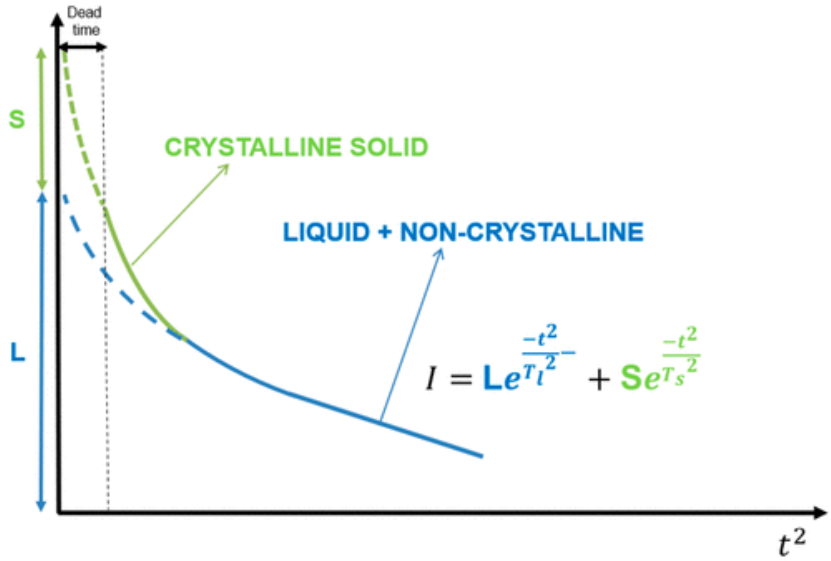

Figure 17: Schematic representation of the two-exponential separation for each NMR curve at a selected temperature (*y* axis) plotted as a function of the square of the acquisition time (*x* axis).

7.1.2. High field NMR

High field NMR was used to track the proton content from asphaltenes and PPDs and quantify its evolution, independently of wax.

The high field NMR system comprised of a magnet with a resonance frequency which was about 25-30 times higher than for the low field NMR: 600 MHz, instead of 21 MHz.

When high field NMR is used, the different local chemical environments surrounding a nucleus causes it to resonate at a frequency, specific to the chemical environment [129]. This occurs due to differences in shielding between individual nuclei. This frequency is known to generate what is referred to as the chemical shift (δ). The chemical shift could be influenced by various factors, such as bonds of the nucleus to an electronegative group or hydrogen bonding. The chemical shifts have minor values in comparison to the magnet frequency differences[129]. The scale is Hz, instead of MHz for a magnet. For this reason chemical shifts (δ) are described by the unit ppm on an NMR spectra, and could be calculated using the following Equation[129]:

$$\delta = \left(\frac{H_{ref} - H_{sub}}{H_{machine}}\right) \times 10^6\ ppm \text{ (Eq. 4)}$$

Where H_{ref} is the resonance frequency of the reference (tetramethyl silane), H_{sub} is the resonance frequency of the substance and $H_{machine}$ is the operating frequency of the spectrometer.

In this thesis, the specific chemical shifts for wax, PPDs and asphaltenes have been identified. Their proton intensity in non-crystalline (liquid) range has been quantified, to calculate the co-crystallization rate of PPD and asphaltenes during wax crystallization.

7.2. Differential Scanning Calorimetry (DSC)

DSC is a thermo-analytical technique which measures the heat which a sample releases or absorbs during a temperature scan. For this thesis, power compensated DSC has been used. The technique uses a reference sample, to quantify the heat change in the focus sample, by determining the temperature difference between the two [130]. One can notice in Figure 18 that the focus sample (filled pan) and the reference sample (empty pan) are placed on their corresponding disks in the DSC chamber. Indium is typically used to calibrate the DSC instrument. Inert atmosphere is ensured, by a gas flow (nitrogen), which is continuously

running through the DSC chamber. The specific software of the DSC allows the generation of a temperature program, which in the case of this thesis, simulates temperature ranges for wax crystallization.

DSC has been used to a high extent to quantify wax crystallization in crude oils and in wax-based model systems [61] [68] [67] [131]. Wax crystallization is an exothermic process and therefore, DSC could quantify the heat released during the temperature program. This facilitated the determination of the wax appearance temperature (WAT). Moreover, algorithms were proposed to quantify the wax precipitation rate from the released heat data [67]. However, a number of thermodynamic assumptions are being made. Firstly, wax is very sensitive to thermal history and therefore, the high cooling rate that the DSC requires to achieve a sufficiently strong signal, induces a delay when crystallization rate and WAT are measured. Secondly, the latent heat of wax is required to establish a relation between the released heat and the crystallization. The exact value is difficult to determine, particularly in crude oil systems with complex wax composition.

DSC was used in this thesis as a reference to compare wax crystallization rate results, acquired by the novel NMR techniques. The advantages and disadvantages of NMR and DSC were assessed.

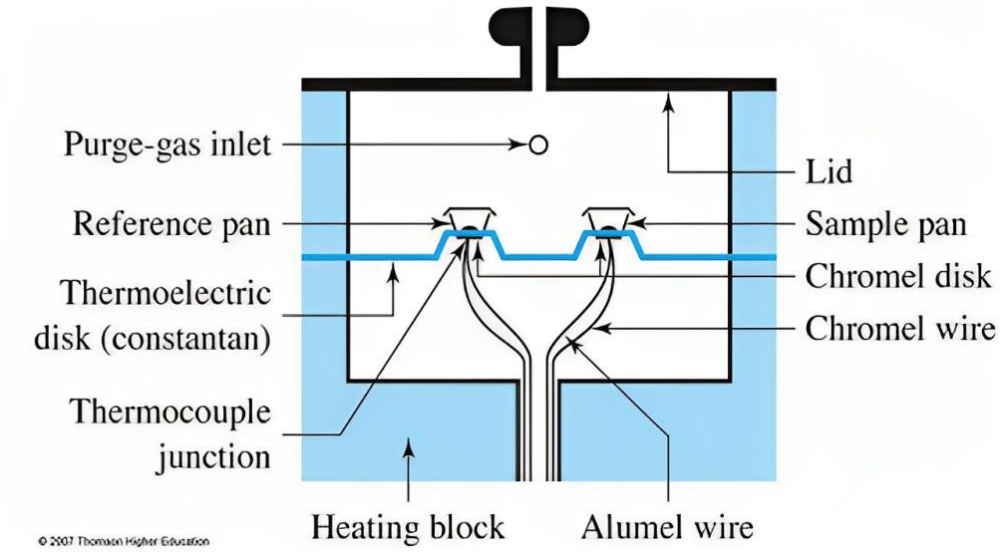

Figure 18: Schematics of a DSC instrument [Copyright from [130]].

7.3. Atomic Force Microscopy

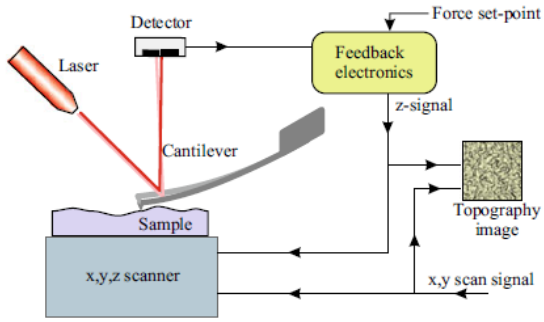

Figure 19: Schematics of AFM operation [Copyright from [132]].

Atomic force microscopy (AFM) is a type of scanning probe microscopy (SPM) with a resolution on the order of decimal fraction of nanometers, which corresponds to approximately 1000 times higher accuracy than the optical diffraction limit encountered with conventional types of microscopy [132] [133] [134] [135]. The basic composition of an AFM instrument is illustrated in Figure 19. The probe has a very sharp tip with a typical radius of 2–20 nm, attached to the end of a microfabricated cantilever, usually made either of silicon (Si) or silicon nitride (Si_3N_4). Scanning of the probe over the sample surface is carried out with a piezoelectric scanner, which expands or contracts in response to applied voltages. A laser beam reflected from the back of the cantilever is detected with a four-segment photodiode detector. Vertical deflections and lateral distortions of the cantilever can be evaluated from the location of the incident beam at the detector. The controller evaluates the signals from the photodetector to adjust the *z*-displacement of the piezo scanner. For example, it automatically moves the sample or the probe upward and downward, to keep the preset feedback control parameter constant. The mapping of the resulting *z*-piezo movements in the *x* and *y* dimensions provides the images of the sample surface [132].

The imaging modes for surface topography of the AFM could be split into 2 main types: contact mode and dynamic mode [132]. In contact mode, the AFM pyramidal-shaped tip raster scans over the sample, while the tip and the sample keep contact during the scans. Cantilever behaves like a force sensor and thus, low stiffness cantilevers are normally used to maximize the deflection signal. However, the continuous contact between the tip and sample causes significant lateral force which can distort soft samples or even displace samples which are not strongly attached on the substrate. Contact mode can only be effectively used for scanning very flat surfaces, as

an increased degree of roughness would affect the tip. In dynamic mode, there are 2 subdivisions for scanning: non-contact mode and intermittent contact or tapping mode. In non-contact mode, the surface is scanned by cantilever vibrating up and down at a constant high resonance frequency, maintained using the feedback controller, by a technique called frequency modulation. The cantilever deflection is used as a drive signal in the loop controller, so that the cantilever continuously adapts to changes in the resonance frequency. The drawback of this method is the poor sensitivity and resolution. Tapping mode combines contact and non-contact modes. The cantilever which holds the tip is oscillated at around its set resonance frequency during the scan. The tip oscillates and gets in contact with the sample for a small time during the oscillation cycle. The height of the cantilever is constantly adjusted by the feedback controller [136]. Although tapping mode provides a lower risk to damage the sample, adjusting scanning parameters to get very high-resolution images might prove difficult. Moreover, even the tapping mode cannot accurately track high steps or high degrees of roughness on the surface [137]. For this study, an advanced tapping mode, also known as QI™ was used [138]. This scanning mode was optimized to achieve the highest possible resolution with the minimum tip-sample interaction, preserving both the tip and the sample to the highest possible extent.

The main purpose behind AFM is to measure the force between the surface and the scanning tip in order to create the surface topography map[132]. The total force between tip and sample is composed of several long-range and short-range contributions. The latter contributions include phenomena such as chemical bonding and Pauli repulsion. On the other hand, the most important part of the analysis is the long-range contribution, which often relies on a van der Waals force. In the case of AFM, this is a London dispersion force resulted at the interaction between neutral atoms or molecules without a permanent dipole moment. This interaction can be described as a spontaneous attraction between fluctuating electric dipoles. The origin of the van der Waals force is of quantum mechanical nature and can be defined by the Schrödinger equation. However, it is very difficult to find the exact solution of the Schrödinger equation of a complex system with many electrons, alike the ones most frequently used in AFM scanning [132]. Therefore, a model potential is utilized for the qualitative description of tip-sample interaction. Lennard-Jones potential is the most frequent model potential used for this quantification, as the tip-sample interaction in AFM follows a similar pattern to the force between two neutral atoms: attractive force for large distances, a potential minimum and a strong repulsive interaction at short distances. The potential consists of a term describing the

attractive part of the van der Waals interaction and another term describing the repulsive part of the van der Waals interaction, as the following Equation illustrates:

$$U_{LJ}(r) = 4U_0\left[\left(\frac{R_a}{r}\right)^{12} - \left(\frac{R_a}{r}\right)^{6}\right] \quad \text{(Eq. 5)}$$

where U_0 is the depth of the potential well, r is the distance between the atoms and R_a is the distance at which U_{LJ} is 0. In Figure 20a. the Lennard-Jones potential is illustrated as a red line, as well as the two contributions, the attractive $-\left(\frac{1}{r}\right)^6$ contribution (green) and the repulsive $\left(\frac{1}{r}\right)^{12}$ contribution (blue). Figure 20 displays the Lennard-Jones potential, the corresponding force $F = -\frac{\partial U}{\partial r}$ and the force gradient, which are relevant in applications with AFM dynamic mode.

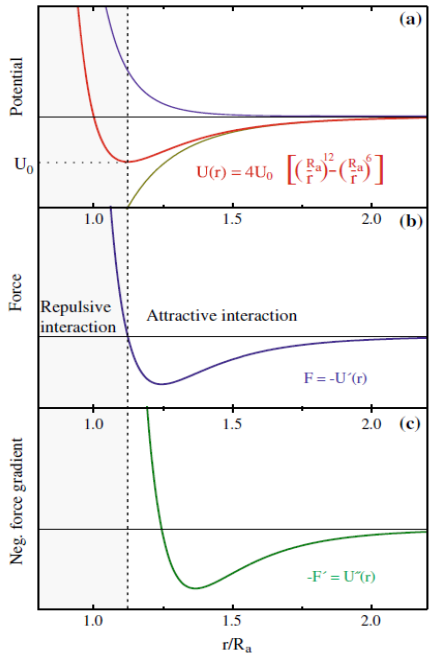

Figure 20: (a) Lennard-Jones potential model as a function of distance; (b) First derivative of the Lennard-Jones potential model as a function of distance; (c) Second derivative of the Lennard Jones potential as a function of distance [132].

In AFM force measurements, *r* in Equation 1 becomes the tip-sample distance *d*. The attractive regime where attractive interactions dominate corresponds to the tip approaching the surface. The initial part of the attractive regime of the force illustrated in Figure 20b is often generated without a direct contact of the tip and the surface. A turnaround occurs where the Coulomb repulsion between the tip and the surface exceeds the attractive force. The repulsive force dominates more as the tip further approaches the surface. The force gradient presented in Figure 20c is essential to perform amplitude modulation in tapping mode. When the gradient starts to increase from the minimum point, the resonance frequency of the system starts to shift abruptly and thus, the amplitude needs to be continuously adjusted [132].

The QI mode , used in this study, allows for force-distance curve quantification at every point on the surface [139 140 141]. It also includes an integrated feature that continuously adjusts the amplitude to the most optimal values [138].

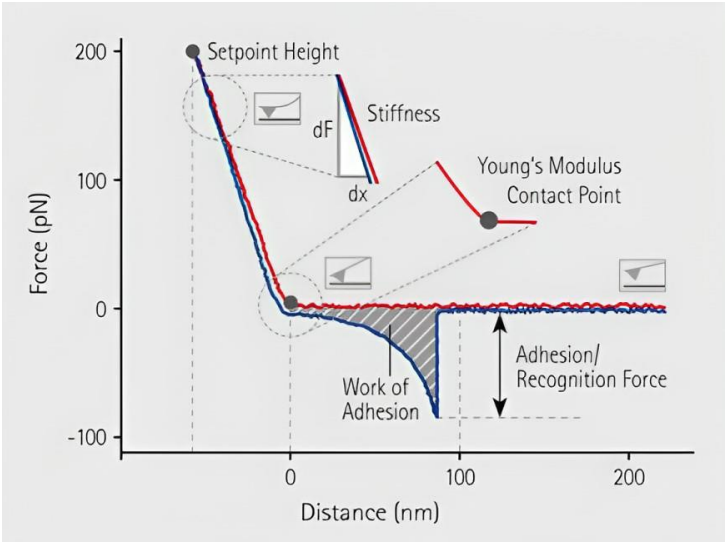

Figure 21: Schematics of force-distance curve acquired with QI™ mode scanning mode[138].

The slope of the repulsive interaction on the approach force could be quantified to characterize the stiffness of the sample (Figure 21) [140 141 142] . The lower the slope is, the softer the sample is. As the tip retracts from the surface, an attractive force arises, opposing the retraction (Figure 21). This force is often referred to as adhesion in previous AFM studies. Other forces, which influence tip-sample interactions during AFM scanning are viscous forces, representing the resistance force provided by a fluid when it is subjected to tangential force on its surface (shear) [143]. Viscous forces could alter force-distance curves by interacting with the tip during approach

and retraction [144]. These forces alter the force-distance curves, by modifying adhesion and slope properties on the approach. Therefore, the stiffness, often quantified through the Young Modulus could be altered [145]. AFM has been used before to study wax and asphaltene surfaces [135] [146]. However, its use for the analysis of wax-inhibitor interactions that is presented in this thesis represents a novelty.

7.4. Challenges with experimental techniques

The main challenge encountered with NMR CPMG was the detection limit for relaxation times. With NMR CPMG, the T_2 was often acquired as a distribution in the measurable range (10^{-4}-10^{1} s). To overcome the detection limit challenge and to better separate the peaks at high T_2 and low T_2, 2 inter-echo spacings were used (τ_1 and τ_2), with more echoes for the region with shorter inter-echo spacing. This allowed a higher resolution for the peak at short relaxation times, which included a significant percentage of the signal of interest. Moreover, the lower detection limit of the T_2 cannot be accurately described, although previous measurements estimated it at around 0.5 x 10^{-3} s.

For NMR FID, the dead time of the NMR instrument was the main limitation, as it decreased the number of points available to generate the exponential model for the solid (crystalline) phase.

For high resolution NMR, the mobility of the molecules identified by the measured signal was unclear in systems where crystallization was already ongoing. Due to the high frequency of the field, there was no control of the relaxation times, and the magnetic field could have been sensitive to the formation of solid phases, due to radiation damping. Preliminary diffusion experiments with high resolution NMR confirmed that the NMR could record the peak at lower T2 values (10^{-2} s), but the intensity of the recorded signal was not always consistent with CPMG. Moreover, it is not known how the heterogeneity induced in the sample by crystallization affected the intensity of the high-resolution NMR signal.

The main challenge encountered with AFM was associated with the roughness of wax surfaces. To resolve this problem, the height at which the tip was positioned before each approach (z-length) was set at 1000 nm. The identification of the most optimal parameters for AFM scanning was a lengthy process, with multiple trial and error attempts. The final parameters were decided after attempts on all relevant systems of interest, which confirmed the quality of the scan. This also had to ensure that scanning over an amorphous layer formed at the top of

wax and wax-asphaltene surfaces would not lead to tip contamination under the scanning conditions. For this purpose, the scanning speed and the force setpoint were adjusted accordingly. Another challenge which arose with AFM was the measurement of Young Modulus for multiple force-distance slope regions, corresponding to multiple layers. Each experiment involved 16384 scans at 16384 points along the surface. This generated 16384 force-distance curves. Due to heterogeneity and variations on the surface, the borders between multiple slope regions were difficult to identify in a consistent manner. Therefore, multiple attempts to separate were performed. The most optimal border was chosen when the artefacts in the individual separated slope regions reached a minimum.

Attempts were made to scan wax in liquid environment (toluene, heptane) with AFM. However, due to high solubility of wax, it was difficult to obtain stable systems and consistent results. An intermediate step would be to scan waxy gels in air and then to introduce the AFM tip in progressively more liquid gels.

8. Main Results

The main results from the four publications in this thesis are summarized in this Chapter. The first three publications follow the characterization of interactions between wax and inhibitors, and they are closely related. Paper II starts from hypotheses developed in Paper I and investigates them quantitatively with novel techniques. Paper I and Paper II focus on the quantification of mobility of dissolved species in the fluid. Paper III assesses modifications in the crystal network structure, which are closely linked to conclusions about mobility changes in Paper I and Paper II. Paper IV has a different focus than Papers I-III. It introduces a novel NMR technique for the quantification of solid content during crystallization, which is adapted for complex crude oil systems, containing asphaltenes and resins.

8.1. Paper I

New NMR approaches on the evolution of wax mobility during wax crystallization

Paper I introduced NMR CPMG as a method to quantify the mobility of dissolved species (wax, asphaltene, PPD) in model systems based on wax, wax-asphaltene and wax-PPD mixtures.

Commercial macrocrystalline wax (Sasolwax 5405) was used. The asphaltenes used in Papers I-III were extracted from a widely investigated crude oil from the Norwegian continental shelf, as described in the corresponding experimental section of the articles. The PPD used in Papers I-III was chosen so that it had a high level of efficiency in wax inhibition and was firstly introduced by Ruwoldt et al [61].

The solvent used for all systems in Paper I was deuterated toluene. This implied that the contribution of the solvent on the NMR signal was insignificant, and the focus of this paper was thereby the quantification of the proton content of wax, asphaltenes and PPDs. The NMR CPMG sequence, adapted for the available instrument, generated T_2 distributions for the analyzed systems. However, the instrument had a detection limit which narrowed the accuracy of the T_2 measurement within the 10^{-3}-10^{1} s range, which corresponded to the non-crystalline state. Changes of mobility within this interval were quantified and associated with phenomena related to wax gelation.

Crystallization was induced in the selected system, by stepwise cooling. Each of the experiments started at 45°C, which is about 20-25°C above the wax appearance temperature. This ensured complete dissolution of waxes. The temperature was decreased to 0°C, at an average cooling rate of 0.2°C/min. The low cooling rate ensured a low delay induced by thermal history, generating crystallization conditions which were close to thermodynamic equilibrium (cooling along the supersaturation line of a phase diagram).

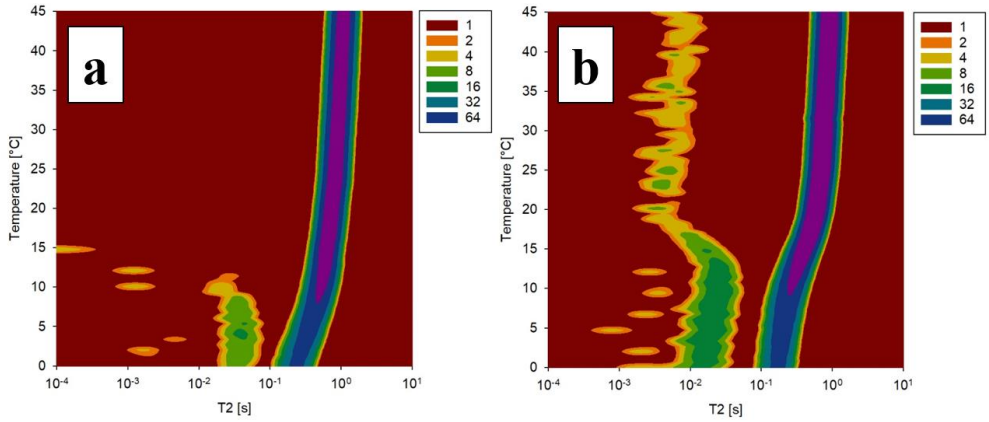

Figure 22: Evolution of T_2 (x-axis) and intensity of T_2 (scatter map) as a function of temperature for: (a) 5% wax in deuterated toluene, (b) 5% wax, 1% asphaltene in deuterated toluene – no correction for the Boltzmann factor.

The typical T_2 distribution acquired by this technique could be observed in Figure 21. The values depicted by colors in the 3D contour map represent an intensity proportional to proton content at each corresponding temperature and T_2. A main, dominating peak, was formed at high T_2 values, of 10^{-1}-10^{0} s (Figure 22). This peak was generated by dissolved wax, which had very high mobility before crystallization started. Once the temperature reached low values, the wax crystallization process was triggered. At that point, both the mobility (T_2) and the proton content in this peak started decreasing. The wax precipitation curve was calculated by tracking the amount of lost content in the high mobility dissolved wax peak. Most of the content lost from the main peak was completely lost from the measured T_2 interval, due to formation of crystalline phases, with T_2 values below 10^{-3} s. However, some of the content lost from the main peak could still be found in the measured interval, but at lower T_2 values. Later in the crystallization process, 5-10°C below the crystallization onset, a secondary peak at lower T_2 values was generated. A low mobility dissolved wax region developed and remained present until the lowest temperature was reached. This low mobility region was associated with dissolved wax species which became trapped in the pores of the newly interlocked wax crystal network, inducing a gel matrix. When wax concentration was increased to higher values, both the wax precipitation rate and the amount of low mobility wax increased almost proportionally, demonstrating that higher amounts of crystalline wax accelerated the trapping of wax within the gel matrix.

When asphaltenes were present (Figure 22 b), a third, distinctive peak at very low mobility (10^{-3}-10^{-2} s) was generated before the start of crystallization. The protons forming this peak were from asphaltenes nanoaggregates and nanoclusters with reduced mobility. The third peak was not observable after the onset of wax crystallization, which suggested that the size of nanoaggregates and nanoclusters increased, due to interaction with wax crystallization by co-crystallization. The behavior of asphaltene nanoaggregates as nucleation sites for wax and the co-crystallization of wax and asphaltenes during crystal growth explained the formation of larger wax-asphaltene particles, with lower mobility than asphaltene nanoaggregates and nanoclusters. The result of these processes was an altered wax-asphaltene co-crystal network, which trapped a different amount of dissolved wax molecules, depending on the asphaltene concentration.

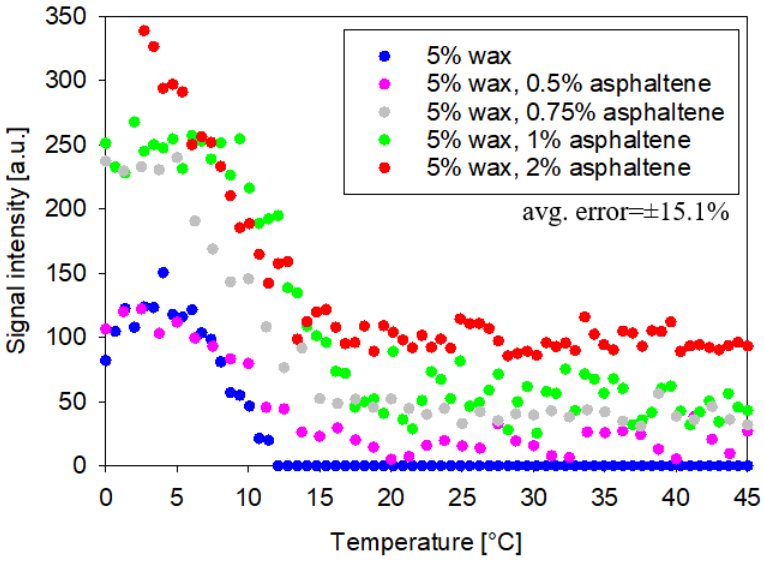

Figure 23: Evolution of total secondary peak intensity with temperature for wax-asphaltene systems.

At low asphaltene concentration (i.e. 0.5%), the amount of trapped wax was similar or even marginally lower than in the absence of asphaltenes (Figure 23). However, from 0.75% to 2%, there was a gradual increase in the amount of low mobility dissolved wax (Figure 23). The reasons for this included the change in aggregation state of asphaltenes and the change in the number of asphaltene centers which could impose steric hindrance on wax crystal growth. The percentage of asphaltene nanoaggregates and nanoclusters increases with concentration. A

higher amount of nanoaggregates and nanoclusters led to a higher number of nucleation centers for wax molecules. This accelerated crystallization and the transition towards the next crystallization stages. Wax precipitation curve results also supported this argument since higher precipitation rates were recorded for high asphaltene concentrations (0.75-2%) than for low asphaltene concentrations (Figure 24). Asphaltenes' behavior as nucleation sites also led to steric hindrance imposed on crystal growth and shielding of the wax nuclei, which most likely co-crystallized with surrounding asphaltenes at higher rates than at lower asphaltene concentrations. Asphaltene are known as polydisperse and are therefore likely to induce the formation of non-uniform crystals with strong defects. Therefore, the resulting wax-asphaltene co-crystal network was most likely less crystalline, due to the higher amounts of trapped dissolved phases and due to the polydisperse character of asphaltenes. Consequently, a weaker gel resulted.

The behavior of the mixtures with PPD were significantly different. The secondary peak with low mobility dissolved wax did not form, even at the lowest PPD concentration (Figure 25). There were therefore no indications that a gel matrix with trapped liquid was formed. This demonstrated the PPD's effect for preventing gelling of wax-based systems. Unlike asphaltenes, the PPD alleviated the formation of the gel completely. At high PPD concentration, PPD molecules self-associated, inducing phases with very low mobility which were observable at low T_2 (10^{-3}-10^{-2} s) in Figure 25b. This peak disappeared after the start of wax crystallization (<20°C), demonstrating that larger PPD-based species co-crystallized with wax during nucleation and crystal growth. The precipitation rates were also decreased by approximately 30% when 1% PPD was added to 5% wax.

Paper I introduced a method to quantitatively characterize the gel matrix formed during the gelation phase. Uncertainties remained about the aggregation state of asphaltenes, co-crystallization rate of asphaltenes and PPDs, the mobility of solvent molecules during crystallization stages and the exact crystal network properties (i.e. crystal shape, size, interlocking properties, degree of crystallinity) which determined the results found in paper I. Papers II and III will thereby focus on developing quantitative method to assess the aforementioned characteristics.

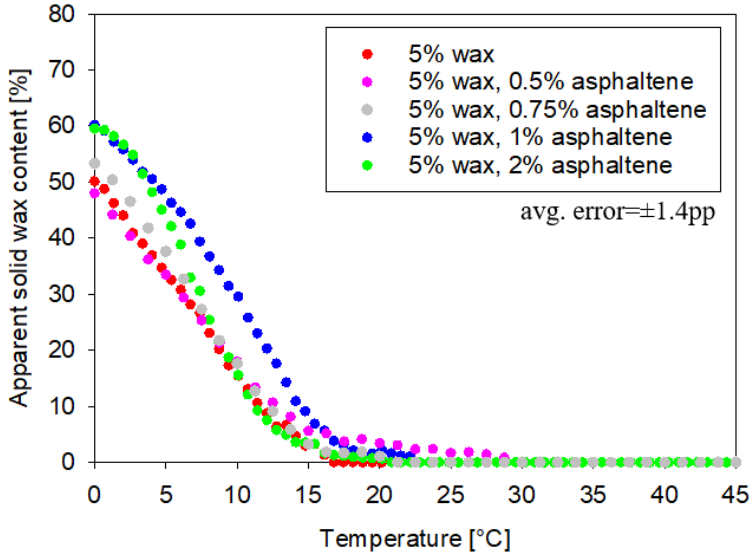

Figure 24: Apparent percentage of precipitated wax as a function of temperature for wax-asphaltene systems.

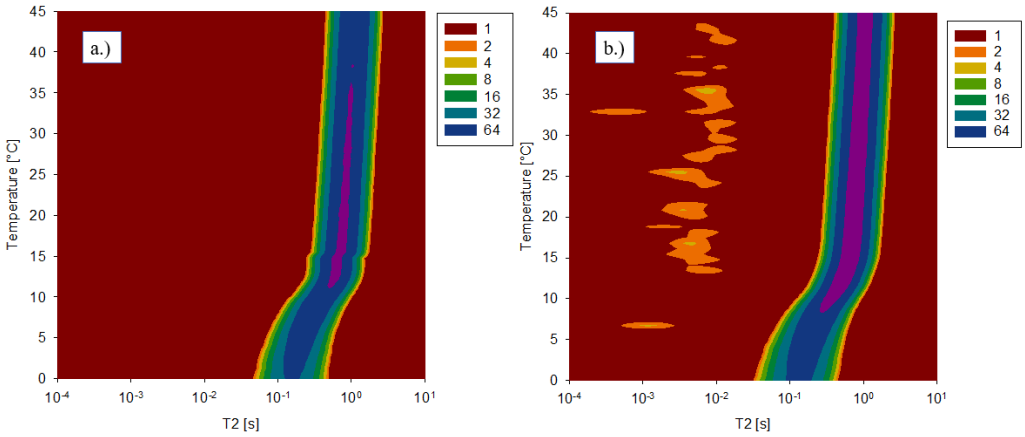

Figure 25: Evolution of T_2 (x-axis) and of intensity of T_2 (scatter map) with temperature for: (a) 5% wax, 0.1% PPD in deuterated toluene; (b) 5% wax, 1% PPD in deuterated toluene – before correction for the Boltzmann factor.

8.2. Paper II

Understanding the effect of asphaltenes and wax inhibitors on wax crystallization by improved NMR techniques

Paper II introduced 3 different NMR methods which each focused on a different perspective, directly or indirectly related to uncertainties on the wax crystallization mechanisms identified in Paper I. The first method was high-resolution NMR and its focus was to quantitatively demonstrate that asphaltenes and PPDs co-crystallize with wax in model systems closely related to the ones in Paper I. The second method was NMR CPMG. The same NMR principles used in Paper I were followed. The purpose of NMR CPMG in this study was to quantify the mobility of asphaltenes and separate between monomers and nanoaggregates/nanoclusters. Then, the evolution of the aggregation state with asphaltene concentration was monitored and was linked to findings about the influence of asphaltenes on wax crystallization in Paper I. The third method was NMR PFGSTE. The purpose of this method was to identify the mobility of toluene molecules in wax-asphaltene and wax-PPD systems with similar concentrations as in Paper I. Due to the long duration for one measurement, isothermal conditions had to be used for this method as well.

The first method used in this study relied on high resolution NMR. The NMR spectrum regions for wax, asphaltenes and PPDs were quantified (Figure 26 a-d). By comparison, chemical decays specific to asphaltenes and PPDs were identified. For asphaltenes, the aromatic region was identified as a decay with weak intensity, occurring over a long distance, from 10 ppm to 6.5 ppm (Figure 26 c,e,f). For PPD, groups specific to esters were identified as chemical decays with weak intensities at 3.3-3.47 ppm, marked as region A and at 4-4.35 ppm, marked as region B (Figure 26 d).

The proton content was tracked for the inhibitor-specific regions in wax-inhibitor systems scanned isothermally at 30°, 10° and 0° C. High resolution NMR only recorded the proton content in non-crystalline phases, at high mobility. Due to a strong level of heterogeneity of the system with macrocrystalline wax and asphaltenes at 0 °C, the resonance frequency of the high-resolution NMR was affected, altering the results. Therefore, microcrystalline wax, which formed a weaker gel, was used instead for wax-asphaltene systems with high resolution NMR. When wax-asphaltene and wax-PPD systems were scanned, results indicated a significant drop in the proton content of asphaltenes and PPDs in non-crystalline phase from 30 °C to 10 °C or 0 °C (Figure 27). This drop was lower or not present in asphaltene-only and PPD-only systems

(Figure 27). Consequently, the conclusion was that a high percentage of asphaltenes and PPDs lost mobility due to the ongoing wax crystallization. Co-crystallization was the only likely explanation for this behavior.

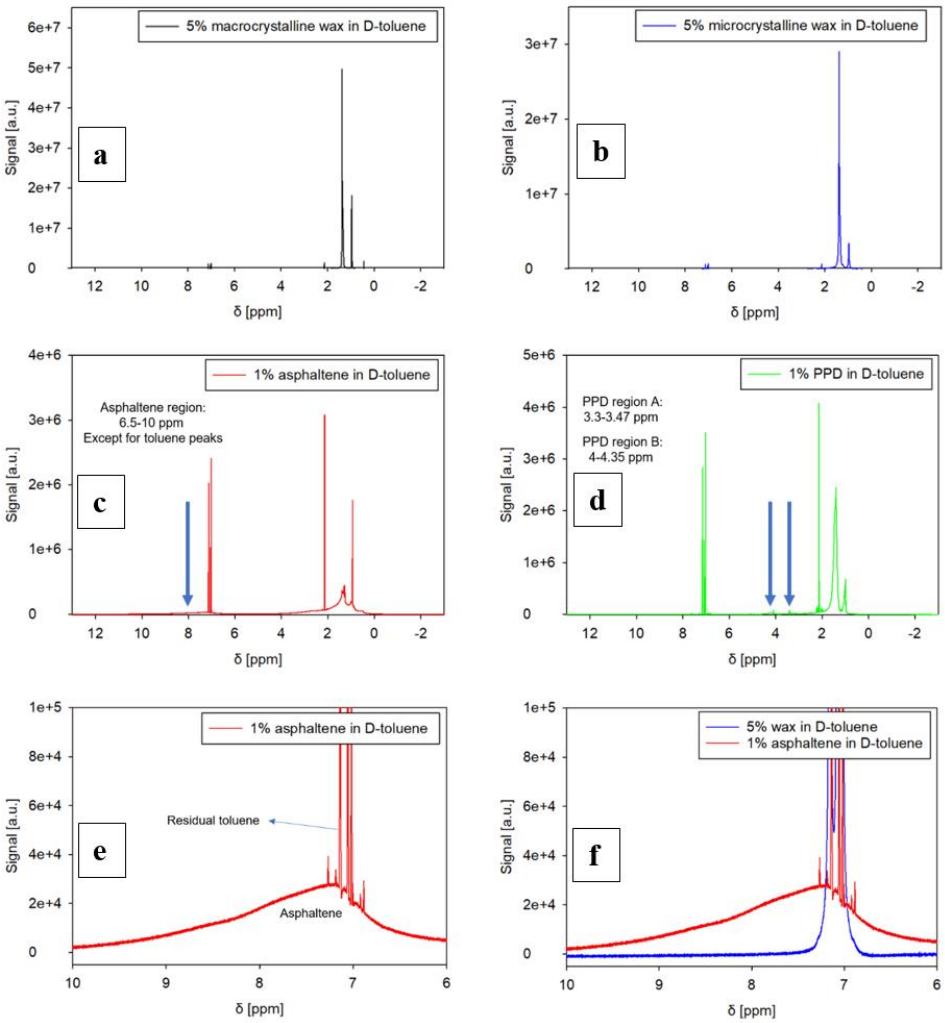

Figure 26: (a-d) ^{1}H NMR spectrum for (a) 5% macrocrystalline wax in deuterated toluene, (b) 5% microcrystalline wax in D-toluene, (c) 1% asphaltene in deuterated toluene (d) 1% PPD in deuterated toluene; (e-f) Slices from 10 to 6 ppm in the ^{1}H NMR spectrum for (e) 1% asphaltene in deuterated toluene, (f) 5% microcrystalline wax in deuterated toluene, with a comparison to 1% asphaltene in deuterated toluene; Markings for inhibitor-specific peaks indicate the corresponding regions in figures (c), (d).

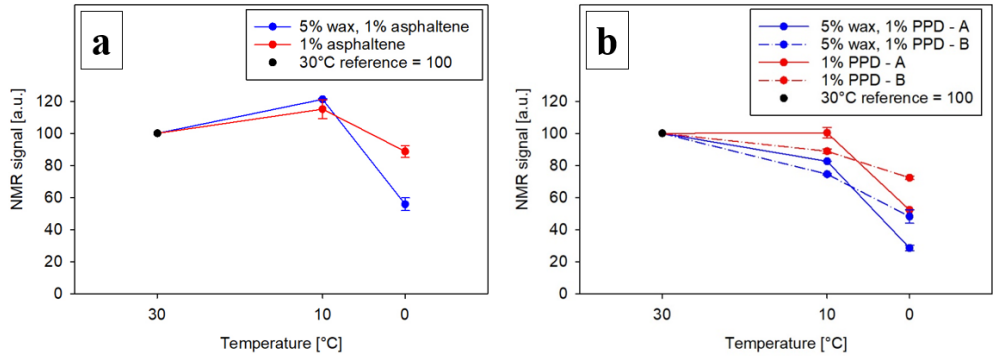

Figure 27: Variation of signal with temperature for (a) asphaltene-specific peak in 5% microcrystalline wax, 1% asphaltene in deuterated toluene and in 1% asphaltene in deuterated toluene, (b) PPD-specific peaks A and B in 5% macrocrystalline wax, 1% PPD in deuterated toluene and in 1% PPD in deuterated toluene; The values at 30°C is fixed at 100 for all systems, while the values at 10°C and 0°C are normalized accordingly.

The second part of the paper assessed the nanoaggregation state of asphaltenes, as a function of concentration. NMR CPMG scans at 30° C showed that asphaltene-only systems in extra pure deuterated toluene generated 3 peaks within the measurable T_2 range, 10^{-3}-10^{1} s (Figure 28). One of the peaks was at high T_2 values (>0.5 s), specific to pure solvents, such as toluene, hexadecane or hexane. Therefore, this peak was generated by asphaltene monomers, which were completely dissolved. The other 2 peaks which occurred between 10^{-3} and 0.5 s were asphaltenes with reduced mobility, present as nanoaggregates (2-5 nm) or nanoclusters (>5nm). Two regions were thereby conventionally set: asphaltene monomers at T_2 values above 0.5 s and asphaltene nanoaggregates/nanoclusters at T_2 values below 0.5 s. These regions were monitored as a function of the asphaltene concentration. At 0.2%, the monomers were dominant, with a monomer: nanoaggregate ratio of about 1.4:1 (Figure 28). At 0.5 and 1%, the nanoaggregate/nanocluster proportion increased and a constant monomer: nanoaggregate ratio of about 1:1.7 was recorded (Figure 29). From 1.25% to 2%, the monomer peak became insignificant, and the nanoaggregate/nanocluster region dominated the T_2 distribution (Figures 28, 29). This confirmed what was assumed in Paper I: a transition from monomers to nanoaggregates and nanoclusters occurred around the 1% concentration point, stimulating stronger interaction between asphaltene and wax during nucleation and crystal growth, which resulted in a heavily altered crystal network and gel. The exact concentration value differed

from observations in Paper I, where a shift in wax-asphaltene gel behavior started at 0.75%. Different scanning conditions (dynamic ramping vs isothermal at 30° C) and the ongoing wax crystallization which altered real asphaltene concentrations could be the causes for the minor difference.

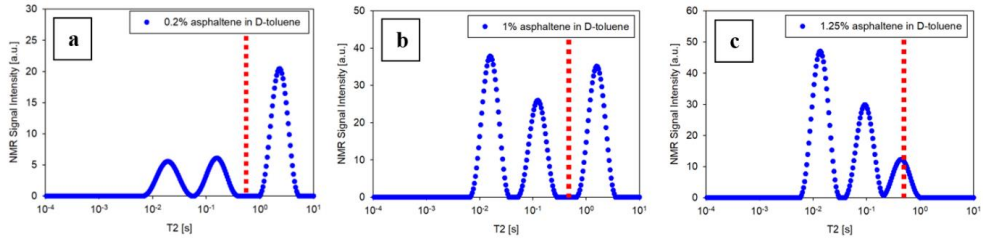

Figure 28: Relaxation time distribution in liquid domain for: (a) 0.2% asphaltene in deuterated toluene, (b) 1% asphaltene in deuterated toluene, (c) 1.25% asphaltene in deuterated toluene; the red line marks the border between high mobility asphaltene monomers and low mobility asphaltene nanoaggregates/nanoclusters.

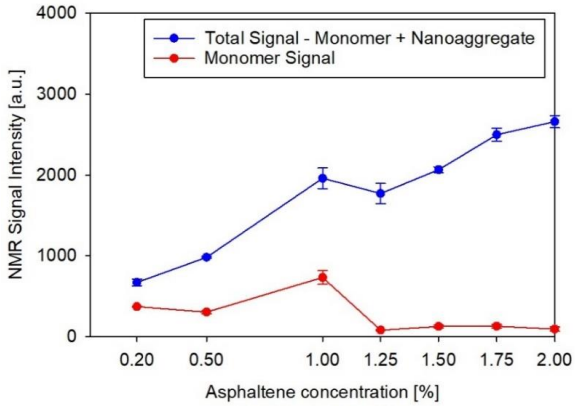

Figure 29: Total signal and monomer signal, as a function of asphaltene concentration in asphaltene-only solutions in deuterated toluene.

The last part of the paper quantified the unrestricted (free) and restricted diffusion of toluene in wax, wax-asphaltene and wax-PPD crystal networks in systems with the same concentrations as in Paper I. Hydrogenated solvent was used in this case, so that toluene could be the bulk fluid dominating the NMR signal intensity. This technique showed that the restricted mobility of the toluene was significantly higher when asphaltenes were present in wax systems. Higher

asphaltene concentration (2%) promoted higher mobility for the solvent, although little differences were recorded between 0.5% and 1% (Figure 30). The PPD increased the mobility of the solvent to even higher values than the highest asphaltene concentrations (Figure 29). These results quantitatively showed that the presence of asphaltenes weakened the waxy gel. As observed in Paper I, a higher amount of dissolved waxes were trapped in the gel. Moreover, it is highly likely that the co-crystallization of wax with asphaltenes with high polydispersity induced the formation of crystals with strong defects, such as an altered shape, rounder and more dendritic. This prevented the interlocking of wax into a well-ordered crystal network with large pores between the needle-shaped crystals, which could trap toluene in the stronger gel. The PPD distorted the crystals to an even higher extent. As discussed previously in Section 6.2., the wax-PPD co-crystal is often shielded by the polar groups of the PPD, which form a solvation layer. This solvation layer induced by the polycarboxylate-based PPD has a stronger solubilization effect than the presence of asphaltenes.

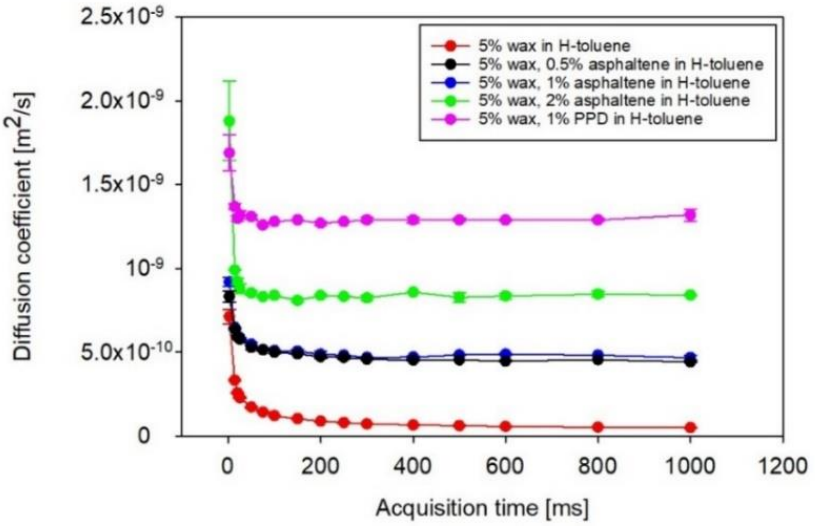

Figure 30: Diffusion coefficient profile at 0°C, as a function of acquisition times for wax, wax-asphaltene and wax-PPD systems in toluene.

The NMR studies in Paper I and Paper II all concluded that a weaker gel, with strongly altered wax crystal networks was induced by the presence of asphaltene and PPDs at high concentrations. One of the key findings was the presence of a low mobility dissolved wax region in wax and wax-asphaltene systems. This was stronger in wax-asphaltene systems at high concentration but was not present in the wax-PPD system, even though both type of

systems induced weaker gelling and higher mobility for the bulk fluid (toluene). Although interlocking of the wax crystal networks is considered one of the most likely reason for the generation of this region (Figure 30, 1a-1d), 2 more mechanisms were proposed. The first was the trapping of wax within the pores of individual wax crystals (Figure 30, 2a-2d), which provide more restriction on dissolved species when wax forms more dendritic crystals. The stronger solvation layer on the wax-PPD co-crystal explained why trapping was less likely in the presence of PPD. The second additional mechanism was the formation of an amorphous layer on the top of the crystals or the formation of less crystalline, more amorphous crystals (Figure 30, 3a-3d). This layer might be formed by wax-asphaltene structures which did not crystallize completely due to the strong steric hindrance induced by the polydispersity of large asphaltenes species. Thus, the trapped dissolved species recorded by NMR could be represented by this layer or by species closely interacting with this layer. This would explain why dissolved wax, interacting with asphaltenes had lower mobility, while toluene, which did not interact with asphaltenes, had higher mobility.

The PPD, on the other hand, formed much more ordered complexes with wax which co-crystallized until full crystallinity was reached. Smaller crystals with more dendritic shape are common, similarly to wax-asphaltene co-crystals. However, no dissolved wax was trapped, since gelation was delayed. More time was needed for wax-PPD complexes to start crystallizing, since PPD's solubility was significantly higher. The wax-PPD co-crystals had a configuration which trapped less dissolved wax and toluene, due to the formation of a more ordered crystal network structure, without the strong defects in the wax-asphaltene co-crystal network. This was most likely due to the higher solubility of the polar groups of PPD and a lower level of polydispersity than asphaltenes.

Paper II further investigated the evolution of mobility of dissolved species (asphaltene, PPD, toluene) in the context of wax crystallization. The conclusions of this paper often relied on assumptions about the crystal network properties, such as crystal size, crystal shape, type of interlocking, level of crystallinity. Therefore, Paper III used AFM to characterize such properties and clarify uncertainties about conclusions in papers I and II.

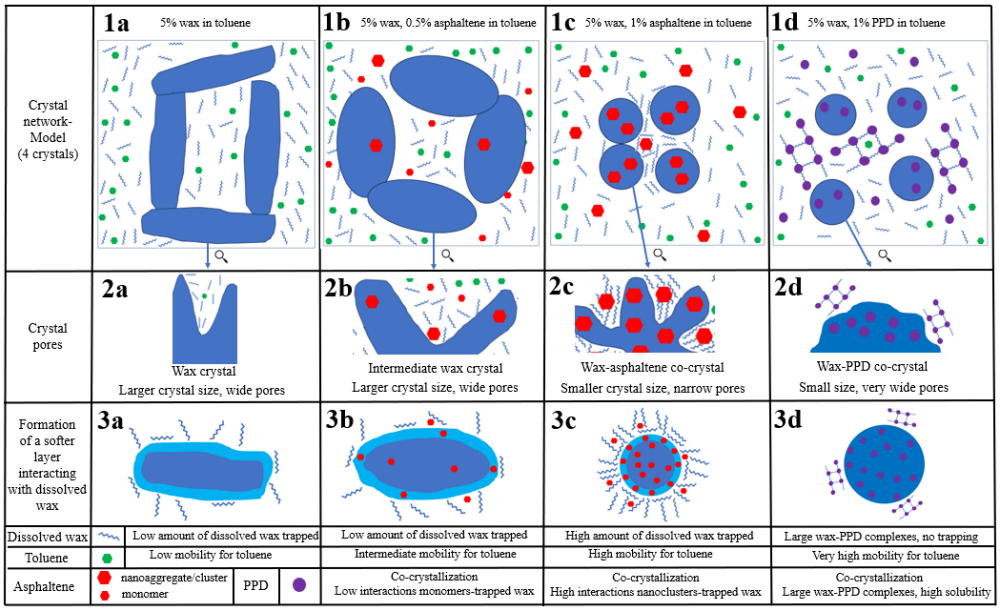

Figure 31: Model schematics for crystal networks and liquid phases for wax and wax-asphaltene systems at 0 °C.

8.2. Paper III

Alterations in paraffin wax crystal networks induced by asphaltenes and pour point depressants, investigated by atomic force microscopy.

Paper III introduced AFM as a technique to characterize alterations in the characteristics of crystal networks induced by asphaltenes and PPD. AFM was never used before for this purpose and therefore, the focus was to develop a methodology which targeted the most relevant properties for wax crystallization. This methodology was achieved by scanning solids evaporated from mixtures with the same wax and asphaltene or PPD composition as in Paper I. The scans were performed at room temperature. To verify the effectiveness of the methodology, a production wax sample, obtained from a wax deposit, was introduced and studied. Moreover, cold finger conditions for precipitation were used as an alternative to evaporation. This method relied on the introduction of a metal finger at 0 °C in a wax or wax-inhibitor solution at 50 °C for 2 minutes, inducing a temperature gradient, which resembled industrial deposition conditions.

The first parameter of interest in the methodology was the topography of the wax samples, which characterized crystal properties (size, shape) and the extent of interlocking in crystal networks. The scanning size was selected as 100 μm x 100 μm, so that all the parameters could be quantified. The 2D Fourier Transform was used to quantify the frequency of each of the height pattern.

Macrocrystalline wax formed a crystal network with large, needle shaped crystals, with a maximum height difference of 3.7 μm. The interlocking of the crystal network was accompanied by large and deep pores (Figure 32 a,b). On the other hand, asphaltenes did not form a wax crystal network. They formed round, grainy particles, which were most likely partially adsorbed on the mica surface in a rather uniform pattern (Figure 32 c, d). The maximum height difference was in this case around 20 nm. When wax-asphaltenes mixtures were evaporated, the crystal network of wax had modifications. The addition of a low content of asphaltenes (0.5%) only modified crystal size and the space occupied by pores marginally. Nonetheless, crystal shape was rounder, more dendritic. The aspect ratio of the crystals was lower and the surface became more uniform (Figure 32 e,f). At high asphaltene concentrations (1%, 2%), the crystal networks were completely altered. The height decreased by 2.5-4 times,

the pores were more shallow and narrow, but they were more frequent (Figure 32 g,h). The higher amount of trapped wax observed in Papers I and II during crystallization could be related to pore properties. A higher number of narrow pores were more likely to restrict mobility of a higher number of dissolved species. However, the interlocking of the network was much weaker in the presence of polydisperse asphaltenes, when a more uniform surface was generated. This explained the weaker gel strength of the wax-asphaltene co-crystal network.

The addition of PPD also resulted in smaller, more dendritic crystals (Figure 33). However, the surface of the wax-PPD co-crystal network was even more uniform, with more gradual transitions between crystal peaks and pores. This was thereby one of the factors which prevented dissolved wax trapping during the wax-PPD co-crystallization (Paper I, II).

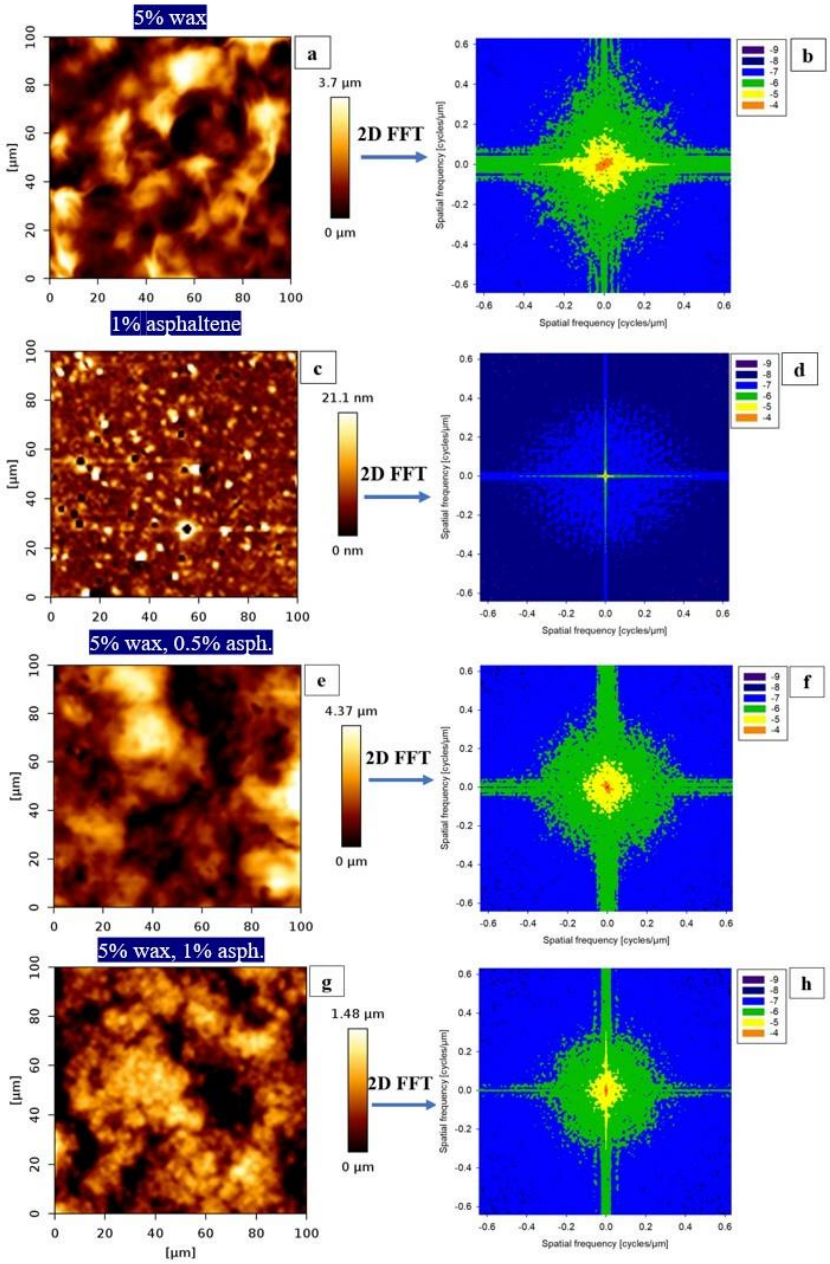

Figure 32: Height features of the solid surface evaporated from 5% model wax in toluene– (a) height map, (b) 2D Fast Fourier Transform of height map; Height features of the solid surface evaporated from 1% asphaltene in toluene – (c) height map, (d) 2D Fast Fourier Transform of height map; Height features of the solid surface evaporated from 5% model wax, 0.5% asphaltene in toluene – (e) height map, (f) 2D Fast Fourier Transform of height map; Height features of the solid surface evaporated from 5% model wax, 1% asphaltene in toluene – (g) height map, (h) 2D Fast Fourier Transform of height map.

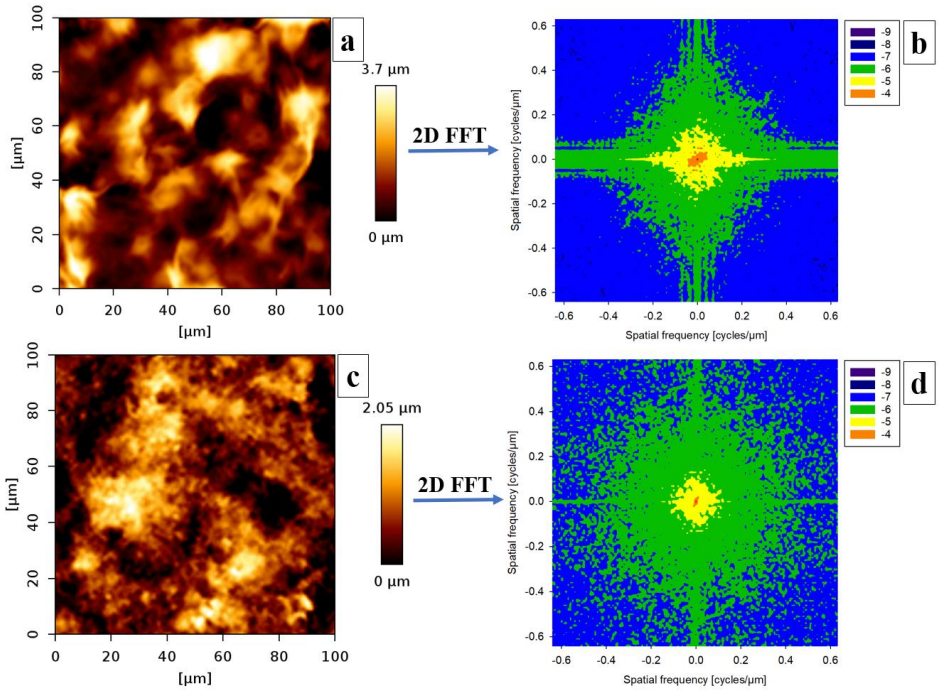

Figure 33: Height features of the solid surface evaporated from 5% model wax in toluene– (a) height map, (b) 2D Fast Fourier Transform of height map; Height features of the solid surface evaporated from 5% wax, 1% PPD in toluene – (c) height map, (d) 2D Fast Fourier Transform of height map.

The second parameter of interest was the elasticity of the surface. Force-distance curve analysis showed a 2-slope profile for the wax and wax-asphaltene systems (Figure 34). A nano-scale layer of 50 nm -100 nm with a lower Young Modulus formed on the top of the surface. This corresponded to softer wax phases, which did not crystallize completely, most likely due to remaining gel-like phases with trapped dissolved species. The addition of asphaltenes at high concentration (1%, 2%) triggered the swelling of the nano-scale layer with amorphous phases and the further decrease in Young Modulus (Figure 35). This could explain the formation of intermediate phases on the outer layers of the crystal networks, which corresponded to a higher amount of low mobility dissolved wax trapping at the same concentrations in Paper I and Paper II. Moreover, this proved that asphaltenes in high concentrations reduced the crystallinity of resulting phases, most likely due to the highly polydisperse character of asphaltenes. On the other hand, the addition of PPD most likely increased the crystallinity of resulting phases, since the amorphous layer was not observed anymore and the Young Modulus values were significantly higher. The wax-PPD complexes reached full crystallinity, which indicated that the amount of amorphous phases was little to none. The reason for this might be the fact that

the wax-PPD crystal network had a more ordered structure, whose interlocking resulted in less constricting pore space than wax-asphaltene agglomerates and even than wax-wax agglomerates. This would translate into a strong reduction in gelation in industrial systems, which would complement the delayed deposition, demonstrated by NMR CPMG in Paper I.
After the development of the AFM methodology on model systems, the focus was moved to investigating its suitability for production wax samples, in presence and in absence of asphaltenes and PPDs, prepared by evaporation and by cold finger. Results showed that the production wax sample probably had a high content of microcrystalline wax, which generated rounder, more dendritic crystals, with smaller pores and a lower degree of interlocking (Figure 35). A potential contamination with resins, asphaltenes and iron particles was also highly likely. The cold finger method induced the precipitation of high molecular weight wax, which had very large, rectangular crystals (Figure 36). The effect of asphaltene was weak in this case, most likely due to the composition of production wax (asphaltenes, resins, iron particles). On the other hand, the PPD still had a very strong effect, causing significant crystal size reduction and shape change towards rounder crystals with more uniform crystal network surfaces.

Production wax had a larger amorphous layer on top, caused by the presence of microcrystalline phases. From this perspective, the production wax resembled macrocrystalline wax treated with asphaltenes. The interlocking produced less constricting pore space, but a more amorphous crystal network, which did not achieve full crystallinity. The presence of large, branched wax molecules induced a similar effect with the presence of large, polydisperse asphaltene species. The cold finger method induced an even thicker and more amorphous layer, corresponding to high molecular weight microcrystalline wax. As expected, the addition of PPD increased the crystallinity of the nano-layer of production wax, but the crystallinity was still weaker than in model macrocrystalline wax with similar PPD content.

Paper III introduced an AFM-based technique to quantify crystal size, shape, the form of interlocking and most importantly, the degree of crystallinity in resulting wax-asphaltene and wax-PPD crystal networks. The techniques presented in Paper I-III propose a novel approach to understanding wax-inhibitor interactions. The sensitivity of these techniques could be improved further in the future, by analyzing a wider range of wax, asphaltene and PPDs, with varying chemical composition.

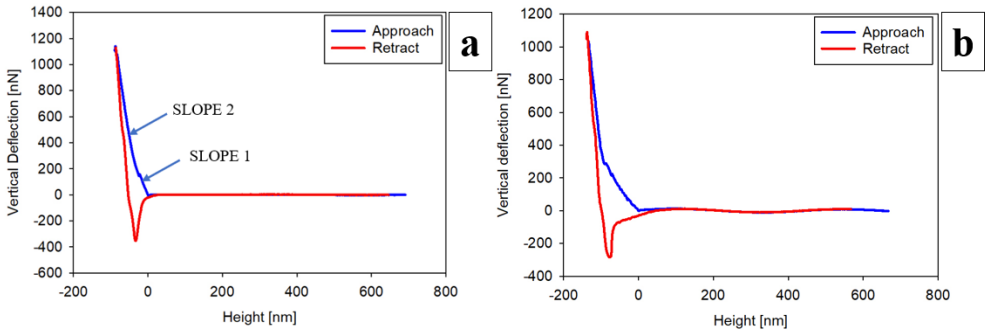

Figure 34: Force-distance profile for the surface evaporated from (a) 5% model wax in toluene, (b) 5% model wax, 1% asphaltene in toluene (random selection of a single force-distance curve for the illustration of typical 2-slope profile).

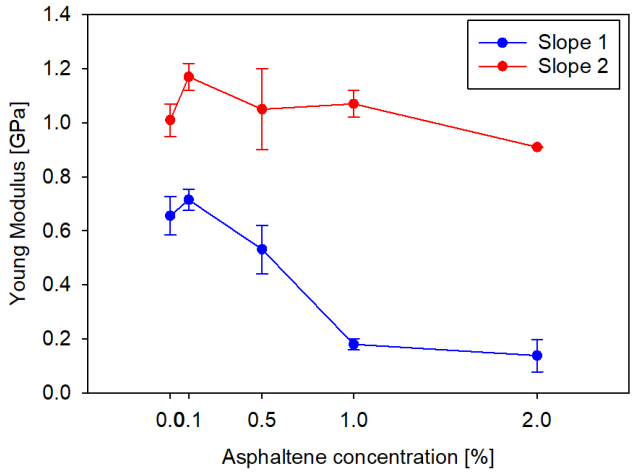

Figure 35: Average Young Modulus for slope 1 and slope 2 as a function of asphaltene concentration in surfaces evaporated from model wax and model wax-asphaltene solutions in toluene.

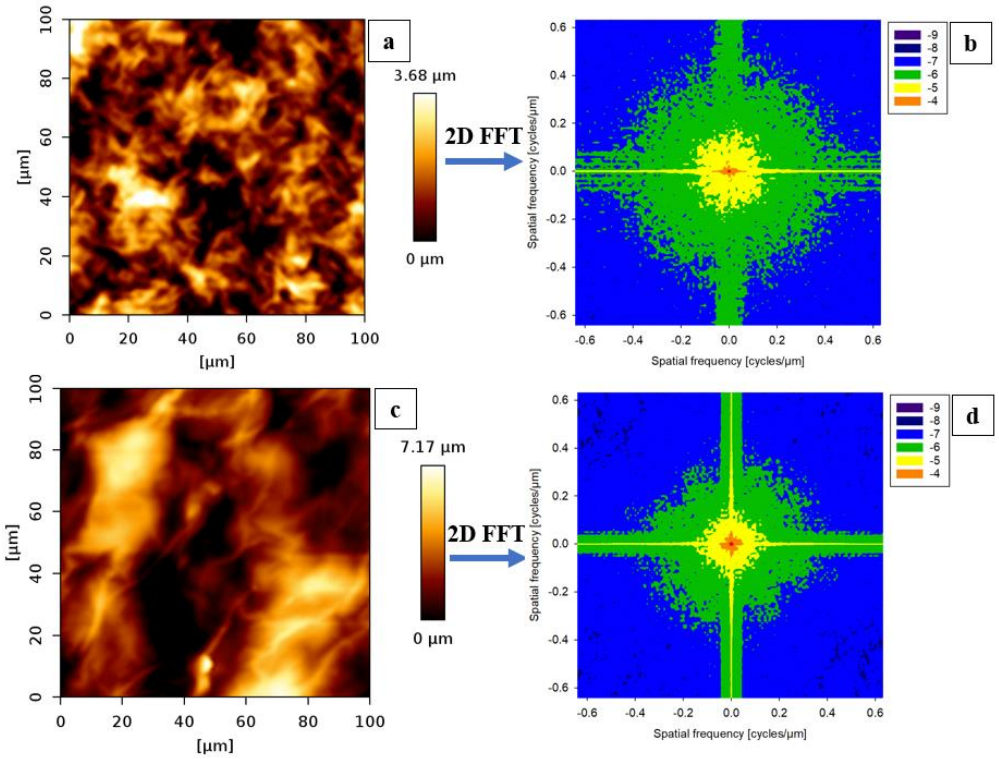

Figure 36: (a), (b) Height features of the solid surface evaporated from 2% production wax in toluene– (a) height map, (b) 2D Fast Fourier Transform of height map; (c), (d) Height features of the solid surface prepared by cold finger from 2% production wax in toluene – (c) height map, (d) 2D Fast Fourier Transform of height map.

8.4. Paper IV

Novel NMR techniques to assess the wax precipitation evolution in crude oil systems

Paper IV introduced an adapted NMR FID method to determine wax precipitation curves for complex crude oil systems, with different wax and asphaltene concentrations. DSC was used as an established technique to relatively assess the advantages and the disadvantages of NMR FID. In addition to DSC, the NMR CPMG method developed in Paper I was also used to compare the efficiency of NMR FID. The NMR scans were performed during cooling, with the same temperature interval and average cooling rate as for NMR CPMG in Paper I.

Above the wax appearance temperature, the NMR FID signal generated a 1-exponential decay, corresponding to non-crystalline phase. After wax crystallization started, a 2-exponential decay was observed, due to the sharp transition between the modified relaxation time of the crystalline phases and the modified relaxation times in the remaining fluid (non-crystalline). As explained in Section 7.1.1.3, a multi-exponential model is the real thermodynamic fit of the NMR FID data. However, instrument limitations made the separation of multiple exponentials within the non-crystalline range impossible.

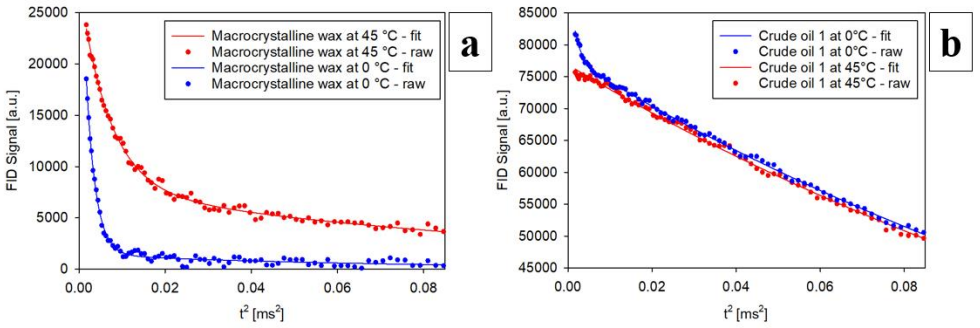

Figure 37: FID signal fitting with 2 exponentials at 45° C and at 0° C for (a) pure macrocrystalline wax, (b) selected crude oil (crude oil 1).

Results in Figure 37 showed the NMR FID decay for pure macrocrystalline wax and for a waxy crude oil at 45 °C and at 0°C. The 2-exponential separation (Equation 3) could be easily performed for pure macrocrystalline wax with high solid content (>70%) at both temperatures. However, for a crude oil with a wax content which was lower than 20% at 0°C (Figure 37 b), the 2-exponential separation became less accurate. In this case, the crystalline exponential was recreated from a maximum of 7 or 8 NMR FID data points, which generated a high degree of error. This happened because the dead time of the instrument, 13 μs, reduced the number of

points which could be acquired for the crystalline phase. Therefore, a second calculation method for the solid content was proposed. This method, referred to in the paper as the "FID non-crystallized signal", used the non-crystalline component of the 2-exponential separation, which was generated from a high number of points (72-73 points). The extrapolated non-crystalline component was normalized by the extrapolated non-crystalline component of a pure solvent (toluene). The change of the normalized value with temperature was equal to the negative of the change in the solid fraction in the system since toluene did not undergo crystallization. This was summarized by the following Equation:

$$f = f_{45°C} + \frac{\frac{L_{45°C}}{L_{toluene,45°C}} - \frac{L_T}{L_{toluene,T}}}{\frac{L_{45°C}}{L_{toluene,45°C}}} \quad \text{(Eq. 6)}$$

where f is the fraction of protons in crystalline form at the desired temperature, $f_{45°C}$ is the fraction of protons in crystalline form at 45°C and is usually equal to 0, L_T is the non-crystalline component in the wax-based system at temperature T, $L_{toluene,T}$ is the non-crystalline component in the toluene-only system at temperature T.

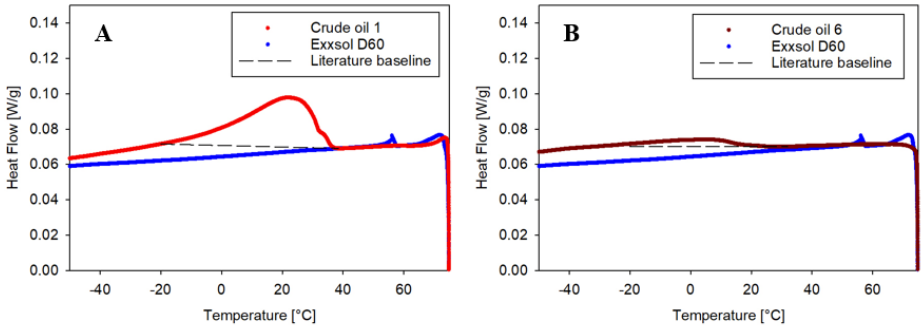

Figure 38: Baseline fitting using Exxsol D60, relative to baseline fitting using the method suggested by literature [67] : A – crude oil 1 (high wax content) ; B – crude oil 6 (low wax content).

DSC quantified the heat released by wax crystallization in selected crude oil samples. A higher cooling rate (2 °C/min) was needed to identify the released heat in crude oils with low wax content (Figure 38). Exxsol D60, an oil with a very low melting point, was used to determine the slope for the baseline, above which the released heat was quantified (Figure 38). The wax content was derived from the released heat, through division by the latent heat enthalpy of paraffin wax, used in industrial DSC applications for solid content determination in crude oils.

In the early stages of method verification, NMR FID was used to scan pure macrocrystalline and microcrystalline waxes (Figure 39). The quantification of the evolution in solid content with temperature was highly accurate and reproducible for these sample, since the solid content was very high (>70%). Results also highlighted that both macro- and micro- crystalline wax contained non-crystalline phases at 45°C (Figure 39), since the solid content was 77% and 52%, respectively. At room temperature, the amount of non-crystalline phases was still significant. This could be correlated to AFM results in Paper III, which identified an amorphous layer on top of macrocrystalline wax crystal networks and an even more amorphous layer on the production wax, which was likely to contain a high content of microcrystalline phases.

The analysis of crude oil samples with NMR FID showed a higher degree of reproducibility and certainty for samples with higher contents of wax, i.e. >15%, than for samples with lower contents of wax (<10%) at 0°C (Figure 40). For crude oil 1 (Figure 40), a high degree of accuracy was achieved for solid content determination at 0°C. Nonetheless, the identification of wax crystallization onset was less accurate, since that point was close to the detection limit of the solid exponential. NMR FID by tracking the non-crystalline signal generated similar results to DSC and NMR CPMG, which proved its reliability.

“FID non-crystallized signal”, CPMG and DSC had a higher level of relative error for crude oils with low wax content (Figure 41). A higher number of reproducibility experiments, by all available methods could improve the accuracy of the measurements.

Overall, “FID non-crystallized signal” was a reliable alternative to DSC for solid content calculation in crude oils. In literature, the method had a much more extensive use in fats, with higher levels of crystalline contents. Nonetheless, this study adapted its use for lower crystalline content in crude oils, by focusing on the evolution of the normalized non-crystalline component. Some limitations were generated by the instrument dead time, the inability to separate phases at the border between crystalline and non-crystalline and chemical composition assumptions about the wax in crude oil. Nevertheless, these barriers can be overcome, as NMR instruments get more advanced, by lowering the noise and the dead times. The comparison between NMR FID and DSC indicated higher reliability and lower sensitivity on assumptions with the FID method based on the non-crystalline signal.

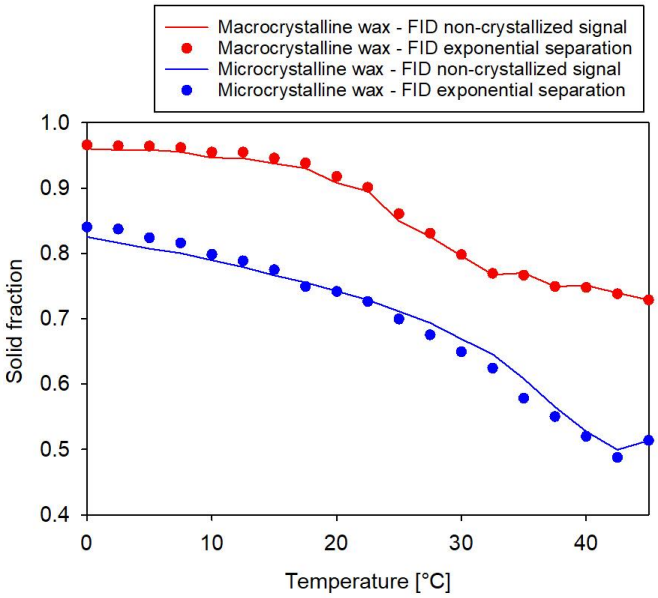

Figure 39: Solid fraction evolution with temperature for pure wax systems, as calculated with the 2 proposed computation methods from FID data.

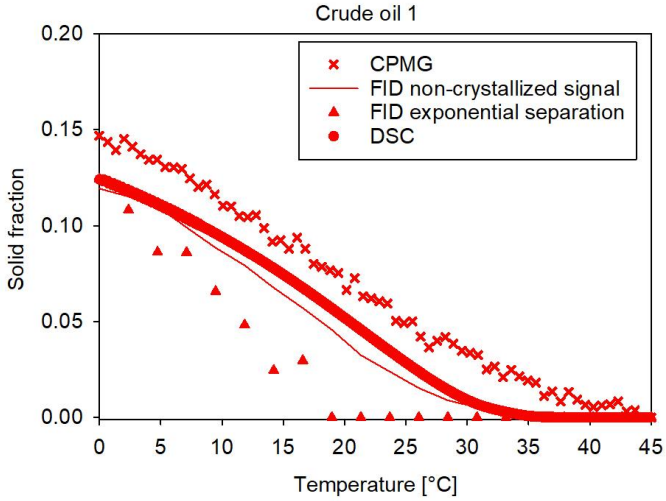

Figure 40: Solid fraction evolution with temperature for crude oil 1, with all proposed methods.

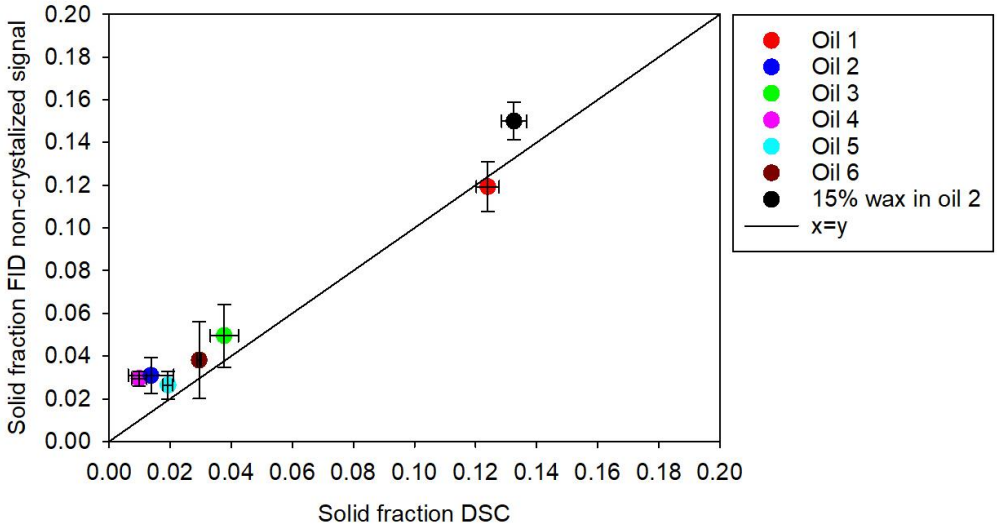

Figure 41: Solid fraction with FID non-crystallized signal calculation technique, as a function of solid fraction with DSC, at 0°C.

9. Conclusion

This thesis introduced novel NMR and AFM techniques to characterize the interactions between wax and asphaltenes or pour point depressants quantitatively and to assess the evolution of crystalline content in complex systems. Robust workflows were tested and validated with model systems and, for some methods, crude oils also.

Despite some limitations, this work managed to quantitatively assess phenomena related to wax-inhibitor interactions and asphaltene research, which were widely assumed in literature, but never quantified. The main such phenomena which were quantitatively demonstrated for the first time were:

- Dissolved wax trapping in crystal networks – quantification at various wax and inhibitor concentrations, with temperature (NMR CPMG)

The main finding was that an intermediate mobility region, corresponding to dissolved wax with reduced mobility was formed in wax and wax-asphaltene systems. High asphaltene content increased the amount of wax with low mobility, while the addition of PPD prevented this region from forming.

- Co-crystallization of asphaltenes and PPDs with wax – quantification of the evolution of the non-crystalline amount of asphaltene and PPDs, with temperature (high resolution NMR)

The non-crystalline signal of asphaltenes and PPDs decreased more with temperature in the presence of wax than in the absence of wax. This quantitatively demonstrated co-crystallization.

- Nano-aggregation/nano-clustering of asphaltenes – quantification of the monomer percentage as a function of asphaltene concentration (NMR CPMG)

The preponderance of monomers decreased with higher asphaltene concentration. The asphaltene monomers rearranged into larger nanoaggregates and nanoclusters, which corresponded to approximately the entire NMR signal at concentrations above 1%.

- Free diffusion of molecules in the bulk fluid - quantification of restricted and unrestricted diffusion of toluene in wax and wax-inhibitor systems (NMR PFGSTE)

The diffusion of toluene through crystalline networks (restricted diffusion) was quantified. Wax-only crystal networks lowered the diffusion significantly, relative to free toluene.

Wax-asphaltene co-crystal networks allowed a higher diffusion for toluene, while wax-PPD co-crystal networks generated the highest diffusion for toluene among the selected waxy systems.

- The formation of an amorphous layer in the crystal network structure of wax and wax-asphaltene mixtures – quantification of Young Modulus of a nano-scale amorphous layer (AFM)

Wax and wax-asphaltene crystal networks had two layers: a softer, more amorphous upper layer, likely with a lower degree of crystallinity and a stiffer, more crystalline bottom layer. High asphaltene content induced a decrease in stiffness and a swelling of the amorphous layer. The wax-PPD crystal networks had only one layer, which was even stiffer than the bottom layer of wax and wax-asphaltene crystal networks.

- The formation of wax-PPD and wax-asphaltene co-crystal networks with less interlocking and modified size and shape (AFM)

Lower crystal size was observed for wax-asphaltene co-crystal networks with high asphaltene content and wax-PPD co-crystal networks. The shape changed from needle (wax) to rounder, dendritic. The pores of the crystal network became smaller and more frequent for wax-asphaltene crystal networks. For wax-PPD, there was a more gradual transition between maximum height (crystal peak) and minimum height (pores), resulting in wider and more shallow pores.

The key starting point of this thesis was the determination of a low mobility dissolved wax region during the precipitation of wax and wax-asphaltene systems in Paper I. The amount of wax in this region increased when asphaltenes reached a critical concentration, associated with a transition to higher asphaltene nanoaggregate and nanocluster content (Paper II). Moreover, the presence of PPD prevented this region to form (Paper I). Three potential reasons were proposed for the explanation of this phenomenon (Figure 31). The first was interlocking during the agglomeration of wax crystals and the formation of the wax crystal network. This was expected in wax crystal networks with individual plate crystals, whose interlocking induced the formation of large pores, in which dissolved wax could be trapped. Moreover, the formation of wax-PPD complexes, which resulted in more ordered, dendritic crystal networks with smaller crystals and a higher level of crystallinity (Paper III) could also be associated with the formation of wider and more shallow pores (less interlocking), which explained the absence of a region with trapped wax. However, although asphaltenes also formed smaller crystals and

dendritic crystal networks (Paper III), they still trapped a higher quantity of dissolved wax during gelation (Paper I). Therefore, a second and a third explanation were considered. The second proposed the trapping of dissolved species in the pores of individual crystals, which were more frequent and narrower for wax-asphaltene co-crystal networks than for wax or wax-PPD co-crystal networks (Paper III). The third and most likely explanation was based on the formation of an amorphous layer in the outer structure of wax and wax-asphaltene crystal networks (Paper III), which became less crystalline when asphaltenes in high content were present (Paper III). This layer was formed of wax and asphaltenes which did not crystallize completely, due to the steric hindrance on crystal growth induced by the high size and high polydispersity of asphaltene species (monomers, nanoaggregates, nanoclusters). Despite trapping more wax, the presence of asphaltenes induced the formation of a weaker gel in the bulk fluid, which allowed for higher diffusion of molecules in the bulk fluid (Paper II). This demonstrated that the intensification of dissolved wax trapping in wax-asphaltene systems was more likely caused by the formation of the amorphous layer than by interlocking.

Novel NMR CPMG (Paper I, IV) and NMR FID (Paper IV) methods were introduced to quantify the amounts of crystalline and non-crystalline content in model and real systems and to improve the relationship between wax-inhibitor interactions and the level of crystallization. NMR FID was demonstrated as a reliable alternative to DSC for the measurement of wax precipitation curves, with less thermodynamic assumptions. High resolution NMR was adapted to quantify the rate of co-crystallization for asphaltene and PPD in wax-asphaltene and wax-PPD systems (Paper II).

10.Future work

The techniques proposed in this thesis provide a novel insight into gelation and deposition of waxy fluids. In the future, rheological simulations should be performed to establish a relationship between the properties which could be quantified with the methods in this thesis and the macro-scale behavior of the resulting fluids with temperature.

More research should also be focused on understanding the molecular interactions between wax and asphaltenes during nucleation and crystal growth. This would better explain the altered crystallinity, which promoted dissolved species trapping during gelation. For this purpose, the methods in this thesis could be used to test a wider range of asphaltenes with different chemical composition. This could establish a relationship between the chemical composition of asphaltenes and the wax-asphaltene co-crystallization mechanism, which would clarify remaining uncertainties. Additionally, the proposed methods could also be used to obtain a multi-parameter perspective regarding the efficiency of a wider range of PPDs with different chemical compositions.

NMR and AFM methods could also be improved to obtain a more detailed insight into wax crystallization mechanisms. As the technology for NMR instruments advances, dead times and uncertainties about the detection limit between non-crystalline and crystalline phases will decrease, overcoming some limitations encountered in this study. In what regards AFM, it could be used to monitor wax and wax-inhibitor surfaces in bulk fluid during crystallization. Limitations include the impossibility to scan in high viscosity environments, crystallization on the AFM tip and dissolution/gelation of the surface. An easier approach would be to scan in air on the top layers of waxy gels.

The developed methodology could also be used to characterize the properties of paraffin wax or other chemicals used as phase change materials (PCM) for heat storage in building materials. Seasonal solar energy cycles trigger melting in the summer and crystallization in the winter. The resulting heat could be stored into a battery. Therefore, such building materials often contain paraffin wax or other organic substances, coated with electrically conductive materials, such as carbon nanotubes, diamond or nucleators, which alter the properties of wax crystallization. NMR and AFM could quantify the mobility of wax and the nano-structural changes of crystal networks, which could be related to the thermodynamic properties of the resulting mixtures.

11.Bibliography

(1) BP. *BP Statistical Review of World Energy Outlook, 71st Edition*; 2022.

(2) IEA. *World Energy Balances: Overview*; Paris, 2021.

(3) Jordhus-Lier, D.; Houeland, C.; Holmås, H. E.; Szulecki, K.; Østring, P. R. *Petroleum Transition Pathways in Norway: How Do Norwegian Stakeholders Envision Pathways to Net-Zero and Phase-out for the Country's Oil and Gas Sector?*; 2022.

(4) Zou, C.; Zhai, G.; Zhang, G.; Wang, H.; Zhang, G.; Li, J.; Wang, Z.; Wen, Z.; Ma, F.; Liang, Y.; Yang, Z.; Li, X.; Liang, K. Formation, Distribution, Potential and Prediction of Global Conventional and Unconventional Hydrocarbon Resources. *Pet. Explor. Dev.* **2015**, *42* (1), 14–28. https://doi.org/10.1016/S1876-3804(15)60002-7.

(5) Kelland, M. *Production Chemicals for the Oil and Gas Industry*; 2009; Vol. 1. https://doi.org/10.1201/9781420092974.

(6) Huang, Z.; Zheng, S.; Fogler, H. S. *Wax Deposition: Experimental Characterizations, Theoretical Modeling, and Field Practices*; CRC Press: Boca Raton (FL), USA, 2015.

(7) Bern, P. A.; Withers, V. R.; Cairns, R. J. R. Wax Deposition in Crude Oil Pipelines. *European Offshore Technology Conference and Exhibition*. October 21, 1980, p SPE-206-1980-MS. https://doi.org/10.2118/206-1980-MS.

(8) Al-Yaari, M. Paraffin Wax Deposition: Mitigation and Removal Techniques. *Soc. Pet. Eng. - Saudi Arab. Sect. Young Prof. Tech. Symp. 2011* **2011**. https://doi.org/10.2118/155412-MS.

(9) Kriz, P.; Andersen, S. I. Effect of Asphaltenes on Crude Oil Wax Crystallization. *Energy & Fuels* **2005**, *19* (3), 948–953. https://doi.org/10.1021/ef049819e.

(10) Ariza-León, E.; Molina-Velasco, D. R.; Chaves-Guerrero, A. Review of Studies on Asphaltene - Wax Interaction and the Effect Thereof on Crystallization. *CTyF - Ciencia, Tecnologia y Futuro*. scieloco 2014, pp 39–53. https://doi.org/10.29047/01225383.32.

(11) Zhang, X.; Yang, F.; Yao, B.; Li, C.; Liu, D.; Sun, G. Synergistic Effect of Asphaltenes and Octadecyl Acrylate-Maleic Anhydride Copolymers Modified by

Aromatic Pendants on the Flow Behavior of Model Waxy Oils. *Fuel* **2020**, *260*, 116381. https://doi.org/https://doi.org/10.1016/j.fuel.2019.116381.

(12) Yi, S.; Zhang, J. Relationship between Waxy Crude Oil Composition and Change in the Morphology and Structure of Wax Crystals Induced by Pour-Point-Depressant Beneficiation. *Energy & Fuels* **2011**, *25* (4), 1686–1696. https://doi.org/10.1021/ef200059p.

(13) Li, N.; Mao, G.; Shi, X.; Tian, S.; Liu, Y. Advances in the Research of Polymeric Pour Point Depressant for Waxy Crude Oil. *J. Dispers. Sci. Technol.* **2018**, *39* (8), 1165–1171. https://doi.org/10.1080/01932691.2017.1385484.

(14) Hedberg, H. D. Geologic Aspects of Origin of Petroleum1. *Am. Assoc. Pet. Geol. Bull.* **1964**, *48* (11), 1755–1803. https://doi.org/10.1306/BC743DB7-16BE-11D7-8645000102C1865D.

(15) Formation of Fossil Fuels. In *Chemistry of Fossil Fuels and Biofuels*; Schobert, H., Ed.; Cambridge Series in Chemical Engineering; Cambridge University Press: Cambridge, 2013; pp 103–131. https://doi.org/DOI: 10.1017/CBO9780511844188.009.

(16) Speight, J. G. The Chemistry and Technology of Petroleum. Marcel Dekker: New York 1999.

(17) Jewell, D. M.; Albaugh, E. W.; Davis, B. E.; Ruberto, R. G. Integration of Chromatographic and Spectroscopic Techniques for the Characterization of Residual Oils. *Ind. Eng. Chem. Fundam.* **1974**, *13* (3), 278–282.

(18) Fan, T.; Wang, J.; Buckley, J. S. Evaluating Crude Oils by SARA Analysis. *SPE/DOE Improved Oil Recovery Symposium*. April 13, 2002, p SPE-75228-MS. https://doi.org/10.2118/75228-MS.

(19) Aske, N.; Kallevik, H.; Sjöblom, J. Determination of Saturate, Aromatic, Resin, and Asphaltenic (SARA) Components in Crude Oils by Means of Infrared and Near-Infrared Spectroscopy. *Energy & Fuels* **2001**, *15* (5), 1304–1312. https://doi.org/10.1021/ef010088h.

(20) Riazi, M. R. *Characterization and Properties of Petroleum Fractions*; ASTM international, 2005; Vol. 50.

(21) Oliveira, L.; Nunes, R.; Melo, I.; Ribeiro, Y.; Guimaraes, L.; Dias, J.; Guimarães, R.; Lucas, E. Evaluation of the Correlation between Wax Type and Structure/Behavior of the Pour Point Depressant. *Fuel Process. Technol.* **2016**, *149*, 268–274. https://doi.org/10.1016/j.fuproc.2016.04.024.

(22) Zaky, M. T.; Mohamed, N. H. Comparative Study on Separation and Characterization of High Melting Point Macro- and Micro-Crystalline Waxes. *J. Taiwan Inst. Chem. Eng.* **2010**, *41* (3), 360–366. https://doi.org/https://doi.org/10.1016/j.jtice.2009.09.003.

(23) Barker, A. Chapter 3 The Chromatographic Analysis of Refined and Synthetic Waxes. In *Chromatography in the Petroleum Industry*; Adlard, E. R. B. T.-J. of C. L., Ed.; Elsevier, 1995; Vol. 56, pp 55–93. https://doi.org/https://doi.org/10.1016/S0301-4770(08)61282-8.

(24) Bacon, M. M.; Romero-Zerón, L. B.; Chong, K. K. Using Cross-Polarized Microscopy to Optimize Wax-Treatment Methods. *SPE Annual Technical Conference and Exhibition*. October 4, 2009, p SPE-124799-MS. https://doi.org/10.2118/124799-MS.

(25) Zhao, Y.; Kumar, L.; Paso, K.; Ali, H.; Safieva, J.; Sjöblom, J. Gelation and Breakage Behavior of Model Wax–Oil Systems: Rheological Properties and Model Development. *Ind. Eng. Chem. Res.* **2012**, *51* (23), 8123–8133.

(26) Kurniawan, M.; Subramanian, S.; Norrman, J.; Paso, K. Influence of Microcrystalline Wax on the Properties of Model Wax-Oil Gels. *Energy & Fuels* **2018**, *32* (5), 5857–5867. https://doi.org/10.1021/acs.energyfuels.8b00774.

(27) He, B.; Martin, V.; Setterwall, F. Phase Transition Temperature Ranges and Storage Density of Paraffin Wax Phase Change Materials. *Energy* **2004**, *29* (11), 1785–1804. https://doi.org/https://doi.org/10.1016/j.energy.2004.03.002.

(28) Goia, F.; Boccaleri, E. Physical–Chemical Properties Evolution and Thermal Properties Reliability of a Paraffin Wax under Solar Radiation Exposure in a Real-Scale PCM Window System. *Energy Build.* **2016**, *119*, 41–50. https://doi.org/https://doi.org/10.1016/j.enbuild.2016.03.007.

(29) Nada, S. A.; Alshaer, W. G. Comprehensive Parametric Study of Using Carbon Foam Structures Saturated with PCMs in Thermal Management of Electronic Systems. *Energy Convers. Manag.* **2015**, *105*, 93–102.

https://doi.org/https://doi.org/10.1016/j.enconman.2015.07.071.

(30) Azizian, S.; Khosravi, M. Chapter 12 - Advanced Oil Spill Decontamination Techniques. In *Advanced Low-Cost Separation Techniques in Interface Science*; Kyzas, G. Z., Mitropoulos, A. C. B. T.-I. S. and T., Eds.; Elsevier, 2019; Vol. 30, pp 283–332. https://doi.org/https://doi.org/10.1016/B978-0-12-814178-6.00012-1.

(31) Alshareef, A. H. Asphaltenes: Definition, Properties, and Reactions of Model Compounds. *Energy & Fuels* **2020**, *34* (1), 16–30. https://doi.org/10.1021/acs.energyfuels.9b03291.

(32) Podgorski, D. C.; Corilo, Y. E.; Nyadong, L.; Lobodin, V. V; Bythell, B. J.; Robbins, W. K.; McKenna, A. M.; Marshall, A. G.; Rodgers, R. P. Heavy Petroleum Composition. 5. Compositional and Structural Continuum of Petroleum Revealed. *Energy & Fuels* **2013**, *27* (3), 1268–1276. https://doi.org/10.1021/ef301737f.

(33) Groenzin, H.; Mullins, O. C. Molecular Size and Structure of Asphaltenes from Various Sources. *Energy & Fuels* **2000**, *14* (3), 677–684. https://doi.org/10.1021/ef990225z.

(34) Mullins, O. C.; Sabbah, H.; Eyssautier, J.; Pomerantz, A. E.; Barré, L.; Andrews, A. B.; Ruiz-Morales, Y.; Mostowfi, F.; McFarlane, R.; Goual, L.; Lepkowicz, R.; Cooper, T.; Orbulescu, J.; Leblanc, R. M.; Edwards, J.; Zare, R. N. Advances in Asphaltene Science and the Yen–Mullins Model. *Energy & Fuels* **2012**, *26* (7), 3986–4003. https://doi.org/10.1021/ef300185p.

(35) Ok, S.; Mal, T. K. NMR Spectroscopy Analysis of Asphaltenes. *Energy & Fuels* **2019**, *33* (11), 10391–10414. https://doi.org/10.1021/acs.energyfuels.9b02240.

(36) Majumdar, R. D. *A Nuclear Magnetic Resonance Spectroscopic Investigation of the Molecular Structure and Aggregation Behavior of Asphaltenes*; University of Lethbridge (Canada), 2016.

(37) Barré, L.; Jestin, J.; Morisset, A.; Palermo, T.; Simon, S. Relation between Nanoscale Structure of Asphaltene Aggregates and Their Macroscopic Solution Properties. *Oil Gas Sci. Technol. - Rev. IFP* **2009**, *64* (5), 617–628.

(38) Eyssautier, J.; Levitz, P.; Espinat, D.; Jestin, J.; Gummel, J.; Grillo, I.; Barré, L. Insight into Asphaltene Nanoaggregate Structure Inferred by Small Angle Neutron and X-Ray

Scattering. *J. Phys. Chem. B* **2011**, *115* (21), 6827–6837. https://doi.org/10.1021/jp111468d.

(39) Janesko, B. G.; Brothers, E. N. Virtual Experiments on Real Asphaltenes: Predicting Properties Using Quantum Chemical Simulations of Structures from Non-Contact Atomic Force Microscopy. *Energy & Fuels* **2022**, *36* (16), 8714–8724. https://doi.org/10.1021/acs.energyfuels.2c00921.

(40) Ruiz-Morales, Y. Application of the Y-Rule and Theoretical Study to Understand the Topological and Electronic Structures of Polycyclic Aromatic Hydrocarbons from Atomic Force Microscopy Images of Soot, Coal Asphaltenes, and Petroleum Asphaltenes. *Energy & Fuels* **2022**, *36* (16), 8725–8748. https://doi.org/10.1021/acs.energyfuels.2c01170.

(41) Mullins, O. C. The Modified Yen Model. *Energy & Fuels* **2010**, *24* (4), 2179–2207. https://doi.org/10.1021/ef900975e.

(42) Magnini, M.; Matar, O. K. Fundamental Study of Wax Deposition in Crude Oil Flows in a Pipeline via Interface-Resolved Numerical Simulations. *Ind. Eng. Chem. Res.* **2019**, *58* (47), 21797–21816. https://doi.org/10.1021/acs.iecr.9b05250.

(43) Kané, M.; Djabourov, M.; Volle, J.-L.; Lechaire, J.-P.; Frebourg, G. Morphology of Paraffin Crystals in Waxy Crude Oils Cooled in Quiescent Conditions and under Flow. *Fuel* **2003**, *82* (2), 127–135. https://doi.org/https://doi.org/10.1016/S0016-2361(02)00222-3.

(44) Oliveira, G. E.; Mansur, C. R. E.; Lucas, E. F.; González, G.; de Souza, W. F. The Effect of Asphaltenes, Naphthenic Acids, and Polymeric Inhibitors on the Pour Point of Paraffins Solutions. *J. Dispers. Sci. Technol.* **2007**, *28* (3), 349–356. https://doi.org/10.1080/01932690601107526.

(45) Singh, P.; Walker, J.; Lee, H. S.; Gharfeh, S.; Thomason, B.; Blumer, D. An Application of Vacuum-Insulation Tubing for Wax Control in an Arctic Environment. *SPE Drill. Complet.* **2007**, *22* (02), 127–136. https://doi.org/10.2118/111006-PA.

(46) Sarmento, R. C.; Ribbe, G. A. S.; Azevedo, L. F. A. Wax Blockage Removal by Inductive Heating of Subsea Pipelines. *Heat Transf. Eng.* **2004**, *25* (7), 2–12. https://doi.org/10.1080/01457630490495797.

(47) Bidmus, H. O.; Mehrotra, A. K. Solids Deposition during “Cold Flow” of Wax−Solvent Mixtures in a Flow-Loop Apparatus with Heat Transfer. *Energy & Fuels* **2009**, *23* (6), 3184–3194. https://doi.org/10.1021/ef900224r.

(48) Li, W.; Huang, Q.; Wang, W.; Gao, X. Advances and Future Challenges of Wax Removal in Pipeline Pigging Operations on Crude Oil Transportation Systems. *Energy Technol.* **2020**, *8* (6), 1901412. https://doi.org/https://doi.org/10.1002/ente.201901412.

(49) Jemmett, M. R. Rheology and Deposition of Heterogeneous Organic Mixtures: An Expansion of “Cold Flow” Research. 2012. *Univ. Utah*.

(50) Jafari Ansaroudi, H. R.; Vafaie-Sefti, M.; Masoudi, S.; Behbahani, T. J.; Jafari, H. Study of the Morphology of Wax Crystals in the Presence of Ethylene-Co-Vinyl Acetate Copolymer. *Pet. Sci. Technol.* **2013**, *31* (6), 643–651. https://doi.org/10.1080/10916466.2011.632800.

(51) Sun, M.; Rezaei, N.; Firoozabadi, A. Mitigating Paraffin Wax Deposition by Dispersants and Crystal Modifiers in Flow Testing. *Fuel* **2022**, *324*, 124687. https://doi.org/https://doi.org/10.1016/j.fuel.2022.124687.

(52) Chi, Y.; Yang, J.; Sarica, C.; Daraboina, N. A Critical Review of Controlling Paraffin Deposition in Production Lines Using Chemicals. *Energy & Fuels* **2019**, *33* (4), 2797–2809. https://doi.org/10.1021/acs.energyfuels.9b00316.

(53) Buckley, J. S. Asphaltene Deposition. *Energy & Fuels* **2012**, *26* (7), 4086–4090. https://doi.org/10.1021/ef300268s.

(54) Gharbi, K.; Benyounes, K.; Khodja, M. Removal and Prevention of Asphaltene Deposition during Oil Production: A Literature Review. *J. Pet. Sci. Eng.* **2017**, *158*, 351–360. https://doi.org/https://doi.org/10.1016/j.petrol.2017.08.062.

(55) Koh, C. A.; Westacott, R. E.; Zhang, W.; Hirachand, K.; Creek, J. L.; Soper, A. K. Mechanisms of Gas Hydrate Formation and Inhibition. *Fluid Phase Equilib.* **2002**, *194–197*, 143–151. https://doi.org/https://doi.org/10.1016/S0378-3812(01)00660-4.

(56) Mpelwa, M.; Tang, S.-F. State of the Art of Synthetic Threshold Scale Inhibitors for Mineral Scaling in the Petroleum Industry: A Review. *Pet. Sci.* **2019**, *16* (4), 830–849. https://doi.org/10.1007/s12182-019-0299-5.

(57) Andrade, D. E. V; Marcelino Neto, M. A.; Negrão, C. O. R. The Importance of

Supersaturation on Determining the Solid-Liquid Equilibrium Temperature of Waxy Oils. *Fuel* **2017**, *206*, 516–523. https://doi.org/https://doi.org/10.1016/j.fuel.2017.06.042.

(58) De Castro Machado, A. L.; Lucas, E. F. Poly(Ethylene-Co-Vinyl Acetate) (EVA) Copolymers as Modifiers of Oil Wax Crystallization. *Pet. Sci. Technol.* **1999**, *17* (9), 1029–1041. https://doi.org/10.1080/10916469908949763.

(59) Huang, H.; Wang, W.; Peng, Z.; Ding, Y.; Li, K.; Li, Q.; Gong, J. The Influence of Nanocomposite Pour Point Depressant on the Crystallization of Waxy Oil. *Fuel* **2018**, *221*, 257–268. https://doi.org/https://doi.org/10.1016/j.fuel.2018.01.040.

(60) Haj-Shafiei, S.; Workman, B.; Trifkovic, M.; Mehrotra, A. K. In-Situ Monitoring of Paraffin Wax Crystal Formation and Growth. *Cryst. Growth Des.* **2019**, *19* (5), 2830–2837. https://doi.org/10.1021/acs.cgd.9b00052.

(61) Ruwoldt, J.; Humborstad Sørland, G.; Simon, S.; Oschmann, H.-J.; Sjöblom, J. Inhibitor-Wax Interactions and PPD Effect on Wax Crystallization: New Approaches for GC/MS and NMR, and Comparison with DSC, CPM, and Rheometry. *J. Pet. Sci. Eng.* **2019**, *177*, 53–68. https://doi.org/https://doi.org/10.1016/j.petrol.2019.02.046.

(62) Miyazaki, Y.; Marangoni, A. G. Structural-Mechanical Model of Wax Crystal Networks—a Mesoscale Cellular Solid Approach. *Mater. Res. Express* **2014**, *1* (2), 25101. https://doi.org/10.1088/2053-1591/1/2/025101.

(63) Hoffmann, R.; Amundsen, L.; Huang, Z.; Zheng, S.; Fogler, H. S. Wax Deposition in Stratified Oil/Water Flow. *Energy & Fuels* **2012**, *26* (6), 3416–3423. https://doi.org/10.1021/ef2018989.

(64) Rehan, M.; Nizami, A.-S.; Taylan, O.; Al-Sasi, B. O.; Demirbas, A. Determination of Wax Content in Crude Oil. *Pet. Sci. Technol.* **2016**, *34* (9), 799–804. https://doi.org/10.1080/10916466.2016.1169287.

(65) Venkatesan, R.; Nagarajan, N.; Paso, K.; Yi, Y.-B.; Sastry, A.; Fogler, H. S. The Strength of Paraffin Gels Formed under Static and Flow Conditions. *Chem. Eng. Sci.* **2005**, *60*, 3587–3598. https://doi.org/10.1016/j.ces.2005.02.045.

(66) Roenningsen, H. P.; Bjoerndal, B.; Baltzer Hansen, A.; Batsberg Pedersen, W. Wax Precipitation from North Sea Crude Oils: 1. Crystallization and Dissolution

Temperatures, and Newtonian and Non-Newtonian Flow Properties. *Energy & Fuels* **1991**, *5* (6), 895–908. https://doi.org/10.1021/ef00030a019.

(67) Chen, J.; Zhang, J.; Li, H. Determining the Wax Content of Crude Oils by Using Differential Scanning Calorimetry. *Thermochim. Acta* **2004**, *410* (1), 23–26. https://doi.org/https://doi.org/10.1016/S0040-6031(03)00367-8.

(68) Zhao, Y.; Paso, K.; Norrman, J.; Ali, H.; Sørland, G.; Sjöblom, J. Utilization of DSC, NIR, and NMR for Wax Appearance Temperature and Chemical Additive Performance Characterization. *J. Therm. Anal. Calorim.* **2015**, *120* (2), 1427–1433. https://doi.org/10.1007/s10973-015-4451-1.

(69) Roehner, R. M.; Hanson, F. V. Determination of Wax Precipitation Temperature and Amount of Precipitated Solid Wax versus Temperature for Crude Oils Using FT-IR Spectroscopy. *Energy & Fuels* **2001**, *15* (3), 756–763.

(70) Coto, B.; Martos, C.; Espada, J. J.; Robustillo, M. D.; Peña, J. L. Analysis of Paraffin Precipitation from Petroleum Mixtures by Means of DSC: Iterative Procedure Considering Solid–Liquid Equilibrium Equations. *Fuel* **2010**, *89* (5), 1087–1094. https://doi.org/https://doi.org/10.1016/j.fuel.2009.12.010.

(71) Baltzer Hansen, A.; Larsen, E.; Batsberg Pedersen, W.; Nielsen, A. B.; Roenningsen, H. P. Wax Precipitation from North Sea Crude Oils. 3. Precipitation and Dissolution of Wax Studied by Differential Scanning Calorimetry. *Energy & Fuels* **1991**, *5* (6), 914–923. https://doi.org/10.1021/ef00030a021.

(72) Batsberg Pedersen, W.; Baltzer Hansen, A.; Larsen, E.; Nielsen, A. B.; Roenningsen, H. P. Wax Precipitation from North Sea Crude Oils. 2. Solid-Phase Content as Function of Temperature Determined by Pulsed NMR. *Energy & Fuels* **1991**, *5* (6), 908–913. https://doi.org/10.1021/ef00030a020.

(73) ASTM International. *Standard Test Method for Pour Point of Petroleum Products. D97.*; 2017.

(74) ASTM International. *Standard Test Method for Pour Point of Petroleum Products (Automatic Pressure Pulsing Method). D5949.*; 2016.

(75) ASTM International. *Standard Test Method for Pour Point of Petroleum Products. D5985*; 2014.

(76) ASTM International. Standard Test Method for Pour Point of Crude Oils. D5853. **2016**.

(77) Paso, K. G. Comprehensive Treatise on Shut-in and Restart of Waxy Oil Pipelines. *J. Dispers. Sci. Technol.* **2014**, *35* (8), 1060–1085.

(78) Li, W.; Huang, Q.; Dong, X.; Gao, X. A New Model for Predicting Oil-Wax Gel Strength as a Function of Wax Crystal Precipitation and Structural Characteristics. *J. Pet. Sci. Eng.* **2020**, *188*, 106811.

(79) Tinsley, J. F.; Prud'homme, R. K.; Guo, X. Effect of Polymer Additives upon Waxy Deposits. In *The 7th International Conference on Petroleum Phase Behavior and Fouling; Asheville, NC*; 2006.

(80) Xue, H.; Zhang, J.; Han, S.; Sun, M.; Yan, X.; Li, H. Effect of Asphaltenes on the Structure and Surface Properties of Wax Crystals in Waxy Oils. *Energy & Fuels* **2019**, *33* (10), 9570–9584. https://doi.org/10.1021/acs.energyfuels.9b01825.

(81) Venkatesan, R.; Östlund, J.-A.; Chawla, H.; Wattana, P.; Nydén, M.; Fogler, H. S. The Effect of Asphaltenes on the Gelation of Waxy Oils. *Energy & Fuels* **2003**, *17* (6), 1630–1640. https://doi.org/10.1021/ef034013k.

(82) Tinsley, J. F.; Jahnke, J. P.; Adamson, D. H.; Guo, X.; Amin, D.; Kriegel, R.; Saini, R.; Dettman, H. D.; Prud'home, R. K. Waxy Gels with Asphaltenes 2: Use of Wax Control Polymers. *Energy & Fuels* **2009**, *23* (4), 2065–2074. https://doi.org/10.1021/ef800651d.

(83) Lei, Y.; Han, S.; Zhang, J. Effect of the Dispersion Degree of Asphaltene on Wax Deposition in Crude Oil under Static Conditions. *Fuel Process. Technol.* **2016**, *146*, 20–28. https://doi.org/https://doi.org/10.1016/j.fuproc.2016.02.005.

(84) Ruwoldt, J.; Subramanian, S.; Simon, S.; Oschmann, H.; Sjöblom, J. Asphaltene Fractionation Based on Adsorption onto Calcium Carbonate: Part 3. Effect of Asphaltenes on Wax Crystallization. *Colloids Surfaces A Physicochem. Eng. Asp.* **2018**, *554*, 129–141. https://doi.org/https://doi.org/10.1016/j.colsurfa.2018.06.025.

(85) Bai, Y.; Bai, Q. 16 - Wax and Asphaltenes; Bai, Y., Bai, Q. B. T.-S. E. H. (Second E., Eds.; Gulf Professional Publishing: Boston, 2019; pp 435–453. https://doi.org/https://doi.org/10.1016/B978-0-12-812622-6.00016-6.

(86) Alcazar-Vara, L. A.; Buenrostro-Gonzalez, E. Experimental Study of the Influence of Solvent and Asphaltenes on Liquid–Solid Phase Behavior of Paraffinic Model Systems by Using DSC and FT-IR Techniques. *J. Therm. Anal. Calorim. J Therm Anal Calorim* **2012**, *107* (3), 1321–1329. https://doi.org/https://doi.org/10.1007/s10973-011-1592-8.

(87) García, M. del C.; Carbognani, L. Asphaltene−Paraffin Structural Interactions. Effect on Crude Oil Stability. *Energy & Fuels* **2001**, *15* (5), 1021–1027. https://doi.org/10.1021/ef0100303.

(88) Lei, Y.; Han, S.; Zhang, J.; Bao, Y.; Yao, Z.; Xu, Y. Study on the Effect of Dispersed and Aggregated Asphaltene on Wax Crystallization, Gelation, and Flow Behavior of Crude Oil. *Energy & Fuels* **2014**, *28* (4), 2314–2321. https://doi.org/10.1021/ef4022619.

(89) Cao, H.; Cao, X.; Zhao, X.; Guo, D.; Liu, Y.; Bian, J. Molecular Dynamics Simulation of Wax Molecules Aggregational Crystallization Behavior during Cooling of Crude Oil Mixture. *Case Stud. Therm. Eng.* **2022**, *37*, 102298. https://doi.org/https://doi.org/10.1016/j.csite.2022.102298.

(90) Rogel, E.; Ovalles, C.; Moir, M. Asphaltene Stability in Crude Oils and Petroleum Materials by Solubility Profile Analysis. *Energy & Fuels* **2010**, *24* (8), 4369–4374. https://doi.org/10.1021/ef100478y.

(91) Singh, P.; Youyen, A.; Fogler, H. S. Existence of a Critical Carbon Number in the Aging of a Wax-Oil Gel. *AIChE J.* **2001**, *47* (9), 2111–2124. https://doi.org/https://doi.org/10.1002/aic.690470921.

(92) Tinsley, J. F.; Jahnke, J. P.; Dettman, H. D.; Prud'home, R. K. Waxy Gels with Asphaltenes 1: Characterization of Precipitation, Gelation, Yield Stress, and Morphology. *Energy & Fuels* **2009**, *23* (4), 2056–2064. https://doi.org/10.1021/ef800636f.

(93) García, M. del C. Crude Oil Wax Crystallization. The Effect of Heavy n-Paraffins and Flocculated Asphaltenes. *Energy & Fuels* **2000**, *14* (5), 1043–1048. https://doi.org/10.1021/ef0000330.

(94) Molina V., D.; Ariza León, E.; Chaves-Guerrero, A. Understanding the Effect of

Chemical Structure of Asphaltenes on Wax Crystallization of Crude Oils from Colorado Oil Field. *Energy & Fuels* **2017**, *31* (9), 8997–9005. https://doi.org/10.1021/acs.energyfuels.7b01149.

(95) Savulescu, G. C.; Simon, S.; Sørland, G.; Øye, G. New Nuclear Magnetic Resonance Approaches on the Evolution of Wax Mobility during Wax Crystallization. *Energy & Fuels* **2022**, *36* (1), 350–360. https://doi.org/10.1021/acs.energyfuels.1c03613.

(96) Yang, F.; Zhao, Y.; Sjöblom, J.; Li, C.; Paso, K. Polymeric Wax Inhibitors and Pour Point Depressants for Waxy Crude Oils: A Critical Review. *J. Dispers. Sci. Technol.* **2014**, *36*, 213–225. https://doi.org/10.1080/01932691.2014.901917.

(97) Radulescu, A.; Schwahn, D.; Stellbrink, J.; Kentzinger, E.; Heiderich, M.; Richter, D.; Fetters, L. J. Wax Crystallization from Solution in Hierarchical Morphology Templated by Random Poly (Ethylene-Co-Butene) Self-Assemblies. *Macromolecules* **2006**, *39* (18), 6142–6151.

(98) Taraneh, J. B.; Rahmatollah, G.; Hassan, A.; Alireza, D. Effect of Wax Inhibitors on Pour Point and Rheological Properties of Iranian Waxy Crude Oil. *Fuel Process. Technol.* **2008**, *89* (10), 973–977.

(99) Naiya, T. K.; Banerjee, S.; Kumar, R.; Mandal, A. Heavy Crude Oil Rheology Improvement Using Naturally Extracted Surfactant. In *SPE Oil and Gas India Conference and Exhibition?*; SPE, 2015; p SPE-178133.

(100) Wu, C.; Zhang, J.; Li, W.; Wu, N. Molecular Dynamics Simulation Guiding the Improvement of EVA-Type Pour Point Depressant. *Fuel* **2005**, *84* (16), 2039–2047. https://doi.org/https://doi.org/10.1016/j.fuel.2004.12.009.

(101) Alcazar-Vara, L. A.; Buenrostro-Gonzalez, E.; Elkordy, A. A. Liquid-Solid Phase Equilibria of Paraffinic Systems by DSC Measurements. *Appl. Calorim. a wide Context. scanning calorimetry, iso-thermal titration Calorim. Microcalorim. intech, rijeka, Croat.* **2013**, 253–276.

(102) Harish, S.; Orejon, D.; Takata, Y.; Kohno, M. Enhanced Thermal Conductivity of Phase Change Nanocomposite in Solid and Liquid State with Various Carbon Nano Inclusions. *Appl. Therm. Eng.* **2017**, *114*, 1240–1246. https://doi.org/https://doi.org/10.1016/j.applthermaleng.2016.10.109.

(103) Madureira, A. R.; Campos, D. A.; Fonte, P.; Nunes, S.; Reis, F.; Gomes, A. M.; Sarmento, B.; Pintado, M. M. Characterization of Solid Lipid Nanoparticles Produced with Carnauba Wax for Rosmarinic Acid Oral Delivery. *RSC Adv.* **2015**, *5* (29), 22665–22673.

(104) Yang, F.; Li, C.; Yang, S.; Zhang, Q.; Xu, J. Effect of Dodecyl Benzene Sulfonic Acid (DBSA) and Lauric Amine (LA) on the Associating State and Rheology of Heavy Oils. *J. Pet. Sci. Eng.* **2014**, *124*, 19–26.

(105) Soni, H. P.; Kiranbala; Agrawal, K. S.; Nagar, A.; Bharambe, D. P. Designing Maleic Anhydride-α-Olifin Copolymeric Combs as Wax Crystal Growth Nucleators. *Fuel Process. Technol.* **2010**, *91* (9), 997–1004. https://doi.org/https://doi.org/10.1016/j.fuproc.2010.02.019.

(106) Ruwoldt, J.; Simon, S.; Norrman, J.; Oschmann, H.-J.; Sjöblom, J. Wax-Inhibitor Interactions Studied by Isothermal Titration Calorimetry and Effect of Wax Inhibitor on Wax Crystallization. *Energy & Fuels* **2017**, *31* (7), 6838–6847. https://doi.org/10.1021/acs.energyfuels.7b00749.

(107) Ruffier-Meray, V.; Roussel, J.; Defontaines, A. Use of Pulsed Nmr Spectroscopy to Measure the Amount of Solid Deposits As a Function of Temperature in Waxy Crudes. *Oil Gas Sci. Technol. L Inst. Fr. Du Pet. - OIL GAS SCI TECHNOL* **1998**, *53*, 531–535. https://doi.org/10.2516/ogst:1998048.

(108) Kané, M.; Djabourov, M.; Volle, J.-L.; Rutledge, D. N. Correction of Biased Time Domain NMR Estimates of the Solid Content of Partially Crystallized Systems. *Appl. Magn. Reson.* **2002**, *22* (3), 335. https://doi.org/10.1007/BF03166115.

(109) Slichter, C. P. *Principles of Magnetic Resonance*; Springer-Verlag Berlin Heidelberg: Springer Science & Business Media., 2013.

(110) Meiboom, S.; Gill, D. Modified Spin-Echo Method for Measuring Nuclear Relaxation Times. *Rev. Sci. Instrum.* **1958**, *29* (8), 688–691. https://doi.org/10.1063/1.1716296.

(111) Hoult, D. I.; Bhakar, B. NMR Signal Reception: Virtual Photons and Coherent Spontaneous Emission. *Concepts Magn. Reson.* **1997**, *9* (5), 277–297. https://doi.org/https://doi.org/10.1002/(SICI)1099-0534(1997)9:5<277::AID-CMR1>3.0.CO;2-W.

(112) Humborstad Sørland, G. *Pulsed-Field-Gradient NMR*; Springer Series in Chemical Physics, 2014.

(113) Hornak, J. P.; Science, R. I. of T. C. for I. *The Basics of NMR*; Rochester Institute of Technology, Center for Imaging Science, 1996.

(114) Pradhan, S.; Rajamani, S.; Agrawal, G.; Dash, M.; Samal, S. K. 7 - NMR, FT-IR and Raman Characterization of Biomaterials; Tanzi, M. C., Farè, S. B. T.-C. of P. B., Eds.; Woodhead Publishing, 2017; pp 147–173. https://doi.org/https://doi.org/10.1016/B978-0-08-100737-2.00007-8.

(115) Duus, J. Roger S. Macomber. A Complete Introduction to Modern NMR Spectroscopy. Wiley, Chichester, 1998, Xvii+ 383 Pp. Price £45. ISBN 0 471 15736 8. *Magn. Reson. Chem.* **2002**, *40* (6), 430. https://doi.org/https://doi.org/10.1002/mrc.1025.

(116) Elster, A. Questions and Answers in MRI https://mri-q.com/why-is-t1--t2.html#:~:text=T2 relaxation always proceeds at,than or equal to T2.&text=To the left is a,nuclei in various biological tissues.

(117) Provencher, S. W. A Constrained Regularization Method for Inverting Data Represented by Linear Algebraic or Integral Equations. *Comput. Phys. Commun.* **1982**, *27* (3), 213–227. https://doi.org/https://doi.org/10.1016/0010-4655(82)90173-4.

(118) Sørland, G. H.; Hafskjold, B.; Herstad, O. A Stimulated-Echo Method for Diffusion Measurements in Heterogeneous Media Using Pulsed Field Gradients. *J. Magn. Reson.* **1997**, *124* (1), 172–176. https://doi.org/https://doi.org/10.1006/jmre.1996.1029.

(119) Sørland; Aksnes; Gjerdåker. A Pulsed Field Gradient Spin-Echo Method for Diffusion Measurements in the Presence of Internal Gradients. *J. Magn. Reson.* **1999**, *137 2*, 397–401.

(120) Tourell, M. C.; Pop, I.-A.; Brown, L. J.; Brown, R. C. D.; Pileio, G. Singlet-Assisted Diffusion-NMR (SAD-NMR): Redefining the Limits When Measuring Tortuosity in Porous Media. *Phys. Chem. Chem. Phys.* **2018**, *20* (20), 13705–13713. https://doi.org/10.1039/C8CP00145F.

(121) Latour, L. L.; Mitra, P. P.; Kleinberg, R. L.; Sotak, C. H. Time-Dependent Diffusion Coefficient of Fluids in Porous Media as a Probe of Surface-to-Volume Ratio. *J.*

Magn. Reson. Ser. A **1993**, *101* (3), 342–346. https://doi.org/https://doi.org/10.1006/jmra.1993.1056.

(122) Halim, N.; Ali, S.; Nadeem, M. N.; Abdul Hamid, P.; Tan, I. M. Synthesis of Wax Inhibitor and Assessment of Squeeze Technique Application for Malaysian Waxy Crude. *SPE Asia Pacific Oil and Gas Conference and Exhibition*. Society of Petroleum Engineers: Jakarta, Indonesia 2011, p 15. https://doi.org/10.2118/142288-MS.

(123) Ward-Williams, J. A.; Karsten, V.; Guédon, C. M.; Baart, T. A.; Munnik, P.; Sederman, A. J.; Mantle, M. D.; Zheng, Q.; Gladden, L. F. Extending NMR Tortuosity Measurements to Paramagnetic Catalyst Materials Through the Use of Low Field NMR. *Chemistry–Methods* **2022**, *2* (8), e202200025. https://doi.org/https://doi.org/10.1002/cmtd.202200025.

(124) Declerck, A.; Nelis, V.; Rimaux, T.; Dewettinck, K.; Van der Meeren, P. Influence of Polymorphism on the Solid Fat Content Determined by FID Deconvolution. *Eur. J. Lipid Sci. Technol.* **2018**, *120* (3), 1700339. https://doi.org/https://doi.org/10.1002/ejlt.201700339.

(125) Trezza, E.; Haiduc, A. M.; Goudappel, G. J. W.; van Duynhoven, J. P. M. Rapid Phase-Compositional Assessment of Lipid-Based Food Products by Time Domain NMR. *Magn. Reson. Chem.* **2006**, *44* (11), 1023–1030. https://doi.org/https://doi.org/10.1002/mrc.1893.

(126) Dieffenbacher, A.; Pocklington, W. D. *Standard Methods for the Analysis of Oils, Fats and Derivatives - 1st Supplement to the 7th Revised and Enlarged Edition*; Blakcwell Scientific Publications: Oxford, 1992.

(127) Declerck, A.; Nelis, V.; Danthine, S.; Dewettinck, K.; Van der Meeren, P. Characterisation of Fat Crystal Polymorphism in Cocoa Butter by Time-Domain NMR and DSC Deconvolution. *Foods* . 2021. https://doi.org/10.3390/foods10030520.

(128) Declerck, A.; Vermeir, L.; Nelis, V.; Dewettinck, K.; Van der Meeren, P. Development of a Method to Determine the SFC in the Fat Phase of Emulsions Using TD-NMR FID-CPMG Deconvolution. *Magn. Reson. Chem.* **2022**, *n/a* (n/a). https://doi.org/https://doi.org/10.1002/mrc.5251.

(129) Raja, P. M. V; Barron, A. R. Physical Methods in Chemistry. *Nature* **1934**, *134*

(3384), 366–367. https://doi.org/10.1002/jctb.5000533702.

(130) Kodre, K. V; Attarde, S. R.; Yendhe, P. R.; Patil, R. Y.; Barge, V. U. Differential Scanning Calorimetry: A Review. *Res. Rev. J. Pharm. Anal.* **2014**, *3* (3), 11–22.

(131) Agarwal, A.; Sarviya, R. M. Characterization of Commercial Grade Paraffin Wax as Latent Heat Storage Material for Solar Dryers. *Mater. Today Proc.* **2017**, *4* (2, Part A), 779–789. https://doi.org/https://doi.org/10.1016/j.matpr.2017.01.086.

(132) Bert, V. *Atomic Force Microscopy*, Second Edi.; Springer, 2019. https://doi.org/https://doi.org/10.1007/978-3-030-13654-3.

(133) Giessibl, F. J. Advances in Atomic Force Microscopy. *Rev. Mod. Phys.* **2003**, *75* (3), 949–983. https://doi.org/10.1103/RevModPhys.75.949.

(134) Schuler, B.; Meyer, G.; Peña, D.; Mullins, O. C.; Gross, L. Unraveling the Molecular Structures of Asphaltenes by Atomic Force Microscopy. *J. Am. Chem. Soc.* **2015**, *137* (31), 9870–9876. https://doi.org/10.1021/jacs.5b04056.

(135) Żbik, M.; Horn, R. G.; Shaw, N. AFM Study of Paraffin Wax Surfaces. *Colloids Surfaces A Physicochem. Eng. Asp.* **2006**, *287* (1), 139–146. https://doi.org/https://doi.org/10.1016/j.colsurfa.2006.03.043.

(136) Zhong, Q.; Inniss, D.; Kjoller, K.; Elings, V. B. Fractured Polymer/Silica Fiber Surface Studied by Tapping Mode Atomic Force Microscopy. *Surf. Sci.* **1993**, *290* (1), L688–L692. https://doi.org/https://doi.org/10.1016/0039-6028(93)90582-5.

(137) Martin, Y.; Williams, C. C.; Wickramasinghe, H. K. Atomic Force Microscope–Force Mapping and Profiling on a Sub 100-Å Scale. *J. Appl. Phys.* **1987**, *61* (10), 4723–4729. https://doi.org/10.1063/1.338807.

(138) Bruker/JPK BioAFM. QI(TM) Mode https://www.jpk.com/products/atomic-force-microscopy/qi-mode/pid1205.

(139) Savulescu, G. C.; Rücker, M.; Scanziani, A.; Pini, R.; Georgiadis, A.; Luckham, P. F. Atomic Force Microscopy for the Characterisation of Pinning Effects of Seawater Micro-Droplets in n-Decane on a Calcite Surface. *J. Colloid Interface Sci.* **2021**, *592*, 397–404. https://doi.org/https://doi.org/10.1016/j.jcis.2021.02.070.

(140) Yesufu-Rufai, S.; Marcelis, F.; Georgiadis, A.; Berg, S.; Rücker, M.; van Wunnik, J.;

Luckham, P. Atomic Force Microscopy (AFM) Study of Redox Conditions in Sandstones: Impact on Wettability Modification and Mineral Morphologyfile:///C:/Users/Georgecs/Downloads/10.1007_s003960050551-Citation (1).Ris. *Colloids Surfaces A Physicochem. Eng. Asp.* **2020**, *597*, 124765. https://doi.org/https://doi.org/10.1016/j.colsurfa.2020.124765.

(141) Ekanem, E. M.; Rücker, M.; Yesufu-Rufai, S.; Spurin, C.; Ooi, N.; Georgiadis, A.; Berg, S.; Luckham, P. F. Novel Adsorption Mechanisms Identified for Polymer Retention in Carbonate Rocks. *JCIS Open* **2021**, *4*, 100026. https://doi.org/https://doi.org/10.1016/j.jciso.2021.100026.

(142) Efremov, Y. M.; Wang, W.-H.; Hardy, S. D.; Geahlen, R. L.; Raman, A. Measuring Nanoscale Viscoelastic Parameters of Cells Directly from AFM Force-Displacement Curves. *Sci. Rep.* **2017**, *7* (1), 1541. https://doi.org/10.1038/s41598-017-01784-3.

(143) Brinkman, H. C. A Calculation of the Viscous Force Exerted by a Flowing Fluid on a Dense Swarm of Particles. *Flow, Turbul. Combust.* **1949**, *1* (1), 27–34. https://doi.org/10.1007/BF02120313.

(144) Méndez-Méndez, J. V; Alonso-Rasgado, M. T.; Correia Faria, E.; Flores-Johnson, E. A.; Snook, R. D. Numerical Study of the Hydrodynamic Drag Force in Atomic Force Microscopy Measurements Undertaken in Fluids. *Micron* **2014**, *66*, 37–46. https://doi.org/https://doi.org/10.1016/j.micron.2014.05.004.

(145) Nawaz, S.; Sánchez, P.; Bodensiek, K.; Li, S.; Simons, M.; Schaap, I. A. T. Cell Visco-Elasticity Measured with AFM and Optical Trapping at Sub-Micrometer Deformations. *PLoS One* **2012**, *7* (9), e45297.

(146) Ese, M.-H.; Sjöblom, J.; Djuve, J.; Pugh, R. An Atomic Force Microscopy Study of Asphaltenes on Mica Surfaces. Influence of Added Resins and Demulsifiers. *Colloid Polym. Sci.* **2000**, *278* (6), 532–538. https://doi.org/10.1007/s003960050551.

Paper I

New NMR approaches on the evolution of wax mobility during wax crystallization

energy&fuels

pubs.acs.org/EF

Article

New Nuclear Magnetic Resonance Approaches on the Evolution of Wax Mobility during Wax Crystallization

George Claudiu Savulescu,* Sébastien Simon, Geir Sørland, and Gisle Øye

Cite This: *Energy Fuels* 2022, 36, 350−360

Read Online

ACCESS | Metrics & More | Article Recommendations | Supporting Information

ABSTRACT: Wax crystallization at low temperature is one of the main problems affecting flow assurance during oil production. Wax inhibitors, such as pour point depressants (PPDs), and crude oil components, such as asphaltenes, are estimated to impact wax precipitation by both cocrystallization and the formation of complexes with waxes. However, the exact mechanism behind these interactions is not fully understood. Low field nuclear magnetic resonance (LF-NMR) methods have rarely been implemented for the analysis of wax precipitation in crude oil in spite of very promising results. This paper presents an improved method focused on the measurement of relaxation times which characterize the mobility of wax, asphaltene, and PPD molecules. As a wax crystal network forms at low temperature due to wax precipitation, dissolved wax molecules display a reduction in mobility as they become trapped in the pores and interact with the species of solids in the crystal network. The aim of this article is to analyze wax−wax and wax−inhibitor interactions by quantifying the amount of wax molecules trapped inside the crystal network. This paper focuses on investigating the effect of wax, asphaltene, and PPD concentrations on the percentage of precipitated wax with temperature and on the intensity of the reduced mobility wax region. The novelties of this work include the identification and quantification of a low mobility asphaltene nanoaggregate region, which may be used in future studies to characterize the changes in asphaltene aggregation state over selected concentration ranges. Additionally, the new NMR method allows us to understand and quantify with high resolution how asphaltenes in evolving aggregation states or other inhibitors impact the mobility of the dissolved wax within the wax crystal network. The new methods and breakthroughs about the wax precipitation mechanism may be correlated and extended in future studies to observations in real crude oil systems.

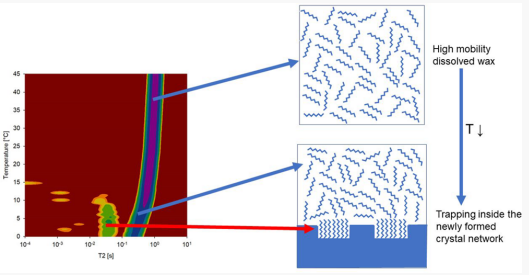

1. INTRODUCTION

Paraffin waxes are components of crude oil, consisting of *n*-, iso-, or cyclo-alkanes, usually with a carbon chain between C_{20} and C_{100} or even higher.[1] Wax precipitation occurs in a fluid environment at temperatures lower than the wax appearance temperature (WAT). This phenomenon negatively impacts flow assurance during crude oil extraction. Wax deposition during continuous flow pipeline restart issues caused by waxy gelling and increased fluid viscosity are among the problems most often encountered as a result of wax precipitation.[2]

Wax crystallization is expected to take place in three stages: nucleation, growth, and agglomeration. When temperature is gradually decreased, nucleation is delayed by a time lag, required to overcome the gap from steady-state conditions. This delay is dependent on the cooling rate,[3] and thus, the observed cloud point in such experiments is lower than the actual solubility point of wax. During the last phase of crystallization, a gel is usually formed in systems with a high enough wax content (at least 1%−2%).[4] The properties of the gel are dependent on several factors. including the wax composition. For example, macrocrystalline wax, usually composed of low molecular weight *n*-alkanes (C_{18}−C_{40}) with a more linear structure, is expected to manifest high yield strength gels, due to larger and less compact crystal structures. On the other hand, microcrystalline wax, composed of high molecular weight (C_{40} and above), iso-alkanes and cyclo-alkanes usually generate weak gels due to smaller and more compact crystal structures.[5]

A conventional method to combat wax-related issues is the use of wax inhibitors, such as pour point depressants (PPDs).[6] Although it was not completely demonstrated, the wide perception is that PPDs react with wax by cocrystallization and by affecting wax nucleation and solubility.[7] The presence of asphaltenes, polar components in crude oil, can also impact

Received: October 22, 2021
Revised: December 10, 2021
Published: December 23, 2021

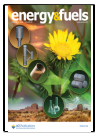

wax precipitation. Asphaltenes represent high molecular compounds in crude oil, which are insoluble in low molecular weight *n*-alkanes but are soluble in aromatic solvents such as toluene.[8] In some cases, asphaltenes were found to cocrystallize with wax to smaller and distorted crystals, which creates significant improvements to crude oil flowability.[9] Also, asphaltenes can act as a nucleation site for wax, generating more finely dispersed wax crystals, which again allow better crude oil flow but might increase WAT.[9−12] However, the exact mechanism behind the impact of asphaltenes on wax precipitation remains to be further investigated. Previous studies often have contradicting conclusions. Some works show that asphaltenes inhibit wax precipitation in certain concentration regions, specific to each type of asphaltenes, but they might promote wax precipitation in other concentration regions.[13,14] The pattern of the concentration ranges for crystallization inhibition or promotion is in most cases rather irregular, mainly because of the polydisperse character of asphaltenes,[15] and remains to be investigated with higher accuracy. In addition to PPDs and asphaltenes, isomer waxes with more branched alkane composition (microcrystalline) present in relatively high concentrations (1 wt % microcrystalline, 5 wt % macrocrystalline wax system) have recently been investigated as a modifier to macrocrystalline wax crystallization patterns.[16] The microcrystalline waxes have been shown to prevent interlocking in macrocrystalline waxes through spatial hindrances. This phenomenon leads to the formation of only small and discrete macrocrystalline wax crystals, which make the system behave like a microcrystalline gel.[16]

Researchers in this field have so far studied the effects of wax inhibitors on wax deposition with analytical methods such as differential scanning calorimetry (DSC), cross-polarized microscopy (CPM), isothermal titration calorimetry (ITC), and more recently low field NMR.[2,17−21]

Batsberg Pedersen et al. first introduced low field NMR for the analysis of wax precipitation in crude oils.[22] They compared the amount of precipitated waxes and the amount of waxes determined by the acetone precipitation method for 17 crude oils. Throughout time, the procedure has been extensively developed and improved in accuracy.[23,24]

In recent years, an adapted Carr−Purcell−Meiboom−Gill (CPMG) sequence (see below) has been used to characterize crude oil systems. For example, Yalaoui et al.[25] investigated the behavior of the crude oil within the crystal network formed during crystallization and illustrated the presence of a region with lower mobility liquid trapped in the crystal network. However, these regions could not be entirely separated and quantified due to the strong proton signal generated by the other liquid components of the crude oil.

Zhao et al. adapted the CPMG sequence to characterize model wax systems in deuterated toluene in order to prevent this form of overlapping.[21] Wax precipitation curves, tracking the apparent solid content, were generated by quantifying the change in the dissolved wax signal in various wax and wax−PPD systems. Ruwoldt et al. extended the method to study the impact of a wider range of inhibitors on wax precipitation,[19] demonstrating the effectiveness and sensitivity of the method. Direct comparison of wax precipitation curves with DSC proved that the two methods generated consistent results.

This study aims to create a higher resolution NMR method which provides additional insight into the interactions behind the wax inhibition mechanism, such as complex formation between dissolved wax and particles in the newly formed crystal network and cocrystallization of wax and inhibitor molecules.

2. THEORY

2.1. Nuclear Magnetic Resonance (NMR). When placing a sample containing protons in an external field, the nuclear magnetic moment of the protons will align against this field. By applying for a short time an oscillating magnetic field with a frequency corresponding to the energy needed to induce transitions between the nuclear energy levels (the resonance frequency), the system is brought out of thermal equilibrium. When switching off this field, the nuclear magnetic moment will tend to align against the external field again at a rate that is dependent on the so-called relaxation times. This will produce a change in the magnetic flux and may generate an electrical current through a coil, where the current is proportional to the proton content and the change in intensity is proportional to the relaxation times.[26−30] This feature is applied to monitor the characteristics, such as relaxation times, bulk, and solid fractions of the sample as the temperature is varied.

2.2. Carr−Purcell−Meiboom−Gill (CPMG) Experiment. To monitor the characteristics of the sample mentioned above, we use the Carr−Purcell−Meiboom−Gill (CPMG) NMR experiment.[30,31] This experiment consists of an initial oscillating magnetic field pulse, radio frequency (RF), which brings the net nuclear magnetic moment 90° away from the direction of the external field (i.e., in the transverse plane to the external field). Then a loop of 180° RF pulses are applied, separated by a time $2 \times \tau$, and the induced current (the NMR signal) is recorded at the time of the spin echoes[32] (Figure S1, Supporting Information). This NMR signal, I, will decay as a function of the transverse relaxation time T_2 and with the corresponding fraction as follows:

$$I = \sum_i I_i e^{-2n\tau/T_2^i} \tag{1}$$

where I is the component number, T_2^i the relaxation time of the component, I_i the corresponding intensity, τ half of the interecho spacing, and n the echo number.[30,31] The experimental data which, in general, has a multiexponential decay can then be fitted to an inverse Laplace transform[32] and will result in a distribution of T_2 values and with their corresponding intensities.

T_1 and T_2 values of molecules are therefore influenced by variations of the NMR interactions due to molecular motion. As a result, T_1 and T_2 measurements have become common approaches to study molecular characteristics such as reorientation of molecules and interaction between them.[27] In this study, T_2 distributions, acquired by CPMG are used to characterize wax crystallization and the mobility of dissolved wax molecules with temperature. Liquids display higher T_2 ranges, conventionally set at above 3×10^{-3} s, while solids are characterized by low T_2 values (10^{-4} to 10^{-3} s).

3. EXPERIMENTAL SECTION

3.1. Materials. Solvents used in this study are deuterated toluene (anhydrous, 99.6% deuterated), toluene (anhydrous, 99.8%), and hexadecane (anhydrous, 99%) from Sigma-Aldrich, Norway. Macrocrystalline wax was provided by Sasolwax from Sasol, Germany (wax 5405). The composition and properties of this wax sample are presented previously.[19] Asphaltenes were precipitated from a heavy crude oil (API 19°) originating from the Norwegian shelf of the

https://doi.org/10.1021/acs.energyfuels.1c03613
Energy Fuels 2022, 36, 350−360

North Sea, using *n*-hexane (HPLC grade, ≥97%). Properties of the asphaltenes precipitated from this crude oil have previously been published.[33,34] The pour point depressant used in this study was based on polycarboxylate (proprietary) from BASF, Germany, and was presented as PPD A previously.[19] As a reference, all concentrations presented in this study are in weight percentages (% wt).

3.2. Sample Preparation. For asphaltene preparation, the selected crude oil was heated to 60 °C for 1 h and shaken strongly before use to ensure homogeneity of the sample. Asphaltenes were precipitated by diluting the crude oil sample with 40 mL *n*-hexane per gram of crude oil and stirring overnight. The resulting mixture was then filtered through a 0.45 μm HVLP-type Millipore filter membrane and afterward rinsed with warm *n*-hexane until the filtrate was clear. The yield of asphaltenes accounted for 2.3%−2.7% of the crude oil.

The PPD originally contained different petroleum cuts having 80% active content, according to manufacturer specifications. The polymers were solvent purified, according to the procedure detailed previously.[19]

In order to prepare the samples used for CPMG NMR analysis, PPDs and asphaltenes were first dissolved in deuterated toluene, obtaining stock solutions with concentrations of 1.05 wt %. These were shaken overnight at 200 rpm to allow for an optimal degree of solubilization. Then, a range of wax−PPD and wax−asphaltene solutions were obtained by dilution of the initial PPD and asphaltene solutions if needed and then by addition of the desired macrocrystalline wax content. A range of wax-only solutions were also prepared by dissolution of wax in deuterated toluene. All wax-containing systems were heated at 60 °C for 1 h and shaken thoroughly. Lastly, 3 g of each solution were introduced into a NMR tube. The solubility of asphaltenes at high concentration (2%) in the wax−asphaltene system was further confirmed with an optical microscope. Two independent parallel experiments were performed with NMR for each system in order to ensure reproducibility. The overall error was calculated from the difference in results obtained with the two parallel experiments and is displayed in the corresponding figures presented in this study.

3.3. Nuclear Magnetic Resonance: CPMG Analysis. NMR experiments were conducted on a low field (21 MHz) NMR spectrometer, which was supplied by Anvendt Teknologi AS, Norway. A CPMG sequence was used to acquire T_2 distributions.[31] In this study, two types of experiments were employed: dynamic experiments, involving a temperature decrease between the measurement points, and some static experiments at constant temperature, described in the Supporting Information.

For the dynamic experiments, the interecho spacing was selected for two regions: a first region with τ_1 of 200 μs and with 6000 echoes, focusing with higher detail on the more sensitive low T_2 area and a second region with τ_2 of 600 μs and with 2000 echoes. T_2 distributions were generated from the multiexponentially decaying curve, using the one-dimensional inverse Laplace transform.[32] They represented a qualitative form of system comparison through the use of 3D contour maps but also a quantitative measure by tracking the intensity of T_2 with temperature in selected regions. Several algorithms in Matlab 2021b were used to further process data and separate signal intensities in different T_2 areas.

In this study, ramping by a rate of 0.2 °C/min was conducted for the dynamic experiments to allow for the system to stabilize during the NMR scan. Stepwise scanning was used from 45 to 0 °C, leaving the system at constant temperature while the measurement at each temperature point was acquired. Selecting the number of scans was performed after some initial trials. A higher number of scans generates a higher amount of time needed for a measurement point at a temperature step and thus a lower number of steps in the temperature ramping. However, in order to have a more detailed temperature history, more temperature steps inside the same time interval are needed, so that the evolution of the system with temperature can be followed with higher resolution. Therefore, although a higher number of scans provide more accurate T_2 results due to the consolidation of the NMR signal, the history-dependent evolution of T_2 is less accurate. First, the number of scans was set at a conventional value of 16, which allowed 68 temperature steps in the 45−0 °C interval. Nevertheless, the number of scans was increased to 32 for experiments where the advantages generated by improvements to the noise reduction and resonance frequency were found to significantly overcome the drawbacks generated by reducing the resolution of the history-dependent scanning. Here, 42 measurement points were achieved in this case in order to ensure the same cooling rate as before. Data were later normalized for these systems to be able to compare the results.

The temperature inside the NMR was controlled with an air flow. First, the air was cooled below room temperature using a water bath with a 60:40 diethylene glycol/water mixture. Then, as it passed through the NMR, the air flow was heated using a high precision thermal controller supplied by Anvendt Teknologi AS. First, a calibration with hexadecane was performed to find the temperature correction needed to account for the inefficiency in thermal exchange between air and the sample in the NMR instrument. Hexadecane dissolved in deuterated toluene (5%) is liquid in the desired temperature range (45−0 °C) and shows a strong signal from the hydrogen atoms. The signal was first acquired dynamically with the desired thermal ramping (0.2 °C/min), and then, static experiments were performed at five constant temperatures inside this interval. As one can observe in Figure S2 in the Supporting Information, the thermal correction needed in our study is negligible, as the gap between the dynamic and the static calibrations is marginal. The dynamic calibration with hexadecane also allows one to correct for signal variation with temperature generated by the different repartitions of hydrogen atoms at different energy levels and quantified by the Boltzmann factor.[30] Thus, the net intensity of the wax signal at each temperature, W_T, is divided by the intensity of hexadecane signal at the corresponding temperature, H_T, and thus, normalized wax signals at each temperature, $W_{\mathrm{normal},T}$ is obtained (eq 2). Then, a set point, W_{sp}, is created by averaging the resulted values inside the expected WAT-45 °C interval, above the wax appearance temperature (eq 3). The apparent dissolved wax content at a defined temperature, $f_{\mathrm{liquid},T}$ is thus determined by dividing the normalized intensity of the wax at that temperature by the averaged set point (eq 4). The equivalent apparent solid wax content, $f_{\mathrm{solid},T}$ is obtained by deducting $f_{\mathrm{liquid},T}$ from 1 (eq 5).

$$W_{\mathrm{normal},T} = \frac{W_T}{H_T} \tag{2}$$

$$W_{sp} = \overline{W_{\mathrm{normal},T}}\ ,\ WAT \le T \le 45°\mathbf{C} \tag{3}$$

$$f_{\mathrm{liquid},T} = \frac{W_{\mathrm{normal},T}}{W_{\mathrm{sp}}} \tag{4}$$

$$f_{\mathrm{solid},T} = 1 - f_{\mathrm{liquid},T} \tag{5}$$

4. RESULTS AND DISCUSSION

This section focuses on selected wax, wax−asphaltene, and wax−PPD systems in deuterated toluene. The analysis of results for each type of system starts from the qualitative correlation of T_2 with the mobility of molecules, continues with wax precipitation evolution, and ends with a new approach to analyze the interactions between the wax crystals and the dissolved wax through the intensity of T_2 in the reduced mobility dissolved wax region. The impact of wax, asphaltene, and PPD concentration is investigated, using each type of analysis.

4.1. Effect of Wax Concentration on Interactions between Wax Crystals and Dissolved Wax. T_2 patterns of wax precipitation in a system comprising of 5% macrocrystalline wax in deuterated toluene are summarized in Figure 1. At high T_2 (10^{-1} to 10^{-0} s), one can notice a main peak corresponding to the wax dissolved in deuterated toluene.

https://doi.org/10.1021/acs.energyfuels.1c03613
Energy Fuels 2022, 36, 350−360

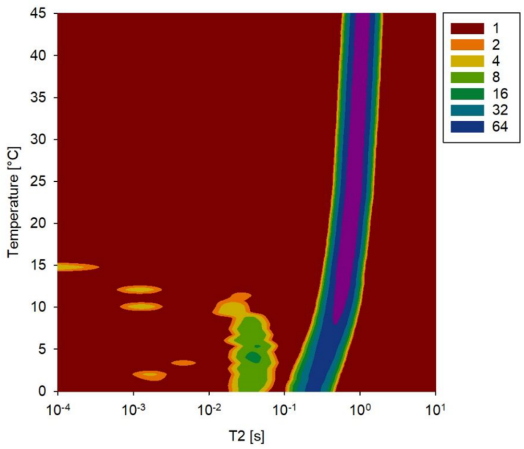

Figure 1. Evolution of T_2 (*x*-axis) and intensity of T_2 (scatter map) as a function of temperature for 5% wax in deuterated toluene, with no correction for the Boltzmann factor.

From 45 to 20 °C, this peak displays a linear increasing pattern in total intensity from 902 to 1002 a.u. This occurs due to the different repartition of hydrogen atoms at different energy levels generated along the temperature range.[30] The phenomenon is quantified by the Boltzmann factor, which generates linear increases in the intensity of the dissolved wax signal, before wax precipitation starts. Inside this same interval, one can also notice a linear decrease in the T_2 range, generated by an increase of viscosity and an associated reduction of the diffusion coefficient of wax molecules.

As the temperature is reduced further below the wax appearance temperature (≤20 °C), the peak has lower intensity and shifts more abruptly toward lower T_2 values. This is due to wax precipitation. At low T_2, a secondary peak is observed at temperatures below 10 °C. The T_2 of this peak (10^{-3} to 10^{-1} s) corresponds to a region between the liquid phase and phase change to a solid. This region was first qualitatively observed by Ruwoldt et al.,[19] but their method did not allow its quantification.

There are several hypotheses explaining this peak. The decrease in T_2 for a fraction of the dissolved wax molecules corresponds to a decrease in their molecular mobility. The most likely cause for this variation is the fact that molecular mobility decreases when spatial hindrances are imposed on dissolved wax molecules, trapped within the newly formed wax crystal network.[35] The NMR instrument tracks the hydrogen signal of the wax molecules. Thus, the intensity of the secondary peak is directly proportional to the amount of dissolved wax molecules with decreased mobility. The intensity of the peak allows one to quantitatively observe the effect of spatial hindrances imposed on dissolved wax molecules. Consequently, this reflects the amount of interactions between dissolved wax molecules and the wax crystal network. Therefore, the analysis of interactions between dissolved wax molecules and the wax crystal network can be performed qualitatively through the decrease in T_2 and quantitatively through an increase in intensity of the low T_2 region.

Lastly, the precipitated solid wax cannot be observed in the 3D contour map, as the NMR instrument does not record signals at T_2 values characteristic to solids, below 10^{-3}, when measured using a CPMG sequence.

Two more systems, 10% wax in deuterated toluene and 15% wax in deuterated toluene, are investigated with this method to analyze the effect of concentration on wax precipitation and interactions. The 3D contour maps obtained for these systems are presented in Figure S3 and S4 in the Supporting Information. The quality of the measurement is validated through the quasilinear intensification of the main peak with temperature observed above the wax appearance temperature; the intensity is confirmed to be 2.04−2.12 as high for 10% wax than for 5% wax and 3.08−3.20 times as high for 15% wax than for 5% wax. Moreover, similar patterns in the 3D contour maps are observed for the 10% and 15% systems, below the wax appearance temperature: a decrease in T_2 and intensity of T_2, along with the formation of a secondary peak corresponding to reduced mobility dissolved wax.

Wax precipitation curves are determined using eqs 2−5 (i.e., by integrating the signal of the dissolved wax in the main peak at $T_2 = 10^{-1}$ to 10^{0} s, without considering the intensity of the secondary peak). Figure 2 demonstrates a relationship between

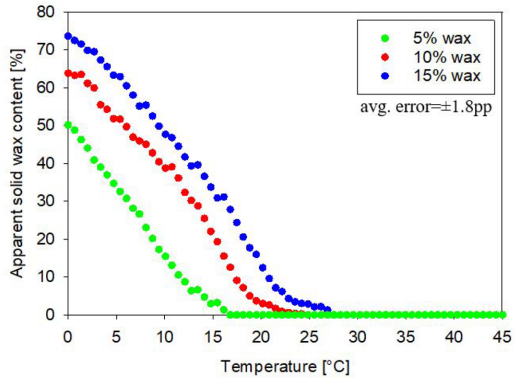

Figure 2. Apparent percentage of precipitated wax as a function of temperature for macrocrystalline wax systems.

the wax precipitation onset temperature and the concentration of wax in solution; the higher the wax concentration is, the higher the wax appearance temperature is. Thus, one can observe that there is a 4−6 °C delay between the points at which precipitation reaches the same level in the 5% wax system and the 10% wax system. A similar 4−6 °C delay is noticed between the corresponding points in the 10% wax system and 15% wax system. For example, the apparent wax solid content reaches 50% at approximately 0 °C for 5% wax, at approximately 5 °C for 10% wax, and at approximately 10 °C for 15% wax.

The novelty with this NMR method is a significant increase in resolution of the reduced mobility dissolved wax peak. This facilitates the analysis of the interactions in the wax crystal network. The approach in this study focuses on quantifying the total secondary peak intensity evolution, as illustrated in Figure 3. This value becomes a parameter which can be correlated to the total amount of dissolved wax molecules whose mobility is reduced by interactions with the new crystals; the more dissolved wax molecules become trapped within the wax crystal network, the stronger in intensity the low mobility dissolved

https://doi.org/10.1021/acs.energyfuels.1c03613
Energy Fuels 2022, 36, 350−360

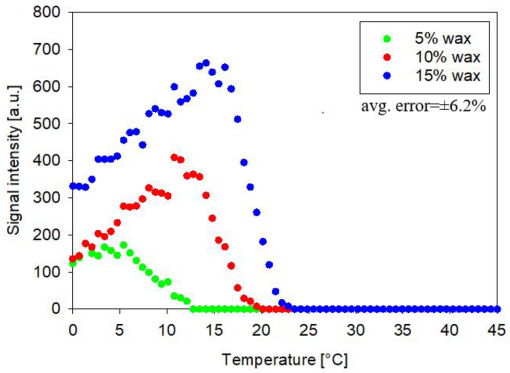

Figure 3. Evolution of total secondary peak intensity as a function of temperature for macrocrystalline wax systems.

wax region is. The secondary peak intensity has a quasisymmetric profile which shows maximums at 18, 12, and 5 °C for 15%, 10%, and 5% wax. More and more dissolved wax has reduced mobility as temperature decreases until the maximum secondary peak intensity is reached. After that point, the amount of reduced mobility dissolved wax molecules progressively decreases. There are two main factors contributing to the total secondary peak intensity. The first factor is the crystallization of dissolved wax molecules trapped in the wax crystal network, which generates further decreases in T_2, shifting their signals to values specific to the solid phase, below the measured range ($<10^{-3}$ s). The second factor is the rate at which molecules at high T_2 become trapped themselves in the wax crystal network to replace the low mobility molecules that are already crystallized. Until the maximum is reached, the rate at which molecules become trapped is higher than the rate of crystallization from the reduced mobility region. After the maximum is reached, the opposite happens. The reason is the fact that at the maximum, precipitation has already been going for a significant time, and the amount of dissolved wax molecules at high T_2 available to become trapped significantly decreases, as one can observe in the wax precipitation curve in Figure 2.

One can also notice a quasilinear trend between the temperature of the secondary peak maximum and the wax concentration. The average total intensity of the dissolved wax trapped in the wax crystal network above 0 °C also shows an increase with wax concentration (114.5, 229.2, and 426.5 a.u. for 5%, 10%, and 15%, respectively). The last two observations demonstrate that the higher the wax concentration in solution is, the more dissolved wax molecules become trapped in the newly formed wax crystal network, and the higher the temperature at which the maximum signal from these complexes occurs. Therefore, one can conclude that inside the analyzed concentration range, wax precipitation and the intensity of the corresponding reduction in mobility of dissolved wax follow a similar pattern, dependent on concentration.

4.2. Characterization of Wax−Asphaltene Interactions. *4.2.1. Behavior of Asphaltenes with Temperature.* The behavior of asphaltenes in the selected temperature range is investigated by using a model asphaltene−hexadecane system. The signal of asphaltenes alone is not enough for the NMR instrument to find the resonance frequency, and therefore, an inert hydrogenated solvent (hexadecane), which does not interact with asphaltenes and does not precipitate, has been added. The analysis of asphaltene behavior is essential to identify the differences between the asphaltene−hexadecane and asphaltene−wax systems presented in the next section. Subsequently, the role of asphaltenes in the observed wax crystals−dissolved wax interactions can be assessed.

Figure 4 emphasizes two reference systems, 5% hexadecane and 5% hexadecane with 1% asphaltenes, both in deuterated toluene. The results illustrate the high T_2, liquid hexadecane peak at $T_2 = 10^{-1}$ to 10^{0} s in both reference systems. However, when asphaltenes are added, an additional low T_2 peak can be observed close to the liquid−solid phase change region (10^{-3}

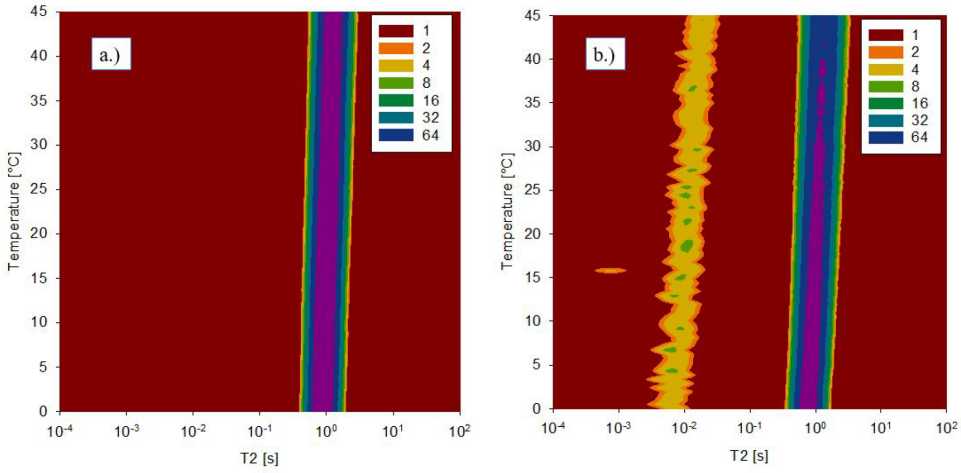

Figure 4. Evolution of T_2 (x-axis) and of intensity of T_2 (scatter map) with temperature for (a) 5% hexadecane in deuterated toluene and (b) 5% hexadecane, 1% asphaltene in deuterated toluene, with no correction for the Boltzmann factor.

https://doi.org/10.1021/acs.energyfuels.1c03613
Energy Fuels 2022, 36, 350−360

to 10^{-2} s). This most likely corresponds to asphaltene nanoaggregates in the system.

Asphaltenes are expected to coexist in the system both in dissolved monomer form at high T_2 (in the same region as hexadecane) and in nanoaggregate form at low T_2.[13] The influence of the asphaltenes on the main hexadecane peak was investigated to quantify the part of the peak that does not correspond to hexadecane. Example results at 45 °C show that the intensity of the main peak in the hexadecane system is 961 ± 1.2% a.u., while for the hexadecane/asphaltene system the corresponding intensity is 1019 ± 0.5% a.u. A first assumption would be that the difference of 58 a.u. (5.6%) between the averaged intensities corresponds to liquid asphaltene monomers having a similar T_2 as hexadecane. Over the entire temperature range, there is a 3.5%−7.2% increase in the average main peak intensity in the system with asphaltenes. However, the increase attributed to monomers is partially converging to the uncertainty in the intensity values, generated by noise in the NMR system. This varies in the 0.4%−5.7% interval over the temperature range. Therefore, the monomers will be considered negligible in this study, inside the NMR noise range. The exact quantification of monomers over the entire temperature range remains to be analyzed in the future with a higher precision method.

4.2.2. Effect of Asphaltene Concentration on Interactions between the Crystal Network and Dissolved Wax. To quantify the effect of asphaltene concentration on the dissolved molecules−wax crystals interactions, four systems with the same content of wax (5%) and varying contents of asphaltenes (0.5%, 0.75%, 1%, 2%) were selected. The 0.5% and 0.75% asphaltene systems were scanned using a double number of scans (NS = 32, instead of NS = 16) to overcome the NMR resonance frequency and noise limitations, triggered by low asphaltene concentration and consequently low asphaltene signal, as explained in Section 3.3. Therefore, the intensity values displayed for these systems in the Supporting Information in Figures S5 and S6 are normalized in Figure 7 from NS = 32 to NS = 16 to be able to perform a comparison with the other systems. The 3D contour map for the 2% asphaltene, 5% wax system is also presented in the Supporting Information in Figure S7.

Figure 5 presents the qualitative impact of the addition of 1% asphaltenes to the 5% wax system. When asphaltenes are added, one can observe the expected peak corresponding to wax dissolved in liquid at high T_2 values. At short T_2, above the wax appearance temperature, asphaltene nanoaggregates appear at $T_2 = 10^{-3}$ to 10^{-2} s. The T_2 range of this peak corresponds to the secondary peak observed in Figure 4, and the average intensity above 25 °C is comparable (50.7 a.u. for Figure 5; 47.2 a.u. for Figure 4), with an error inside the noise range of the NMR instrument (≤5%). Once wax precipitation starts, below the wax appearance temperature, the asphaltene nanoaggregate peak present in Figure 5 disappears (only some negligible traces are observed). A new secondary peak with significantly higher intensity is progressively generated at slightly higher T_2 (10^{-2} to 10^{-1} s) by the dissolved wax molecules whose mobility decrease due to interaction with the newly formed crystal network. This peak corresponds to the secondary peak observed in the wax-only system in Figure 1, being recorded in a similar T_2 range (10^{-2} to 10^{-1} s). However, it is generated at a higher temperature and has a higher intensity in the system with asphaltenes. The secondary peak evolution leads to some possible suggestions. The first is

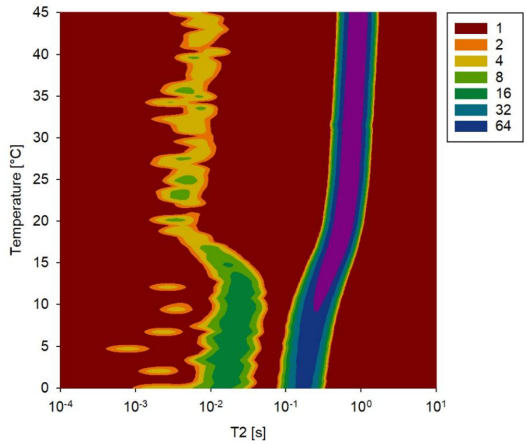

Figure 5. Evolution of T_2 (*x*-axis) and intensity of T_2 (scatter map) with temperature for 5% wax, 1% asphaltene in deuterated toluene − no correction for the Boltzmann factor

that more wax liquid molecules become trapped in the newly formed crystal network with 1% asphaltene than in the system presented in Figure 1 without 1% asphaltene. The second suggestion is that cocrystallization of wax and asphaltenes is the cause for stronger spatial hindrance and thus stronger interactions between the newly formed solid particles and dissolved wax. However, the cocrystallization hypothesis needs to be tested in the future using high resolution NMR for higher accuracy.

A possible physical explanation for the disappearance of the asphaltene nanoaggregate peak is a decrease of the asphaltene nanoaggregate size once wax starts precipitating that would generate an increase in the mobility of asphaltene molecules. This is, however, not likely. A more likely explanation is that cocrystallization of wax and asphaltene occurs, decreasing the T_2 of asphaltenes outside the measured range to solid-specific T_2. The potential cocrystallization behavior has been reported in several publications.[9,15,36] Another explanation for the disappearance of the peak might be the impossibility to separate the NMR signal of the peak corresponding to decreased mobility dissolved wax and of the nanoaggregate peak once wax starts precipitating. However, Figure 7 demonstrates that the increase in secondary peak intensity from above to below WAT for the 5% wax, 1% asphaltene system is higher than the intensity of the secondary peak of 5% wax system. Therefore, the impossibility to separate the peaks due to instrument limitations could only be partially associated with the secondary peak evolution.

Wax precipitation curves in Figure 6 display a significant increase in crystallization rate when 0.75%, 1%, or 2% asphaltenes are added. When the concentration of asphaltenes is 0.5%, one can notice an insignificant effect on wax precipitation. Slight inhibition tendencies below C.A.C. (critical asphaltene concentration) in the 0.05%−0.3% concentration range have also been confirmed in previous studies.[13] Thus, there is a change from little or no effect to wax precipitation promotion from 0.5% to 0.75% for the analyzed type of asphaltenes. Another observation is the shift in precipitation patterns between the four analyzed systems. Crystallization rates and onsets do not vary regularly in the

https://doi.org/10.1021/acs.energyfuels.1c03613
Energy Fuels 2022, 36, 350−360

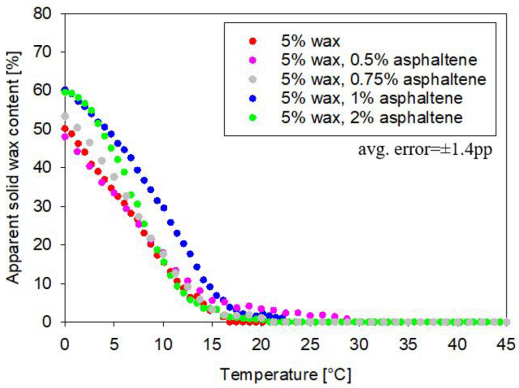

Figure 6. Apparent percentage of precipitated wax as a function of temperature for wax−asphaltene systems.

selected intervals. For example, although the system with 2% asphaltene reaches the highest crystallization rate, recorded in the 5−15 °C interval, its onset is way slower than for the 1% asphaltene system.

An important correction to consider is the part of the main peak at high T_2 caused by the presence of asphaltene monomers, as discussed in Section 4.2.1. If these monomers are deducted in eq 2 from the dissolved wax signal, the calculated solid wax content will increase from the value not accounting for asphaltene monomers, presented in Figure 6. By extrapolating from rough estimations presented in Section 4.2.1, one can expect an upward correction of 3.5%−7.2% for 1% asphaltene system. As a result, the addition of high concentration (≥0.75%) asphaltene most likely leads to crystallization rates, which are higher than the ones presented in Figure 6 by the corresponding correction percentages. However, these values need to be updated with a higher resolution NMR method for higher accuracy, as explained in Section 4.2.1.

Overall, the wax precipitation patterns presented in Figure 6 have links to developments in the literature, which track asphaltene behavior in relation to the critical asphaltene concentration (C.A.C.). This concentration corresponds to the value at which asphaltenes start forming nanoaggregates.[37,38] It is generally considered that above this value the nanoaggregate state of asphaltenes is dominant, whereas below this value, approximately all asphaltenes are in monomer state. Lei and coworkers showed in their study that monomer asphaltenes tend to inhibit wax precipitation just below the corresponding critical asphaltene concentration of 0.3%, while asphaltenes present in aggregate state above 0.3% generate an increase in wax precipitation rate as concentration increases.[14,37] This is in agreement with the results of our study and suggests that the corresponding critical asphaltene concentration for the analyzed kind of asphaltenes is close to the 0.5% concentration point.

A previous study by Kriz and Andersen[13] measured the WAT evolution in crude oil with asphaltene concentration by polarized light microscopy, one of the most accurate WAT identification methods. Their study indicates an irregular pattern for WAT with temperature and a very slow insignificant increase in WAT with asphaltene concentration at values above 0.2%. This is consistent with the results presented in Figure 6, which show very close wax crystallization onsets for the 0.5%−2% concentration range. The authors also illustrate that at high concentration there are two main opposing factors affecting wax precipitation. First, there is an influence of the presence of more asphaltene molecules acting as precipitation sites and thus enhancing the wax precipitation. Second, there are spatial hindrances imposed by the asphaltene particles, possibly larger in volume, on the wax molecules, leading to wax inhibition. However, the authors conclude that at high concentration the effect of concentration is prevailing, although high spatial interference is still present. Therefore, as the amount of aggregated asphaltenes present in the system increases for higher concentration, waxes tend to precipitate faster as a result of the dominant effect of the presence of more asphaltenes acting as precipitation sites. This trend can be observed in the wax precipitation patterns of our study, which show higher precipitation rates at higher concentration. However, the nonlinearity and the irregularities of the precipitation rate with concentration demonstrate that other factors affect this phenomenon too (i.e., nonlinear spatial hindrances, surface area of asphaltenes). As mentioned earlier, the literature also shows that the highest level of inhibition occurs in the monomer dominant region, around C.A.C. At that point, asphaltenes are less likely to act as wax precipitation sites, impose enough spatial hindrances, and are also sufficiently dispersed to affect waxes at molecular level.[9,13]

The hypotheses presented above are further emphasized by the analysis of interactions for wax−asphaltene systems through the total secondary peak intensity. The amount of wax is constant in the selected wax−asphaltene systems (5% wax), and therefore, by quantifying the secondary peak, one can observe the relative change in the amount of reduced mobility dissolved wax molecules when asphaltene concentration is modified. Figure 7 presents values normalized by the

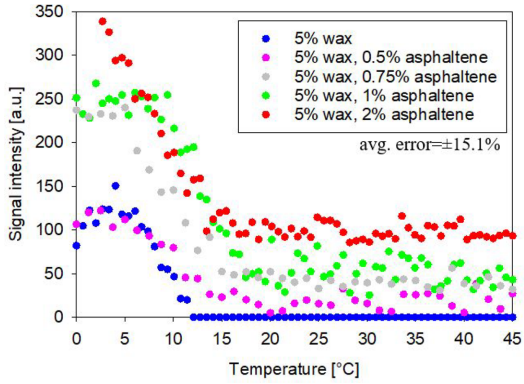

Figure 7. Evolution of total secondary peak intensity with temperature for wax−asphaltene systems, normalized to NS = 16.

number of scans to NS = 16 for the total secondary peak intensity. Above the wax appearance temperature, one can observe the intensity of the asphaltene nanoaggregate peak. The limitation of the NMR system is emphasized by the fact that the lower the concentration of asphaltenes is, the higher the noise in the asphaltene nanoaggregate peak is. However, average values in the 25−45 °C region confirm that for each increase of the asphaltene concentration the secondary peak

https://doi.org/10.1021/acs.energyfuels.1c03613
Energy Fuels 2022, 36, 350−360

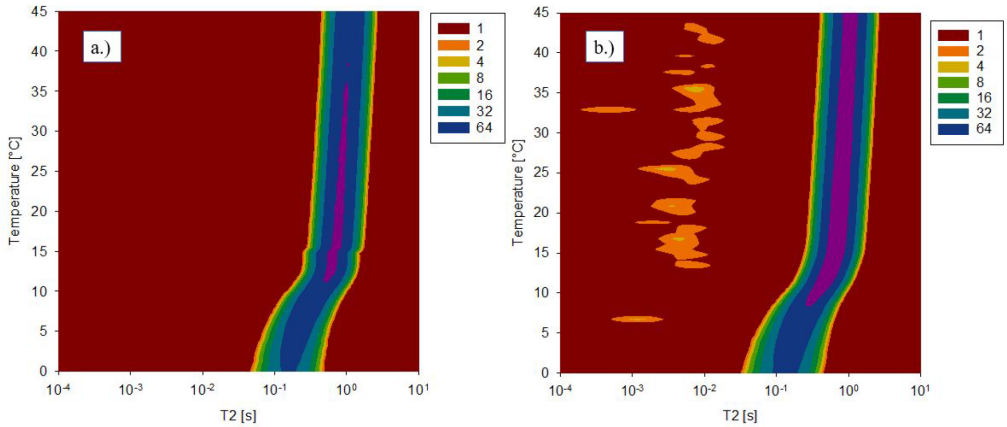

Figure 8. Evolution of T_2 (x-axis) and of intensity of T_2 (scatter map) with temperature for (a) 5% wax, 0.1% PPD in deuterated toluene and (b) 5% wax, 1% PPD in deuterated toluene, before correction for the Boltzmann factor.

intensity increases approximately linearly. This proves the reliability of the method and highlights once again that the secondary peak above WAT at very low T_2 corresponds to asphaltenes. Also, this shows that the percentage of the asphaltenes present in nanoaggregate form is constant above WAT in the analyzed concentration range. On the other hand, below WAT, one can notice an enhancement in the low mobility dissolved wax region for high asphaltene concentrations (0.75%, 1%, and 2%) than for the system without asphaltenes. This demonstrates that when asphaltene concentration is high enough, the signal from wax molecules trapped in the wax−asphaltene crystal network increases significantly with concentration. On the other hand, the system with 0.5% asphaltene shows an insignificant effect on the wax molecules trapped in the crystal network, which can be associated with the same insignificant impact observed in Figure 6 for the wax precipitation rate. This observation can be associated with the results obtained by Ruwoldt et al. with low asphaltene concentration (1000 ppm asphaltene), where a similar trend was noticed.[19]

The results show that a change in asphaltene behavior occurs inside the 0.5%−0.75% interval. One of the potential explanations is a transition in the aggregation state of asphaltenes.[14,39,40] Another explanation is that more, larger asphaltene particles, cocrystallized or "bound" to wax, may be generated at higher asphaltene concentrations, and therefore, they may cause stronger spatial hindrance, generating higher intensity in the corresponding relaxation time region. Consequently, more dissolved wax molecules display a decrease in mobility, as concentration increases. However, the nonlinearity of the pattern can most likely be attributed to the opposing effect of higher asphaltene concentration: higher precipitation rate as a result of more aggregate asphaltene molecules acting as precipitation sites for waxes.

Experiments for systems of 5% wax with and without 1% asphaltenes (Figures S8 and S9, Supporting Information) were carried out at constant temperature (5 and 10 °C) to investigate the evolution of the system over time and to track the intensity of the reduced mobility dissolved wax peak with higher resolution at selected temperatures. Results displayed stability with time and comparable conclusions with the dynamic systems.

Figures S10−S12 of the Supporting Information illustrate the degree of reproducibility of the method for the 5% wax, 1% asphaltene system.

4.3. Effect of PPD Addition on Wax Precipitation. Figure 8 qualitatively presents the effect of PPD addition on wax crystallization. A first observation is that the main peak at high T_2 now broadens more at low temperature than for wax−asphaltenes (Figure 5) or only wax (Figure 1), indicating that dissolved waxes in the main peak have a wider distribution of the mobility range when the PPD is added. Both dissolved wax and dissolved PPD molecules interacting with wax are expected to be present in the high T_2 peak. At low T_2, above the wax appearance temperature, a secondary peak is noticed in the high concentration PPD system (1%). Below the wax appearance temperature, there is no visible peak at short T_2 for both concentrations. The explanation is that a proportion of PPD molecules most likely modify dissolved wax behavior by liquid complex formation and fast cocrystallization, preventing dissolved wax molecules from being trapped in a higher viscosity crystal network, like in wax and wax−asphaltene systems. The secondary peak that we observe for the 1% system at temperatures higher than 15 °C can thus be associated with PPD macromolecules, displaying weak constant intensity in the 45−15 °C interval. However, below 15 °C, when wax precipitation is ongoing at a fast rate, this peak starts to disappear, most likely due to PPD crystallization with wax, which shifts the PPD signal outside the analyzed the T_2 range (in solid state). The presence of the secondary peak in the PPD−wax system is compared with the presence of a similar peak in a reference PPD−hexadecane system in the entire 45−0 °C range. The 3D contour map for this reference system is presented in the Supporting Information in Figure S13. Moreover, the effect of the PPD addition on the main hexadecane peak is insignificant, generating an increase within 5%, which is assumed to be either due to the noise of the NMR instrument or due to dissolved PPD molecules being involved in complex formation with dissolved waxes even above the wax appearance temperature. Therefore, the PPD influence on the main peak

https://doi.org/10.1021/acs.energyfuels.1c03613
Energy Fuels 2022, 36, 350−360

is considered marginal for the generation of the wax precipitation curve.

The secondary peak at high temperature is not observed in the system with 0.1% PPD in Figure 8a. The reason is the inability of the NMR instrument to detect very low signals, corresponding to 10 times less than at 1% PPD, which already has a very low PPD signal at low T_2.

This behavior is comparable to recent advances in PPD studies, which emphasize the cocrystallization of wax and PPD molecules.[7] Moreover, the literature reviews the active role of the incorporated PPD molecule on imposing steric hindrances to wax molecules that further precipitate on the crystal, a process which is achieved through polar moieties in the polymer molecules. This may explain the broadening in the mobility range of dissolved wax molecules at low temperature when more PPD is added. The wax−PPD complexes, however, unlike wax−wax and wax−asphaltene complexes, are more likely to be in high T_2 liquid form and then to directly crystallize. They do not seem to cause persistent significant reductions in dissolved wax mobility as a transition state toward the solid phase.

Additionally, by analyzing wax precipitation curves in Figure 9, one can notice a substantial decrease in wax precipitation

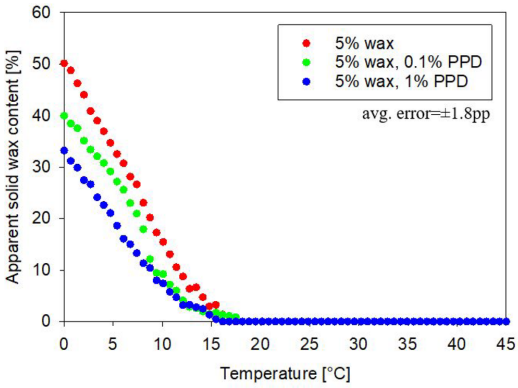

Figure 9. Apparent percentage of precipitated wax as a function of temperature for wax−PPD systems.

rates, which is stronger for higher concentrations. This demonstrates the wax inhibition effect of the PPD and emphasizes the fact that the broadening of T_2 and slight shift to lower T_2 in the main peak may also be attributed to more liquid complexes between the dissolved wax molecules and the inhibitor present at low temperatures than for the other analyzed systems. This consequently also links to developments in the literature which illustrate that PPD polymers increase the thermodynamic solubility of wax through the formation of liquid complexes.[41] Overall, the inhibitor behavior is comparable with other studies about PPD effects on wax precipitation.[42−45]

5. CONCLUSION

This study presents a new low field NMR approach for the analysis of paraffin wax precipitation patterns in model systems, along with the qualitative and quantitative characterizations of wax−wax, wax−asphaltenes, and wax−PPD interactions with temperature through the measurements of relaxation times and their intensities. This method represents an addition to the more established techniques (CPM, DSC) of characterizing wax precipitation patterns and allows a higher resolution NMR characterization of the effects of interactions which influence the wax precipitation mechanism in wax, wax−asphaltenes, and wax−PPD systems.

The main conclusions of this study are summarized below:

(a) In wax-only systems, the T_2 distributions indicate the formation of an intermediate low mobility liquid region, corresponding to dissolved wax molecules on which spatial hindrances are imposed by the newly formed wax crystals. Interactions between dissolved wax and the wax crystal network were previously indicated as a factor influencing wax crystallization. However, this method now allows one to quantify the amount of dissolved wax molecules with reduced mobility generated by trapping inside the wax crystal network as a result of spatial hindrance.

(b) In wax−asphaltene systems, asphaltene nanoaggregates were recorded at low relaxation times above the wax appearance temperature. As wax starts crystallizing, this peak disappears, and an area of reduced mobility dissolved wax is again developed. In this case, the intensity of the dissolved wax molecules with reduced mobility is significantly higher than for the wax-only systems with the same wax content, most likely due to higher spatial hindrances imposed by the larger wax−asphaltene cocrystals. The increase in nanoaggregate asphaltene molecules present at high concentration, acting as nucleation sites, promotes wax precipitation. However, there is no linear pattern, most likely due to the secondary, opposite effect of higher asphaltene concentration: higher spatial hindrances on the dissolved wax, which tend to inhibit crystal formation. Asphaltene nanoaggregate identification and relative quantification represent a novelty in LF-NMR oil research. Moreover, this method allows for the first time one to quantify the effect of asphaltene concentration on the mobility of dissolved wax molecules and on wax precipitation rate. The technique might thus be used in the future to the quantify asphaltene monomer/nanoaggregate ratio or even to approximate the range of critical asphaltene concentration by analyzing the effect of asphaltenes on the wax crystallization rate.

(c) In wax−PPD systems, the higher the PPD concentration is, the lower both wax precipitation rate and wax crystallization onset are, as expected. Liquid complexes between wax and PPD and consequent steric hindrances imposed by the incorporated PPD modify the wax crystallization behavior. PPD macromolecules are observed at low T_2 at high PPD concentration, above the wax appearance temperature, but the recorded peak disappears as wax starts precipitating. This qualitative form of validating wax−PPD interactions such as complex formation and cocrystallization represents a novelty in the LF-NMR oil research.

■ ASSOCIATED CONTENT

Supporting Information

The Supporting Information is available free of charge at https://pubs.acs.org/doi/10.1021/acs.energyfuels.1c03613.

https://doi.org/10.1021/acs.energyfuels.1c03613
Energy Fuels 2022, 36, 350−360

Figures presenting the NMR sequence profile; NMR calibration with hexadecane solution; and 3D contour maps for 10% wax, 15% wax, 5% wax with 0.5% asphaltene, 5% wax with 0.75% asphaltene, 5% wax with 2% asphaltene, and 5% hexadecane with 1% PPD (everything in deuterated toluene). Section detailing the work with static experiments for 5% wax, 1% asphaltene in deuterated toluene. (PDF)

AUTHOR INFORMATION

Corresponding Author

George Claudiu Savulescu − *Ugelstad Laboratory, Norwegian University of Science and Technology, 7491 Trondheim, Norway;* orcid.org/0000-0003-3278-0745; Email: george.c.savulescu@ntnu.no

Authors

Sébastien Simon − *Ugelstad Laboratory, Norwegian University of Science and Technology, 7491 Trondheim, Norway;* orcid.org/0000-0002-3101-4267

Geir Sørland − *Ugelstad Laboratory, Norwegian University of Science and Technology, 7491 Trondheim, Norway; Anvendt Teknologi AS, 7022 Trondheim, Norway*

Gisle Øye − *Ugelstad Laboratory, Norwegian University of Science and Technology, 7491 Trondheim, Norway*

Complete contact information is available at: https://pubs.acs.org/10.1021/acs.energyfuels.1c03613

Notes

The authors declare no competing financial interest.

ACKNOWLEDGMENTS

This work is part of SUBPRO SFI, a research-based center within subsea production and processing. The authors hereby acknowledge the financial support from SUBPRO, which is financed by the Research Council of Norway, major industry partners, and NTNU. Moreover, we hereby acknowledge Dr. Jost Ruwoldt for insightful conversations regarding sample preparation and method background.

REFERENCES

(1) Oliveira, L. M.S.L.; Nunes, R. C.P.; Melo, I. C.; Ribeiro, Y. L.L.; Reis, L. G.; Dias, J. C.M.; Guimaraes, R. C.L.; Lucas, E. F. Evaluation of the Correlation between Wax Type and Structure/Behavior of the Pour Point Depressant. *Fuel Process. Technol.* **2016**, *149*, 268−274.

(2) Kelland, M. *Production Chemicals for the Oil and Gas Industry*; CRC Press, 2009. DOI: 10.1201/9781420092974.

(3) Paso, K.; Senra, M.; Yi, Y.; Sastry, A. M.; Fogler, H. S. Paraffin Polydispersity Facilitates Mechanical Gelation. *Ind. Eng. Chem. Res.* **2005**, *44* (18), 7242−7254.

(4) Venkatesan, R.; Nagarajan, N.; Paso, K.; Yi, Y.-B.; Sastry, A.; Fogler, H. S. The Strength of Paraffin Gels Formed under Static and Flow Conditions. *Chem. Eng. Sci.* **2005**, *60*, 3587−3598.

(5) Yang, F.; Zhao, Y.; Sjöblom, J.; Li, C.; Paso, K. Polymeric Wax Inhibitors and Pour Point Depressants for Waxy Crude Oils: A Critical Review. *J. Dispersion Sci. Technol.* **2015**, *36*, 213−225.

(6) Al-Yaari, M. Paraffin Wax Deposition: Mitigation and Removal Techniques. In *SPE Saudi Arabia Section Young Professionals Technical Symposium*, Dhahran, Saudi Arabia, March 2011; SPE-155412-MS. DOI: 10.2118/155412-MS.

(7) Wei, B. Recent Advances on Mitigating Wax Problem Using Polymeric Wax Crystal Modifier. *J. Pet. Explor. Prod. Technol.* **2015**, *5* (4), 391−401.

(8) Bai, Y.; Bai, Q. Wax and Asphaltenes. In. *Subsea Engineering Handbook*, Second ed.; Bai, Y., Bai, Q., Eds.; Gulf Professional Publishing: Boston, **2019**; pp 435−453. .

(9) Venkatesan, R.; Östlund, J.-A.; Chawla, H.; Wattana, P.; Nydén, M.; Fogler, H. S. The Effect of Asphaltenes on the Gelation of Waxy Oils. *Energy Fuels* **2003**, *17* (6), 1630−1640.

(10) Oliveira, G. E.; Mansur, C. R. E.; Lucas, E. F.; González, G.; de Souza, W. F. The Effect of Asphaltenes, Naphthenic Acids, and Polymeric Inhibitors on the Pour Point of Paraffins Solutions. *J. Dispersion Sci. Technol.* **2007**, *28* (3), 349−356.

(11) García, M. del C. Crude Oil Wax Crystallization. The Effect of Heavy n-Paraffins and Flocculated Asphaltenes. *Energy Fuels* **2000**, *14* (5), 1043−1048.

(12) Molina, V. D.; Ariza León, E.; Chaves-Guerrero, A. Understanding the Effect of Chemical Structure of Asphaltenes on Wax Crystallization of Crude Oils from Colorado Oil Field. *Energy Fuels* **2017**, *31* (9), 8997−9005.

(13) Kriz, P.; Andersen, S. I. Effect of Asphaltenes on Crude Oil Wax Crystallization. *Energy Fuels* **2005**, *19* (3), 948−953.

(14) Lei, Y.; Han, S.; Zhang, J. Effect of the Dispersion Degree of Asphaltene on Wax Deposition in Crude Oil under Static Conditions. *Fuel Process. Technol.* **2016**, *146*, 20−28.

(15) Ariza Leon, E.; Molina Velasco, D. R.; Chavez Guerrero, A. Review of Studies on Asphaltene-Wax Interaction and the Effect Thereof on Crystallization. *Ciencia, Tecnología y Futuro* **2014**, *5*, 39−54.

(16) Kurniawan, M.; Subramanian, S.; Norrman, J.; Paso, K. Influence of Microcrystalline Wax on the Properties of Model Wax-Oil Gels. *Energy Fuels* **2018**, *32* (5), 5857−5867.

(17) Ruwoldt, J.; Kurniawan, M.; Oschmann, H.-J. Non-Linear Dependency of Wax Appearance Temperature on Cooling Rate. *J. Pet. Sci. Eng.* **2018**, *165*, 114−126.

(18) Ruwoldt, J.; Simon, S.; Norrman, J.; Oschmann, H.-J.; Sjöblom, J. Wax-Inhibitor Interactions Studied by Isothermal Titration Calorimetry and Effect of Wax Inhibitor on Wax Crystallization. *Energy Fuels* **2017**, *31* (7), 6838−6847.

(19) Ruwoldt, J.; Humborstad Sørland, G.; Simon, S.; Oschmann, H.-J.; Sjöblom, J. Inhibitor-Wax Interactions and PPD Effect on Wax Crystallization: New Approaches for GC/MS and NMR, and Comparison with DSC, CPM, and Rheometry. *J. Pet. Sci. Eng.* **2019**, *177*, 53−68.

(20) Ruwoldt, J.; Kurniawan, M.; Humborstad Sørland, G.; Simon, S.; Sjöblom, J. Influence of Wax Inhibitor Molecular Weight: Fractionation and Effect on Crystallization of Polydisperse Waxes. *J. Dispersion Sci. Technol.* **2020**, *41* (8), 1201−1216.

(21) Zhao, Y.; Paso, K.; Norrman, J.; Ali, H.; Sørland, G.; Sjöblom, J. Utilization of DSC, NIR, and NMR for Wax Appearance Temperature and Chemical Additive Performance Characterization. *J. Therm. Anal. Calorim.* **2015**, *120* (2), 1427−1433.

(22) Batsberg Pedersen, W.; Baltzer Hansen, A.; Larsen, E.; Nielsen, A. B.; Roenningsen, H. P. Wax Precipitation from North Sea Crude Oils. 2. Solid-Phase Content as Function of Temperature Determined by Pulsed NMR. *Energy Fuels* **1991**, *5* (6), 908−913.

(23) Ruffier-Meray, V.; Roussel, J.; Defontaines, A. Use of Pulsed Nmr Spectroscopy to Measure the Amount of Solid Deposits As a Function of Temperature in Waxy Crudes. *Rev. Inst. Fr. Pet.* **1998**, *53*, 531−535.

(24) Kané, M.; Djabourov, M.; Volle, J.-L.; Rutledge, D. N. Correction of Biased Time Domain NMR Estimates of the Solid Content of Partially Crystallized Systems. *Appl. Magn. Reson.* **2002**, *22* (3), 335.

(25) Yalaoui, I.; Chevalier, T.; Levitz, P.; Darbouret, M.; Palermo, T.; Vinay, G.; Barré, L. Probing Multiscale Structure and Dynamics of Waxy Crude Oil by Low-Field NMR, X-Ray Scattering, and Optical Microscopy. *Energy Fuels* **2020**, *34* (10), 12429−12439.

(26) Pradhan, S.; Rajamani, S.; Agrawal, G.; Dash, M.; Samal, S. K. NMR, FT-IR and Raman Characterization of Biomaterials. In *Characterization of Polymeric Biomaterials*; Tanzi, M. C., Farè, S.,

Eds.; Woodhead Publishing, 2017; pp 147−173. DOI: 10.1016/B978-0-08-100737-2.00007-8.
(27) Hornak, J. P.; *Basics of NMR*; Rochester Institute of Technology, Center for Imaging Science, 1996.
(28) Duus, J. Roger S. Macomber. A Complete Introduction to Modern NMR Spectroscopy. Wiley, Chichester, 1998, Xvii+ 383 Pp. Price £45. ISBN 0 471 15736 8. *Magn. Reson. Chem.* **2002**, *40* (6), 430.
(29) Sørland, G. H. *Dynamic Pulsed-Field-Gradient NMR*; Springer Series in Chemical Physics; Springer, 2014.
(30) Slichter, C. P. *Principles of Magnetic Resonance*; Springer Science & Business Media, 2013.
(31) Meiboom, S.; Gill, D. Modified Spin-Echo Method for Measuring Nuclear Relaxation Times. *Rev. Sci. Instrum.* **1958**, *29* (8), 688−691.
(32) Provencher, S. W. A Constrained Regularization Method for Inverting Data Represented by Linear Algebraic or Integral Equations. *Comput. Phys. Commun.* **1982**, *27* (3), 213−227.
(33) Subramanian, S.; Sørland, G. H.; Simon, S.; Xu, Z.; Sjöblom, J. Asphaltene Fractionation Based on Adsorption onto Calcium Carbonate: Part 2. Self-Association and Aggregation Properties. *Colloids Surf., A* **2017**, *514*, 79−90.
(34) Pinto, F. E.; Barros, E. V.; Tose, L. V.; Souza, L. M.; Terra, L. A.; Poppi, R. J.; Vaz, B. G.; Vasconcelos, G.; Subramanian, S.; Simon, W.; et al. Fractionation of Asphaltenes in N-Hexane and on Adsorption onto CaCO3 and Characterization by ESI(+)FT-ICR MS: Part I. *Fuel* **2017**, *210*, 790−802.
(35) Jestin, J.; Barré, L. Application of NMR Solvent Relaxation and SAXS to Asphaltenes Solutions Characterization. *J. Dispersion Sci. Technol.* **2004**, *25*, 341−347.
(36) Alcazar-Vara, L. A.; Garcia-Martinez, J. A.; Buenrostro-Gonzalez, E. Effect of Asphaltenes on Equilibrium and Rheological Properties of Waxy Model Systems. *Fuel* **2012**, *93*, 200.
(37) Lei, Y.; Han, S.; Zhang, J.; Bao, Y.; Yao, Z.; Xu, Y. Study on the Effect of Dispersed and Aggregated Asphaltene on Wax Crystallization, Gelation, and Flow Behavior of Crude Oil. *Energy Fuels* **2014**, *28* (4), 2314−2321.
(38) Mullins, O. C. The Modified Yen Model. *Energy Fuels* **2010**, *24* (4), 2179−2207.
(39) Mullins, O. C.; Sabbah, H.; Eyssautier, J.; Pomerantz, A. E.; Barré, L.; Andrews, A. B.; Ruiz-Morales, Y.; Mostowfi, F.; McFarlane, R.; Goual, L. R. N.; et al. Advances in Asphaltene Science and the Yen−Mullins Model. *Energy Fuels* **2012**, *26* (7), 3986−4003.
(40) Eyssautier, J.; Levitz, P.; Espinat, D.; Jestin, J.; Gummel, J.; Grillo, I.; Barré, L. Insight into Asphaltene Nanoaggregate Structure Inferred by Small Angle Neutron and X-Ray Scattering. *J. Phys. Chem. B* **2011**, *115* (21), 6827−6837.
(41) Claudy, P.; Létoffé, J.-M.; Bonardi, B.; Vassilakis, D.; Damin, B. Interactions between N-Alkanes and Cloud Point-Cold Filter Plugging Point Depressants in a Diesel Fuel. A Thermodynamic Study. *Fuel* **1993**, *72* (6), 821−827.
(42) Wu, Y.; Ni, G.; Yang, F.; Li, C.; Dong, G. Modified Maleic Anhydride Co-Polymers as Pour-Point Depressants and Their Effects on Waxy Crude Oil Rheology. *Energy Fuels* **2012**, *26* (2), 995−1001.
(43) Paso, K. G.; Krückert, K. K.; Oschmann, H.-J.; Ali, H.; Sjöblom, J. PPD Architecture Development via Polymer−Crystal Interaction Assessment. *J. Pet. Sci. Eng.* **2014**, *115*, 38−49.
(44) Jung, T.; Kim, J.-N.; Kang, S.-P. Influence of Polymeric Additives on Paraffin Wax Crystallization in Model Oils. *Korean J. Chem. Eng.* **2016**, *33* (6), 1813−1822.
(45) Pedersen, K. S.; Rønningsen, H. P. Influence of Wax Inhibitors on Wax Appearance Temperature, Pour Point, and Viscosity of Waxy Crude Oils. *Energy Fuels* **2003**, *17* (2), 321−328.

https://doi.org/10.1021/acs.energyfuels.1c03613
Energy Fuels 2022, 36, 350−360

SUPPLEMENTARY MATERIAL

New NMR approaches on the evolution of wax mobility during wax crystallization

George Claudiu Savulescu[1] (george.c.savulescu@ntnu.no*) Sébastien Simon[1], Geir Sørland[1,2], Gisle Øye[1]

[1]: *Ugelstad Laboratory, Norwegian University of Science and Technology, 7491 Trondheim, Norway*

[2]: *Anvendt Teknologi AS, Munkvollvegen 56, 7022 Trondheim, Norway*

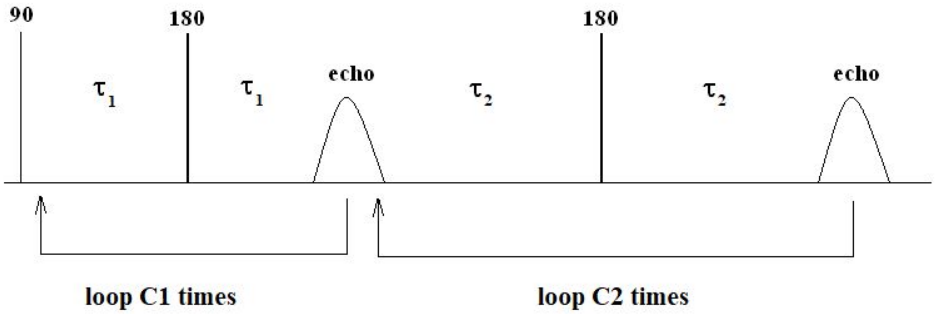

Figure S1: CPMG profile sequence used for the NMR procedure

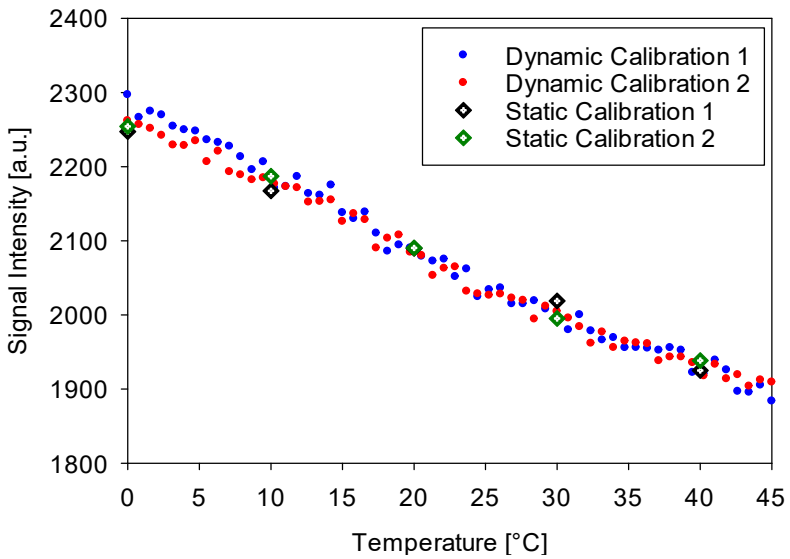

Figure S2: Dynamic and static calibrations for the NMR instrument, using 5 wt% hexadecane in deuterated toluene

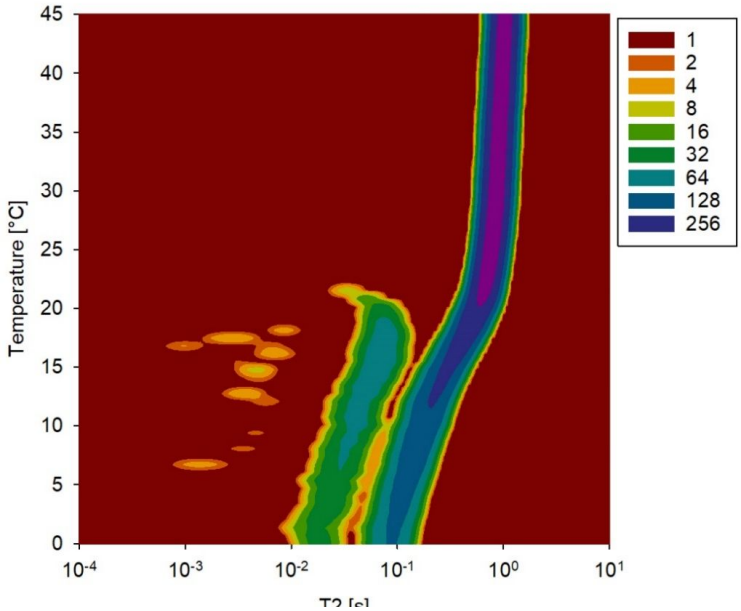

Figure S3: Evolution of T_2 (x-axis) and intensity of T_2 (scatter map) with temperature for 10% wax in deuterated toluene – no correction for Boltzmann factor

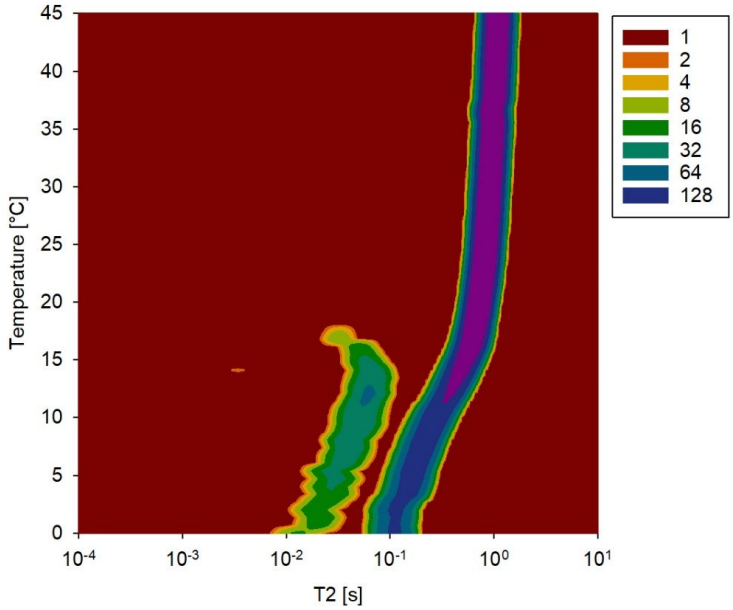

Figure S4: Evolution of T_2 (x-axis) and intensity of T_2 (scatter map) with temperature for 15% wax in deuterated toluene – no correction for Boltzmann factor

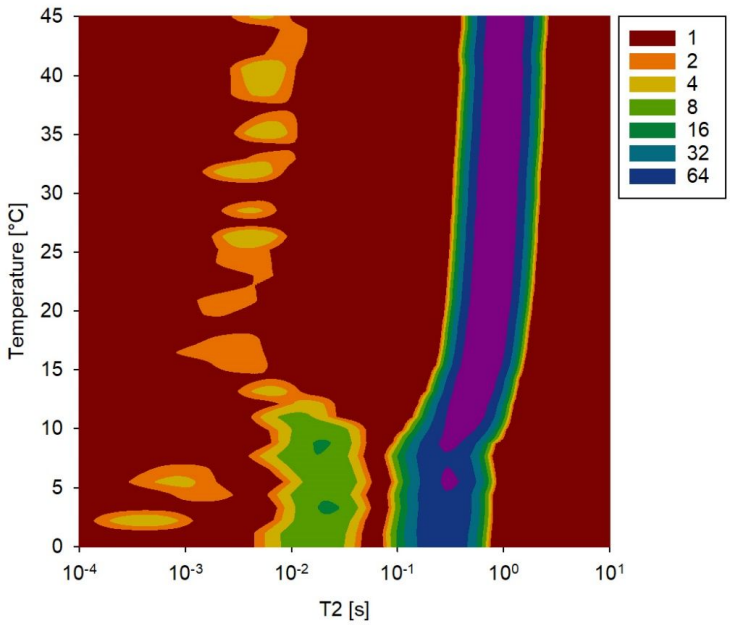

Figure S5: Evolution of T_2 (x-axis) and intensity of T_2 (scatter map) with temperature for 5% wax, 0.5% asphaltene in deuterated toluene (NS=32-double number of scans than standard) – no correction for Boltzmann factor

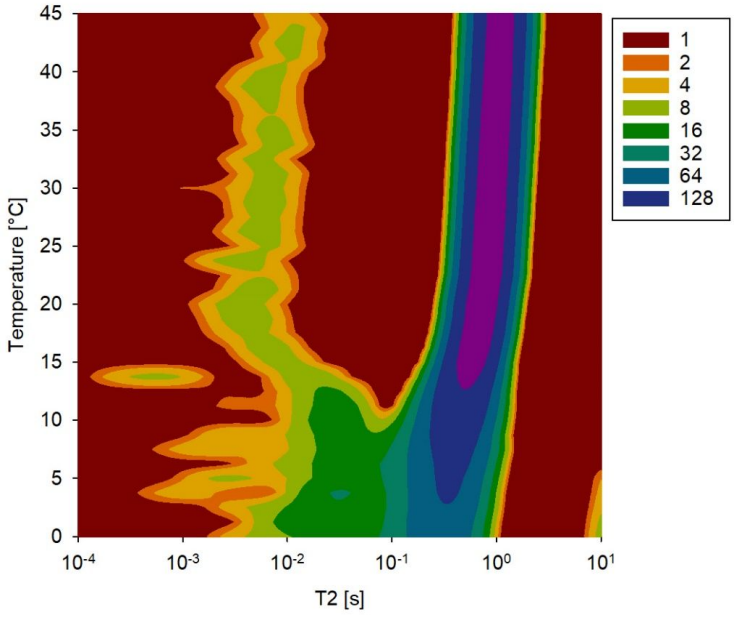

Figure S6: Evolution of T_2 (x-axis) and intensity of T_2 (scatter map) with temperature for 5% wax, 0.75% asphaltene in deuterated toluene (NS=32 – double number of scans than standard) – no correction for Boltzmann factor

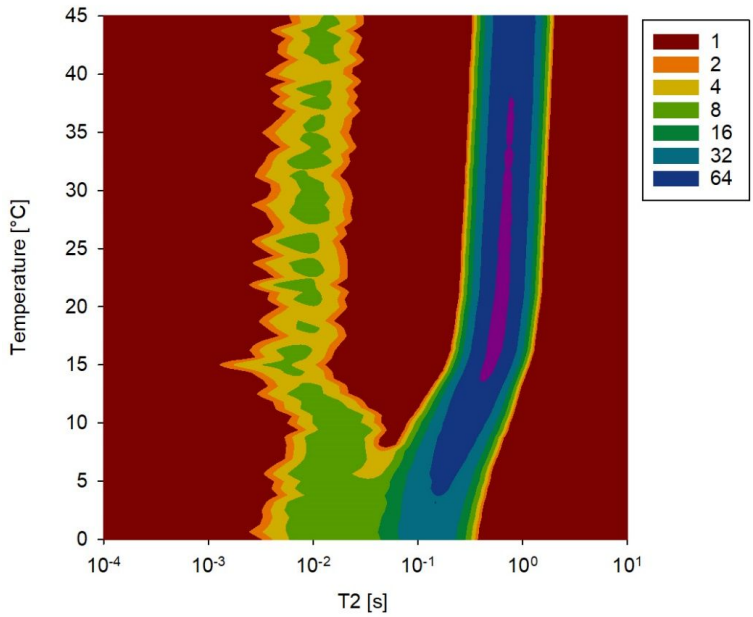

Figure S7: Evolution of T_2 (x-axis) and intensity of T_2 (scatter map) with temperature for 5% wax, 2% asphaltene in deuterated toluene – no correction for Boltzmann factor

Effect of asphaltene addition on interactions between the crystal network and dissolved wax in isothermal, static conditions

Experimental procedure

For the static experiments, the inter echo spacing was again selected for two regions: a first region with τ_1 of 150 μs and with 6000 echoes, focusing with higher detail on the more sensitive low T_2 area and a second region with τ_2 of 1000 μs and with 2000 echoes. The number of scans was fixed at 32. These settings allowed for higher resolution scans. However, they could not be used in the dynamic experiment, due to frequent failures in finding resolution frequency, as changes in the system occurred during temperature ramping. In the static experiments, this issue did not represent such an important drawback, as the same experiment was repeated for 20 times in stable conditions. Thus, twenty 12-minutes measurements were performed at 10°C and 5°C, after the system was left 30 minutes to stabilize, using the same type of cooling and heating employed for the dynamic experiments. However, at 5°C, due to unstable signal, only 15 scans were recorded. Data was further processed with the same method as for the dynamic experiments.

Results and discussion

Experiments for systems of 5% wax with and without 1% asphaltenes were carried out at constant temperature to investigate the evolution of the system over time and to track the intensity of the reduced mobility dissolved wax peak with higher resolution at selected temperatures. Figures S8 and S9 illustrate that at both temperatures, the systems display rigid stability, with acceptable levels of noise, throughout the repeated experiments. At 10°C, the 5% wax, 1% asphaltene system (Figure S9, left) again shows a high intensity main peak at high T_2, corresponding to dissolved wax and a secondary peak at lower T_2, corresponding to dissolved wax with reduced mobility. This peak displays an irregular distribution in the 10^{-3}-10^{-1} s range, with overall almost constant intensities. However, the intensity of the peak is higher than for the 5% wax system at the same temperature (Figure S8, left) and is distributed on a broader T_2 range. At 5°C however, for the system with asphaltenes (Figure S9, right), the T_2 ranges of the two peaks decrease, with a more defined low mobility dissolved wax region, fully separated from the main peak. This observation is consistent with Figures 6, 7 and 8, which show that at 10°C, the precipitation rate and interaction evolution rate are higher than at 5°C, when the mobility and the amount of dissolved wax molecules interacting with the solids start to settle. On the other hand, the 5% wax system without asphaltenes displays a weaker secondary peak at 5°C, with a higher T_2 range (10^{-2}-10^{-1} s, rather than 10^{-3}-10^{-2} for the system with asphaltenes). This indicates that less wax molecules have reduced mobility and the decrease in mobility is weaker when asphaltenes are not in the system. Thus, one can conclude again that the particles formed in the wax-asphaltene crystal network not only reduce the mobility of more dissolved wax molecules, but also generate stronger spatial hindrances. Co-crystals and wax attached to asphaltenes acting as nucleation sites are most likely generating this phenomenon.

The main peak in the wax-asphaltene system at the lower temperature is split in 2 when 32 scans are used, as a result of either asphaltene monomers, higher mobility dissolved wax molecules or residual hydrogenated toluene, from the deuterated toluene solvent, which drags a part of the main peak corresponding to dissolved wax to higher T_2. The effect of this residual hydrogenated toluene in the solvent has been investigated by low field NMR in a separate

experiment and was proven to represent less than 1% of the main peak, generating a negligible degree of error. Constant temperature experiments also confirm the high thermal efficiency of the NMR system with no temperature delay. Intensity values in the static experiments are approximately identical to the ones acquired in the history-dependent dynamic experiment at the corresponding points, demonstrating the absence of a significant time gap in the history-dependent measurements. The main advantage of the static method remains, however, the higher resolution in tracking the evolution of the secondary peak.

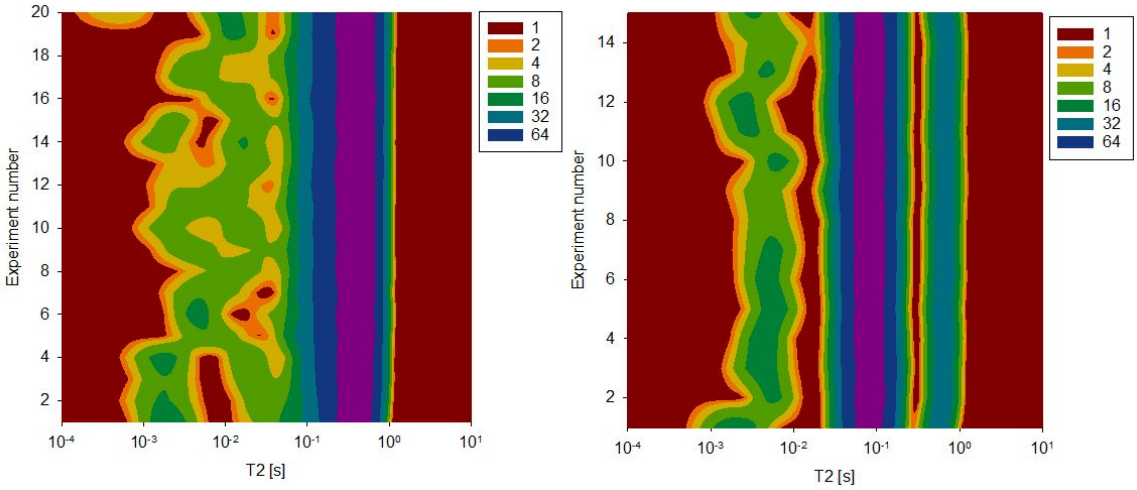

Figure S8: Evolution of T_2 (x-axis) and intensity of T_2 (scatter map) for 5% wax in deuterated toluene at 10°C (left side) and 5°C (right side)

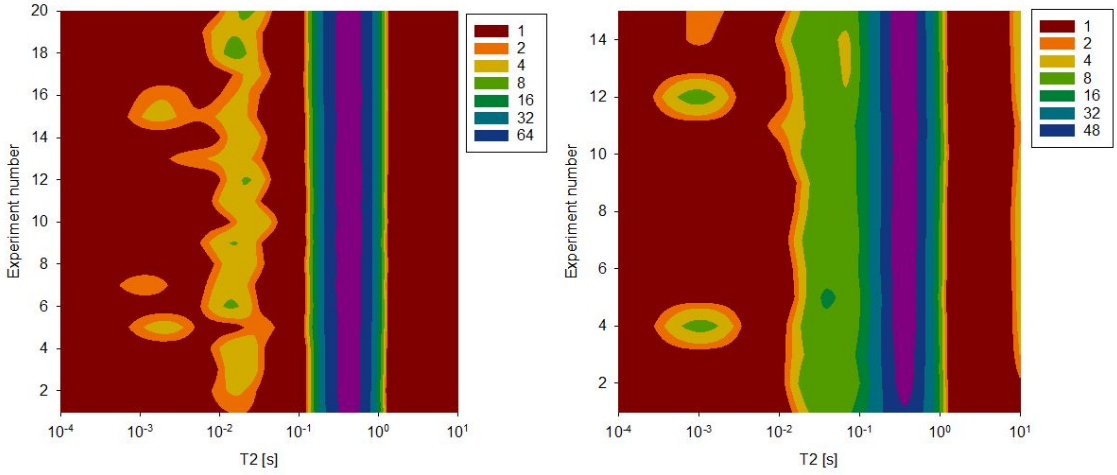

Figure S9: Evolution of T_2 (x-axis) and intensity of T_2 (scatter map) for 5% wax, 1% asphaltene in deuterated toluene at 10°C (left side) and 5°C (right side)

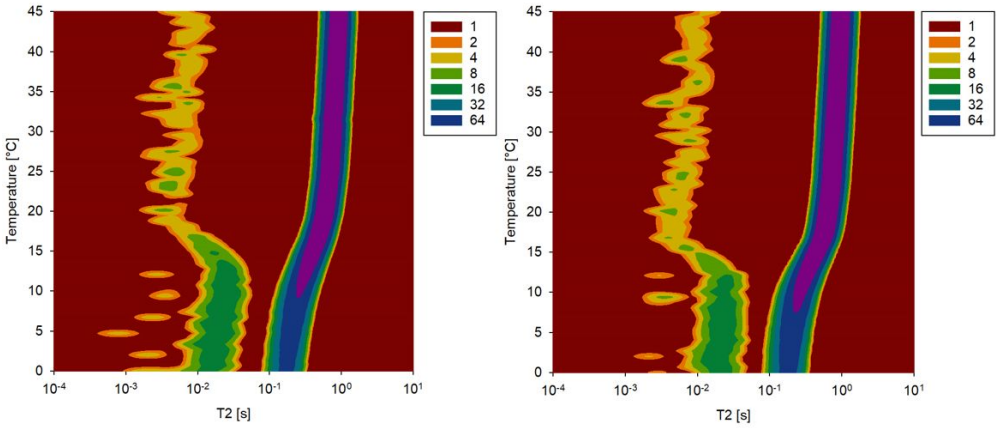

Figure S10: 3D contour maps illustrating reproducibility of the dynamic scan for 5% wax, 1% asphaltene: first experiment with a first sample on the left side, second experiment with a second sample on the right side

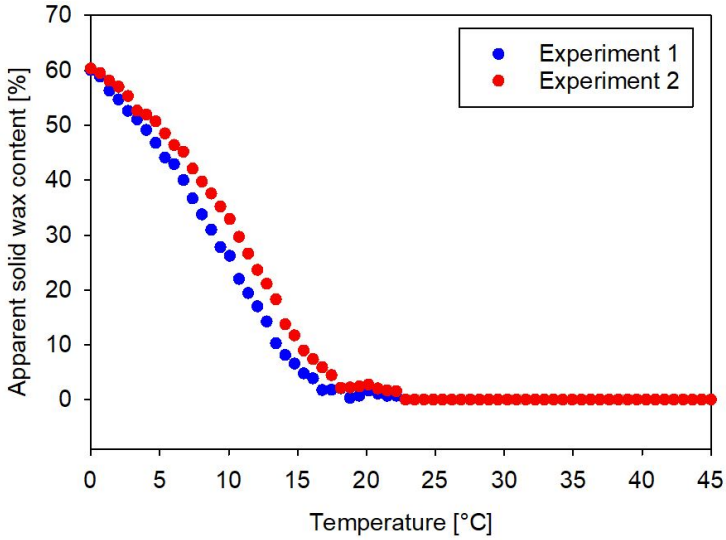

Figure S11: Figure illustrating reproducibility for the wax precipitation curve for 5% wax, 1% asphaltene system

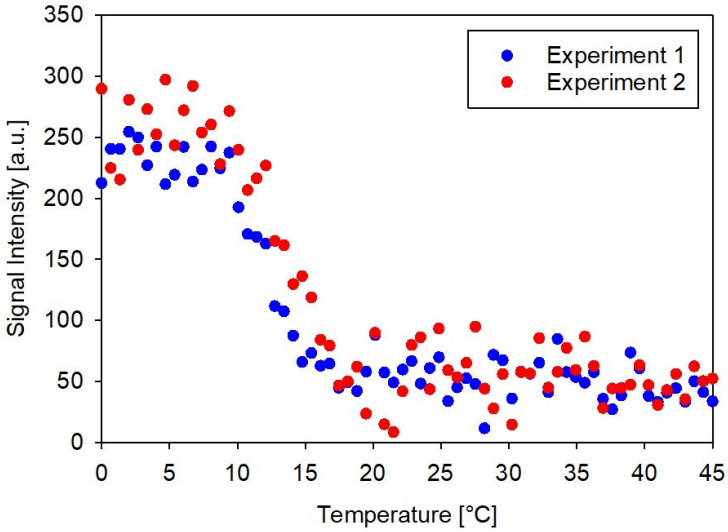

Figure S12: Figure illustrating reproducibility of the secondary peak quantification for 5% wax, 1% asphaltene in deuterated toluene

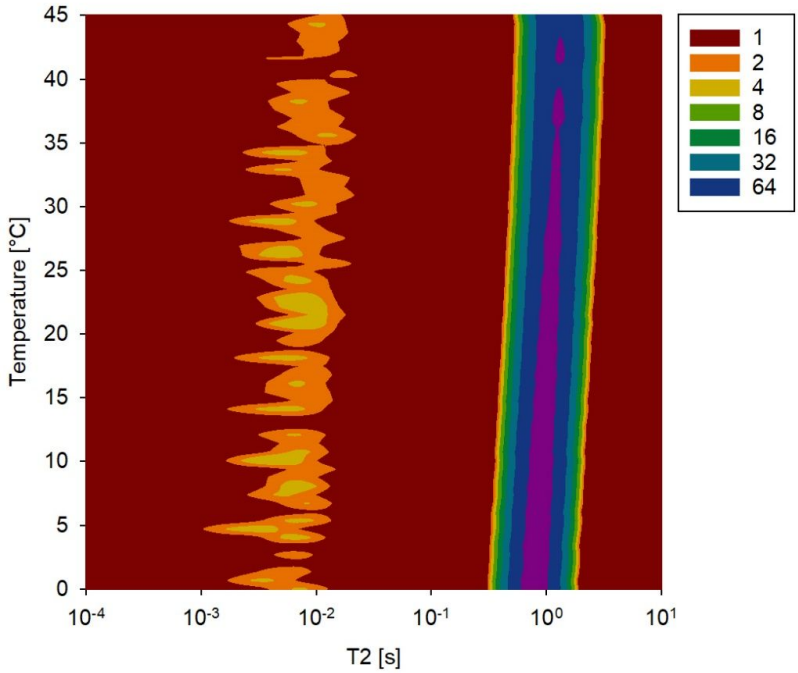

Figure S13: Evolution of T_2 (x-axis) and intensity of T_2 (scatter map) with temperature for 5% hexadecane, 1% PPD in deuterated toluene

Paper II

Understanding the effect of asphaltenes and wax inhibitors on wax crystallization by improved NMR techniques

I&EC research
Industrial & Engineering Chemistry Research
pubs.acs.org/IECR

Article

Understanding the Effect of Asphaltenes and Wax Inhibitors on Wax Crystallization by Improved NMR Techniques

George Claudiu Savulescu,* Sébastien Simon, Geir Sørland, and Gisle Øye

Cite This: *Ind. Eng. Chem. Res.* 2023, 62, 18251−18262

Read Online

ACCESS | Metrics & More | Article Recommendations | Supporting Information

ABSTRACT: Wax crystallization represents one of the main factors impacting flow assurance during oil production. Pour point depressants (PPDs) and asphaltenes present in crude oil have been linked to modifications in wax crystallization behavior by cocrystallization and formation of complexes with wax. Wax precipitation has recently been assessed by low-field nuclear magnetic resonance (NMR) techniques. However, improvements remain to be made regarding the mechanism of the interactions between wax and the components that can alter the precipitated crystal network. In this article, wax−asphaltene and wax−PPD interactions were quantified by combining, for the first time, different low- and high-field NMR methods. First, the variation in the concentration of asphaltenes and PPD in solution with temperature was determined by a high-field NMR approach in model systems in the presence and in the absence of wax. Cocrystallization was demonstrated by observing a reduced content of asphaltenes and PPDs when wax was present. Second, the ratio between asphaltene monomers and nanoaggregates was quantified by low-field NMR relaxation time methods. Above a threshold asphaltene concentration, all asphaltenes were present as nanoaggregates. The same threshold concentration was associated with faster wax crystallization and an increase in the number of low-mobility dissolved wax molecules, interacting with the wax crystal network. Last, the impact of wax−PPD and wax−asphaltene crystallization patterns on the diffusion of the solvent through the wax network was quantified by using low-field NMR diffusion methods, followed by tortuosity calculations. Diffusion of solvent through the crystal network increased at higher asphaltene concentration and increased even further in the presence of PPD, indicating that these components lead to more open network structures. These new methods and breakthroughs about the wax precipitation mechanism may be extended to future studies of real crude oil systems.

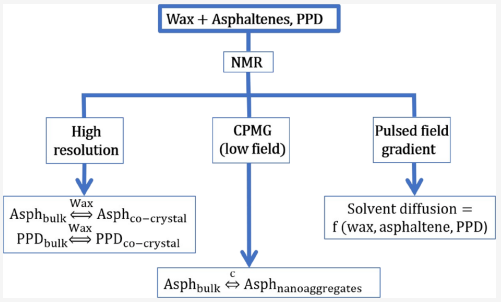

1. INTRODUCTION

Paraffin waxes are *n*-, iso-, or cycloalkanes with carbon chains between C_{18} and C_{100} or sometimes higher.[1] They are present in crude oils in varying concentrations, usually dependent on the oil field. There are 2 main types of waxes: macrocrystalline and microcrystalline. Macrocrystalline waxes have more linear structures and usually between 18 and 40 carbon atoms.[2] On the other hand, microcrystalline waxes contain iso-alkanes and cycloalkanes and usually have more than 40 carbon atoms.[2] Each waxy crude oil has a wax appearance temperature (WAT), at which wax starts to precipitate upon cooling. Subsequent gelation and deposition have a negative impact on flow assurance during crude oil production and transport. Several known effects are reduction of the crude oil flow in the pipeline, pressure abnormalities, pipeline restart issues, increased fluid viscosity, changes in the composition of the reservoir fluid, and in the worst case, a complete blockage of the flow.[3]

A conventional method to delay wax crystallization and to decrease the pour point below the industrial operating temperatures is the use of wax inhibitors, such as pour point depressants (PPDs).[4] PPDs are designed to show high affinity for the nonpolar moieties of wax, which often leads to cocrystallization or formation of complexes. These complexes undergo a crystallization mechanism different from that of pure wax crystals. The consequences are often higher solubility and altered crystal properties, such as lower aspect ratio and surface area.[5,6]

The presence of asphaltenes, polar components of crude oil, has also been demonstrated to affect wax precipitation. Asphaltenes are high molecular compounds in crude oil, insoluble in low molecular weight *n*-alkanes, such as hexane, but soluble in aromatic solvents, such as toluene.[7] At low concentrations, asphaltenes dissolve as monomers in toluene

Received: July 13, 2023
Revised: October 4, 2023
Accepted: October 6, 2023
Published: October 24, 2023

https://doi.org/10.1021/acs.iecr.3c02218
Ind. Eng. Chem. Res. 2023, 62, 18251−18262

or other aromatic solvents. However, as the concentration increases, asphaltenes start forming nanoaggregates (2−5 nm) at a concentration point often referred to as critical asphaltene concentration in the wax network (C.A.C.) or critical nanoaggregate concentration (C.N.A.C.).[8,9] As concentration increases further, the amount of asphaltene nanoaggregates will grow and secondary aggregation will begin through the formation of nanoclusters (>5 nm). These nanoaggregates and nanoclusters have often been referred to as nucleation sites for wax, generating more finely dispersed, smaller wax crystals inside the wax−asphaltene crystal network. While aggregated asphaltenes act as nucleation sites, the nonpolar groups of monomer asphaltenes are expected to act as connectors between the wax crystals, speeding the gelation process and increasing the gel strain but weakening the wax crystal network.[10−12] Although the modified crystals allow for better crude oil flow, they might increase WAT and the wax precipitation rate.[13−16,10,17] As expected from the opposing effects of asphaltenes, results of multiple studies generate contradicting conclusions about the role of asphaltenes during wax precipitation.[11] Some articles showed that asphaltenes inhibit wax precipitation in certain concentration regions but promote wax precipitation in other concentration regions, specific to each type of crude oil or wax−asphaltene model system.[9,18] The pattern of the concentration ranges for crystallization inhibition or promotion is in most cases irregular, probably because of the polydisperse character of asphaltenes and variable chemical composition of asphaltenes in each individual crude oil.[11,19] The exact mechanism behind the impact of asphaltenes on wax precipitation is not clear. That is the reason why this study aims to cover gaps in the literature by introducing a direct method to demonstrate cocrystallization of wax and asphaltenes. A second scope is to quantitatively investigate the effect of asphaltene nanoaggregation on wax precipitation.

Wax nucleation is affected not only by asphaltenes and PPDs but also by the addition of wax with different chemical compositions. Microcrystalline waxes are known to form gels with lower yield strength that precipitate at a lower rate than macrocrystalline wax.[2,20] Therefore, crystallization of macrocrystalline wax (linear alkane structure) has been investigated with and without the presence of microcrystalline wax (branched alkane structure).[21] When present, the microcrystalline waxes weakened the macrocrystalline wax crystal networks through spatial hindrances that prevent interlocking. This phenomenon leads to the formation of smaller and more finely dispersed macrocrystalline wax crystals, which make the system behave like a microcrystalline gel, despite the dominant macrocrystalline wax composition.[21]

The effect of wax inhibitors on wax crystallization was initially researched using multiple analytical methods such as differential scanning calorimetry (DSC), cross-polarized microscopy (CPM), and isothermal titration calorimetry (ITC). The analysis of wax precipitation by low-field NMR was introduced by Pedersen et al., who calculated wax content in crude oil, from relaxation time data.[22] In recent years, wax crystallization has been characterized by an adapted Carr−Purcell−Meiboom−Gill (CPMG) sequence,[23,24] which focuses on the effect of asphaltene and PPD in model wax-based systems. The temperature dependence of the percentage of solid in model wax and wax−PPD systems was assessed by Zhao et al. with NMR CPMG.[25] Ruwoldt et al. extended the range of PPDs used in the wax-based systems and considered the influence of asphaltenes for the first time.[26] An advantage of NMR compared to DSC was the use of fewer thermodynamic assumptions to determine the wax content. In this study, the authors identified for the first time a transition of a low-mobility dissolved wax. The newly formed wax−asphaltene particles interact with dissolved wax molecules, trapping them and decreasing their mobility. Starting from this finding, Savulescu et al.[19] proposed a method to characterize both the evolution of wax precipitation rate and the evolution of dissolved wax mobility in wax−asphaltene and wax−PPD model systems. Their study found that a threshold asphaltene concentration generated an increase in the amounts of both precipitated wax and dissolved wax trapped inside the crystal network. Formation of asphaltene nanoaggregates acting as nucleation sites for wax and interactions between the altered wax−asphaltene crystal network and dissolved wax were indicated as potential causes for these observations. Regarding the PPD, its presence was observed through a low mobility peak, which disappeared once wax precipitation stars, due to complex formation and subsequent cocrystallization between wax and PPD.

The previous studies referred to cocrystallization and complex formation without providing quantitative proof. This article aims to remove this ambiguity and comes as a continuation of the previous work.[19] The first focus is the demonstration of wax−asphaltene and wax−PPD cocrystallization with high-resolution NMR. Second, a quantitative link between asphaltene nanoaggregation state and wax precipitation was studied using an adapted CPMG sequence. Last, the focus shifted toward the diffusion of the solvent to understand the effect of PPD and asphaltenes on flowability during wax crystallization. The restricted and unrestricted diffusion coefficients were calculated using diffusion-focused low-field NMR. The sum of these three sections improved the knowledge of the wax crystallization mechanism in the presence of asphaltenes or PPD.

2. EXPERIMENTAL SECTION

2.1. Materials. The solvents used in this study were deuterated toluene (anhydrous, 99.6% deuterated), toluene (anhydrous, 99.8%) from Sigma-Aldrich, Norway, and extra pure deuterated toluene (99.94%) from ChemSupport AS, Norway. Macrocrystalline and microcrystalline waxes were provided by Sasolwax from Sasol, Germany (wax 5405 and 3971, respectively). The composition and properties of these wax samples were presented previously.[26] Asphaltenes were precipitated from a crude oil (API 19°) originating from the Norwegian shelf of the North Sea, using *n*-hexane (HPLC grade, ≥97%), and the same procedure as reported before.[19] Properties of the asphaltenes precipitated from this crude oil were also published previously.[27,28] The pour point depressant was based on polycarboxylate (proprietary) from BASF, Germany, and was presented as PPD A by Ruwoldt et al.[26] and as PPD by Savulescu et al.[19] The PPD was solvent-purified using the procedure detailed previously.[26] All concentrations presented in this study are in weight percentages (wt %).

2.2. Experimental Techniques. *2.2.1. Sample Preparation.* To prepare the samples for high-resolution NMR analysis, PPDs and asphaltenes were first dissolved in deuterated toluene (99.6%), obtaining stock solutions with concentrations of 1.05 and 2.1 wt %, respectively. These were shaken overnight at 200 rpm to ensure complete dissolution. Then, a range of wax−PPD and wax−asphaltene solutions

https://doi.org/10.1021/acs.iecr.3c02218
Ind. Eng. Chem. Res. 2023, 62, 18251−18262

were prepared by dilution of the initial solutions, and the desired macrocrystalline wax content was added. A range of wax-only solutions was also prepared by dissolution of wax in deuterated toluene. All wax-containing systems were heated at 60 °C for 1 h and shaken thoroughly. Last, the NMR tubes were filled to a line of 40 mm. The solubility of asphaltenes at a high concentration (2%) in the wax−asphaltene system was further confirmed with an optical microscope. For wax−PPD mixtures, macrocrystalline wax was chosen, while for wax−asphaltene mixtures, microcrystalline wax was used. Each type of wax was scanned individually with high-resolution NMR.

For NMR CPMG, a stock solution of 2% asphaltene was prepared in extra pure deuterated toluene (99.94%) to ensure an extremely low content of residual hydrogenated solvent (max 0.06%) in asphaltene-only solutions. Dissolved asphaltene monomers and hydrogenated toluene have NMR signals in the same relaxation time region (high mobility). Therefore, the low concentrations of asphaltenes used in this study determined the necessity of reducing the residual hydrogenated solvent to the highest achievable extent. A range of asphaltene solutions with concentrations ranging from 0.2 to 2% was prepared by diluting the stock solution. All of the solutions were shaken overnight at 200 rpm to optimally dissolve the asphaltenes. Then, 3 g of each was transferred into NMR tubes for scanning.

For the tortuosity measurements, there were 3 differences in preparation of the solutions compared to the sample preparation for high-resolution NMR. The first is that the solvent was hydrogenated toluene, instead of deuterated toluene. The second is that for tortuosity measurements, the quantity of solution in the measurement tube was 3 g. The last difference is that the type of wax for all systems was a macrocrystalline wax.

Two independent parallels were performed with NMR for each system to ensure reproducibility. The overall error was calculated from the variation between the 2 parallels, and it is displayed in the corresponding figures.

2.2.2. Nuclear Magnetic Resonance: High-Field Analysis. For the high-field NMR study, a Bruker 600 MHz Avance III HD equipped with a 5 mm cryogenic CP-TCI z-gradient probe was used. The chemical spectra were acquired isothermally at 30, 10, and 0 °C, with 15 min allowed for temperature stabilization before each scan. The selected temperatures were determined by the wax appearance temperature, which is between 15 and 25 °C for the selected systems.[19,26] The residual toluene signals were expected to increase with lower temperature but only as a consequence of signal fluctuation induced by the temperature change.[23] Therefore, they were considered as a reference to normalize the other signals, which were used for the quantitative analysis of each species.

The reason for the choice of microcrystalline wax for wax−asphaltene mixtures (Section 2.2.1) was the inability to obtain accurate high-resolution NMR data with asphaltenes and macrocrystalline wax at low temperature. Wax−asphaltene precipitation generated a sharp drop in diffusion values and a high level of heterogeneity in the sample, which altered the consistency of the values for signal intensity: the reference residual toluene had a drop in signal, although the toluene molecules remained in the same phase (Figure S1a,b in the Supporting Information). This is because of strong radiation damping effects that distort the liquid signal when inhomogeneity is present. The high-field NMR is more sensitive than the low-field NMR and cannot record low mobility or a low diffusion signal in inhomogeneous systems. To decrease the heterogeneity of the wax−asphaltene system at low temperature, the microcrystalline wax with lower viscosity and a lower precipitation rate[20] was used.

2.2.3. Nuclear Magnetic Resonance: CPMG Analysis. Low-field NMR studies were performed using a 21 MHz NMR spectrometer supplied by Anvendt Teknologi AS, Norway. A CPMG procedure was used to acquire T_2 distributions for asphaltene-only solutions in extra pure deuterated toluene,[24] following the procedure presented previously.[19] The recycle delay was in this case 5 s, while the inter-echo spacing was selected to adapt for the low signal expected from 0.2 to 2% asphaltene-only solutions. A first region was selected at τ_1 of 200 μs and with 1000 echoes to account for the short T_2 region for low-mobility molecules (asphaltene nanoaggregates) and a second region was selected at τ_2 of 600 μs and with 3000 echoes for the long T_2 region for high-mobility molecules (asphaltene monomers). The number of scans was 128, except for the 0.2% asphaltene system, where 512 scans were needed to compensate for the very low signal. After acquiring raw CPMG data, a map of the proton intensity at each T_2 was generated from the multiexponentially decaying curve using the Anahess/one-dimensional Inverse Laplace Transform approach.[29] The proton intensity at each T_2 is a quantitative measure of the liquid signal, which allows for the quantification of high- and low-mobility asphaltene regions. A boundary was set between the two mobility regions for asphaltene at a T_2 of 0.5 s. Values above this threshold are specific to pure solvents at 30°C (hexane and toluene), and therefore, they most likely correspond to dissolved asphaltene monomers with high mobility in the analyzed systems or to residual toluene. However, the amount of residual toluene is very low, since 99.94% pure deuterated solvent was used. Moreover, a decrease of about 70% in the high peak intensity occurred when the asphaltene concentration was increased (Section 3.2), demonstrating that the contribution of the residual hydrogenated toluene in the peak is negligible. Figure S2 in the Supporting Information confirmed the peaks for hexane and toluene at high T_2 (10^0 to 10^1 s). The same values could be observed for high T2 peaks in Section 3.2 in this study for asphaltene-only systems. Previous studies have confirmed that model asphaltene monomers have a diameter of around 15−20 Å,[30] which is about 2−3 times higher than for toluene (5−6 Å).[31] T_2 values for toluene monomers should be slightly higher than for asphaltene monomers, but the measurement showed that they are in the same range (1−10 s). When it came to T_2 peaks at values below the threshold at T_2 = 0.5 s, they were associated with larger asphaltene nanoaggregates and nanoclusters, whose mobility and T_2 value decreased. However, low-field NMR was not able to distinguish between nanoaggregates and nanoclusters, as the relation between the exact molecular size and the T_2 could not be quantified directly to an extent that would allow separation between sizes of 2−5 nm and >5 nm.

The asphaltene experiments were performed isothermally at 30 °C after allowing 15 min for the temperature to stabilize. The temperature inside the NMR was controlled by using an integrated temperature controller connected to the NMR system.

2.2.4. Nuclear Magnetic Resonance: Tortuosity Determination. A pulsed field gradient-stimulated echo sequence with bipolar gradients[32] was used to acquire the diffusion coefficient at increasing observation times (Δ). Also, a pulsed field

https://doi.org/10.1021/acs.iecr.3c02218
Ind. Eng. Chem. Res. 2023, 62, 18251−18262

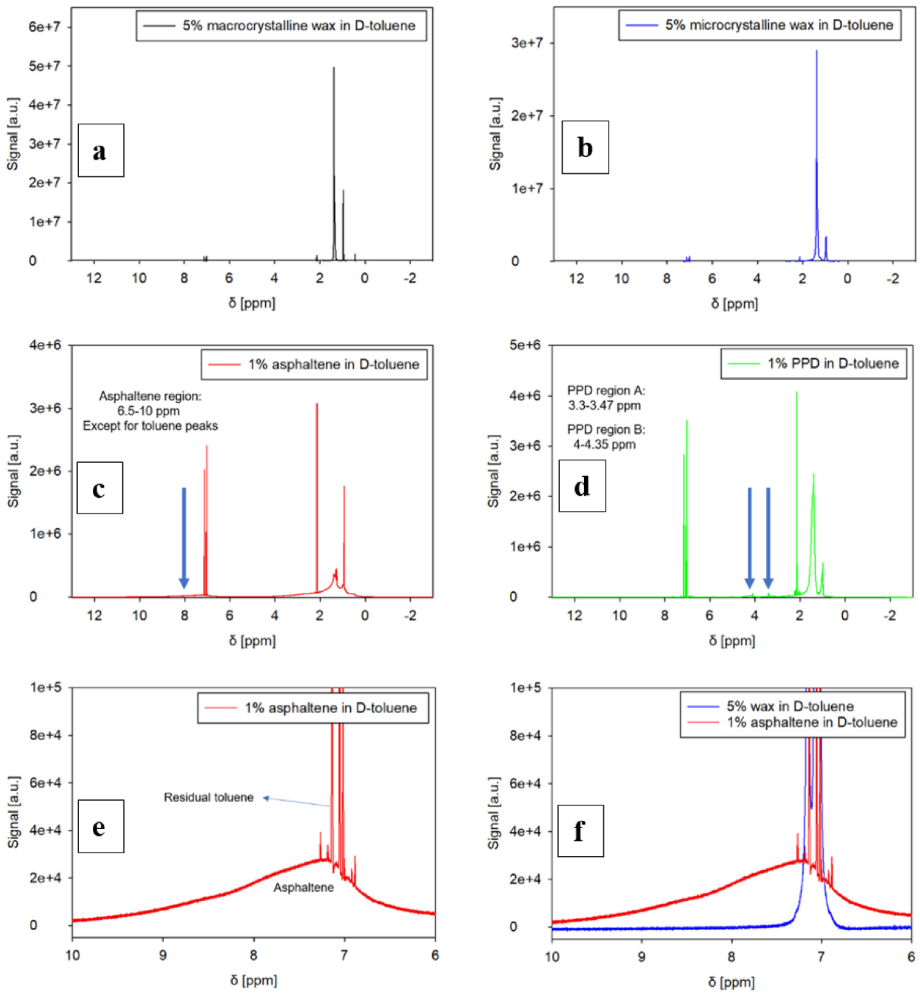

Figure 1. (a–d) ^{1}H NMR spectrum for (a) 5% macrocrystalline wax in deuterated toluene, (b) 5% microcrystalline wax in D-toluene, (c) 1% asphaltene in deuterated toluene, and (d) 1% PPD in deuterated toluene; (e, f) slices from 10 to 6 ppm in the ^{1}H NMR spectrum for (e) 1% asphaltene in deuterated toluene and (f) 5% microcrystalline wax in deuterated toluene, with a comparison to 1% asphaltene in deuterated toluene. Markings for inhibitor-specific peaks indicate the corresponding regions in panels (c) and (d).

gradient spin echo sequence with bipolar gradients[33] was used to measure the diffusion coefficient at the shortest observation time possible. The sequence for the pulses is summarized graphically in Figure S3 in the Supporting Information. The samples were scanned isothermally at 30, 10, and 0 °C, with 15 min for temperature stabilization before each acquisition. The diffusion was acquired over a range of values, starting from 2.7 ms (the dead time of the instrument) to 1000 ms. The tortuosity factor is usually calculated as the ratio between free diffusion (at zero observation time) and restricted diffusion (at 1000 ms).[34,35] In this study, the tortuosity was calculated using the point at 2.7 ms for the free diffusion. Extrapolation to 0 ms would have been inaccurate because of the low number of data points at very short times (<30 ms). The restricted diffusion coefficient is acquired at very long times, at which the displacement of the diffusing solvent molecules through the constricting space is much larger than the length scale of the constricting space.[35,36] Thus, the measured diffusion coefficient approached an asymptotic value, independent of the measurement time but dependent on the constricting space, which in this case was the resulting wax or wax–inhibitor crystal networks and the corresponding intermediate gels.

3. RESULTS AND DISCUSSION

3.1. Cocrystallization of Wax and Asphaltenes and PPD. *3.1.1. Choice of Resonance Domain.* High-resolution NMR was used to determine the cocrystallization of wax with asphaltenes and PPDs quantitatively. This was performed by determining the variations of the intensity of the NMR peaks specific to the asphaltenes and wax at temperatures above and below the wax appearance temperature. The first step was to compare the spectra of the wax with the spectra of the

https://doi.org/10.1021/acs.iecr.3c02218
Ind. Eng. Chem. Res. 2023, 62, 18251–18262

asphaltenes and PPD. The purpose was to determine asphaltene-specific and PPD-specific regions in the spectra, which afterward could be used to determine their intensity in the liquid state in wax−asphaltene and wax−PPD systems. High-resolution NMR signals focused on the high-mobility liquid region, so any decrease from the wax (macrocrystalline and microcrystalline), asphaltene, and PPD peaks could be linked to the phase change toward very-low-mobility liquid or solid states. The detection limit remained a limitation of the method because the exact diffusion value at which the signal is lost was unknown.

Figures 1a−d illustrates that a signal specific to chemical shifts for aliphatic hydrogen atoms developed for all four systems at 0.8−3 ppm. The distribution of the signal inside the 0.8−3 ppm interval varies for wax, asphaltenes, and PPD due to different chemical compositions. For macrocrystalline wax, this corresponds to $-CH_3$ and $-CH_2$ groups, while for microcrystalline wax, this most likely corresponds to $-CH_3$, $-CH_2$, and −CH groups.[21,26] The small difference between relevant chemical shifts and the very high percentage of protons from wax in wax−inhibitor systems made the compositional determination inaccurate. Therefore, the focus for inhibitor-specific regions was placed on chemical shifts above 3 ppm. For PPD, two weaker peaks were observed at 3.3−3.47 and 4−4.35 ppm, referred to as PPD region A and PPD region B, respectively. These regions most likely correspond to alcohol or ester groups present in the structure of the PPD. The difference between the 2 regions was associated with the difference between the types of carbon with which the oxygen atom bonds with. For example, $-CH_2-O-$ groups were expected to generate a signal at a slightly higher chemical shift than CH_3-O- groups. Figure S4 presents a comparison between the PPD spectrum and the macrocrystalline wax spectrum inside the 3−5 ppm region and confirms that only the PPD generated a positive signal inside this region. For asphaltenes, a signal was found from 6.5 to 10 ppm (Figure 1 e,f). This region overlapped with aromatic components of residual toluene from 7.5 to 6.75 ppm. These toluene peaks were deducted from the total signal of the region to calculate the asphaltene-specific signal. The asphaltene signal in this region was generated by aromatic components in the asphaltene structure. One can notice in Figure 1 e,f that the spectrum for 5% wax only recorded the aromatic part of the residual toluene in the 6.75−7.5 ppm interval.

3.1.2. Evolution of Inhibitor Content during Wax Crystallization. After the identification of the inhibitor-specific resonance domains, the second step of the analysis of high-resolution NMR results was the quantification of inhibitor-specific signals with temperature in the wax−inhibitor model systems.

3.1.2.1. Wax−PPD Cocrystallization. The evolution of the two PPD-specific regions (A and B) with the temperature is quantified in Figure 2. The decrease in the PPD signal with decreasing temperature demonstrated that the parts of PPD corresponding to region A and region B underwent either precipitation or a strong decrease in diffusion from 30 to 0 °C and, in particular, between 10 and 0 °C. This was not the case for all the chemical species of the PPD, as one can notice in Figure S5 in the Supporting Information. The region between 0.8 and 3 ppm (aliphatic) only recorded an insignificant decrease from 30 to 0 °C. This showed that regions A and B behaved different than the rest of the PPD. However, A and B represented about 1.5% of the total proton signal and

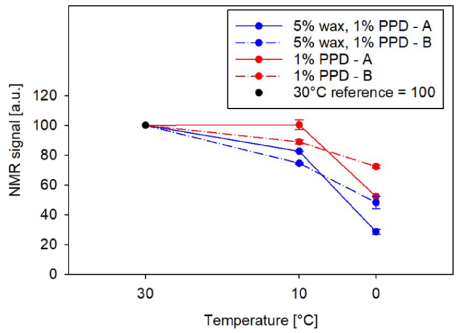

Figure 2. Variation of signal with temperature for PPD-specific peaks A and B in 5% macrocrystalline wax, 1% PPD in deuterated toluene, and 1% PPD in deuterated toluene. The value at 30 °C is fixed at 100 for all systems, while the values at 10 and 0 °C are normalized accordingly.

corresponded to polar groups such as esters, which are connected to a larger chemical structure with a polar and nonpolar part, the latter of which has a high likelihood to interact with wax.[37]

In the wax−PPD system, the relative intensity of region A at 0 °C was 28% lower than that in the PPD-only system. Region B had a relative intensity at 0 °C that was 42% lower in the wax−PPD system than that in the PPD-only system. The decrease in liquid PPD in the presence of wax indicated cocrystallization and could be agreed with studies in the literature, which demonstrated complex formation between wax and PPD in the dissolved state, followed by complex crystallization. PPDs are also known to modify wax crystals by being incorporated in the wax crystal network and then imposing steric hindrance on further wax crystal network evolution.[2,5]

It is worth noting that in a previous study, it was found by NMR CPMG that the addition of 1% PPD decreased the average wax precipitation rate by about 30% at 0 °C.[19] Using high-resolution NMR, on the other hand, the average wax precipitation rate decreased by only 12−15% upon addition of PPD (Figure 3). The main reasons for the difference between the two methods are the assumptions behind the calculations

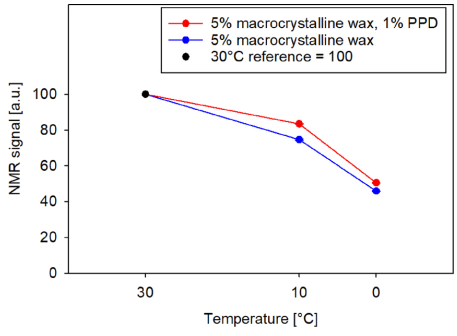

Figure 3. Variation of signal of aliphatic peak with temperature for 5% macrocrystalline wax and 5% macrocrystalline wax with 1% PPD, both in deuterated toluene. The value at 30 °C is fixed at 100 for all systems, while the values at 10 and 0 °C are normalized accordingly.

https://doi.org/10.1021/acs.iecr.3c02218
Ind. Eng. Chem. Res. 2023, 62, 18251−18262

for each of the methods and the detection limit, which is higher for high-resolution NMR (higher radiation damping).

3.1.2.2. Wax–Asphaltene Cocrystallization. To check whether the asphaltene-specific aromatic region was representative for the whole asphaltene sample, its evolution with temperature was compared with the evolution of the aliphatic region (Figure S6 in the Supporting Information). A quasi-similar decrease was noticed from 30 to 0 °C, but there are some small differences at 10 °C, most likely due to the polydispersity of asphaltenes. The high proportion of aromatic signal in the total signal (6–7%) also consolidated the fact that the asphaltene-specific signal was representative for the entire range of asphaltene species for the purpose of this study.

The next step was the investigation of the asphaltene signal in the presence and absence of wax (Figure 4). One can notice

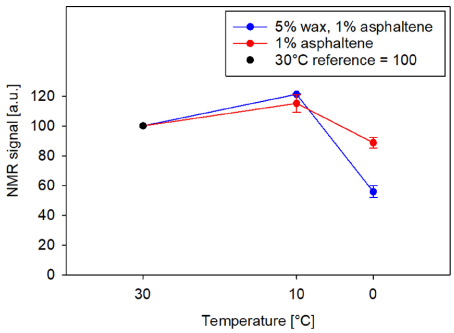

Figure 4. Variation of signal with temperature for asphaltene-specific peak in 5% microcrystalline wax, 1% asphaltene in deuterated toluene, and 1% asphaltene in deuterated toluene. The value at 30 °C is fixed at 100 for all systems, while the values at 10 and 0 °C are normalized accordingly.

a slight increase of signal from 30 to 10 °C, which corresponded to signal fluctuation induced by the difference in energy levels of atoms as a result of thermal change.[23] Consequently, one can conclude that no transition toward solid or aggregate phases occurred at 10 °C. However, when the temperature was decreased to 0 °C, the asphaltene-specific peak in the asphaltene-only system decreased by about 15%, while the one in the wax–asphaltene system decreased by about 45%. The former could be linked with asphaltene aggregation,[38] which caused a decrease in the diffusion of asphaltenes to very low values, outside of the measured liquid range. The latter demonstrated a marked decrease in the level of asphaltene diffusion when wax was present. This emphasized the interaction between asphaltenes and wax during wax gelation and crystallization and demonstrated cocrystallization. The additional decrease in asphaltene liquid signal could also be associated with a higher rate of nanoaggregate formation and even flocs, incorporated in the newly formed wax crystal networks. This supported the hypothesis that nonpolar parts of the dissolved monomers and nanoaggregate asphaltenes interact with the nonpolar wax molecules, forming wax–asphaltene networks that crystallize together.

The rate of wax–asphaltene precipitation was also quantified using the aliphatic region (Figure S7). This region consisted mainly of wax due to the weak proton signal coming from asphaltenes. A reduction of 4–6% in the wax precipitation rate was noticed at both 10 and at 0 °C. Asphaltenes were therefore inhibiting microcrystalline wax at these temperatures. Moreover, one can also notice in Figure S7 that wax precipitation was taking place at both 10 and 0 °C. However, asphaltene precipitation started between 10 and 0 °C, which implies that there was a delay between the wax appearance point and wax–asphaltene coprecipitation point. When analyzed with NMR CPMG, the same system generated a low-mobility wax region, corresponding to trapped dissolved molecules inside the newly formed crystal network, with a similar delay from the start of wax precipitation.[19] This demonstrated that during the gelation phase, the trapping of dissolved wax is accelerated by the formation of wax–asphaltene cocrystals.

In their study with NMR CPMG, Savulescu et al.[19] concluded that asphaltenes exceeding a threshold concentration, estimated to be 0.75%, enhanced the amount of low-mobility dissolved wax trapped inside the crystal networks and promoted wax precipitation. Formation of larger asphaltene nanoaggregates and nanoclusters was indicated as a potential cause of this effect. Findings in Figure 4 present a system with asphaltenes above the threshold concentration. Thus, the decrease in asphaltene liquid content observed with high-resolution NMR was most likely caused by the presence of larger asphaltene nanoaggregates or nanoclusters, which interfered with wax crystallization by acting as nucleation sites or by binding to wax through nonpolar moieties. This study aimed to quantify the asphaltene aggregation state at various asphaltene concentrations and link it to patterns in wax crystallization. Therefore, the second part of the results section

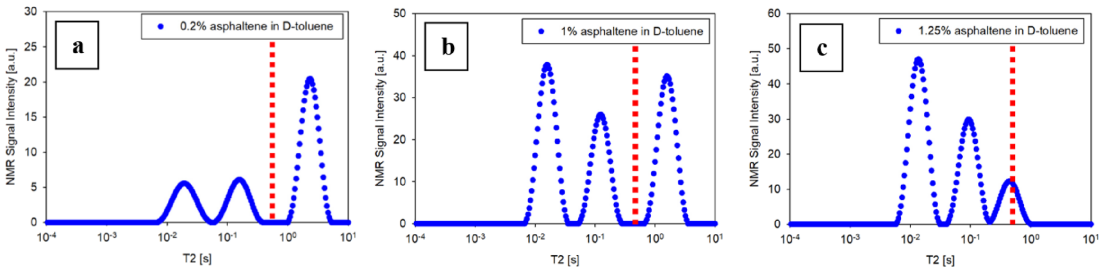

Figure 5. Relaxation time distribution in liquid domain for (a) 0.2% asphaltene in deuterated toluene, (b) 1% asphaltene in deuterated toluene, and (c) 1.25% asphaltene in deuterated toluene. The red line marks the border between high-mobility asphaltene monomers and low-mobility asphaltene nanoaggregates.

https://doi.org/10.1021/acs.iecr.3c02218
Ind. Eng. Chem. Res. 2023, 62, 18251–18262

will focus on the determination of the monomer/aggregate ratio in asphaltene-only systems.

3.2. The Effect of Asphaltene Nanoaggregation State on Wax Precipitation. T_2 relaxation times measured by NMR CPMG were correlated with the mobility of hydrogen species. The higher the mobility, the higher the T_2. As the mobility is a function of the size of molecular species/aggregates, measuring the T_2 distribution of a sample allowed us to probe the size distribution of molecules or aggregates present in the sample. It is worth noting that the T_2 distributions were highly reproducible (Figures S8 and S9 in the Supporting Information).

Figure 5a presents the distribution of T_2 relaxation times for the system with the lowest concentration (0.2%) of asphaltenes. This minimum concentration was selected after taking into consideration the limitations of NMR resonance frequency detection. Figure 5a comprises of 3 signal peaks, a stronger one that formed in the asphaltene monomer region (T_2 > 0.5 s) and two weaker ones in the asphaltene nanoaggregate/nanocluster region. As the asphaltene concentration was increased to 1%, the distribution of the peaks changed and the signal in the nanoaggregate/nanocluster region had higher relative intensity compared to the monomer signal (Figure 5b). This pattern intensified when the concentration was increased to 1.25% asphaltenes, where little to no monomer peak signal was observed (Figure 5c). This indicated an almost complete shift in equilibrium toward >90% nanoaggregates/nanoclusters between 1 and 1.25% asphaltenes. The total intensity of the signal (Figure 6) also followed

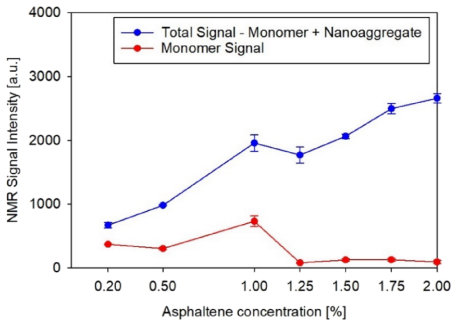

Figure 6. Total signal and monomer signal as a function of asphaltene concentration in asphaltene-only solutions in deuterated toluene.

a modified pattern from 1 to 1.25%. The signal varied linearly with asphaltene concentrations below 1% and above 1.25%. However, from 1 to 1.25%, the total signal was almost constant, indicating that part of the asphaltenes aggregated or clustered to such an extent that they underwent loss of mobility, which shifted the T_2 to a value below the measured range.

This observation was linked to previous findings,[19] where asphaltenes reaching a threshold concentration of 0.75% promoted wax precipitation and provided reduced mobility on dissolved wax molecules, which became trapped in the gaps of the wax−asphaltene cocrystal network or in the wax−asphaltene cocrystal pores. This process prevented further crystal growth.[19] The asphaltene nanoaggregation state was highlighted as the reason for the change in behavior. Thus, the demonstration of the complete shift from monomer to aggregates/clusters at 1.25% asphaltene confirmed the explanation in the previous article. However, a gap remains between the asphaltene concentration at which the shift was observed: 0.75% in wax−asphaltene systems and 1.25% in asphaltene-only systems. Two potential explanations arise for this gap. First, the previous experiments were performed dynamically from 45 to 0 °C. The change in wax precipitation behavior and the intensification of the amount of trapped dissolved wax were observed at temperatures lower than 15 °C when wax started precipitating. In the current study, the temperature was isothermally set at 30 °C. The asphaltenes were expected to form larger nanoaggregates/nanoclusters with lower mobility at lower temperature,[39] which would decrease the threshold concentration. The second explanation is that the factor triggering the changes in wax precipitation behavior was not the complete shift toward nanoaggregates/nanoclusters but the shift toward a threshold nanoaggregate/nanocluster content relative to the wax content. Figures 6 and 7 solidify this hypothesis. Although the monomer and

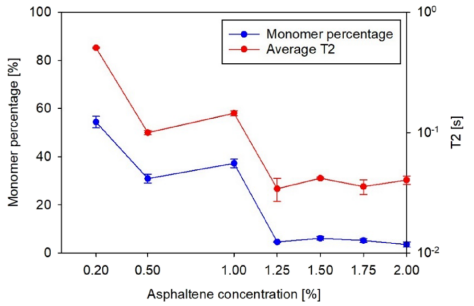

Figure 7. Monomer percentage and average T_2 (monomer + nanoaggregate/nanocluster) as a function of asphaltene concentration in asphaltene-only solutions in deuterated toluene.

nanoaggregate/nanocluster percentages were quasi-constant from 0.5 to 1% asphaltene, the amount of nanoaggregates/nanoclusters was approximately 2-fold in the system with 1% asphaltene. When the wax concentration was fixed, the ratio between nanoaggregate/nanoclusters and wax became twice as high at 1% asphaltene compared to 0.5% asphaltene. The asphaltene nanoaggregate/nanocluster to wax ratio was thus likely to dominate the wax precipitation behavior.

Another observation in Figure 6 is the shift in nanoaggregate/nanocluster percentage that occurred from 0.2 to 0.5%. At a low asphaltene concentration, the nanoaggregate/nanocluster content was very low. This was associated with a different behavior of wax−asphaltene systems with a very low asphaltene concentration. For example, previous studies concluded that low asphaltene content could lead to wax precipitation inhibition.[9,26] A lower content of nanoaggregates/nanoclusters could be associated with a lower likelihood for asphaltenes to act as wax nucleation sites, which explains why the precipitation was not accelerated. Simultaneously, asphaltenes were still present in the monomer state, which implied that they could act as wax binders and modify crystal networks, preventing normal crystal growth. The equilibrium between the latter and former effects is most likely a function of the total asphaltene concentration. Thus, at low asphaltene concentrations, the former effect dominated, making inhibition

https://doi.org/10.1021/acs.iecr.3c02218
Ind. Eng. Chem. Res. 2023, 62, 18251−18262

more likely, while at high asphaltene concentrations, the latter effect dominated, making promotion more likely.

The results analyzed so far were consolidated through the quantification of the average T_2 (Figure 7), which has a quasilinear trend similar to the monomer percentage. This observation reaffirmed the choice of T_2 at 0.5 s as a border between the monomer and the nanoaggregate: the loss in monomer percentage accounts for the loss in mobility that occurs with increasing concentration.

The formation of asphaltene nanoaggregates and nanoclusters was demonstrated before with SAXS and SANS.[8,40−42] However, the quantification of the monomer:nanoaggregate ratio represents a novelty in asphaltene research.

3.3. The Effect of Asphaltenes and PPDs on the Diffusion of Solvent through the Wax Crystal Network.

The previous subsections focused on the evolution of the molecular mobility of the inhibitors in wax−inhibitor systems. The last subsection will focus on the diffusion of the solvent to understand how modifications in the wax crystal networks affect the mobility of dissolved molecules.

Figures 8 and 9 present the diffusion coefficient as a function of time for the liquid species, representing toluene and the

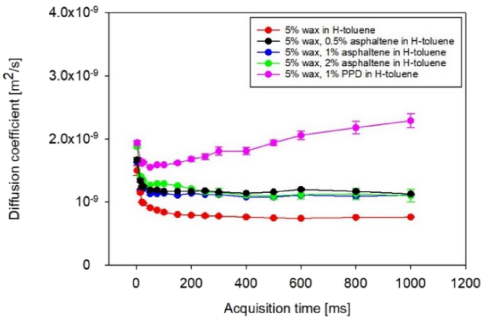

Figure 8. Diffusion coefficient profile at 10 °C as a function of acquisition times for wax, wax−asphaltene, and wax−PPD systems in toluene.

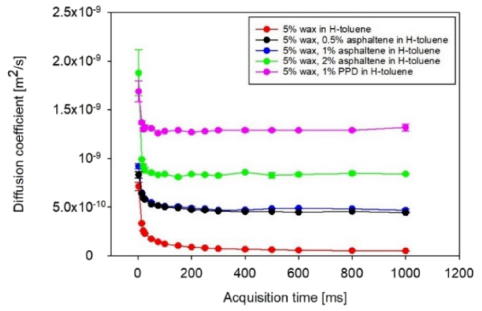

Figure 9. Diffusion coefficient profile at 0 °C as a function of acquisition times for wax, wax−asphaltene, and wax−PPD systems in toluene.

remaining dissolved species (<7%) at 10 and 0 °C (i.e., below the WAT), respectively. The calculated diffusion coefficients represented the remaining fluid during wax crystallization and were mostly influenced by the diffusion of toluene molecules (>93%). The precipitation of wax was expected to impact the free diffusion coefficient of the solvent molecules. One can observe in Figure 9 that at 0 °C, the diffusion coefficient decreased exponentially at short times and then remained constant at longer times. The coefficient at zero time corresponds to the unrestricted diffusion coefficient, while the coefficient at high time is the restricted diffusion coefficient, which results from the solvent being surrounded by the wax crystal network.

The values at the first measured point were closer to the self-diffusion values for toluene from the literature, but there were some deviations. For example, the literature value for self-diffusion of toluene at 0 °C was 1.5×10^{-9} m^2/s,[43] while the unrestricted diffusion values determined at 2.7 ms were in the range of 7×10^{-10} to 1.8×10^{-9} m^2/s for the wax-based systems (Figure 9). One reason for this discrepancy was the presence of dissolved wax or asphaltenes, which altered the liquid diffusion value from the toluene value. Another reason was the restriction imposed already during the dead time (2.7 ms). To demonstrate this, one can notice that the lower the unrestricted diffusion coefficient, the lower the restricted diffusion coefficient (Figure 9).

The restricted diffusion coefficient was 5−9 times higher when asphaltenes were present at 0 °C (Figure 9). The difference was lower at 10 °C (Figure 8): the restricted diffusion coefficient was higher by about 30% when asphaltenes were added and was not sensitive to the asphaltene concentration. At both temperatures, the increase in the restricted diffusion coefficient could be linked to the alteration of the wax crystal network generated by the asphaltenes.[11] The higher solvent diffusion indicated less restriction imposed by the altered wax−asphaltene crystal network on the solvent molecules. This was consistent with previous cross-polarized microscopy results that demonstrated smaller, more finely dispersed crystals when asphaltenes were present.[26] An increased asphaltene concentration (2%) could be associated with significantly less restriction on the solvent molecules but only at 0 °C when the precipitation reached a certain threshold (Figures 8 and 9). This confirmed that high asphaltene concentration induced more open crystal networks, which led to higher solvent flowability.

A different pattern can be observed for the wax−PPD system in both Figures 8 and 9. At 10 °C, it followed a similar decreasing exponential pattern at low acquisition times (Figure 8). However, there was a shift to a linear increase at high times. This demonstrates that in the wax−PPD system, the amount of solid was not high enough at 10 °C to form a network, and therefore, the system still behaved partially like a liquid. When the gel forms, only Brownian motion influences the diffusion coefficient at high times. On the other hand, for liquids, convection distorts the NMR signal, generating the linear increase observed for the wax−PPD system at high times. Consequently, one can conclude that the PPD inhibited gel formation, which was otherwise undergoing at the same temperature in the wax system without PPD. When the temperature was decreased to 0 °C (Figure 9), the linear increase was not present anymore, which demonstrated that the newly precipitated solid wax prevented convection. The restricted diffusion coefficient for wax−PPD was about 13 times higher than that for wax only. The reason was the formation of a highly altered wax crystal network, with smaller and more dispersed crystals, as described in the literature.[2,5]

Tortuosity values derived from the diffusion coefficients in Figures 8 and 9 are presented in Figures S10 and S11 in the

https://doi.org/10.1021/acs.iecr.3c02218
Ind. Eng. Chem. Res. 2023, 62, 18251−18262

Scheme 1. Model Schematics for Crystal Networks and Liquid Phases for Wax and Wax−asphaltene Systems at 0 °C

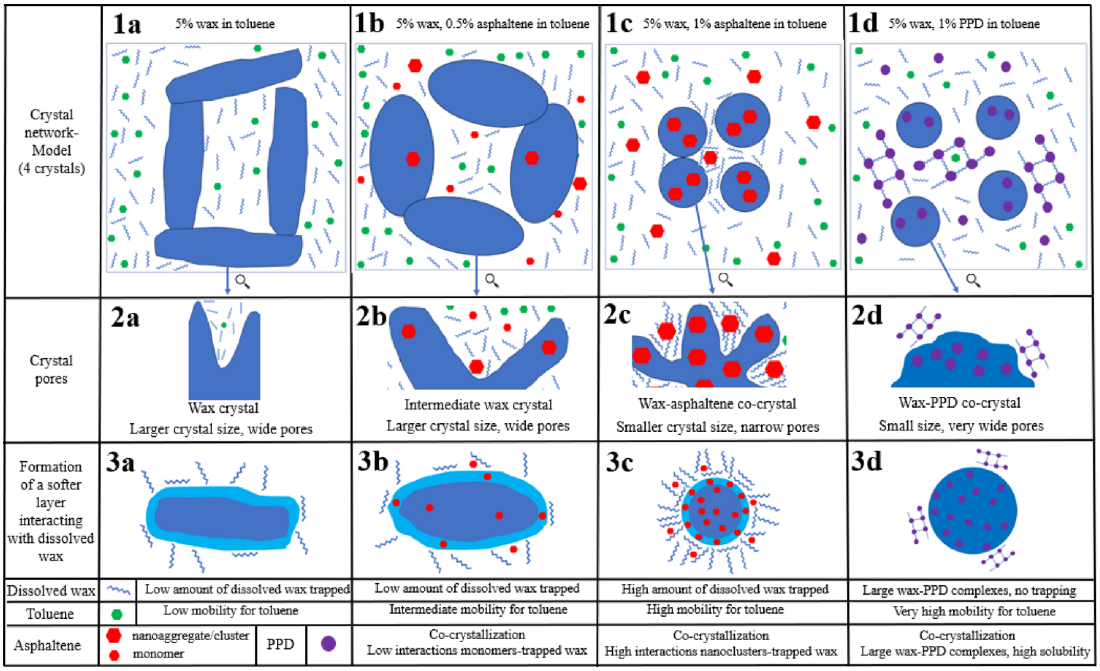

Supporting Information, respectively. As expected, the presence of asphaltenes generated a much more significant decrease at 0 °C than at 10 °C. The presence of PPD had a comparable effect at 0 °C. This demonstrated that the solvent pathway through the crystal network became less convoluted when wax crystals were altered by asphaltenes or PPDs.

The tortuosity analysis can be correlated with results in the previous study by Savulescu et al.[19] The formation of a low-mobility dissolved wax region at a low temperature was identified in wax and wax−asphaltene systems. Different trends were observed for dissolved wax and toluene when asphaltenes were present. Although the previous study found that higher asphaltene concentrations increased the amount of trapped dissolved wax, the tortuosity measurements decreased the restriction on toluene molecules when the asphaltene content increased. The explanation for this lies in the nature of the chemical structures of wax and toluene. The dissolved wax at low mobility can interact with asphaltene nanoaggregates, which behave either as wax crystal network binders or as nucleation sites. On the other hand, toluene does not interact with the other components during this process.

Asphaltenes and PPDs have a different mechanism of interaction with wax during precipitation. PPDs reduce wax solubility through the formation of liquid complexes, which then precipitate as a modified wax−PPD crystal network.[5] On the other hand, asphaltenes are highly unlikely to alter wax crystals until the gelation phase. This can also be observed in the results in Figures 8 and 9. The PPD had an inhibiting effect on the wax precipitation at 10 °C, delaying the formation of a strong solid network. On the other hand, wax precipitation was in more advanced stages (higher viscosity) in the wax−asphaltene systems at 10 °C. At 0 °C, when gelation and precipitation were rapidly occurring, the restricted diffusion was 6−9 times higher when asphaltenes were present and asphaltene concentration had a distinguishable effect.

Another thing to mention is that the restricted diffusion coefficient for wax−PPD at 0 °C was higher than the restricted diffusion coefficient of wax at 10 °C. This illustrated a delay of over 10 °C in restriction on the solvent movement through the wax crystal network when 1% PPD was added. The same could be observed for the system with the highest asphaltene concentration (2%). One can conclude that although asphaltenes at high concentration were found to promote wax precipitation (i.e., higher crystallized amount)[19] and to intensify the amount of low-mobility dissolved wax, the resulting crystals had modified properties that increased the restricted solvent diffusion. In real systems, this would translate to a higher quantity of wax but with more open networks, giving a better flowability for the liquid components in the crude oil.

3.4. Interpretation of the Wax Crystal and Network Structures. Our interpretation of the influence of asphaltenes and PPDs on the wax crystal and network structures in toluene is summarized in this section. Scheme 1 shows an overview of cross sections of the different wax systems below the WAT that have been studied. The first line (1a−1d) illustrates crystal networks, represented by four crystals for simplicity. The second line (2a−2d) illustrates part of single crystals with varying porosity, while single crystals are drawn on the third line (3a−3d).

The wax network formed with only wax dissolved in toluene was considered as the reference case. It is well known that elongated wax crystals form in such systems[26] and that these crystals interlock to form a porous network. This was

https://doi.org/10.1021/acs.iecr.3c02218
Ind. Eng. Chem. Res. 2023, 62, 18251−18262

confirmed by the strongly reduced mobility of solvent molecules (toluene) in Figure 8 and 9. Previously, a population of wax with intermediate mobility, i.e., mobility between that of liquid and solid wax, was identified below the WAT.[44] Several possibilities for the origin of this population have been put forward: trapping of wax molecules between the interlocking wax crystals[19,44] (illustrated in Scheme 1, 1a), formation of pores within the precipitated wax crystal containing less mobile wax[12,26] (illustrated in Scheme 1, 2a), and an amorphous, softer layer of less mobile wax surrounding the wax crystals[44] (illustrated in Scheme 1, 3a). All these mechanisms need further verification but are nevertheless considered in the following discussion of how the presence of asphaltenes and PPD can alter the wax crystal network.

The presence of asphaltenes was considered first. The amount of asphaltenes significantly influenced the wax precipitation and network structures significantly. Below a threshold range (about 0.75−1% asphaltenes in 5% wax), asphaltene monomers were predominantly present. In this concentration range, asphaltenes induced rounder wax−asphaltene cocrystals, with less interlocking and wider, less deep pores (Scheme 1 and Figures 1b−3b). This was shown by the increase in toluene mobility and ongoing atomic force microscopy studies. The low amount of nanoaggregates in this concentration range did not have a significant impact on wax crystallization in the nucleation stage. The low content of asphaltenes, relative to wax (<1:7), also induced a lower likelihood for asphaltene monomers and nanoaggregates to act as wax crystal binders. This resulted in a crystal network that resembled wax-only systems in the way that it had similar capacity to trap wax.[19]

Above the threshold range (>1% asphaltene), mostly asphaltene nanoaggregates and nanoclusters were present. These acted as nucleation sites for wax due to the formation of a larger nonpolar region after nanoaggregation/nanoclustering and/or due to the increased surface area for heterogeneous nucleation.[9] During the initial stages of nucleation and growth, the nonpolar parts of asphaltene aggregates might interact with the nonpolar wax molecules through London forces[10,11] and lead to cocrystallization of wax and asphaltene aggregates. The incorporation of asphaltene nanoclusters in the wax crystals also imposed steric hindrances that restricted their growth,[12] resulting in smaller cocrystals with rounder shapes.[26] These cocrystals might be packed closer and formed network structures with smaller confinements between individual crystals (Figures 8 and 9). Moreover, higher amounts of liquid wax with reduced mobility were found in these structures.[19] This wax population occurs due to the same mechanisms as outlined above: trapping of wax in a more confined space between the smaller interlocked cocrystals (Scheme 1, 1c), less mobile wax in smaller pores of the wax−asphaltene aggregate cocrystals (Scheme 1, 2c), and the presence of a softer, amorphous wax−asphaltene layer surrounding the cocrystals that possibly also interacted with dissolved wax (Scheme 1, 3c).

Notably, the population of dissolved wax with reduced mobility increases, while dissolved toluene had an increase in mobility in these structures in comparison to the wax-only system. This demonstrated that the trapping of dissolved wax was not only caused by spatial hindrance due to gaps in the crystal networks and pores but could have reduced the mobility of toluene as well. An additional factor was most likely interactions of dissolved wax with the species in the altered wax−asphaltene crystal network or with species undergoing nucleation/gelation[19] (Scheme 1, 2c−3c).

Finally, the presence of polycarboxylate PPD also had a marked effect on the crystal network formed upon crystallization. Also in this case, interactions between hydrophobic segments of the PPD and wax during the nucleation and growth stage were considered to give rise to cocrystallization of wax and PPD. Steric hindrance provided by the PPD on growing crystals limited the cocrystal growth, giving smaller and rounder crystals similar to those formed in the presence of asphaltene aggregates. The geometry of the resulting cocrystal networks, however, was markedly different in the way that the wax−PPD networks had less interconnections between the cocrystals and hence were more open (Figures 8 and 9). Also, the wax−PPD complexes in the liquid state were significantly larger, requiring more space to crystallize, which delayed crystallization and improved solubility (Scheme 1, 1d): PPD at 1% reduced the wax crystallization rate significantly.[19] The wax−PPD cocrystal network did not trap dissolved wax molecules.[19] The crystal network formation did not follow any of the 3 mechanisms proposed for wax and wax−asphaltene systems for dissolved wax trapping. First, there is little interlocking and wide gaps between individual crystals (Scheme 1, 1d). Second, ongoing atomic force microscopy studies show no noticeable pore structure (Scheme 1, 2d). Last, intermediate amorphous phases were not recorded with any of the proposed experimental techniques or ongoing studies (Scheme 1, 3d).

4. CONCLUSIONS

This study highlighted novel approaches that consolidated the knowledge about wax−modifier interactions using improved NMR techniques to overcome the limitations of previous wax crystallization characterization methods:

1 Identification and quantification of asphaltene-specific and PPD-specific peaks at various temperatures were performed with high-resolution NMR, leading to the demonstration of wax−asphaltene and wax−PPD cocrystallization. This confirmed cocrystallization as a factor for changes in wax crystal behavior. Moreover, the approach could be used in future research to compare the behavior of systems with different degrees of cocrystallization.

2 Changes in molecular mobility with increasing asphaltene concentration were detected with NMR CPMG in asphaltene-only systems. A shift toward low mobility peaks was noticed above a threshold concentration. The same concentration corresponded to the asphaltene concentration at which the wax−asphaltene crystals provided spatial hindrance on dissolved wax molecules, trapping them and preventing further crystal growth. This demonstrated the nanoaggregation of asphaltenes and its impact on the modification of wax crystallization behavior. The determination of the monomer:nanoaggregate ratio inside the liquid-specific mobility region consolidated previous SANS and SAXS studies that proved the existence of these nanoaggregates.

3 The effect of crystal modification on the tortuosity and free diffusion of the solvent was assessed using pulsed field gradient NMR. Higher diffusion of solvent molecules through the wax crystal network was recorded when asphaltenes were present, and even higher values

https://doi.org/10.1021/acs.iecr.3c02218
Ind. Eng. Chem. Res. 2023, 62, 18251−18262

were obtained with PPD. This represented a quantitative measure of the effects of wax crystal alteration, weaker, smaller, and more finely dispersed crystals, which allowed for higher flowability.

■ ASSOCIATED CONTENT

Supporting Information

The Supporting Information is available free of charge at https://pubs.acs.org/doi/10.1021/acs.iecr.3c02218.

Additional figures that clarify observations in the main paper (PDF)

■ AUTHOR INFORMATION

Corresponding Author

George Claudiu Savulescu − *Ugelstad Laboratory, Norwegian University of Science and Technology, Trondheim 7491, Norway;* orcid.org/0000-0003-3278-0745; Email: george.c.savulescu@ntnu.no

Authors

Sébastien Simon − *Ugelstad Laboratory, Norwegian University of Science and Technology, Trondheim 7491, Norway*

Geir Sørland − *Ugelstad Laboratory, Norwegian University of Science and Technology, Trondheim 7491, Norway; Anvendt Teknologi AS, Trondheim 7022, Norway*

Gisle Øye − *Ugelstad Laboratory, Norwegian University of Science and Technology, Trondheim 7491, Norway;* orcid.org/0000-0002-6391-3750

Complete contact information is available at: https://pubs.acs.org/10.1021/acs.iecr.3c02218

Notes

The authors declare no competing financial interest.

■ ACKNOWLEDGMENTS

This work is part of SUBPRO SFI, a research-based center within subsea production and processing. The authors hereby acknowledge the financial support from SUBPRO, which is financed by the Research Council of Norway, major industry partners and NTNU.

■ REFERENCES

(1) Oliveira, L. M. S. L.; Nunes, R. C. P.; Melo, I. C.; Ribeiro, Y. L. L.; Reis, L. G.; Dias, J. C. M.; Guimarães, R. C. L.; Lucas, E. F. Evaluation of the Correlation between Wax Type and Structure/Behavior of the Pour Point Depressant. *Fuel Process. Technol.* **2016**, *149*, 268−274.

(2) Yang, F.; Zhao, Y.; Sjöblom, J.; Li, C.; Paso, K. G. Polymeric Wax Inhibitors and Pour Point Depressants for Waxy Crude Oils: A Critical Review. *J. Dispersion Sci. Technol.* **2015**, *36*, 213−225.

(3) Kelland, M. A. *Production Chemicals for the Oil and Gas Industry*; 2009; Vol. *1*. CRC Press.

(4) Al-Yaari, M. Paraffin Wax Deposition: Mitigation and Removal Techniques. *SPE - Saudi Arabia Section Young Professionals Technical Symposium (conference)*. paper nr. SPE-155412-MS. 2011.

(5) Paso, K. G.; Krückert, K. K.; Oschmann, H.-J.; Ali, H.; Sjöblom, J. PPD Architecture Development via Polymer−Crystal Interaction Assessment. *J. Pet. Sci. Eng.* **2014**, *115*, 38−49.

(6) Wei, B. Recent Advances on Mitigating Wax Problem Using Polymeric Wax Crystal Modifier. *J. Pet. Explor. Prod. Technol.* **2015**, *5* (4), 391−401.

(7) Bai, Y.; Bai, Q. 16 - Wax and Asphaltenes. In *Subseas Engineering Handbook*; Second edition Eds.; Gulf Professional Publishing: Boston, 2019; pp 435−453.

(8) Mullins, O. C.; Sabbah, H.; Eyssautier, J.; Pomerantz, A. E.; Barré, L.; Andrews, A. B.; Ruiz-Morales, Y.; Mostowfi, F.; McFarlane, R.; Goual, L.; Lepkowicz, R.; Cooper, T.; Orbulescu, J.; Leblanc, R. M.; Edwards, J.; Zare, R. N. Advances in asphaltene Science and the Yen−Mullins Model. *Energy Fuels* **2012**, *26* (7), 3986−4003.

(9) Kriz, P.; Andersen, S. I. Effect of Asphaltenes on Crude Oil Wax Crystallization. *Energy Fuels* **2005**, *19* (3), 948−953.

(10) Lei, Y.; Han, S.; Zhang, J.; Bao, Y.; Yao, Z.; Xu, Y. Study on the Effect of Dispersed and Aggregated asphaltene on Wax Crystallization, Gelation, and Flow Behavior of Crude Oil. *Energy Fuels* **2014**, *28* (4), 2314−2321.

(11) Ariza-León, E.; Molina-Velasco, D.-R.; Chaves-Guerrero, A. REVIEW OF STUDIES ON asphaltene - WAX INTERACTION AND THE EFFECT THEREOF ON CRYSTALLIZATION. *CT&F - Cienc., Tecnol. Futuro* **2014**, *5*, 39−53.

(12) Cao, H.; Cao, X.; Zhao, X.; Guo, D.; Liu, Y.; Bian, J. Molecular Dynamics Simulation of Wax Molecules Aggregational Crystallization Behavior during Cooling of Crude Oil Mixture. *Case Stud. Therm. Eng.* **2022**, *37*, No. 102298.

(13) Venkatesan, R.; Östlund, J.-A.; Chawla, H.; Wattana, P.; Nydén, M.; Fogler, H. S. The Effect of Asphaltenes on the Gelation of Waxy Oils. *Energy Fuels* **2003**, *17* (6), 1630−1640.

(14) Oliveira, G. E.; Mansur, C. R. E.; Lucas, E. F.; González, G.; de Souza, W. F. The Effect of Asphaltenes, Naphthenic Acids, and Polymeric Inhibitors on the Pour Point of Paraffins Solutions. *J. Dispersion Sci. Technol.* **2007**, *28* (3), 349−356.

(15) García, M. D. C. Crude Oil Wax Crystallization. The Effect of Heavy n-Paraffins and Flocculated Asphaltenes. *Energy Fuels* **2000**, *14* (5), 1043−1048.

(16) Molina, V. D.; Ariza León, E.; Chaves-Guerrero, A. Understanding the Effect of Chemical Structure of Asphaltenes on Wax Crystallization of Crude Oils from Colorado Oil Field. *Energy Fuels* **2017**, *31* (9), 8997−9005.

(17) García, M. D. C.; Carbognani, L. asphaltene−Paraffin Structural Interactions. Effect on Crude Oil Stability. *Energy Fuels* **2001**, *15* (5), 1021−1027.

(18) Lei, Y.; Han, S.; Zhang, J. Effect of the Dispersion Degree of asphaltene on Wax Deposition in Crude Oil under Static Conditions. *Fuel Process. Technol.* **2016**, *146*, 20−28.

(19) Savulescu, G. C.; Simon, S.; Sørland, G.; Øye, G. New Nuclear Magnetic Resonance Approaches on the Evolution of Wax Mobility during Wax Crystallization. *Energy Fuels* **2022**, *36* (1), 350−360.

(20) Savulescu, G. C.; Simon, S.; Sørland, G.; Øye, G. Novel Nuclear Magnetic Resonance Techniques To Assess the Wax Precipitation Evolution in Crude Oil Systems. *Energy Fuels* **2023**, *37* (1), 291−300.

(21) Kurniawan, M.; Subramanian, S.; Norrman, J.; Paso, K. Influence of Microcrystalline Wax on the Properties of Model Wax-Oil Gels. *Energy Fuels* **2018**, *32* (5), 5857−5867.

(22) Pedersen, W. B.; Baltzer Hansen, A.; Larsen, E.; Nielsen, A. B.; Roenningsen, H. P. Wax Precipitation from North Sea Crude Oils. 2. Solid-Phase Content as Function of Temperature Determined by Pulsed NMR. *Energy Fuels* **1991**, *5* (6), 908−913.

(23) Slichter, C. P. *Principles of Magnetic Resonance*; Springer Science & Business Media: Springer-Verlag Berlin Heidelberg, 2013.

(24) Meiboom, S.; Gill, D. Modified Spin-Echo Method for Measuring Nuclear Relaxation Times. *Rev. Sci. Instrum.* **1958**, *29* (8), 688−691.

(25) Zhao, Y.; Paso, K.; Norrman, J.; Ali, H.; Sørland, G.; Sjöblom, J. Utilization of DSC, NIR, and NMR for Wax Appearance Temperature and Chemical Additive Performance Characterization. *J. Therm. Anal. Calorim.* **2015**, *120* (2), 1427−1433.

(26) Ruwoldt, J.; Humborstad Sørland, G.; Simon, S.; Oschmann, H.-J.; Sjöblom, J. Inhibitor-Wax Interactions and PPD Effect on Wax Crystallization: New Approaches for GC/MS and NMR, and

Comparison with DSC, CPM, and Rheometry. *J. Pet. Sci. Eng.* **2019**, *177*, 53−68.
(27) Subramanian, S.; Sørland, G. H.; Simon, S.; Xu, Z.; Sjöblom, J. asphaltene Fractionation Based on Adsorption onto Calcium Carbonate: Part 2. Self-Association and Aggregation Properties. *Colloids Surf., A* **2017**, *514*, 79−90.
(28) Pinto, F. E.; Barros, E. V.; Tose, L. V.; Souza, L. M.; Terra, L. A.; Poppi, R. J.; Vaz, B. G.; Vasconcelos, G.; Subramanian, S.; Simon, S.; Sjöblom, J.; Romão, W. Fractionation of Asphaltenes in N-Hexane and on Adsorption onto CaCO3 and Characterization by ESI(+)FT-ICR MS: Part I. *Fuel* **2017**, *210*, 790−802.
(29) Sørland, G. H.; Anthonsen, H. W.; Ukkelberg, Å.; Zick, K. A Robust Method for Analysing One and Two-Dimensional Dynamic NMR Data. *Appl. Magn. Reson.* **2022**, *53* (10), 1345−1359.
(30) Andrews, A. B.; Guerra, R. E.; Mullins, O. C.; Sen, P. N. Diffusivity of asphaltene Molecules by Fluorescence Correlation Spectroscopy. *J. Phys. Chem. A* **2006**, *110* (26), 8093−8097.
(31) Chen, W.; Zhao, H.; Xue, Y.; Chang, X. Adsorption Effect and Adsorption Mechanism of High Content Zeolite Ceramsite on Asphalt VOCs. *Materials* **2022**, *15*, 6100.
(32) Sørland, G. H.; Hafskjold, B.; Herstad, O. A Stimulated-Echo Method for Diffusion Measurements in Heterogeneous Media Using Pulsed Field Gradients. *J. Magn. Reson.* **1997**, *124* (1), 172−176.
(33) Sørland, G. H.; Aksnes, D.; Gjerdåker, L. A Pulsed Field Gradient Spin-Echo Method for Diffusion Measurements in the Presence of Internal Gradients. *J. Magn. Reson.* **1999**, *137* (2), 397−401.
(34) Mitra, P. P.; Sen, P. N.; Schwartz, L. M.; Le Doussal, P. Diffusion Propagator as a Probe of the Structure of Porous Media. *Phys. Rev. Lett.* **1992**, *68* (24), 3555−3558.
(35) Tourell, M. C.; Pop, I.-A.; Brown, L. J.; Brown, R. C. D.; Pileio, G. Singlet-Assisted Diffusion-NMR (SAD-NMR): Redefining the Limits When Measuring tortuosity in Porous Media. *Phys. Chem. Chem. Phys.* **2018**, *20* (20), 13705−13713.
(36) Latour, L. L.; Mitra, P. P.; Kleinberg, R. L.; Sotak, C. H. Time-Dependent Diffusion Coefficient of Fluids in Porous Media as a Probe of Surface-to-Volume Ratio. *J. Magn. Reson. Ser. A* **1993**, *101* (3), 342−346.
(37) Wu, C.; Zhang, J.; Li, W.; Wu, N. Molecular Dynamics Simulation Guiding the Improvement of EVA-Type Pour Point Depressant. *Fuel* **2005**, *84* (16), 2039−2047.
(38) Espinat, D.; Fenistein, D.; Barré, L.; Frot, D.; Briolant, Y. Effects of Temperature and Pressure on Asphaltenes Agglomeration in Toluene. A Light, X-Ray, and Neutron Scattering Investigation. *Energy Fuels* **2004**, *18* (5), 1243−1249.
(39) Roux, J.-N.; Broseta, D.; Demé, B. SANS Study of asphaltene Aggregation: Concentration and Solvent Quality Effects. *Langmuir* **2001**, *17* (16), 5085−5092.
(40) Eyssautier, J.; Levitz, P.; Espinat, D.; Jestin, J.; Gummel, J.; Grillo, I.; Barré, L. Insight into asphaltene Nanoaggregate Structure Inferred by Small Angle Neutron and X-Ray Scattering. *J. Phys. Chem. B* **2011**, *115* (21), 6827−6837.
(41) Eyssautier, J.; Hénaut, I.; Levitz, P.; Espinat, D.; Barré, L. Organization of Asphaltenes in a Vacuum Residue: A Small-Angle X-Ray Scattering (SAXS)−Viscosity Approach at High Temperatures. *Energy Fuels* **2012**, *26* (5), 2696−2704.
(42) Barré, L.; Jestin, J.; Morisset, A.; Palermo, T.; Simon, S. Relation between Nanoscale Structure of asphaltene Aggregates and Their Macroscopic Solution Properties. *Oil Gas Sci. Technol. - Rev. IFP* **2009**, *64* (5), 617−628.
(43) van de Ree, J. Classical Trajectory Calculations of the Scattering of TlF on Ar in Thermal Beams. *J. Chem. Phys.* **1971**, *54* (8), 3249−3262.
(44) Morozov, E. V.; Nizovtseva, P. V.; Martyanov, O. N. From Components to Phase-Dependent Dynamics of Diffusivity in Wax Solutions Subjected to Fluid−Solid Phase Transition: Insights from Pulsed Field Gradient NMR. *Energy Fuels* **2022**, *36* (24), 14696−14709.

https://doi.org/10.1021/acs.iecr.3c02218
Ind. Eng. Chem. Res. 2023, 62, 18251−18262

SUPPLEMENTARY MATERIAL

Understanding the effect of asphaltenes and wax inhibitors on wax crystallization by improved NMR techniques

George Claudiu Savulescu[1] (george.c.savulescu@ntnu.no*) Sébastien Simon[1], Geir Sørland[1,2], Gisle Øye[1]

[1]: Ugelstad Laboratory, Norwegian University of Science and Technology, 7491 Trondheim, Norway

[2]: Anvendt Teknologi AS, Munkvollvegen 56, 7022 Trondheim, Norway

email: george.c.savulescu@ntnu.no

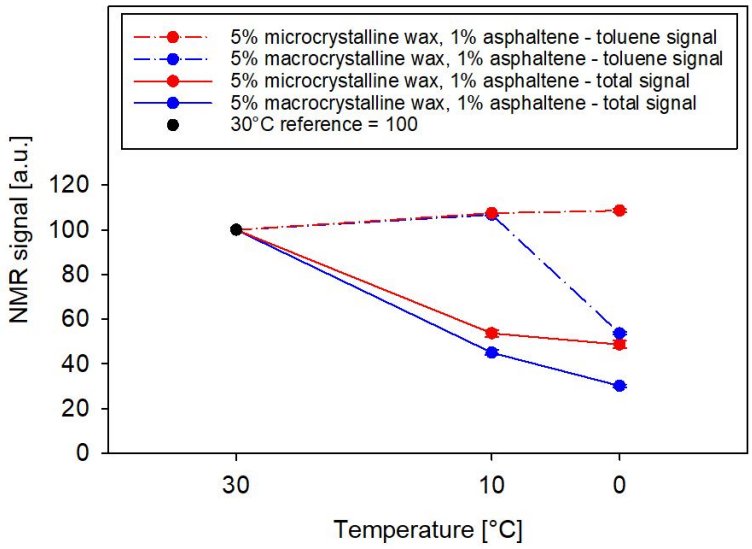

Figure S1a: Evolution of toluene signal and of total signal for 5% microcrystalline wax, 1% asphaltene and 5% macrocrystalline wax, 1% asphaltene in deuterated toluene

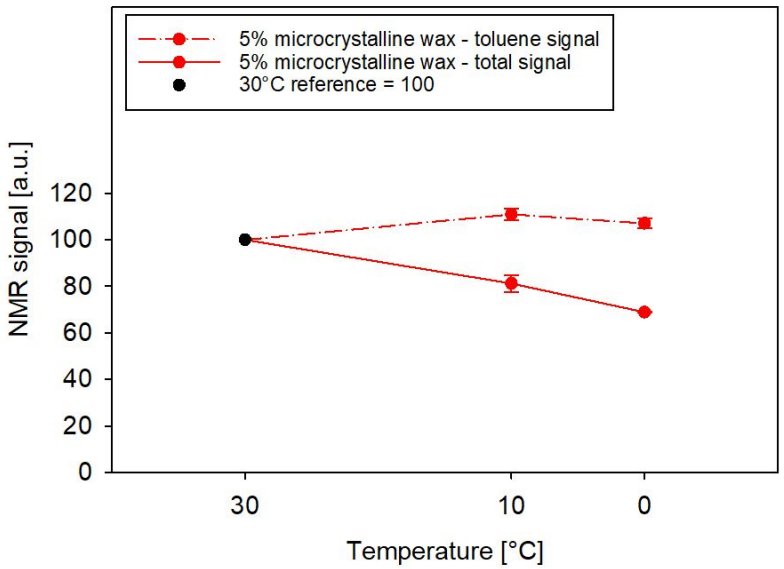

Figure S1b: Evolution of toluene and total signal for 5% microcrystalline wax in deuterated toluene

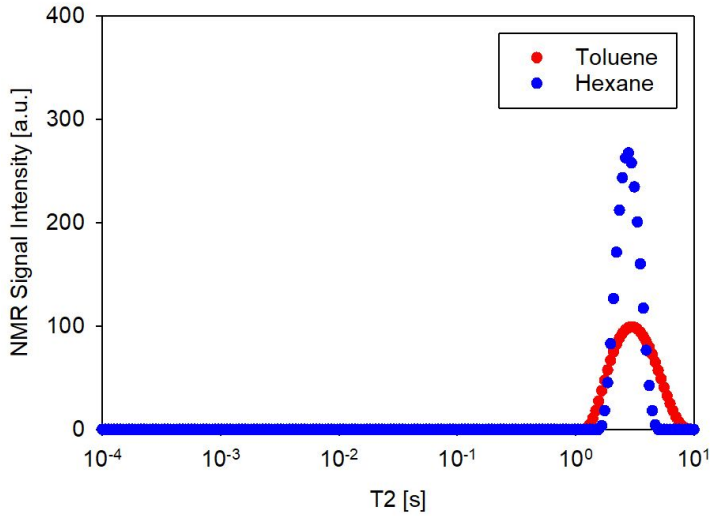

Figure S2: Relaxation time distribution in liquid domain for toluene and n-hexane

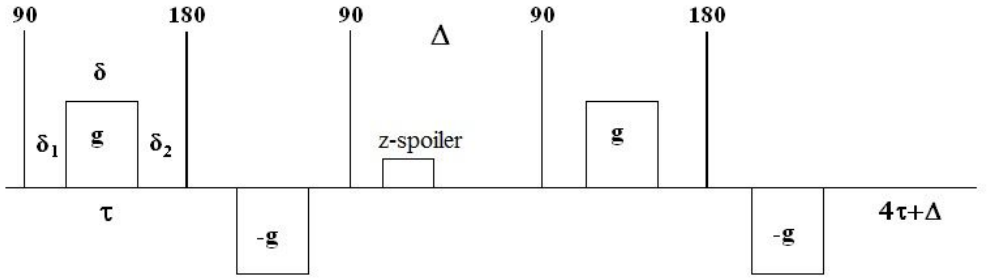

Figure S3: Pulsed field gradient sequence used for diffusion coefficient measurements

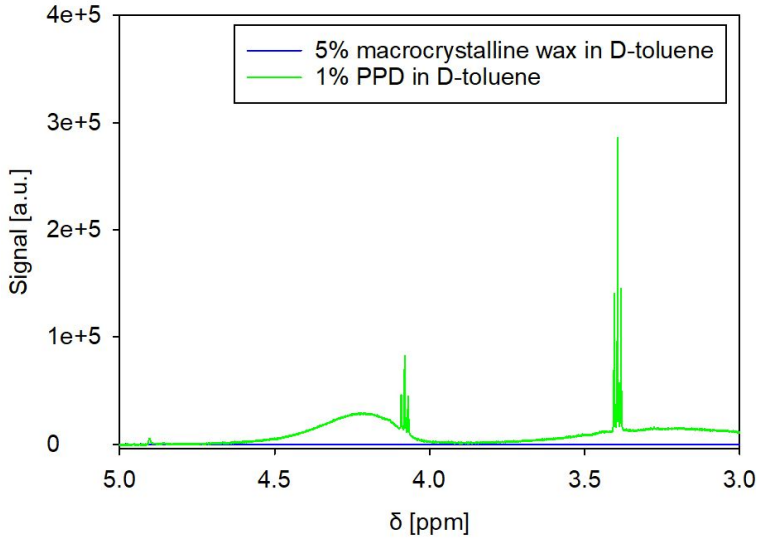

Figure S4: Slice from 5 ppm to 3 ppm on ^{1}H NMR spectrum for 1% PPD in deuterated toluene and for 5% macrocrystalline wax in deuterated toluene

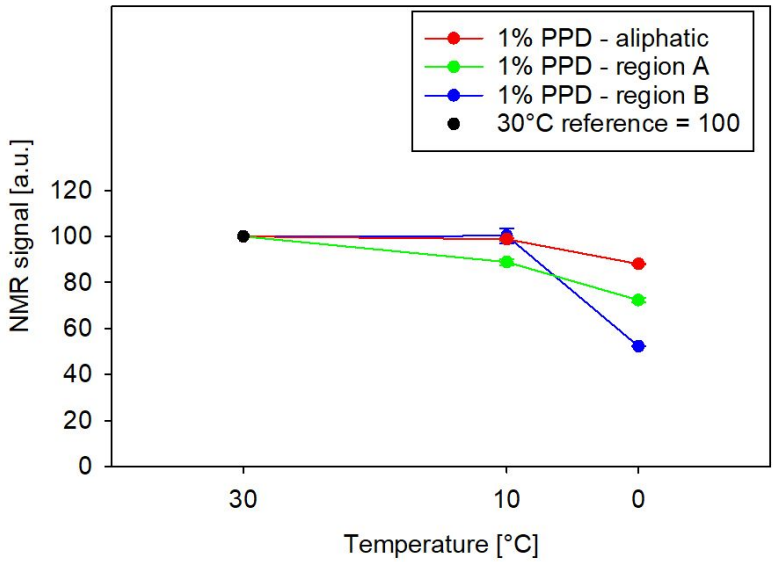

Figure S5: Variation of signal with temperature for PPD-specific peaks A, B and for the aliphatic PPD peak in 1% PPD in deuterated toluene. The value at 30°C is fixed at 100 for all systems, while the values at 10°C and 0°C are normalized accordingly.

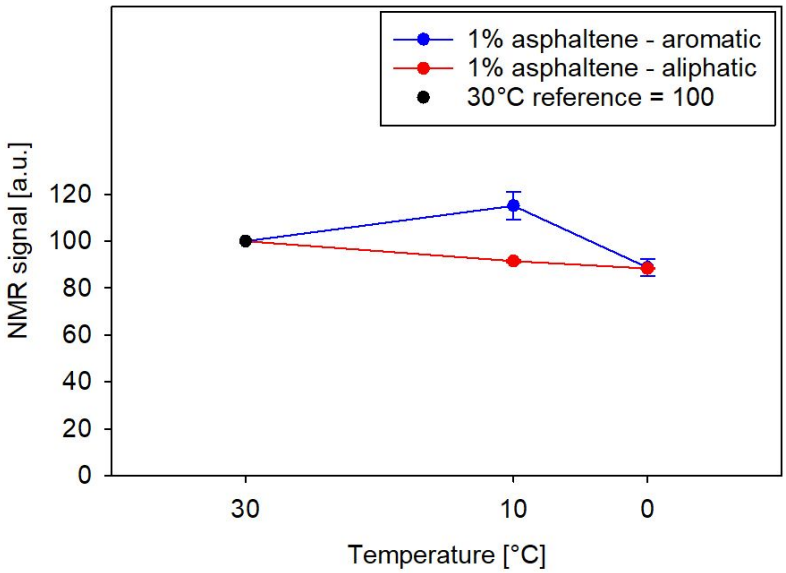

Figure S6: Variation of signal with temperature for aromatic (asphaltene-specific) and aliphatic peaks for 1% asphaltene in deuterated toluene. The value at 30°C is fixed at 100 for all systems, while the values at 10°C and 0°C are normalized accordingly.

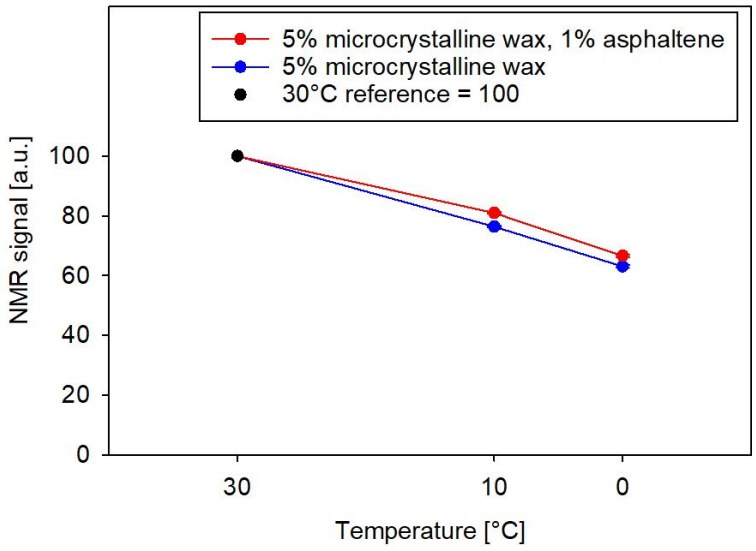

Figure S7: Variation of signal of aliphatic peak with temperature for 5% microcrystalline wax and 5% microcrystalline wax with 1% asphaltene, both in deuterated toluene. The value at 30°C is fixed at 100 for all systems, while the values at 10°C and 0°C are normalized accordingly.

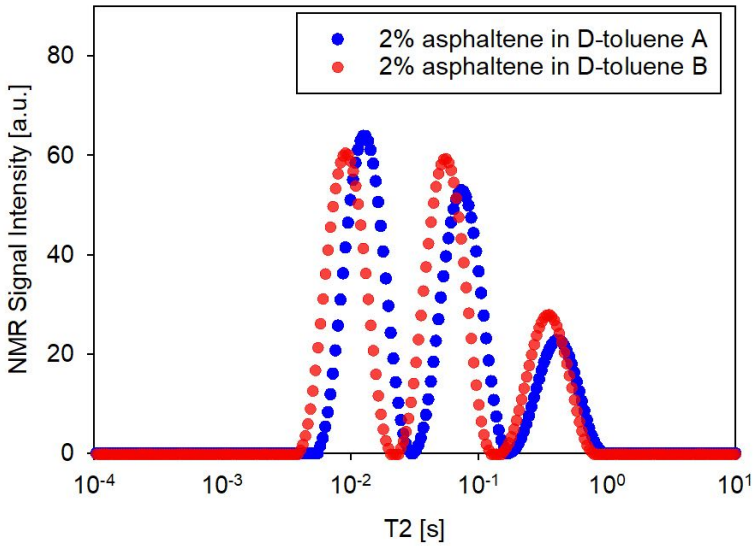

Figure S8: Relaxation time distribution in liquid domain for 2% asphaltene in deuterated toluene. A represents the first scan and B represents the reproducibility scan.

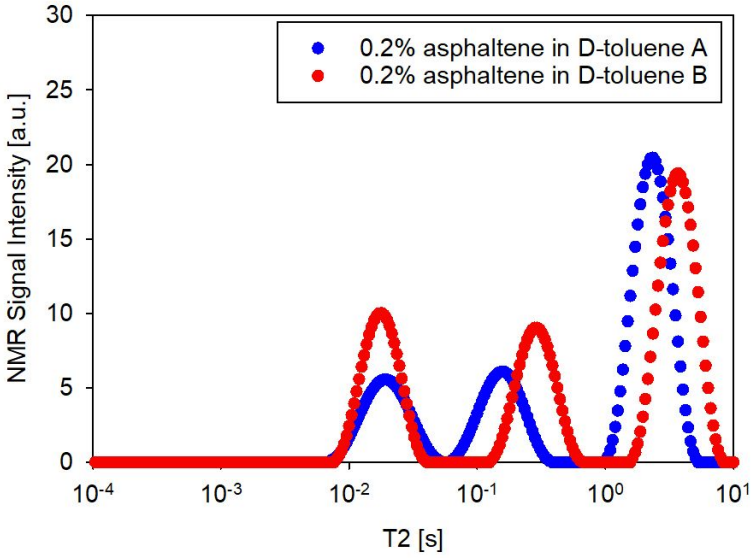

Figure S9: Relaxation time distribution in liquid domain for 0.2% asphaltene in deuterated toluene. A represents the first scan and B represents the reproducibility scan.

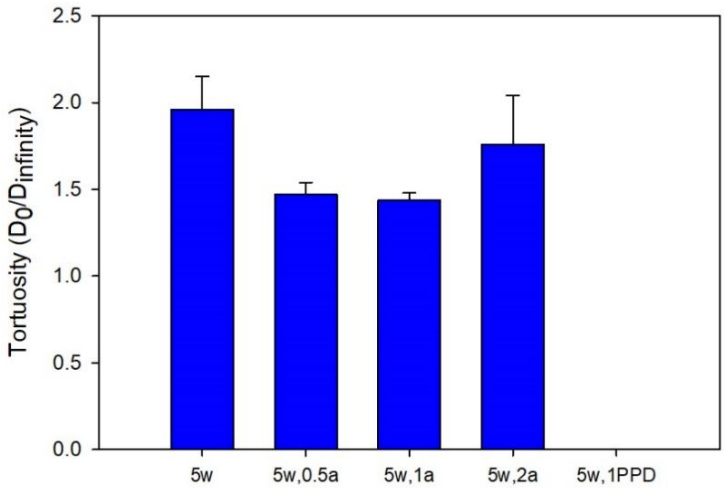

Figure S10: Tortuosity values for wax, wax-asphaltene and wax-PPD systems in toluene at 10°C

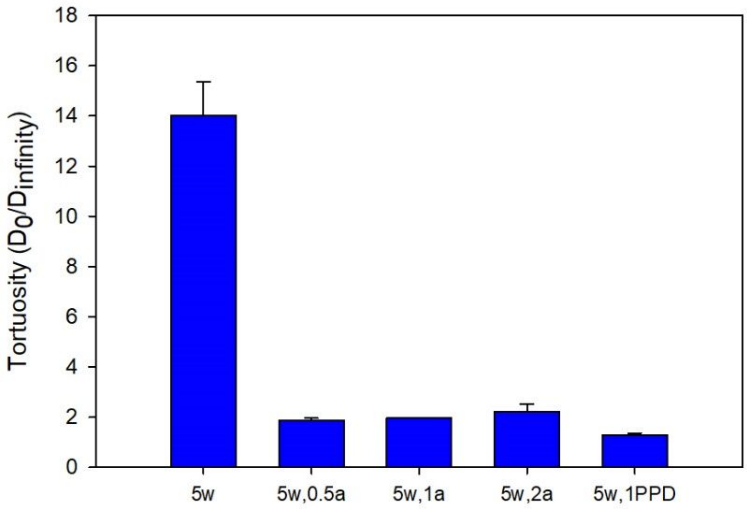

Figure S11: Tortuosity values for wax, wax-asphaltene and wax-PPD systems in toluene at 0°C

Paper III (awaiting publication)

Alterations in paraffin wax crystal networks induced by asphaltenes and pour point depressants, investigated by atomic force microscopy

Paper IV

Novel NMR techniques to assess the wax precipitation evolution in crude oil systems

energy&fuels

pubs.acs.org/EF

Article

Novel Nuclear Magnetic Resonance Techniques To Assess the Wax Precipitation Evolution in Crude Oil Systems

G. C. Savulescu,* S. Simon, G. Sørland, and G. Øye

Cite This: *Energy Fuels* 2023, 37, 291−300

Read Online

ACCESS | Metrics & More | Article Recommendations | Supporting Information

ABSTRACT: Wax crystallization in cold environments constitutes one of the main causes for flow assurance problems during oil production. Several techniques, such as differential scanning calorimetry (DSC) or gas chromatography/mass spectroscopy (GC/MS), are currently the established methods for the quantification of wax precipitation. Low-field nuclear magnetic resonance (NMR) techniques have seldom been used for the investigation of wax precipitation, despite early studies showing their ability to identify the rate of precipitation. This paper highlights three NMR methods, adapted for the purpose of wax crystallization quantification in crude oil systems. The proposed methods are based on free induction decay (FID) and Carr−Purcell−Meiboom−Gill (CPMG) sequences. Both allow for the quantification of a signal that is proportional to the non-crystalline wax content, while FID data can also be used for the computation of the crystalline wax component in systems with a sufficiently high wax content. DSC is also used as a reference method for wax content quantification. Model system analysis demonstrates consistency between the three methods in toluene-based wax solutions and also highlights a thorough comparison between macro- and microcrystalline waxes. Similar results are obtained with the four methods for crude oils with a high wax content, and a relevant comparison between different systems can be achieved for oils with wax concentrations as low as 2% at 0 °C. Overall, the determination of the solid content with FID represents an improved, more reliable method, which can be utilized during the creation of more robust flow assurance methods.

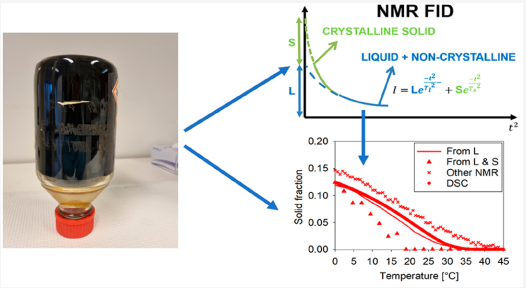

1. INTRODUCTION

Paraffin waxes are components of crude oil consisting of alkanes with variable chemical structures, normally with carbon chains between C_{20} and C_{100}.[1] Wax precipitation occurs in fluid environments at temperatures below the wax appearance temperature (WAT) and has negative effects on flow assurance during crude oil production. For example, the continuous flow might be interrupted by wax deposition and the resulting increase in fluid viscosity, while the restart of pipelines might be delayed by wax gelation.[2] Recently, the precipitation of waxes associated with the loss of gas and the gasoline fraction has been claimed to be involved in the unusual composition of some waxy crude oils.[3]

When the temperature is decreased, wax nucleation is delayed by a time lag required to overcome the shift from steady-state conditions. This delay depends upon the cooling rate,[4] and thus, the observed precipitation temperature with dynamic temperature ramping is usually lower than the actual precipitation temperature. Decreasing the cooling rate to very low values is the only way to overcome this effect.

During the last phase of crystallization, gelation is usually encountered in systems with wax contents above a threshold, which normally lies between 1 and 2%.[5] The gel can behave differently as a function of the chemical composition, particularly the isomerization of the waxes. For example, macrocrystalline wax, consisting of lower molecular weight *n*-alkanes, with up to 40 carbon atoms, is expected to generate gels with a high yield strength as a result of larger and less compact crystal structures. Oppositely, microcrystalline wax, composed of high-molecular-weight (C_{40} and above) iso-alkanes and cycloalkanes, leads to the formation of gels with a lower yield strength as a result of more compact crystal structures with smaller crystal diameters, with a higher percentage of amorphous structures.[6] Wax crystal formation might also be stimulated by introduction of surfaces or surfaces already present in crude oils, such as asphaltene aggregates.[7,8]

The evolution of wax precipitation with temperature has been quantified by following wax precipitation curves (WPCs) using techniques such as differential scanning calorimetry (DSC) and, more recently, low-field nuclear magnetic

Received: September 30, 2022
Revised: November 24, 2022
Published: December 13, 2022

https://doi.org/10.1021/acs.energyfuels.2c03309
Energy Fuels 2023, 37, 291−300

resonance (NMR).[9,10] Although DSC is an established method for calculations of the wax content, significant challenges remain when it comes to the analysis of crude oil systems. This can be mainly attributed to the complex chemical composition of crude oils that generates uncertainties in placing the baseline when estimating the latent enthalpies and heat capacities. Various approaches have been proposed to overcome these barriers;[9,11,12] however, none of them managed to eliminate these uncertainties completely.

NMR approaches have rarely been used to determine WPC in crude oil systems. Pedersen et al. were the first to introduce low-field NMR for the analysis of wax precipitation in crude oils.[13] They correlated the NMR signal intensity with the amount of wax generated by a modified acetone precipitation method performed at −20 °C for 17 crude oils. Later, the procedure has been significantly extended through the analysis of the NMR free induction decay (FID) signal,[14,15] but robust algorithms for calculation of the solid content from the NMR signal are still lacking.

In addition to the FID approach, an adapted Carr−Purcell−Meiboom−Gill (CPMG) sequence has been used to characterize model wax solutions in the presence of pour point depressants (PPDs) and asphaltenes.[16,10,17] Ruwoldt et al. compared the WPC generated with CPMG and DSC, respectively, and found that similar trends are achieved.[16] The most recent improvement was achieved by Savulescu et al., who adapted the CPMG sequence to wax precipitation curves in complex wax−asphaltene model systems.[10]

This study presents an improved NMR FID method combined with a novel algorithm for more accurate computations of the content of crystalline solids in crude oils. This resulted in higher resolution and less uncertainty of the wax precipitation curves compared to a standard computing algorithm used for FID data. Furthermore, wax precipitation curves were determined by NMR CPMG and DSC for comparison. Some weak points were identified for the latter method, and improvements were proposed.

2. EXPERIMENTAL SECTION

2.1. Materials. The solvents used in this study were deuterated toluene (anhydrous, 99.6% deuterated) and (hydrogenated) toluene (anhydrous, 99.8%) from Sigma-Aldrich, Norway. Macrocrystalline wax (coded 5405) and microcrystalline wax (coded 3971) were provided by Sasol, Germany. The composition and properties of the wax samples were presented previously.[16] Six crude oil samples from the Norwegian continental shelf were used. The densities of these oils at 30 °C and their elemental analysis are presented in Table 1. For crude oils 1−3, the elemental composition was determined by analysis at SGS France, while for crude oils 4−6, previously determined values were used.[18−20] For crude oils 1 and 3, the densities were measured with an Anton Paar DMA 5000 densiometer, while for crude oils 2 and 4−6, previously determined values were used.[18−20] All concentrations in this study are in weight percentages (wt %).

Table 1. Densities for Each Selected Crude Oil

crude oil	density (g/mL)	carbon content (%)	hydrogen content (%)	nitrogen content (%)	oxygen content (%)	sulfur content (%)
1	0.866	86.4	12.59	0.05	0.31	0.26
2	0.853	86.6	13.14	0.13	0.19	0.18
3	0.875	86.4	12.47	0.23	0.34	0.48
4	0.929	86.5	11.72	0.29	0.62	0.84
5	0.844	85.68	13.24	0.14	0.67	0.26
6	0.816	86.34	13.1	0.1	0.61	0.05

It can be noticed in Table 1 that the oxygen content is higher than the nitrogen and generally sulfur contents for the investigated oils. This observation can also be found for North Sea crude oils in the literature.[21]

2.2. Sample Preparation. Solid waxes were used as a reference in the NMR FID measurements. Wax solutions with varying concentrations (5−15%) were prepared by dissolution of wax in toluene or deuterated toluene. The systems containing macrocrystalline wax were heated at 60 °C for 1 h and shaken thoroughly. Because the systems containing microcrystalline wax have a higher WAT, they were heated at 80 °C for 1 h and shaken thoroughly. NMR FID and DSC measurements were carried out on these model wax systems. The crude oils were all heated at 80 °C and shaken thoroughly before the experiments. Crude oil 2 was also spiked with macrocrystalline wax and heated at 80 °C. NMR FID, NMR CPMG, and DSC measurements were carried out on these systems.

2.3. NMR Measurements. All NMR experiments were conducted on a low-field (21 MHz) NMR spectrometer, which was supplied by Anvendt Teknologi AS, Norway. The measurements were performed with 3 g of the respective samples in the NMR tubes. For the FID measurements, two independent parallels were performed for the model wax systems, while three independent parallels were performed for the crude oil systems, to ensure a higher degree of accuracy because these samples have variable, unknown chemical composition. For the CPMG measurements, two independent parallels were performed to ensure reproducibility. This method was primarily used on crude oils because its reliability for model systems has been investigated previously.[10]

2.3.1. NMR FID Analysis. The relaxation delay was measured 10 s after a 90° pulse width of 8.6 μs, and the signal was followed from 13 μs (the first point measurable with the NMR instrument) to 268 μs, at 1 μs intervals. The same acquisition was repeated 64 times. The average temperature ramping was fixed at 0.2 °C/min, which allowed for measurements at 19−20 temperature steps.

The FID analysis is based on the difference in relaxation speed for protons in a crystalline and non-crystalline phases. The total intensity of the signal plotted against the square of the acquired time is assumed to follow a bi-Gaussian equation

$$I \approx \mathbf{L}e^{-t^2/T_1^2} + \mathbf{S}e^{-t^2/T_s^2} \quad (1)$$

where **L** represents a parameter proportional to the amount of protons in the non-crystalline phase, T_1 represents the modified FID relaxation time for the non-crystalline phase, **S** represents a parameter proportional to the amount of protons in the crystalline phase, T_s represents the modified FID relaxation time for the crystalline phase, and t is the acquisition time.[22−24] The modified relaxation time of the FID signal is limited by the T_2 relaxation time and can be correlated to it, following a relationship dependent upon the analyzed system.

For each temperature step, eq 1 was fitted to the first 80 points (i.e., from 13 to 92 μs) of the raw NMR signals using the *exp2* function in MATLAB 2021b. If the system was in the non-crystalline state or if a second exponential was not identifiable as a result of method limitations, a one-exponential fit was performed, using the *exp1* function in MATLAB 2021b. Extrapolation of the exponential functions to $t = 0$, illustrated in Figure 1, gave the signal proportional to the number of protons in the crystalline and non-crystalline phases, respectively, corresponding to **S** and **L** in eq 1. The R^2 values were consistently higher than 0.985 at 0 °C for both the two- and one-exponential fits.

Two approaches were used to calculate the fraction of solid-phase protons (f):

(1) "FID exponential separation" method: In this case, f is calculated by inserting the **L** and **S** values resulting from the biexponential fitting procedure above in the following equation:

$$f = \frac{\mathbf{S}}{\mathbf{S} + \mathbf{L}} \quad (2)$$

https://doi.org/10.1021/acs.energyfuels.2c03309
Energy Fuels 2023, 37, 291−300

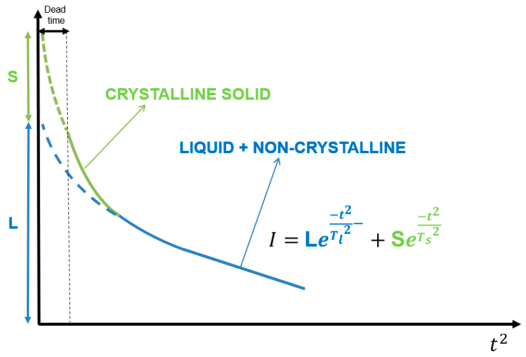

Figure 1. Schematic representation of the two-exponential separation for each NMR curve at a selected temperature (y axis) plotted as a function of the square of the acquisition time (x axis).

Two main challenges arise with this approach. One is accurate separation of the crystalline and non-crystalline regions. This is illustrated in Figure 2, showing the FID signal of pure macrocrystalline wax at 45 and 0 °C. At 0 °C, there is very little non-crystalline wax and there is a marked transition between the region with a low slope at long acquisition times, corresponding to non-crystalline wax, and the region with a high slope at short acquisition times, corresponding to crystalline wax. At 45 °C, on the other hand, the change from the non-crystalline to crystalline region is more gradual. This was attributed to the fact that the non-crystalline phase comprises parts with different mobilities. Higher mobility regions with lower slopes are noticed at higher acquisition times, while lower mobility regions with higher slopes are noticed at lower acquisition times. This results in larger errors for **L** and **S** when using the biexponential fitting. A higher number of exponentials could be theoretically used to separate states with different mobility, but this is not achievable with the results from low-field NMR, because the variation in modified relaxation time is not high enough.

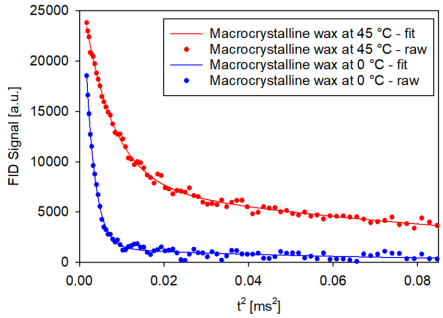

Figure 2. FID signal fitting with two exponentials for macrocrystalline wax at 45 and 0 °C.

The other main challenge with the approach is the dead time. This is illustrated in Figure 3, showing the FID signals and the corresponding two-exponential fits for crude oil 1 at 45 and at 0 °C. It is seen that the dead time limits the number of points obtained for the crystalline component in crude oil systems. Although there was a second exponential at low acquisition times when the temperature decreases to 0 °C, there were only about 7 points available for fitting this additional exponential. This decreased the certainty with which the extrapolated crystalline component was calculated. Crude oil 1 has the highest wax content among the analyzed oils, and thus, the degree of certainty for extrapolation decreases further for the rest of the oils.

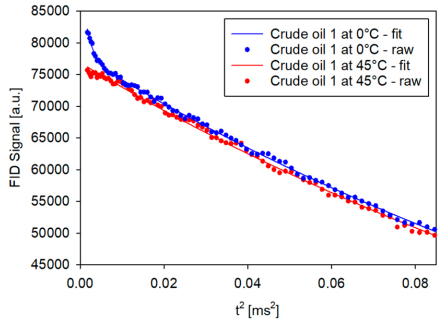

Figure 3. FID signal fitting at 0 °C for crude oil 1.

(2) "FID non-crystallized signal" method: This novel method is proposed in this work to avoid the above challenges when calculating the percentage of protons in the crystalline state. This approach focuses exclusively on the non-crystalline component **L**. Here, toluene was used as a reference to account for the signal change as a result of the variations in the repartition of energy of hydrogen atoms with the temperature.[25]

The drop in the fraction between the non-crystalline component in the system (L_T) and the non-crystalline component of toluene ($L_{\text{toluene},T}$) tracks the percentage of protons in the non-crystalline phase that is lost from the non-crystalline region as the temperature decreases from 45 °C to T. However, if the percentage of protons in the crystalline solid form (f) is higher than 0 at 45 °C (as for pure solid wax in Figure 2 for example), one should add the percentage of crystalline solid at 45 °C ($f_{45\ °C}$) because the normalized non-crystalline signal evolution only quantifies the drop from 45 °C onward. To find the crystalline solid value at 45 °C, the first proposed calculation method based on the two-exponential separation is used. The approach is summarized in the following equation for the fraction of protons in the crystalline solid state:

$$f = f_{45\ °C} + \frac{\frac{L_{45\ °C}}{L_{\text{toluene},45\ °C}} - \frac{L_T}{L_{\text{toluene},T}}}{\frac{L_{45\ °C}}{L_{\text{toluene},45\ °C}}} \quad (3)$$

A method presented by Kane et al.,[15] involving two assumptions, was used in both approaches to transform the fractions of crystalline solid protons into the weight fractions of the solid. The first assumption is that the density of the liquid remains constant during wax crystallization. To verify this, the density of macrocrystalline wax was extrapolated to be 0.792 g/mL from a curve with the inverse of the density plotted as a function of the mass fraction for different concentrations of wax (0, 1, 2.5, 5, 7.5, and 10%) in toluene. The crude oils had densities between 0.81 and 0.93 g/mL (Table 1). All of these densities are less than 20% higher than the estimated density of macrocrystalline wax, and because the maximum weight percentage of wax at 0 °C was found to be about 15% in the analyzed crude oils, it was considered that the actual density of the liquid in the crude oils would increase by a maximum of 3%, which is negligible. The second assumption is that the density and proton density of the precipitated solid are constant. This assumption might fail if asphaltenes or resins co-precipitate with the wax, because they have different proton densities and densities. In some cases, there might also be a significant difference between the density of the crude oil wax and the model wax used here. However, these parameters cannot be quantified, generating a limitation for this technique.

Two parallels were performed for the calibration with toluene, and both were independently used for solid fraction determination. For the analyzed systems, the f value for each parallel represents the average between the two solid fractions computed with each of the

https://doi.org/10.1021/acs.energyfuels.2c03309
Energy Fuels 2023, 37, 291−300

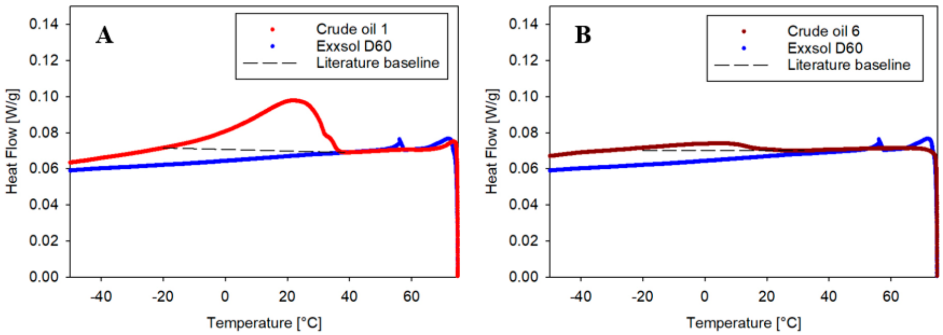

Figure 4. Baseline fitting using Exxsol D60, relative to baseline fitting using the method suggested by Chen et al. in the literature:[11] (A) crude oil 1 (high wax content) and (B) crude oil 6 (low wax content).

two parallels from toluene calibrations. The solid fraction presented in the graphs represents the average between the two or three parallels for each system of interest. For the solid fraction calculation process with FID, the following assumptions were made: constant density of the non-crystalline component of crude oil with the temperature and constant density equal to that of macrocrystalline wax 5405 from Sasol for the crystalline component in crude oils.

2.3.2. NMR CPMG Analysis. A CPMG sequence was used to acquire T_2 distributions,[26] following the procedure presented previously.[10] The recycle delay is 5 s, while the interecho spacing was selected for two regions. For the model systems, these sequence parameters were the same as presented previously.[10] For crude oil systems, on the other hand, they had to be adjusted, because the crude oils have a different distribution of the liquid T_2 region. In this case, there is a first region with τ_1 of 115 μs and 1000 echoes and a second region with τ_2 of 600 μs and 5000 echoes. These were selected to account for large signals in the long T_2 region in crude oil systems. T_2 distributions were generated from the multiexponentially decaying curve, using the one-dimensional inverse Laplace transform.[27] The intensity of T_2 represents a quantitative measure of the liquid signal with the temperature, which allows for the calculation of the lost solid content. Several algorithms in MATLAB 2021b were used to further process the data and separate the signal intensities in different T_2 areas, accordingly.

Stepwise temperature scanning was used from 45 to 0 °C, leaving the system at a constant temperature during signal acquisition at each temperature point. The ramping rate was 0.2 °C/min to ensure stable systems during the signal acquisition. The number of scans was set at a conventional value of 16, which allowed for measurements at 68 temperature steps.

The temperature inside the NMR was controlled with an air flow,[10] and calibration with hexadecane showed no thermal delay associated with the air flow. The average of two calibrations allowed to correct for the change in signal generated by the different repartitions of hydrogen atoms at different energy levels and quantified by the Boltzmann factor.[25] The wax content is calculated afterward using the procedures described previously.[16,10]

2.3.3. Choice of the NMR Sequences and the Intensity of the Magnetic Field. The chosen low-field NMR techniques, FID and CPMG, have significant differences that may impact the way results are acquired. The FID does not correct for magnetic field inhomogeneities, because it attenuates with a phase that is dependent upon fluctuations in the magnetic field experienced by the molecules. This is caused by either inhomogeneities in the external field or local fluctuations caused by the sample itself. In a solid, the local fluctuations are not changing significantly in time (long correlation time), while in a liquid, it is almost averaged out, i.e., fast diffusion limit. Thus, T_2 is much shorter in a solid than in a liquid, because the correlation time is much shorter in the liquid. Also, the external magnetic field inhomogeneities cause the liquid component to have a modified relaxation time, T_2*, of just a few milliseconds, while the true T_2 is of the order of seconds.

CPMG, on the other hand, does correct for external magnetic field inhomogeneities, and this affects the liquid component more than the solid component. For the solid component, the relaxation mechanism is more strongly coupled to the sample itself, because dipole−dipole coupling between molecules becomes important as a result of the long correlation time. This is the most important relaxation mechanism in the solid wax. The chosen method, however, only detects the liquid relaxation of the sample, which will be in this case determined by the true T_2 of the sample. Nonetheless, the noise in crude oil systems with complex chemical composition and proton species could reach high levels, and that is why this paper assesses whether CPMG or FID provides more accurate results with the selected instrument.

Low-field NMR was selected after initially assessing the potential of high-field NMR for the analysis of the desired systems. As an advantage, high-field NMR has a much better signal-to-noise ratio. However, as a result of chemical shifts, it is difficult to produce a CPMG decay properly with high-field NMR, and this prevents the accurate quantification of T_2 relaxation times. CPMG has real-time acquisition, and it will be the only component that is on resonance that will form spin echoes of a constant detection phase. Those molecules in a distance from the resonance frequency will be out of phase with a value dependent upon the interecho spacing, the τ value, and the chemical shift value. Thus, it can be completely out of phase with the spin echo on resonance, and this alters the CPMG acquisition. One could of course run spin echoes one by one and then analyze the spectrum each time, but this will be very time-consuming. In a low-field system, there is no chemical shift information available because the external field is weak and inhomogeneities prevent chemical shift resolution. Thus, it is much more unreliable to determine CPMG at high field using a superconducting magnet. Also, the sample size and price of the system favor the low-field instrumentation.

2.4. DSC. DSC measurements were carried out on a Q2000 model from TA Instruments. The instrument was calibrated by measuring the melting heat and temperature of pure indium. For each experiment, 10−25 mg of sample was weighed into Tzero hermetic aluminum pans and sealed hermetically. The weight of the pans was measured before and after the experiment to ensure that no solvent loss had occurred. Prior to the measurements, the samples were left isothermally at 80 °C for 10 min to ensure stabilization above the WAT. Initially, a constant cooling rate of 0.2 °C/min was used to keep the experimental conditions similar to the NMR experiments. However, it was impossible to set the baseline and identify the peak for several crude oils at such a low cooling rate because the curve flattened. Therefore, the experimental cooling rate was finally set to 2 °C/min. The temperature range was from 75 to −70 °C. Two parallels were performed for all systems.

https://doi.org/10.1021/acs.energyfuels.2c03309
Energy Fuels 2023, 37, 291−300

2.4.1. DSC Data Analysis. Determination of the baseline is essential for calculating the solid content from DSC measurements. Several challenges were encountered when applying different methods from the literature on crude oil systems. Pedersen et al. set the baseline as a straight line from the wax precipitation onset to the point where the heat flow curve flattens at low temperatures (down to −140 °C in their study), where all of the components of crude oil have stopped precipitating.[12] A drawback of this method is that the baseline is assumed to be a straight line, which is thermodynamically inaccurate. From a practical point of view, however, the instrument used in this study only allowed for measurements down to −70 °C, where the heat flow curves still declined. Coto et al.[9] introduced a baseline method based on fitting the liquid region of the heat flow curve at temperatures above the WAT and at temperatures below the end of crystallization into a second-order equation, dependent upon the temperature, following the model of the heat capacity for liquids. Improved models allowing for variations of latent heat with the molecular weight and using second-order equation fitting for the heat capacity were also suggested. Neither of these approaches were applicable for measurements where the heat flow did not flatten.

Chen et al.[11] set the baseline for crude oils as a straight line from the WAT to a temperature of −20 °C and calculated the wax content by correlating the enthalpy peak with the wax content in crude oil determined by a modified acetone precipitation method performed at −20 °C. This specific temperature is the temperature generally mentioned in the standard industrial method.[28] This approach is illustrated in Figure 4 for crude oils used in this study with high (A) and low (B) wax contents. The excess heat is clearly sensitive to the placement of the baseline, especially at low wax contents with less defined heat flows. Using this approach to calculate the wax content in the crude oils gave a loss in the peak as high as 70% compared to the NMR approaches because waxes were still precipitating at −20 °C.

A method using reference measurements of Exxsol D60 to set the baseline was therefore developed. Exxsol D60 was chosen as reference compound for several reasons: It is a mixture of alkanes and isoalkanes with a density similar to the density estimated for macrocrystalline wax (0.792 g/mL); the melting point is between −60 and −70 °C, which is well below the WAT; and the slope of the heat flow was similar to that for the crude oils studied here. Notably, these heat flow curves were modified by adding a constant term (Table S1 of the Supporting Information) to all data points, so that they would overlap with the heat flow curves for the various crude oils above the WAT. The resulting curves are shown in Figure 4 together with data for a crude oil with high (A) and low (B) wax contents. The excess peak was calculated by summing the heat flow from the wax precipitation onset to −20 °C, where all of the wax precipitated.[11] The percentage of the crystallized wax was then calculated as the ratio between the heat of the excess peak per gram and the standard latent heat of paraffin wax per gram. A value of 200 J/g was used for the latter,[29,30] which is an estimated value that might deviate in crude oils where the exact chemical composition is unknown. Furthermore, it was assumed that the specific crystallization heat did not change with the temperature (i.e., the excess heat and the mass of precipitated wax are constantly proportional).

3. RESULTS AND DISCUSSION

The presentation of results starts from selected model wax systems in air and toluene and progresses toward real, crude oil systems. The analysis is based on the comparison of wax precipitation curves from each of the four methods. Weaknesses and advantages of each technique were identified alongside the errors and inaccuracies as a result of assumptions.

3.1. Quantification of Solid Fractions in the Various Wax Systems. *3.1.1. Pure Waxes.* FID analysis of pure macro- and microcrystalline waxes was performed to verify the experimental approach and assess the two FID methods (eqs 2 and 3) for computing the solid fractions. Figure 5 presents the solid crystalline fractions of the pure macro- and microcrystalline waxes. The solid amounts are similar for both calculation methods, showing that both approaches were accurate for solids with uniform chemical composition. Furthermore, the amount of crystalline solid increased from 77 to 96% for macrocrystalline wax and from 52 to 83% for microcrystalline wax when the temperature decreased from 45 to 0 °C. Moreover, the higher amount of crystalline solid indicated a larger and stronger crystal structure for macrocrystalline wax, as explained in the Introduction. This has also been reported by others.[6]

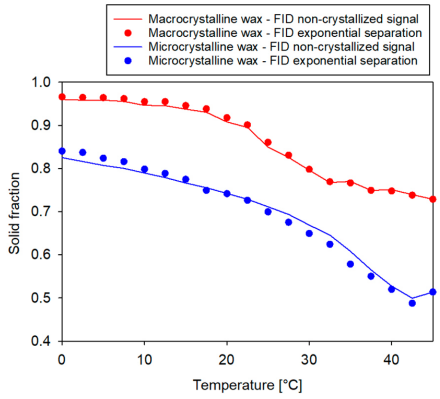

Figure 5. Solid fraction evolution with the temperature for pure wax systems, as calculated with the two proposed computation methods from FID data.

3.1.2. Wax in Toluene Systems. Figure 6 shows the solid crystalline fraction determined by the various techniques for 15% macrocrystalline wax in hydrogenated toluene. An overall trend of increasing solid fractions with decreasing temperature was observed in all cases. However, differences between the experimental techniques and between the FID computing methods emerged. In comparison of the experimental techniques, the wax precipitation curves were similar for the CPMG and DSC measurements and the onset of wax precipitation was detected at a lower temperature compared to the FID measurements. This difference could be explained by the higher cooling rate for DSC,[4,31,32] but because the

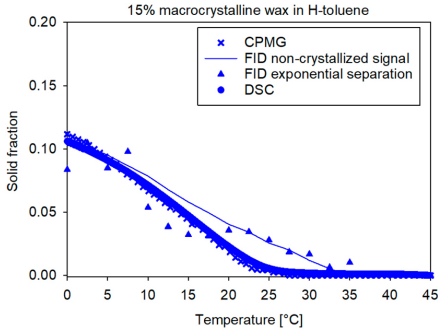

Figure 6. Solid fraction evolution with the temperature for 15% macrocrystalline wax in hydrogenated toluene, with all proposed methods. For CPMG, the value obtained by Savulescu et al.[10] is used.

https://doi.org/10.1021/acs.energyfuels.2c03309
Energy Fuels 2023, 37, 291−300

cooling rate was the same in the CPMG and FID measurements, another factor is most likely dominating. Hence, the presence of amorphous phases in the lower mobility part of the non-crystalline region, specific to the nature of dissolved wax in each system, may affect the exponential separation process and may be accounted for as crystalline solid, leading to an overestimation of the crystalline content at the first stage of crystallization. Nonetheless, between 25 and 35 °C, the wax content determined with FID remains within the maximum absolute error of the method (approximately 2−3%). As temperature decreases, most of these phases are likely to change into crystalline wax, and as the solid exponential becomes stronger, the uncertainty for FID decreases and the gap between FID and CPMG/DSC reduces. In comparison of the two calculation approaches for the FID measurements, the "FID non-crystallized signal" method gave a quasi-linear wax precipitation curve that converged with the DSC and CPMG curves at low temperatures. The "FID exponential separation" method, on the other hand, gave a less even and more disordered curve. This can be associated with the increased signal from the non-crystalline region when going from pure waxes to waxes in hydrogenated toluene, because at least 85% of the mass will generate a signal in this region. The solid exponential thus becomes more difficult to separate and is more likely to extend into the dead time.

To assess the accuracy of the NMR FID approach, wax precipitation was compared for 15% macro- and microcrystalline waxes in both hydrogenated toluene (Figure S1 of the Supporting Information) and deuterated toluene (Figure S2 of the Supporting Information). In the latter solvent, the entire NMR signal was due to the wax and improved the determination of the solid fractions.

The sensitivity of the NMR FID approach was assessed by following the precipitation of solid wax for 5, 10, and 15% wax solutions (Figure S3 of the Supporting Information). A crystalline solid component could be determined at 15 and 10% wax but no longer at 5% wax for the "FID non-crystallized signal" method. This was probably due to a shift of the crystalline solid decay into the dead time as the wax content decreased (Figure S4 of the Supporting Information), making quantification impossible.

3.1.3. Crude Oils with a High Wax Content. Only crude oil 1 had a sufficiently high wax content to be detected at low temperatures by all of the approaches. The wax precipitation curves are shown in Figure 7 and are similar for the DSC and NMR FID measurements using the "FID non-crystallized signal" method, while the CPMG measurements gave a somewhat higher solid content in the entire temperature range. An explanation for this can be that the CPMG signal is only detected in the liquid region defined by a fixed T_2 range (10^{-3}−10^{1} s), while the entire liquid and solid signals are detected in the FID method. Thus, the CPMG approach will count both liquid and solid phases outside the T_2 range as solid, while only the solid fraction will account for the FID non-crystallized method. The FID exponential separation method, on the other hand, gave a lower onset temperature for the wax precipitation and generally lower amounts of solids, even though the difference from the other methods decreased as the temperature approached 0 °C, as a result of difficulties in separating two exponentials at the first few temperatures after the onset of crystallization and the presence of amorphous phases during ongoing precipitation, which alter the exponential separation process. Moreover, the detection limit for the method was 2−3% solid for crude oil 1, which is in accordance with what was observed in the model systems.

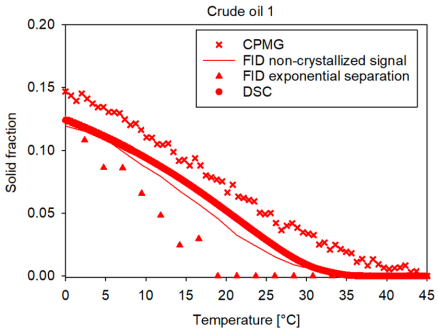

Figure 7. Solid fraction evolution with the temperature for crude oil 1, with all proposed methods.

To study the influence of chemical composition, 15% macrocrystalline wax was dissolved in crude oil 2. The amounts detected by the various methods at a given temperature were different from both crude oils 1 and 2 enriched with wax (Figure S5 of the Supporting Information). Furthermore, the detection limit for the FID exponential separation method was 6−7% solid in this case. This can be attributed to the difference in the chemical composition because the detected amounts might be dependent upon the nature of the wax crystals, specific to each system.

The presented methods and procedures cannot separate between macro- and microcrystalline wax. NMR FID/CPMG focuses on separating crystalline and non-crystalline phases in the crude oil. It is currently not possible to quantify the proportion of macro- and microcrystalline wax molecules in the crystallized phase.

3.1.4. Crude Oils with a Low Wax Content. The wax precipitation curves for the crude oils with a low (<10%) wax content are presented in Figure 8 for crude oil 3 and Figures S6, S7, S8, and S9 of the Supporting Information for crude oils 2, 4, 5, and 6, respectively. For these samples, it was not possible to separate two exponentials in the FID signal; therefore, no solid fractions were calculated with the FID exponential separation method. Furthermore, a low signal-to-noise ratio for CPMG measurements prevented calculations of

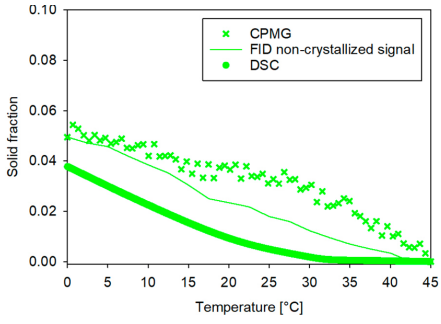

Figure 8. Solid fraction evolution with the temperature for crude oil 3, with all proposed methods.

https://doi.org/10.1021/acs.energyfuels.2c03309
Energy Fuels 2023, 37, 291−300

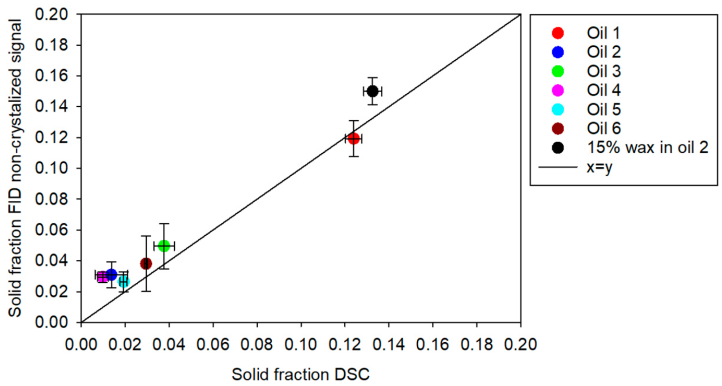

Figure 9. Solid fraction with the FID non-crystallized signal calculation technique as a function of the solid fraction with DSC at 0 °C.

Table 2. Average Errors during Reproducibility at 0 °C with NMR FID, NMR CPMG, and DSC for Model and Real Systems[a]

system	CPMG (wt %)	DSC (wt %)	FID exponential separation (wt %)	FID non-crystallized signal (wt %)
crude oil 1	14.68 ± 0.39	12.40 ± 0.37	12.41 ± 0.18	11.78 ± 1.18 (1.36)
crude oil 2	ND	1.37 ± 0.74	ND	3.09 ± 0.83 (2.19)
crude oil 3	4.94 ± 0.05	3.77 ± 0.46	ND	5.67 ± 1.47 (1.66)
crude oil 4	ND	0.98 ± 0.25	ND	2.95 ± 0.34 (1.46)
crude oil 5	3.52 ± 0.50	1.93 ± 0.16	ND	2.64 ± 0.64 (1.95)
crude oil 6	4.28 ± 0.40	2.95 ± 0.06	ND	3.81 ± 1.80 (3.20)

[a]ND = not detectable. The error bars represent the range of obtained values.

solid fractions for two of the samples (crude oils 2 and 4 in Figures S6 and S7 of the Supporting Information, respectively). In addition, it seems that the solid fraction did not plateau at 0 at the highest temperatures for crude oil 3 (Figure 8) as a result of the very low wax content in this crude oil associated with the uncertainties from instrumental noise issues.

Generally, the CPMG measurements gave solid fractions somewhat higher than for the other methods. However, the onset of wax precipitation and a quasi-linear precipitation pattern are similar to the FID non-crystallized signal method. The DSC measurements, on the other hand, give a lower precipitation onset temperature with an accelerating precipitation rate below 15 °C and lower solid fractions over the investigated temperature for all of the crude oil samples. The causes behind this can be higher cooling rates resulting in delayed precipitation and assumptions about constant heat capacity and proportionality between the amount of heat and the mass of solid, which might not be valid for wax systems with complex chemical composition, where the various latent heat and molecular mass profiles might differ in different regions.[29,30] Moreover, the wax content is sensitive to the baseline, as explained above. It should also be noted that uncertainties in each of the methods can give overlapping results. This is discussed further in the next section.

3.2. Evaluation of the Investigated Techniques. Figure 9 presents a comparison between the solid fraction determined with the FID non-crystallized signal method and DSC for crude oil systems at 0 °C. In most cases, the FID non-crystallized signal method gives somewhat higher wax contents than DSC, likely as a result of the assumptions and differences in the cooling rate discussed above and increases in relative values as the wax content in the oil decreases.

Table 2 shows the solid contents with errors at 0 °C determined for the crude oils by the various techniques. In all cases, the errors between two or three parallels are given, calculated using the average toluene calibration values for the FID non-crystallized signal method. For the latter approach, the error between the four parallels performed for toluene calibration was also considered. These errors are given in parentheses and correspond to the highest possible errors because the most and least favorable parallels were used for both the sample and calibration measurements.

The FID exponential separation method was not applicable for low wax content samples because a minimum solid content of about 2% is needed to distinguish two exponentials in the FID decay.

Determination of low wax contents was also challenging using the CPMG approach, mainly because of instrument noise. Furthermore, a high degree of noise resulted in considerable variations in the solid content from one temperature to another in several circumstances.

This left DSC and the FID non-crystallized method as the two approaches for determining a broad range of wax contents. DSC gave the lowest error (a maximum of 0.74 percentage points) but also included thermodynamic assumptions, assumption of similar chemical composition of the wax for all of the samples, and baseline determination using Exxsol D60 data. The FID non-crystallized signal method, on the other hand, is based on assumptions mainly related to exponential separation and signal-to-noise issues generated by the NMR instrument. Considering the error between parallels, the maximum error was seen at 1.8% for crude oil 6.

With the variation between parallels for the calibration with toluene taken into account, the error increased up to 3.2%. This is generated by the uncertainty in the ratio of the toluene

https://doi.org/10.1021/acs.energyfuels.2c03309
Energy Fuels 2023, 37, 291−300

liquid component at 45 °C and the toluene liquid component at 0 °C. For the four parallels performed for toluene, this ratio was within a 5% error for three cases and deviated up to 15% upward for one case, which causes a significant deviation when used to assess error. However, this error will cause the same effect on the computed solid fraction for all systems of interest. If the FID non-crystallized signal method is routinely used to characterize the wax content in crude oils, the accuracy should most likely be improved, especially for a low wax content. The uncertainties in the FID can be reduced by improving the signal-to-noise ratio, increasing the number of parallels, and advancement in instrumental accuracy.

The FID-based methods for computation of solid fractions can also be discussed in view of methods reported in the literature. A NMR FID method was, for example, standardized to calculate the solid fat content in various systems.[33,34] In this case, the non-crystalline and crystalline contents were separated as linear fractions (rather than using two- or one-exponential models), while a calibration factor, calculated using solid-containing standard samples, was used to account for the dead time.[15,35] This fails to account for the nature of the FID signal[24] and also generated a high degree of error because a linear fit cannot be applied at fixed time points.

Declerck et al. showed that this method was only suitable for fats with a certain chemical composition. In rapeseed and sunflower oils, for example, fats containing mostly α-polymorphs generated good results, while fats based on $\beta(')$ crystals, where the signal decay depended upon the crystal lattice and polymorphism, generated inappropriate results. Better results were obtained using the bi-Gaussian FID approach to calculate the solid fractions.[22]

Several improvements of these approaches were considered in the current work, where samples with solid contents too low for a solid exponential to be detected were often encountered. Hence, a one-exponential alternative normalized with toluene was proposed. Another drawback was that the liquid exponential was calculated only for the FID signal values longer than 50 μs, which is inaccurate for the identification of the crystalline content in crude oils. In the approach presented in this article, the exponentials are fitted on the first 80 points and the abrupt change in T_2 behavior between crystalline and non-crystalline components was the basis of exponential separation. The ratio between the liquid- and solid-modified relaxation times is consistently high, between 4 and 20 (Table S2 of the Supporting Information), confirming the abrupt change in exponent when the crystalline content starts forming, which further solidifies the use of the two-exponential fit. Separating the liquid from 50 μs would mean that the calculated solid fraction would comprise both crystalline and amorphous solid−liquid transition phases, which are non-crystalline and should not account for the crystalline solid fraction. Moreover, the selection of a specific border point at 50 μs represents an additional assumption.

4. CONCLUSION

This work highlights a novel approach to characterize the crystalline wax content in crude oils based on low-field NMR, which represents an addition and an improvement to established procedures based on DSC, because it allows for the quantification of the solid content at a very low cooling rate, without thermodynamic and baseline determination assumptions. The main novelty in this study is the development of a suitable exponential fit for the FID signal, followed by its application to compute the crystalline solid content in crude oils. The method starts from assessing the crystalline solid fraction in model systems with a high content, resembling at this step the procedures previously applied for solid fat calculation. Thus, the NMR methods were all validated for model systems. However, the content of solid states in crude oil is significantly lower than that in fats and pure waxes, particularly in the temperature range of interest for assessing dynamic wax crystallization. Therefore, the exponential-based model was adapted for such systems, and the method of calculation was split into two cases: the first where the crystalline and non-crystalline components were entirely separated and assessed and the second where the non-crystalline component was evaluated relative to a pure liquid. This second approach allows for the assessment of the solid content, starting from early stages of wax crystallization, while the first FID method is only applicable when the crystallized solid content is high enough (a few percentages). There are, however, some limitations generated by the instrument dead time, inability to separate amorphous phases completely, and chemical composition assumptions about the wax in crude oil. Nevertheless, these barriers can be overcome as NMR instruments become more advanced, by lowering the noise and dead times. Moreover, the direct comparison of results and calculation methods with DSC and NMR CPMG confirms the quality of the method and even indicates higher reliability and lower sensitivity on assumptions with the non-crystallized signal FID method. This creates the groundwork for an improvement in wax crystallization studies using NMR as an alternative to established methods.

■ ASSOCIATED CONTENT

Supporting Information

The Supporting Information is available free of charge at https://pubs.acs.org/doi/10.1021/acs.energyfuels.2c03309.

> Normalization of the DSC curves of crude oils to fit Exxsol D60 in the high-temperature region (Table S1), solid fraction calculated with the two FID methods for macro- and microcrystalline wax in both hydrogenated (Figure S1) and deuterated (Figure S2) toluene, comparison between macrocrystalline wax solutions with varying concentrations in toluene to assess the impact of the wax concentration on the accuracy of the method (Figures S3 and S4), solid fraction as calculated with all of the available methods for 15% macrocrystalline wax in crude oil 2 and crude oils 2, 4, 5, and 6 (Figures S5, S6, S7, S8, and S9), respectively, and indication of the crystalline and non-crystalline average exponential times computed in the biexponential fit (Table S2) (PDF)

■ AUTHOR INFORMATION

Corresponding Author

G. C. Savulescu − *Ugelstad Laboratory, Department of Chemical Engineering, Norwegian University of Sciences and Technology (NTNU), N-7491 Trondheim, Norway;* orcid.org/0000-0003-3278-0745; Phone: +4798655325; Email: george.c.savulescu@ntnu.no

Authors

S. Simon − *Ugelstad Laboratory, Department of Chemical Engineering, Norwegian University of Sciences and Technology (NTNU), N-7491 Trondheim, Norway*

G. Sørland − *Ugelstad Laboratory, Department of Chemical Engineering, Norwegian University of Sciences and Technology (NTNU), N-7491 Trondheim, Norway; Anvendt Teknologi AS, N-7022 Trondheim, Norway*

G. Øye − *Ugelstad Laboratory, Department of Chemical Engineering, Norwegian University of Sciences and Technology (NTNU), N-7491 Trondheim, Norway*

Complete contact information is available at: https://pubs.acs.org/10.1021/acs.energyfuels.2c03309

Notes

The authors declare no competing financial interest.

■ ACKNOWLEDGMENTS

This work is part of SUBPRO SFI, a research-based center within subsea production and processing. The authors hereby acknowledge the financial support from SUBPRO, which is financed by the Research Council of Norway, major industry partners, and NTNU.

■ REFERENCES

(1) Oliveira, L. M. S. L.; Nunes, R. C. P.; Melo, I. C.; Ribeiro, Y. L. L.; Reis, L. G.; Dias, J. C. M.; Guimarães, R. C. L.; Lucas, E. F. Evaluation of the Correlation between Wax Type and Structure/Behavior of the Pour Point Depressant. *Fuel Process. Technol.* **2016**, *149*, 268−274.

(2) Kelland, M.*Production Chemicals for the Oil and Gas Industry*; CRC Press: Boca Raton, FL, 2009; Vol. *1*, DOI: 10.1201/9781420092974.

(3) Gan, Y.; Chen, L.; Zhang, J.; Betancourt, S. S.; Mullins, O. C.; Yan, Z.; Gao, X.; Tian, J.; Chen, W.; Wang, W. Wax-Out Cryo-Trapping: A New Trap-Filling Process in Fluid Migration to Oilfields. *Energy Fuels* **2022**, *36* (16), 8844−8852.

(4) Paso, K.; Senra, M.; Yi, Y.; Sastry, A. M.; Fogler, H. S. Paraffin Polydispersity Facilitates Mechanical Gelation. *Ind. Eng. Chem. Res.* **2005**, *44* (18), 7242−7254.

(5) Venkatesan, R.; Nagarajan, N. R.; Paso, K.; Yi, Y.-B.; Sastry, A. M.; Fogler, H. S. The Strength of Paraffin Gels Formed under Static and Flow Conditions. *Chem. Eng. Sci.* **2005**, *60* (13), 3587−3598.

(6) Yang, F.; Zhao, Y.; Sjoblom, J.; Li, C.; Paso, K. G. Polymeric Wax Inhibitors and Pour Point Depressants for Waxy Crude Oils: A Critical Review. *J. Dispersion Sci. Technol.* **2015**, *36* (2), 213−225.

(7) Kriz, P.; Andersen, S. I. Effect of Asphaltenes on Crude Oil Wax Crystallization. *Energy Fuels* **2005**, *19* (3), 948−953.

(8) Norrman, J.; Solberg, A.; Sjöblom, J.; Paso, K. Nanoparticles for Waxy Crudes: Effect of Polymer Coverage and the Effect on Wax Crystallization. *Energy Fuels* **2016**, *30* (6), 5108−5114.

(9) Coto, B.; Martos, C.; Espada, J. J.; Robustillo, M. D.; Peña, J. L. Analysis of Paraffin Precipitation from Petroleum Mixtures by Means of DSC: Iterative Procedure Considering Solid−Liquid Equilibrium Equations. *Fuel* **2010**, *89* (5), 1087−1094.

(10) Savulescu, G. C.; Simon, S.; Sørland, G.; Øye, G. New Nuclear Magnetic Resonance Approaches on the Evolution of Wax Mobility during Wax Crystallization. *Energy Fuels* **2022**, *36* (1), 350−360.

(11) Chen, J.; Zhang, J.; Li, H. Determining the Wax Content of Crude Oils by Using Differential Scanning Calorimetry. *Thermochim. Acta* **2004**, *410* (1−2), 23−26.

(12) Baltzer Hansen, A.; Larsen, E.; Batsberg Pedersen, W.; Nielsen, A. B.; Roenningsen, H. P. Wax Precipitation from North Sea Crude Oils. 3. Precipitation and Dissolution of Wax Studied by Differential Scanning Calorimetry. *Energy Fuels* **1991**, *5* (6), 914−923.

(13) Batsberg Pedersen, W.; Baltzer Hansen, A.; Larsen, E.; Nielsen, A. B.; Roenningsen, H. P. Wax Precipitation from North Sea Crude Oils. 2. Solid-Phase Content as Function of Temperature Determined by Pulsed NMR. *Energy Fuels* **1991**, *5* (6), 908−913.

(14) Ruffier-Meray, V.; Roussel, J.; Defontaines, A. Use of Pulsed NMR Spectroscopy to Measure the Amount of Solid Deposits as a Function of Temperature in Waxy Crudes. *Oil Gas Sci. Technol.* **1998**, *53*, 531−535.

(15) Kané, M.; Djabourov, M.; Volle, J.-L.; Rutledge, D. N. Correction of Biased Time Domain NMR Estimates of the Solid Content of Partially Crystallized Systems. *Appl. Magn. Reson.* **2002**, *22* (3), 335−346.

(16) Ruwoldt, J.; Humborstad Sørland, G.; Simon, S.; Oschmann, H.-J.; Sjöblom, J. Inhibitor-Wax Interactions and PPD Effect on Wax Crystallization: New Approaches for GC/MS and NMR, and Comparison with DSC, CPM, and Rheometry. *J. Pet. Sci. Eng.* **2019**, *177*, 53−68.

(17) Zhao, Y.; Paso, K.; Norrman, J.; Ali, H.; Sørland, G.; Sjöblom, J. Utilization of DSC, NIR, and NMR for Wax Appearance Temperature and Chemical Additive Performance Characterization. *J. Therm. Anal. Calorim.* **2015**, *120* (2), 1427−1433.

(18) Dudek, M.; Kancir, E.; Øye, G. Influence of the Crude Oil and Water Compositions on the Quality of Synthetic Produced Water. *Energy Fuels* **2017**, *31* (4), 3708−3716.

(19) Dudek, M.; Bertheussen, A.; Dumaire, T.; Øye, G. Microfluidic Tools for Studying Coalescence of Crude Oil Droplets in Produced Water. *Chem. Eng. Sci.* **2018**, *191*, 448−458.

(20) Simon, S.; Nenningsland, A. L.; Herschbach, E.; Sjöblom, J. Extraction of Basic Components from Petroleum Crude Oil. *Energy Fuels* **2010**, *24* (2), 1043−1050.

(21) Gaweł, B.; Eftekhardadkhah, M.; Øye, G. Elemental Composition and Fourier Transform Infrared Spectroscopy Analysis of Crude Oils and Their Fractions. *Energy Fuels* **2014**, *28* (2), 997−1003.

(22) Declerck, A.; Nelis, V.; Rimaux, T.; Dewettinck, K.; Van der Meeren, P. Influence of Polymorphism on the Solid Fat Content Determined by FID Deconvolution. *Eur. J. Lipid Sci. Technol.* **2018**, *120* (3), 1700339.

(23) Abragam, A.*Principles of Nuclear Magnetism*; Oxford University Press: Oxford, U.K., 1961.

(24) Trezza, E.; Haiduc, A. M.; Goudappel, G. J. W.; van Duynhoven, J. P. M. Rapid Phase-Compositional Assessment of Lipid-Based Food Products by Time Domain NMR. *Magn. Reson. Chem.* **2006**, *44* (11), 1023−1030.

(25) Slichter, C. P.*Principles of Magnetic Resonance*; Springer-Verlag: Berlin, Germany, 2013.

(26) Meiboom, S.; Gill, D. Modified Spin-Echo Method for Measuring Nuclear Relaxation Times. *Rev. Sci. Instrum.* **1958**, *29* (8), 688−691.

(27) Provencher, S. W. A Constrained Regularization Method for Inverting Data Represented by Linear Algebraic or Integral Equations. *Comput. Phys. Commun.* **1982**, *27* (3), 213−227.

(28) Burger, E. D.; Perkins, T. K.; Striegler, J. H. Studies of Wax Deposition in the Trans Alaska Pipeline. *J. Pet. Technol.* **1981**, *33* (6), 1075−1086.

(29) Agarwal, A.; Sarviya, R. M. Characterization of Commercial Grade Paraffin Wax as Latent Heat Storage Material for Solar Dryers. *Mater. Today Proc.* **2017**, *4* (2, Part A), 779−789.

(30) Mochane, M. J.; Mokhena, T. C.; Motaung, T. E.; Linganiso, L. Z. Shape-Stabilized Phase Change Materials of Polyolefin/Wax Blends and Their Composites. *J. Therm. Anal. Calorim.* **2020**, *139* (5), 2951−2963.

(31) Japper-Jaafar, A.; Bhaskoro, P. T.; Mior, Z. S. A New Perspective on the Measurements of Wax Appearance Temperature: Comparison between DSC, Thermomicroscopy and Rheometry and the Cooling Rate Effects. *J. Pet. Sci. Eng.* **2016**, *147*, 672−681.

(32) Ruwoldt, J.; Kurniawan, M.; Oschmann, H.-J. Non-Linear Dependency of Wax Appearance Temperature on Cooling Rate. *J. Pet. Sci. Eng.* **2018**, *165*, 114−126.

(33) Dieffenbacher, A.; Pocklington, W. D.*Standard Methods for the Analysis of Oils, Fats and Derivatives*, 7th ed.; Blackwell Scientific Publications: Oxford, U.K., 1992.
(34) Leung, H. K.; Anderson, G. R.; Norr, P. J. Rapid Determination of Total and Solid Fat Contents in Chocolate Products by Pulsed Nuclear Magnetic Resonance. *J. Food Sci.* **1985**, *50* (4), 942−945.
(35) Rutledge, D. N.; Diris, J.; Bugner, E.; Belliardo, J.-J. Biological Reference Materials for the Verification of Sample Preparation and Measurement by Low Resolution NMR. *Fresenius J. Anal. Chem.* **1990**, *338* (4), 441−448.

https://doi.org/10.1021/acs.energyfuels.2c03309
Energy Fuels 2023, 37, 291−300

SUPPLEMENTARY MATERIAL

Novel NMR techniques to assess the wax precipitation evolution in crude oil systems

George Claudiu Savulescu[1] (george.c.savulescu@ntnu.no*) Sébastien Simon[1], Geir Sørland[1,2], Gisle Øye[1]

[1]: Ugelstad Laboratory, Norwegian University of Science and Technology, 7491 Trondheim, Norway

[2]: Anvendt Teknologi AS, Munkvollvegen 56, 7022 Trondheim, Norway

Table S1: Normalization term added to all the points of each DSC data set to fit the DSC measurement for Exxsol D60; 2 parallels are considered – the upper and the lower terms illustrate each of the parallels

System	Normalization term [W/g]
5% macrocrystalline wax in H-toluene	0.026±0.013
10% macrocrystalline wax in H-toluene	0.016±0.004
15% macrocrystalline wax in H-toluene	0.0265±0.0085
Crude oil 1	-0.0005625±0.024375
Crude oil 2	0.000875±0.002875
15% macrocrystalline wax in crude oil 2	0.009±0.005
Crude oil 3	-0.000625±0.002875
Crude oil 4	0.00925±0.00225
Crude oil 5	0.01525±0.00775
Crude oil 6	-0.0005±0.005

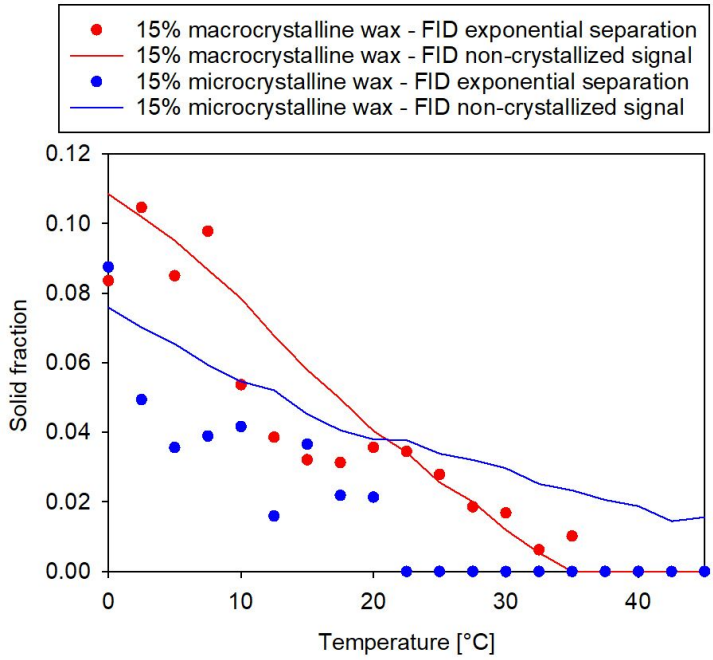

Figure S1: Solid fraction evolution for wax-only systems in hydrogenated toluene, as calculated with the 2 proposed computation methods from FID data

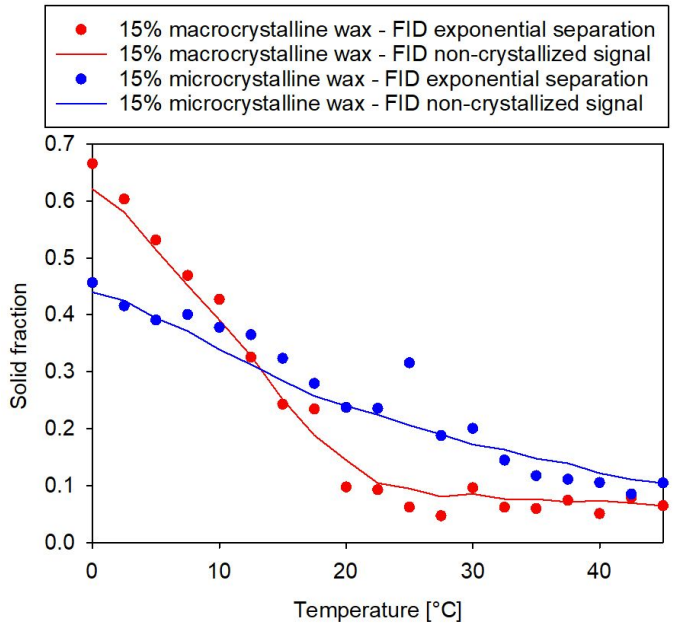

Figure S2: Solid fraction evolution for wax-only systems in deuterated toluene, as calculated with the 2 proposed computation methods from FID data; As the solvent is now deuterated, the signal will be entirely from the 15% of the system that is not deuterated, corresponding the wax. Therefore, the real solid fraction in the entire system will be the solid fraction presented on the y-axis of this figure, multiplied by 0.15.

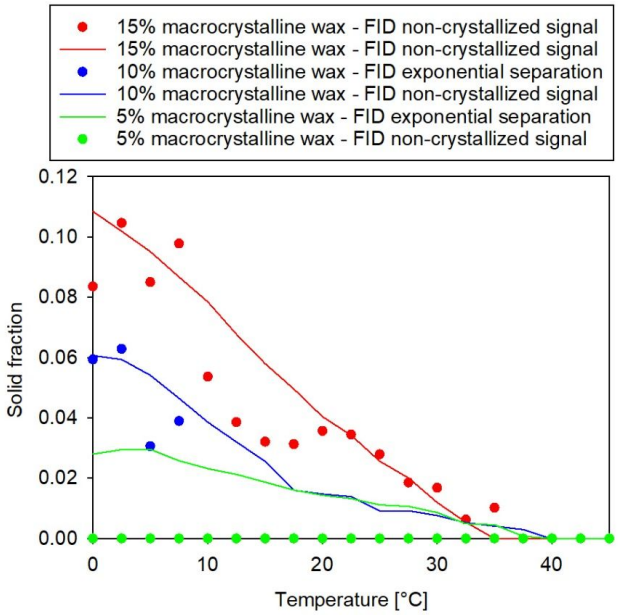

Figure S3: Effect of macrocrystalline wax concentration on solid fraction quantification in wax-only systems in hydrogenated toluene

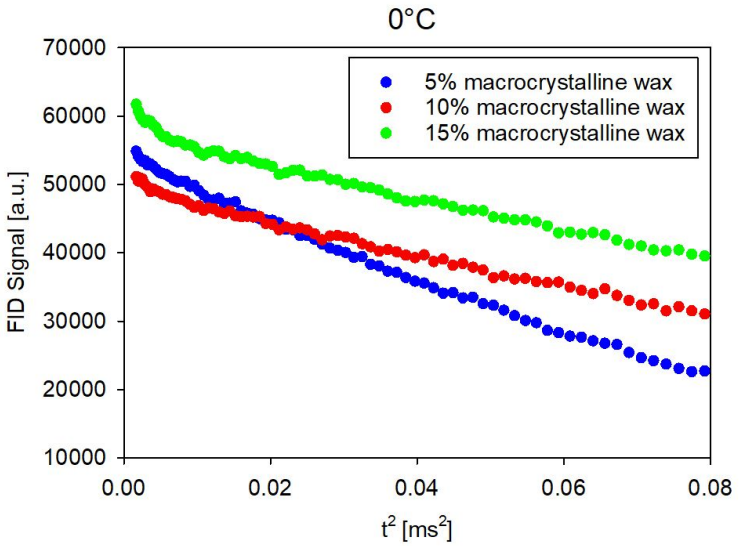

Figure S4: FID signal fitting for 5%, 10% and 15% microcrystalline wax in hydrogenated toluene at 0°C

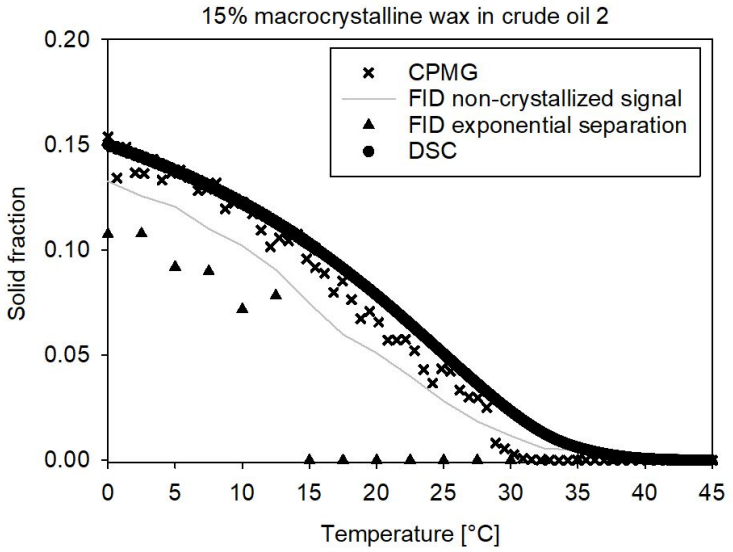

Figure S5: Solid fraction evolution with temperature for 15% macrocrystalline wax in crude oil 2, with all proposed methods

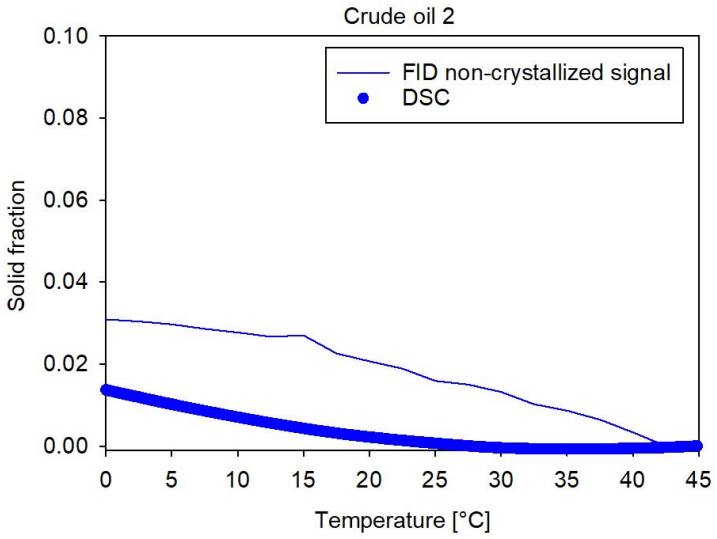

Figure S6: Solid fraction evolution with temperature for crude oil 2, with all proposed methods

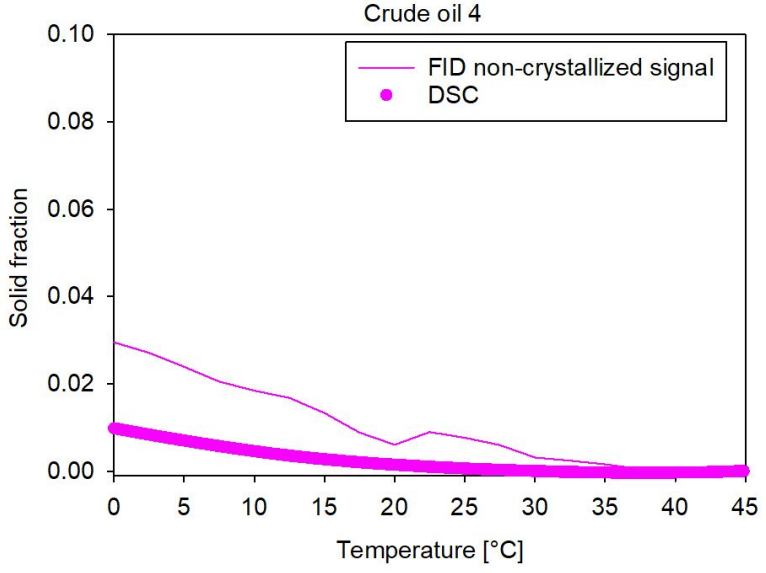

Figure S7: Solid fraction evolution with temperature for crude oil 4, with all proposed methods

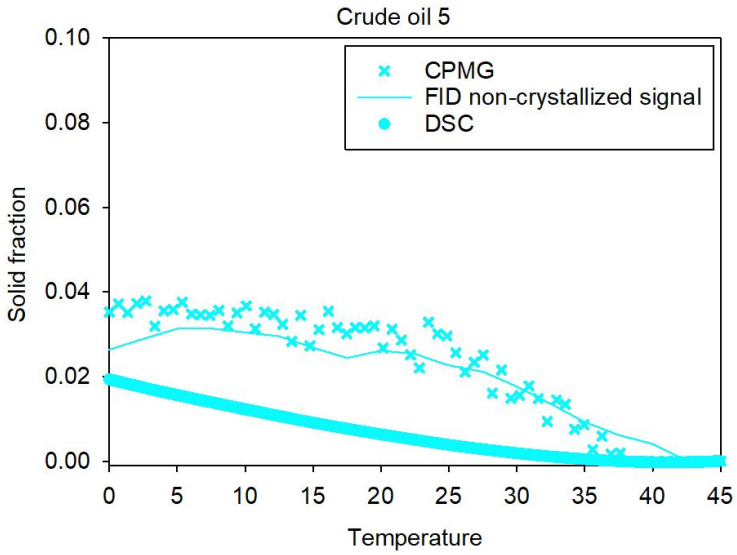

Figure S8: Solid fraction evolution with temperature for crude oil 5, with all proposed methods

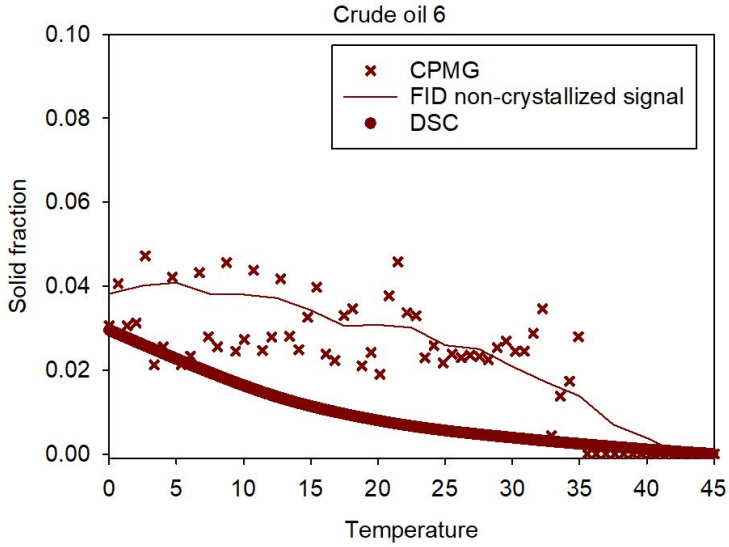

Figure S9: Solid fraction evolution with temperature for crude oil 6, with all proposed methods

Table S2: Evolution of the non-crystalline and crystalline average modified relaxation times. as computed from the fit

Sample	T_l **[ms]**	T_s **[ms]**
Macrocrystalline wax	0.19-0.33	0.04-0.09
Microcrystalline wax	0.25-0.34	0.04-0.06
15% macrocrystalline wax in H-toluene	0.53-0.75	0.04-0.05
15% microcrystalline wax in H-toluene	0.37-0.75	0.03-0.04
15% macrocrystalline wax in D-toluene	0.38-0.80	0.03-0.08
15% microcrystalline wax in D-toluene	0.47-0.72	0.03-0.05
Crude oil 1	0.43-0.67	0.04-0.05
15% macrocrystalline wax in crude oil 2	0.13-0.22	0.01-0.03

ISBN 978-82-326-7734-4 (printed ver.)
ISBN 978-82-326-7733-7 (electronic ver.)
ISSN 1503-8181 (printed ver.)
ISSN 2703-8084 (online ver.)

NTNU
Norwegian University of
Science and Technology